

The Chemical and Dynamical Evolution of Simulated Late-Type Galaxies

Benjamin Bryan Thompson

A THESIS SUBMITTED IN PARTIAL FULFILMENT
OF THE REQUIREMENTS FOR THE DEGREE OF
DOCTOR OF PHILOSOPHY

Jeremiah Horrocks Institute for Maths, Physics and Astronomy
University of Central Lancashire

September 2017

Declaration

The work presented in this thesis was carried out at the Jeremiah Horrocks Institute for Maths, Physics and Astronomy, University of Central Lancashire.

I declare that while registered as a candidate for the research degree, I have not been a registered candidate or enrolled student for another award of the University or other academic or professional institution.

I declare that no material contained in the thesis has been used in any other submission for an academic award. Data and models used in this thesis that are not my own are clearly cited in the text.

Abstract

In this thesis I discuss two projects that have been a major part of my postgraduate studies. The aim of these projects is to study the dynamics and chemodynamics of simulated Milky Way analogues. Specifically, I investigate chemical abundances in the solar-neighbourhood and of the outflow rates of gas of Milky Way analogue discs.

In the first project, I describe a galaxy simulated with the code RAMSES-CH and compare this with chemical abundance data from the Gaia-ESO survey and the RAVE survey. The aim of this work is to improve matching the chemical abundances in stars within the galaxy to those in observational surveys. This is done by sampling our simulation to best match what an observer does in observational surveys. In addition to carrying out an observationally-motivated spatial selection within the simulation and thus comparing like for like, we take into account observational uncertainty and the selection effects (photometric, effective temperature and surface gravity). Incorporating these factors within the simulation data, we find that simply taking a spatial cut alone within a simulation model is not sufficient to match simulated abundances like for like with observational surveys. For complete observational selection functions, like that in the Gaia-ESO survey, the selection function has a minimal impact on the ages and metal abundances. However for a narrower selection function like in the RAVE survey, the impact becomes more noticeable. The method that improves simulation abundance patterns with observations however is the inclusion of an observationally motivated scatter based on

the uncertainties of the observational survey you are studying.

In my second project I study the outflow abundances of gas from the disc of Milky Way-like galaxy in isolation along with inflow from a hot gas halo. I generate a galaxy model from the initial conditions generator code `GALACTICS` and run the simulation with the meshless Lagrangian Godunov-type code `GIZMO`. The simulation's aim is to investigate gravity driven turbulence of a gas disc in the absence of more commonly considered sources of feedback such as supernovae. Our goal is to place a lower limit on this effect in Milky-Way analogues, which from initial investigations conducted without full self-gravity is admittedly anticipated to be small. We present a study the outflow of gas and its relation to the surface density and radius of the disc. In comparison to more idealised parameter studies, we find that the outflows of gas from high surface density regions are suppressed by the cooling flow of the gas halo. This contradicts results from small box simulations, but is reflective of the physics in a full disc model. Nonetheless, outflows up to 1.5 kpc in height are found, and vertical velocity dispersions are in broad agreement with other work that includes additional sources of feedback.

Contents

Declaration	ii
Abstract	iii
Acknowledgements	xv
1 Introduction	1
1.1 Background	1
1.1.1 History and Motivation	1
1.1.2 Dark Matter and Λ CDM	4
1.1.3 Galaxy Evolution, Structure and Morphology	9
1.2 Numerical Simulations	14
1.2.1 Simulation Methodology	14
1.3 Physical Processes of Galaxy Evolution	18
1.3.1 Motivation for Baryonic Feedback	18
1.3.2 Gas Cooling	21
1.3.3 Mergers	24
1.3.4 Star Formation and Supernova Feedback	25
1.3.5 Gas Self Turbulence and Outflows	26
1.4 Chemical Evolution	28
1.4.1 Chemical Evolution Models	28

1.4.2	Chemical Evolution Model Components	32
1.4.3	The Solar Neighbourhood	34
1.5	Thesis Outline	36
2	Comparing Chemo-Dynamical Simulations to Observations of the Milky Way	38
2.1	Introduction and Methodology	39
2.2	Adaptive Mesh Refinement and Galaxy Formation	47
2.2.1	Adaptive Grid	47
2.2.2	N-body Physics	50
2.2.3	Time Evolution	52
2.2.4	Hydrodynamics	53
2.3	RAMSES	56
2.3.1	RAMSES: Cooling Physics and Star Formation	56
2.3.2	RAMSES-CH: Chemical Evolution Supernova Feedback	64
2.3.3	Galaxy Initial Conditions: Selene-CH	73
2.3.4	Choice of Galaxy Feedback Parameters	77
2.4	SynCMD	91
2.5	Observational Surveys	103
2.5.1	The Gaia-ESO Survey	103
2.5.2	The RAVE survey	105
2.6	Comparison Between the Gaia-ESO survey	109
2.6.1	Analysing Selene-CH like an Observer	109
2.6.2	GES-iDR4	111
2.6.3	Selene-CH: The ‘Standard’ Simulation Approach	113
2.6.4	Selene-SCA-G	114
2.6.5	Selene-SYN-G	115
2.7	Gaia-ESO Comparison Results and Discussion	118

2.7.1	Ages	120
2.7.2	Distribution Functions of [Fe/H] and [Mg/Fe]	123
2.7.3	Relationships Between [Fe/H], [Mg/Fe], and Stellar Ages in the Observed and Simulated Solar Neighbourhood	127
2.7.4	Selection Function Subregions	133
2.8	Comparison with RAVE	142
2.8.1	RAVE-DR5	143
2.8.2	Selene-CH-R	145
2.8.3	Selene-SCA-R	146
2.8.4	Selene-SYN-R	147
2.9	RAVE Comparison Results and Discussion	148
2.9.1	Distribution Functions of [Fe/H] and [Mg/Fe]	149
2.9.2	Comparison of Giants, Main Sequence and Turnoff Stars . . .	158
2.10	Conclusions	163
3	Investigation of Halo Inflow and Disc Outflow via Disc-Driven Tur- bulence	171
3.1	Introduction	172
3.2	Simulation Methodology with Gizmo	182
3.2.1	Hydrodynamical Simulations Schemes	182
3.2.2	GIZMO	187
3.2.3	Meshless Methodology	189
3.3	Galaxy Outflow Physics	197
3.4	Methodology	201
3.4.1	Initial Conditions	201
3.4.2	Simulation of an Isolated Galaxy	207
3.4.3	Identifying Giant Molecular Clouds	210
3.5	Morphological Evolution	213

3.5.1	Minimum Timestep Bin and Timestep Evolution.	213
3.5.2	Evolution of Global Properties	214
3.5.3	Giant Molecular Cloud Formation	228
3.5.4	Outflow Physics	233
3.6	Conclusions	241
4	Conclusions and Future Work	247
4.1	Matching Chemo-Dynamical Simulations to Observations of the Milky Way	247
4.2	Investigation of Halo Inflow and Disc Outflow via Disc-Driven Tur- bulence	250
4.3	Future Work	251

List of Tables

2.1	Physical parameters of <i>Selene-CH</i> used in the parameter study	79
2.2	Particle mass and mass properties for each variant of <i>Selene-CH</i> in the parameter study	81
2.3	[Fe/H] and [Mg/Fe] distribution function characteristics in the Gaia-ESO survey comparison.	131
2.4	An outline of the properties of 12 different photometric selection regions on a synthetic CMD	135
2.5	[Fe/H] and [Mg/Fe] distribution function characteristics for the RAVE comparison.	154
3.1	Parameters that are used within GalactICS initial conditions to produce the model galaxy.	203
3.2	The number of particles, masses and softening lengths for the different particle populations of the galaxy simulated in this work.	207

List of Figures

1.1	Hubble Sequence	9
1.2	Halo and galaxy mass function comparison	19
1.3	Cooling rates	23
2.1	Adaptive mesh refinement illustration	49
2.2	Mass of elements ejected by stellar processes in our nucleosynthesis model	69
2.3	Ejection rate of isotopes per $1 M_{\odot}$ formed for stellar particle as a function of cosmic time	71
2.4	Face on gas surface density projection of the simulated galaxy <i>Selene-CH</i>	76
2.5	Gas surface density plots of the <i>Selene-CH</i> variants from the parameter study	83
2.6	Star formation history plots of the <i>Selene-CH</i> variants from the parameter study	84
2.7	Circular and rotational velocity plots of the <i>Selene-CH</i> variants from the parameter study	85
2.8	Star formation rate per stellar surface density density plots for the <i>Selene-CH</i> variants from the parameter study	86
2.9	[Fe/H]-age distribution for the <i>Selene-CH</i> variants from the parameter study.	87

2.10	[Mg/Fe]-age distribution for the <i>Selene-CH</i> variants from the parameter study.	88
2.11	[Fe/H]-[Mg/Fe] distribution for the <i>Selene-CH</i> variants from the parameter study.	89
2.12	Example of a synthetic CMD of synthetic stellar particles generated from the application of SYNCMD to a composite star particle	92
2.13	Scatter plot of $\log(g)$ vs. T_{eff} for <i>GES-iDR4</i>	112
2.14	Synthetic CMD of J vs. J–K in apparent magnitude space for the Gaia-ESO comparison	116
2.15	Synthetic CMD of J vs. J–K in absolute magnitude space for the Gaia-ESO comparison	117
2.16	Distance distribution function results for the Gaia-ESO comparison .	119
2.17	Age distribution function results for the Gaia-ESO comparison	121
2.18	[Fe/H] and [Mg/Fe] normalised distribution functions for the Gaia-ESO comparison.	124
2.19	Age-metallicity relation for the Gaia-ESO comparison	128
2.20	[Mg/Fe] vs. stellar age for the Gaia-ESO comparison.	129
2.21	[Mg/Fe] vs. [Fe/H] for the Gaia-ESO comparison.	130
2.22	A plot of the 12 different photometric selection regions on the synthetic CMD	136
2.23	The distance distribution function corresponding to 12 different photometric selection regions on the synthetic CMD	137
2.24	The [Fe/H] distribution function corresponding to 12 different photometric selection regions on the synthetic CMD.	139
2.25	The age distribution function for the 12 different photometric selection regions on the synthetic CMD	140

2.26	The age-metallicity relation for the 12 different photometric selection regions on the synthetic CMD	141
2.27	Synthetic CMD of the simulated galaxy <i>Selene-CH</i> for the RAVE comparison in apparent magnitude space	150
2.28	Real CMDs of the <i>RAVE-DR5</i> data for the RAVE comparison in apparent magnitude space	151
2.29	Synthetic CMD of the simulated galaxy <i>Selene-CH</i> for the RAVE comparison in absolute magnitude space	152
2.30	The normalised distance distribution function for the RAVE comparison	153
2.31	[Fe/H] and [Mg/Fe] normalised distribution functions for the RAVE comparison	155
2.32	[Fe/H] normalised distribution function for the RAVE as well as the giants, main sequence and turnoff region subsets	159
2.33	Distance normalised distribution function for the RAVE as well as the giants, main sequence and turnoff region subsets	160
2.34	[Mg/Fe] normalised distribution function for the RAVE as well as the giants, main sequence and turnoff region subsets.	161
3.1	An illustration of the volume occupied by particles/cells in different hydrodynamical schemes.	185
3.2	The distribution of gas cells across different timebins for time $t = 200$ Myr	215
3.3	A comparison of the projection of the gas surface density for $t_{\text{bin}} = 2861.0$ yr and $t_{\text{bin}} = 0$ yr	216
3.4	A projection of the absolute difference of the gas surface density between the $t_{\text{bin}} = 2861.0$ yr and $t_{\text{bin}} = 0$ yr	217
3.5	A projection of the gas density distribution of <i>Giz-B</i>	218

3.6	The time evolution of the gas density projection of the galaxy model <i>Giz-B</i>	219
3.7	The density profile of the dark matter halo for <i>Giz-B</i>	220
3.8	The density profile of the gas halo of <i>Giz-B</i>	221
3.9	The temperature profile of the gas of which has its origins as part of the hot gas halo	222
3.10	The relation between the theoretical Jeans mass (M_J) and the particle density of <i>Giz-B</i>	224
3.11	The gas temperature and particle density relation of <i>Giz-B</i>	225
3.12	The evolution of the magnitude of the angular momentum for the gas, dark matter and stellar components of <i>Giz-B</i>	226
3.13	The gas surface density as a function of radius for <i>Giz-B</i>	227
3.14	The tangential (dashed) and circular (solid) velocity profiles as a func- tion of radius for <i>Giz-B</i>	229
3.15	The evolution of the GMC number function	231
3.16	The time evolution of the GMC mass function for <i>Giz-B</i>	232
3.17	The evolution of the velocity dispersion in the z direction for GMCs and disc originating gas for <i>Giz-A</i> and <i>Giz-B</i>	234
3.18	Epcycle frequency κ vs. gas surface density Σ_g for <i>Giz-B</i>	235
3.19	The scale height z_{\max} as a function of radius for <i>Giz-B</i>	236
3.20	The position of disc originating gas particles at height Z above (or below) the disc at radius R with temperature T for <i>Giz-B</i>	237
3.21	Outflow of material per surface area originating from the cold gas disc as a function of time for <i>Giz-A</i> and <i>Giz-B</i>	238
3.22	Outflow rate of material per surface area originating from the cold gas disc as a function of radius for <i>Giz-B</i>	239

3.23	Outflow rate of material per surface area as a function of surface density for <i>Giz-B</i>	240
3.24	Inflow rate of hot halo gas material per surface area as a function of surface density for <i>Giz-B</i>	242
3.25	Flow of gas as a function of time for <i>Giz-B</i>	243
3.26	The velocity dispersion of the disc z axis σ_z as a function of surface density for <i>Giz-B</i>	244

Acknowledgements

I would like to thank my supervisors Brad Gibson, Rob Thacker and Dimitris Stamatellos for their time, energy and support. I would like to thank Dimitris for his support throughout my time as a PhD student. I would like to thank Brad for expanding my range of contacts in Astronomy and opening up opportunities, as well as driving the collaborations that have lead to the production of this thesis. I would like to thank my department director Derek Ward-Thompson for his support and guidance.

I especially like to thank Rob Thacker for the pleasure of hosting me at Saint Mary's University in Halifax, Canada for seven and a half months. Additionally I would like to thank Rob for providing me with extra support and motivation in the final few months of my postgraduate studies. This has been crucial for the timely submission of this thesis. I additionally would like to thank the STFC for providing me with the long term attachment fund. Of which without it, my time in Canada would not have been possible.

I would also thank Gareth Few and Maria Bergemann for their contributions and support.

The comparison with the observational surveys here would not have been done in a timely manner were it not for the support of Maria Bergemann and Andrea Kunder. Maria provided guidance and insights relating to the Gaia-ESO survey. Andrea provided support and guidance relating to the RAVE survey. Additionally, I would like to thank Benjamin Macfarlane and Stefano Pasetto for their support

with SynCMD.

I would like to thank Paul Sutter and Rory Smith for providing collaboration opportunities on work that has not been discussed in this thesis.

None of the work presented here, or the collaborations that have been made would have been possible without funding and technical support, the STFC has funded most of my work but I owe no small debt to UCLan's own HPCF support staff as well as within the Jeremiah Horrocks Institute. Additionally I am grateful for the computing resources that have been provided to me by Rob Thacker at Saint Mary's University in Halifax.

Of course, there is more to life than work. I thank Brad, Gareth and Rob for their time socially outside the office. My thanks additionally goes to those who I have interacted with during my postgraduate studies.

I am not the person I am today without my family and friends. My parents have always been very supportive of me and I would like to thank my mother, Anne, and my father Bryan, for their support.

This thesis is dedicated to Andrea Castro Santos, of which I am grateful and appreciate her kindness, patience and support. Both during my presence and absence. I would like to thank her for her patience during the evenings and weekends I spent writing this thesis. I also would like to thank her parents too for their support whilst I spent my time in Canada.

Chapter 1

Introduction

1.1 Background

1.1.1 History and Motivation

Humanity over known history has always shown a curious desire to understand the nature and evolution of our own Galaxy, the Milky Way. Dating back to the Ancient Greeks, Aristotle wrote in *Meteorologica* (Aristotle 800 BC) that the ancient Greek philosophers Anaxagoras and Democritus proposed that the Milky Way might consist of distant stars.

No actual proof of the Milky Way consisting of many stars came until 1610, when Galileo Galilei (Galilei 1610, 1989) used a telescope to study the Milky Way. He discovered that the Milky Way was composed of a huge number of faint stars. Later Immanuel Kant drawing on the earlier work of Thomas Wright (Wright 1750) suggested that the Milky Way might be a rotating body of a huge number of stars, held together by gravitational forces akin to the Solar System, but on much larger scales (Kant 1755). Kant also theorised that a number of nebulae visible in the night sky might be distant “galaxies” similar to our own and referred to the Milky Way and the “extragalactic nebulae” as “island universes”. In 1771 Charles Messier

CHAPTER 1

published and distributed his catalogue of astronomical objects, which were widely believed to be within the bounds of the Milky Way (Messier 1781).

William Herschel in 1785 (Herschel 1785) attempted to describe the shape of the Milky Way and the position of the Sun. He counted the number of stars in different regions of the visible sky. In his original work, he theorised that the Sun was close to the centre of the Milky Way. In 1845 telescope technology had advanced sufficiently to be able to distinguish between the observed elliptical and spiral-shaped nebulae and additionally resolve individual point sources in some of these nebulae (Hoskin 2002). In 1917, Herber Curtis had observed the nova S Andromedae within what was then known as the Great Andromeda Nebula (Messier object 31). Herber searched through additional photographic records and found 11 more novae. These novae were found to be on average 10 magnitudes fainter than those that occurred in the Milky Way. Curtis then estimated the distance of the Great Andromeda Nebula to be 150 kpc away. This re-enforced the “island universes” hypothesis which held that the spiral nebulae were independent galaxies (Curtis 1988).

In 1920, the Great Debate took place between Harlow Shapley and Heber Curtis, concerning the nature of the Milky Way, the spiral nebulae and the dimensions of the Universe (Shapley & Curtis 1921). This was conclusively settled by Edwin Hubble in 1924, where Hubble measured the distance of some of these nebulae-like objects using Cepheid variables. It was confirmed that these nebulae-like objects were indeed extragalactic objects (Hubble 1929). Hubble was also able to compute the distance of the Andromeda Galaxy to be 275 kpc away, far too distant to be a part of the Milky Way.

The main driving force behind the study of Galaxy Evolution is to understand how our own Galaxy - the Milky Way - formed and evolved with time. From studying the spatial distribution of stars, we can learn about the structure of the galaxy (e.g. Shapley 1918). One can then combine spatial data with stellar abundances and

CHAPTER 1

kinematics to distinguish between idealized formation scenarios (Eggen et al. 1962; Searle & Zinn 1978). If we derive a self-consistent model for gas flows and chemical enrichment, we can then use that model to infer the order which its disc, bulge and halo stars may have formed and understand how they are formed (Tinsley 1980). Additionally if we study how the Milky Way's satellites are moving, then one can infer how much matter there is in the Milky Way and how it is distributed (Schmidt 1956). Overall, one can learn a great deal about the Milky Way's formation and evolution just from studying different physical aspects of the Milky Way and its satellites. The Milky Way is a unique tool for understanding the formation and evolutionary processes of disc galaxies in the Universe. We can study the stellar populations which carry imprints of the history of the Milky Way in greater detail than in any other galaxy through observational surveys.

Astronomers to this day are working on further quantifying the mass of the Milky Way, and why it is that mass (e.g. McMillan 2011). The stellar mass is related to the gas reservoir, but the physics that governs the nature of the gas inflow and the rate of gas accretion is still a highly debated subject (e.g. Marinacci et al. 2010; Martin et al. 2012; Woods et al. 2014). These theories become more interesting upon considering the variation in the different morphologies and overall mass of galaxies (Hubble 1927). The underlying physics would be simple to solve if one could trace the evolution of a sizeable population of galaxies back in time and determine what makes their properties diverge from one another. This can be achieved to a limited degree of accuracy through computational simulations, where we have control over the physics. These physical models are developed from analysing galaxy spectra and stellar populations that use chemical and stellar evolution clocks (Harris & Zaritsky 2001; Thomas et al. 2005). With galaxy formation being a broad field in its own right, this thesis work shall focus on the evolution of chemical elements of the stellar disc and self-turbulent physics of the the gaseous disc.

1.1.2 Dark Matter and Λ CDM

A major milestone in understanding the nature of the Milky Way originates in a discovery by Zwicky in 1933 (Zwicky 1933). Zwicky noticed an inconsistency between the mass inferred from observations of the luminosity of individual galaxies within the Coma cluster and the magnitude of their velocities. There must therefore be non-luminous matter, which is later referred to as dark matter. The idea was discussed widely within the 1970's (Ostriker et al. 1974; Einasto et al. 1974) where observational evidence showed that there must be a 'missing mass' in galaxies. Ostriker & Peebles (1973) theorises that a massive halo is required to stabilise a cold gas disc. Additional evidence for the existence of dark matter is found from a variety of different modes of study. These include the study of the rotation curves of galaxies (Rubin & Ford 1970), the stability of numerical models of galaxy discs (Ostriker & Peebles 1973) and the excess X-ray gas emission from ellipticals (Mathews 1978). Additionally this includes globular cluster dynamics (Huchra & Brodie 1987), gravitational lensing (Tyson et al. 1990) and the study of the Bullet cluster (Clowe et al. 2004). Dark matter in literature is shown to be non-luminous and transparent to light and to have a low interaction cross-section with all phases of matter.

The nature of dark matter itself is a big topic, and one that shall not be delved into too much detail within this thesis. The mass of individual dark matter particles is not fully quantified. However theories of the nature of the mass energy of dark matter vary from it being hot and relativistic (Bond et al. 1980), warm (Shaposhnikov 2008) and cold (Blumenthal et al. 1984) (HDM, WDM and CDM respectively). The ideal candidate for hot dark matter is a light neutrino (such as the τ -neutrino) (Michael et al. 2006). This dark matter candidate is the only theoretical dark matter candidate proven to exist by experiment with particle mass

CHAPTER 1

$m_X \sim 30$ eV. A non standard gravitino was initially suggested as a WDM candidate (Blumenthal et al. 1982) but recently a sterile neutrino seems to be the more likely candidate (Shaposhnikov 2008) of mass $m_X \sim 2$ keV. Possible candidates for cold dark matter include supersymmetric particles (Ellis et al. 1984) or axions (Preskill et al. 1983) with a mass of $m_X \sim 100$ GeV. The idea of hot (relativistic) dark matter particles was ruled out as simulation evidence suggests that galaxies would only form in the most massive clusters (White et al. 1983). Additionally the advancement of large-scale observational surveys such as the CfA galaxy redshift survey (Davis et al. 1982) contradict HDM as the dominant dark matter component since it was unable to explain the clustering of galaxies observed. High mass and low momentum, cold dark matter (Blumenthal et al. 1984) is currently supported by the scientific community. Warm dark matter is also considered still, but the evidence is not as strong (e.g. Schneider et al. 2014) with the physical aspects of warm dark matter can instead be explained by baryonic physical mechanisms (Governato et al. 2012). Additionally, the properties of CDM and WDM on small and large cosmological scales are indistinguishable (Schneider et al. 2014).

In cosmological simulations, cold dark matter particles gravitationally collapse to form large-scale cosmic structure. This forms what is known as the “cosmic web” due to its ‘stringy web-like’ appearance of large-scale filaments (Bond et al. 1996). Dark matter halos form the nodes of these filaments, of which are the regions in the universe where galaxy formation occurs. This is confirmed from comparing the distribution of dark matter halos (e.g. Springel et al. 2005) with galaxy distribution from galaxy redshift surveys (Davis et al. 1982). Dark matter halos form hierarchically (Searle & Zinn 1978; White & Rees 1978) from the continuous merger of less massive dark matter halos to form more massive halo structures (Fall & Efstathiou 1980). These dark matter halos provide a gravitational potential well for gas to cool and condense to form galaxies (White & Rees 1978; Fall & Efstathiou 1980).

CHAPTER 1

The first cosmological simulations of cold dark matter initially used the idea of a flat and high-density (Einstein-de Sitter) Universe (Einstein & de Sitter 1932; Davis et al. 1985) which expands at a constant rate. These simulations produced dark matter density peaks (halos) which matched the density distribution of galaxies in the CfA data (Blumenthal et al. 1984). This was initially the preferred choice (Frenk et al. 1985; White et al. 1987a,b; Frenk et al. 1988, 1990; Efstathiou et al. 1990) of model for the Universe, however galaxy correlations were stronger on large scales than predicted in simulations (White et al. 1993; Jenkins et al. 1998). From the study of Type Ia supernova (SNIa) data (Riess et al. 1998; Perlmutter et al. 1999), as well as the localization of the first peak in the spectrum of microwave fluctuations on the Cosmic Microwave Background (CMB) (de Bernardis et al. 2000; Hanany et al. 2000), one can infer that the Universe expansion rate accelerates. This expansion is governed by a cosmological constant Λ . Thus giving birth to Λ CDM cosmology in which 73% of the universe is composed of dark energy which is responsible for the expansion of the Universe. Additionally, 23% of the universe is composed of dark matter, and 4% is composed of baryons (gas and stars). Studies of SNIa are an active field of research (Maoz et al. 2014). It is a field of interest since SNIa are able to act as a standard candle in measuring cosmological distance scales and thus the inflation of the Universe. This is because SNIa explosions occurs when a carbon-oxygen white dwarf star undergoes a thermonuclear runaway that occurs before the star reaches the point where electron degeneracy can no longer support its mass (Maoz et al. 2014). This means that SNIa produces a consistent peak luminosity which can be used as a standard candle (Das & Mukhopadhyay 2013).

Large-scale density perturbations are required for the cosmic web structure to collapse and form large-scale structure. Rapid cosmic inflation (Linde 1982a; Guth & Pi 1982) in the early universe gave rise to quantum fluctuations that seed the universe with adiabatic, scale invariant density perturbations (Guth & Pi 1982;

CHAPTER 1

Hawking 1982; Linde 1982b; Starobinsky 1982). In the early Universe, these density perturbations occur at a very small amplitude which is modeled with a simple power-law power spectrum $P(k) \sim k^n$. Here n is the power law index which is close to, but smaller than unity. This power spectrum is well constrained from observations of the Cosmic Microwave Background and galaxy distributions (Tegmark 1996; Tegmark & Zaldarriaga 2002; Hinshaw et al. 2013; Larson et al. 2011; Planck Collaboration et al. 2014a,b). As the dark matter distribution expands with the expanding Λ CDM universe so do the density perturbations. These density perturbations increase in amplitude with an expanding universe which causes regions of space to become overdense with respect to their surroundings. Thus the effects of self-gravity within these regions overcome the negative pressure due to the expansion of the Universe. In these overdense regions, dark matter gravitational collapses to form bound and virialized structures called dark matter halos. Dark matter additionally collapses to form filaments between these halos form the cosmic web that we see today.

Although Λ CDM cosmology is not without its issues. We understand in general the physics behind the structure of dark matter, but its interaction with baryonic material is still being a subject of debate today. The presence of very high ‘cored’ density profiles which are found in Λ CDM models but are not observed in surveys (Flores & Primack 1994; de Blok 2010) implies a ‘cuspy halo’ density profile. WDM models could be used to explain the “cuspy-core” problem, but recent work suggests that this is not the case (Macciò et al. 2012a). However with the inclusion of the right baryonic physics, the outflow of baryonic material from the centre of a halo alters the gravitational potential with time. This can flatten the dark matter density profile (Read et al. 2016; Governato et al. 2010; Di Cintio et al. 2014; Macciò et al. 2012b). The Λ CDM model traditionally predicts too many satellite galaxies around a host halo (Moore et al. 1999; Klypin et al. 1999) and overestimates the circular velocities of satellite halos (Boylan-Kolchin et al. 2011; Lovell et al. 2012;

CHAPTER 1

Papastergis et al. 2015) when compared to observations. These are often called the “Missing Satellite Problem” and the “Too Big To Fail Problem”. The former is resolved from the consideration that these galaxies are inefficient at producing stars or are simply not observed (Simon & Geha 2007) or there are baryonic feedback processes which are not yet understood (Brooks et al. 2013). However WDM could resolve this problem (Macciò & Fontanot 2010; Lovell et al. 2014) since the free streaming length of low mass high velocity WDM particles prevents the formation of subhalos, and thus dwarf galaxies would never exist, but this is similar to gas being blown out of the subhalo in Λ CDM models. The latter is resolved from the fact that abundance matching on low mass scales ($M < 10^{9.5} M_{\odot}$) for dwarf galaxies are inaccurate without a correction for baryonic physics which reduces the maximum circular velocity of the subhalos (Sawala et al. 2014, 2015). Finally the abundance distribution of the satellites observed around the Milky Way is aligned in a plane (Kroupa et al. 2005; Metz et al. 2009) with a common direction of rotation (Metz et al. 2008) unlike in simulations where there seems to be no particular alignment. This forms a ‘disc of satellites’ as seen in the Milky Way and Andromeda which is thought to be rare in cosmological simulations (Bahl & Baumgardt 2014; Pawlowski et al. 2012; Pawlowski & McGaugh 2014). There are multiple explanations in Λ CDM which range from filamentary infall of satellites (Libeskind et al. 2005, 2014, 2011), which inherit the spin of the host halo (Libeskind et al. 2009; Lovell et al. 2011; Cautun et al. 2015) or the local shear tensor from neighbouring large-scale structure or voids (Codis et al. 2015; Libeskind et al. 2015) or galaxy mergers (Smith et al. 2016). Overall the discussion here highlights the importance of studying the baryonic physics within high spatial resolution models which aid in developing a more complete understanding of the physics.

CHAPTER 1

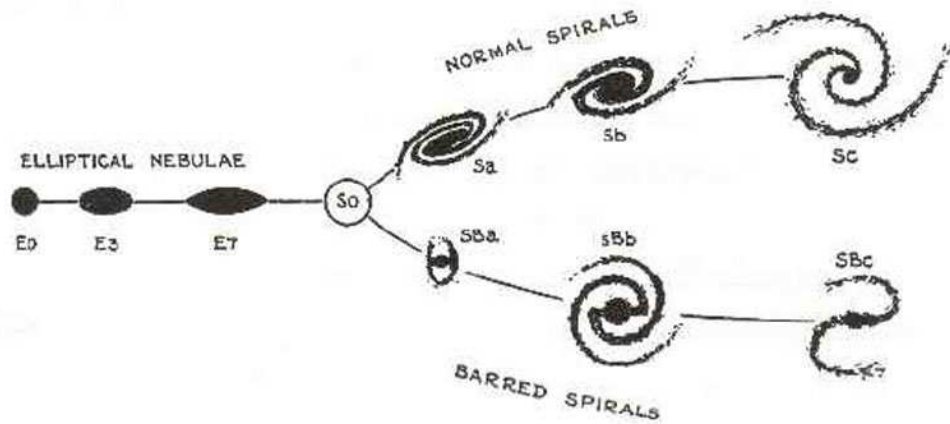


Figure 1.1: The Hubble Sequence figure as shown in (Hubble 1936). Here elliptical galaxies increase in ellipticity e towards the left of the figure. The spheroidal galaxies at the middle have $e = 0$. To the right, spiral galaxies are categorised as either barred or unbarred (stated as “normal” in this figure).

1.1.3 Galaxy Evolution, Structure and Morphology

Our understanding of the formation and evolution of galaxies has been evolving with time just like the paradigm shifts in cosmology. The Hubble Sequence (a.k.a Hubble Tuning Fork), was theorised without any implication of a common evolution track (Hubble 1926b, 1927, 1926a, 1936) as outlined in Figure 1.1 (Hubble 1936; Kormendy & Bender 1996). Originally, one thought that ellipticals - which are also known as early type galaxies - with ellipticity e (Kormendy & Djorgovski 1989) evolved and converged towards $e = 0$ to produce ‘spheroidal’ galaxies (Kormendy et al. 2009). Spheroidal galaxies have similar properties to those of early type and late type galaxies. From here, it was originally thought that the evolution of galaxies forked into two different categories of late type or disc galaxies whose main difference was whether there is a bar structure at the centre of the galaxy (i.e. barred or unbarred). Disc galaxies have a weak spheroidal component and a disc structure with spiral arms that become increasingly loosely wound further along the sequence.

CHAPTER 1

It was later realised that in fact the opposite direction of evolution was true. A dark matter halo hosts the cooling of gas at particular angular momentum which forms a gaseous disc and over time, stars. Over cosmic time the host halos of these galaxies undergo mergers and matter accretes onto the galaxy through hierarchical structure formation. Mergers and collisions of a particular frequency and magnitude eventually disrupt the disc and erase their previous disc structure. Eventually successive mergers form lenticulars, elliptical (Steinmetz & Mueller 1993) or irregular galaxies (Kormendy & Djorgovski 1989; Querejeta et al. 2015). In the standard and well tested Λ CDM cosmological model, galaxies are found to build up their mass through the successive mergers of smaller galaxies via a process known as hierarchical structure formation (e.g. White & Rees 1978; Springel et al. 2005). The result of the merging of smaller galaxies with a disc galaxy like the Milky Way will result in the deposit of stars, gas and dark matter into the Milky Way galaxy and the destruction of the smaller galaxy within the process (e.g. Walker et al. 1996; Abadi et al. 2003; Read et al. 2008).

No two galaxies are likely to ever be the same due to the amount of internal variation of mass, size, structure, stellar populations and gas content that each galaxy has. However, the main contributing factor to the overall shape, morphology and the properties of the galaxy are a result of the internal gas dynamics and baryonic feedback mechanisms in nature. Understanding these processes is one of the main objectives of astronomers who study galaxy formation and understand how they evolved with time. Theorists work towards this iteratively testing their models against observations, and then adjusting the model to address discrepancies (e.g. to constrain the local star formation as shown in Czekaj et al. 2014).

The baryonic components of galaxy models typically consist of the hot gas halo, the cold gas disc, and additionally the stars which originate from the bulge and the disc. Early mass assembly within the Hierarchical Structure Formation paradigm

CHAPTER 1

creates the bulge and halo of disc galaxies (Fall & Efstathiou 1980) with later gas accretion leading to the formation of the galactic disc which fuels star formation. Our understanding of these components and how they have evolved with time is ever improving. For example, the “thick disc” component of a galaxy was discovered in the Milky Way (Gilmore & Reid 1983). The thick disc has a greater scale height, that is the height of which stellar density decreases by a factor of e^1 than the thin disc. Its formation process is still not fully understood and could either be from the accretion of satellites or from the star formation within high velocity dispersion molecular clouds (e.g. Gilmore et al. 1989). Overall the nature of what extent the thick disc is or whether it should be considered as a discrete feature is widely debated (Bovy et al. 2012; Brook et al. 2012a,b).

In 1944, two populations of stars were identified from observations of the Andromeda Galaxy (Andromeda Nebula) and NGC 205 which are “late type” and “early type” galaxies respectively (Baade 1944). Population I stars are young and metal rich and thus represent the more recent phases of star formation, whereas Population II stars are typically older and metal poor. Population II stars are typically found in globular clusters and in the bulge and halo components of disc galaxies. The distribution of stellar populations with different ages and metal abundance ratios is a hot topic in the fields of galactic archaeology and galactic chemical evolution which helps us understand of the evolution of our own galaxy. As such the ages and metal abundance ratios will be an important aspect of this thesis in understanding feedback processes (e.g. Brook et al. 2012a; Few et al. 2012b; Calura et al. 2012; Stinson et al. 2013; Gibson et al. 2013)

The virialized dark matter halo provides gravitational cooling of hot primordial gas which creates an inflow of hot gas that cools on the centre of the dark matter halo. Essentially dark matter halos provide a gravitational potential well for gas to cool and condense to form galaxies (White & Rees 1978). Angular momentum

CHAPTER 1

drives the formation of disc structures during the collapse of the primordial gas clouds which is a result of gravitationally induced tidal torques from large-scale structure (Peebles 1969). Density perturbations within the galactic disc itself drive the formation of spiral arms and the formation of giant molecular clouds (Tasker & Tan 2009) which in turn are active sites of star formation.

Understanding the physics of the baryons and their feedback processes in galaxy formation is one of the main challenges of galaxy formation. These processes include gas infall onto the disc (rate and angular momentum), photoionization heating, star formation, metal enrichment, thermal and kinetic feedback from supernovae, mass loss from evolving stars, galaxy interactions, active galactic nuclei, cosmic rays and radiative cooling just to name some examples. Analytical descriptions of these processes are inherently weak and numerical methods prove to be useful tools in testing models of galaxy formation and evolution. For example, the confirmation of the “angular momentum catastrophe” (often referred to as the “overcooling” problem) (e.g. Navarro et al. 1995) was one of the great insights to come about from numerical simulations. The angular momentum catastrophe is a numerical effect driven by two-body interactions which causes an artificial loss of angular momentum.

The idea for the requirement for galactic feedback processes originated from the “cooling catastrophe” (Blanchard et al. 1992). If there was no feedback, the result is that gas cools too efficiently. This would cause the gas to collapse into the centre of the halo and form too many stars, which contributes towards the loss of angular momentum. This is contradictory to what is seen in observations where much of the baryonic mass seems to be ‘missing’ from galaxies (Gonzalez et al. 2007), which in turn motivated the idea that thermal feedback from supernovae could efficiently expel gas from galaxies (e.g. Mathews & Baker 1971; Larson 1974; Saito 1979; Chevalier & Clegg 1985; Dekel & Silk 1986). The injection for energetic feedback from

CHAPTER 1

stars (winds and supernovae) to counteract this collapse is thus required (White & Rees 1978; Cole 1991) or some form of thermal feedback from supernovae (e.g. Mathews & Baker 1971; Larson 1974; Saito 1979; Chevalier & Clegg 1985; Dekel & Silk 1986). Accurate studies of the feedback mechanisms are not possible without numerical simulations. The non-linear interaction of star formation and supernova feedback has attracted much interest in the astrophysical community. These feedback mechanisms tend to restrain star formation, despite star formation itself being a feedback source via supernova explosions (Strickland & Heckman 2009).

The effects of gravity on the interstellar medium (ISM) can also be considered as a feedback mechanism in its own right. The ISM is dominated by irregular/turbulent gas motions (e.g. Larson 1981; Elmegreen & Scalo 2004) where characteristic velocity dispersions are $\sigma \sim 10$ km/s for HI emission lines in most spiral galaxies. This exceeds the values expected from purely thermal effects such as supernova feedback. This velocity dispersion is typically at its strongest on the outer edges of the galaxy (Petric & Rupen 2007; Dickey et al. 1990), and as observed in NGC 1058, decreases towards the central parts of the galaxy and is uncorrelated to the star formation sites, stars, or gaseous spiral arms.

From measuring the chemistry, ages and dynamics of the individual stars within the Milky Way, we can trace their origins. This is known as “Galactic Archaeology” (Eggen et al. 1962; Freeman & Bland-Hawthorn 2002) in which the underlying principle is that surveys provide a fossil record of the formation and evolution of the Milky Way. Despite significant progress due to the advent of large stellar surveys like the Sloan Digital Sky Survey (SDSS) (York et al. 2000; Eisenstein et al. 2011), we still do not know the precise merger history of the Milky Way.

Galactic chemical evolution (CE) models use predictions based upon the coupling of both the elemental production sites and timescales with phenomenological (but, empirically constrained) parametrisations of star formation and gas outflows/inflows

CHAPTER 1

(Andrews et al. 2016). These model-predicted abundance patterns can be compared directly with observation, as demonstrated in this work, with observations allowing us to shed light on the formation and evolution of the system under study, such as for example our home galaxy, the Milky Way. Studies of the role that CE plays with the physics of the ISM have shown that metallicity-dependent radiative cooling rates of plasmas have an impact on the efficiency of metal transportation through the galactic disc and thus its impact on stellar chemodynamics (Scannapieco et al. 2005).

Additionally, the surrounding extragalactic environment has an impact on their formation processes. These internal galaxy properties influenced by the local density environment include the star formation rate (Muldrew et al. 2012; Wijesinghe et al. 2012), specific star formation rates, metallicities, HI gas (Lara-López et al. 2013), and gas fuelling. Studies of galaxy correlations with environment have led to a variety of work which examines the dependence of galaxy physics upon local environment in both theoretical and observational work (e.g. Norberg et al. 2002; Skibba et al. 2013; Anderson et al. 2014; Skibba et al. 2014). A direct way of quantifying the influence of environment is the local density field of neighbouring galaxies around each galaxy. Overall however there is no one single standard way of defining “environment” (e.g. Muldrew et al. 2012).

1.2 Numerical Simulations

1.2.1 Simulation Methodology

Numerical simulations are at the forefront of theoretical studies of structure formation and provide a genuine insight into the various modes, internal processes and feedback mechanisms of galaxy formation and evolution. In order to model galaxy structure and morphology as described in §1.1.3 the use of numerical simulations

CHAPTER 1

is required in which modern day understanding of cosmology and galaxy formation physics has become increasingly reliant upon it. To construct a theory that can be tested against observations requires combining the theory of the evolution of cosmological density perturbations with a description of the baryonic and other astrophysical processes. The initial conditions of the Universe are very well defined by the power spectrum of primordial density perturbations and are realised from observations of cosmological phenomena (e.g. the cosmic microwave background). The cosmological parameters that define the initial conditions of cosmological simulations are the mean mass density Ω_M , the mean baryon density Ω_b , the dark energy density Ω_Λ , the measurement of the amplitude of the (linear) power spectrum on the scale of $8 h^{-1}$ Mpc σ_8 , and the Hubble constant H_0 . These quantities form phenomena in the Universe such as for example the CMB (Planck Collaboration et al. 2014b; Tegmark 1996), and Type Ia supernova (Riess et al. 1998; Perlmutter et al. 1999). From these initial conditions, we can proceed to model the subsequent evolution of dark matter and baryons.

In principle, the subsequent evolution of the Universe is calculated from Monte Carlo simulations (Sokolowski 2010). Monte Carlo simulations explore the behaviour of a complex system or process which require various samples of parameters or input. These are used to describe systems that are too complex to solve analytically, such as galaxy formation models which have multiple input parameters for initial conditions which are solved over a time series. Overall there are two different methodologies to model the evolution of dark matter and baryons of the Universe. Direct simulations of the physics where the gravitational and hydrodynamical equations in the expanding universe are explicitly solved using numerical simulations. This is achieved using a variety of numerical techniques that have been developed for this purpose (e.g. Katz et al. 1992; Evrard et al. 1994; Frenk et al. 1996, 1999; Katz et al. 1996; Navarro & Steinmetz 1997; Pearce et al. 1999; Blanton et al. 2000; Thacker

CHAPTER 1

et al. 2000). This is the approach that we shall use in this work.

Another approach is known as “semi-analytical modelling” (White & Rees 1978; White & Frenk 1991; Kauffmann et al. 1993; Cole et al. 1994) where the evolution of the baryonic component is calculated using simple analytic models. An example of such code that makes use of this technique is GALFORM (Cole et al. 2000). While the evolution of dark matter is modelled either with direct simulation methods, or using a Monte Carlo technique that follows the formation of dark matter halos via hierarchical merging. Direct simulations model the dynamics of baryons (e.g. cooling gas) in full generality without the need to simplify assumptions. Unlike the direct simulations methodology, semi-analytic modelling does not suffer from resolution limitations, especially when Monte Carlo methods are used to generate halo merger histories, as well as operate at a fraction of computational cost. However there is the need for simplifying assumptions in the calculation of gas properties, such as spherical symmetry. Overall, detailed comparisons between direct and semi-analytic simulations do typically show a good agreement (Pearce et al. 1999; Benson et al. 2000). Although the resolution limitation on direct simulations has improved with recent advances in software techniques and high performance computing (HPC), these improvements with time have lead to simulations of increasingly larger cosmological volumes (e.g. Millennium and Dark Sky Springel et al. 2005; Skillman et al. 2014) or highly resolved but smaller cosmological regions of space (e.g. EAGLE Schaye et al. 2015; Crain et al. 2015). To get around these resolution limitations to better understand the physics, one can simulate the properties of a model galaxy in isolation (e.g. Kim et al. 2016). In this thesis we consider the physics and evolutionary processes of galaxies that are directly simulated in both a cosmological context in Chapter 2 and in an isolated context in Chapter 3.

Within direct simulation (henceforth the words “simulation”, or “numerical simulation” or “direct simulation” thus refer to the same thing) one must simulate the

CHAPTER 1

evolution of dark matter, stars and baryonic gas. The treatment of dark matter, stars and baryonic gas depends entirely on the code that is being used. More likely than not, dark matter and stars are represented by collisionless particles with their dynamics modelled using N-body methods. The baryonic component on the other hand has been handled differently using a multitude of different techniques which either cause fluid to flow in a Lagrangian or an Eulerian manner. These techniques are called Smoothed Particle Hydrodynamics (SPH) (e.g. Springel 2005; Wadsley et al. 2004), Stationary-Grid methods which include Adaptive Mesh Refinement (AMR) methods (e.g. Teyssier 2002; Bryan et al. 2014), Moving-Mesh (e.g. Springel 2010a) and more recently there are Meshless schemes (e.g. Hopkins 2015). The four methods quoted handle the treatment of gas differently using Lagrangian-based or Eulerian-based hydrodynamical solvers. However some form of baryonic feedback is an important feature of galaxy formation simulations. These feedback processes typically involve photoionising ultra-violet (UV) background (Navarro & Steinmetz 1997; Haardt & Madau 1996), Supernova feedback (Katz 1992; Metzler & Evrard 1994; Kay et al. 2002) or AGN (Active Galactic Nuclei) feedback (e.g. Teyssier et al. 2011). In general, the majority of literature concerning these kind of simulations is that the coupling between feedback and the ISM must be efficient (Katz 1992) if galaxies are to avoid overcooling.

In this thesis we consider simulations of spatial resolution on the order of ~ 200 parsecs within a cosmological volume and isolated simulations with spatial resolutions of ~ 50 parsecs. Our cosmological simulation is unable to account for physics on the smaller scale such as ISM turbulence and molecular cloud formation which are parameterised, but allow us to study the chemical evolution of stellar populations in a fine enough detail. However in our isolated simulation we are able to study the formation of Giant Molecular clouds. We describe the cosmological volume in detail in Chapter 2 using a stationary grid method, and the isolated simulation in

Chapter 3 with a Meshless method.

1.3 Physical Processes of Galaxy Evolution

1.3.1 Motivation for Baryonic Feedback

In this section, we discuss the baryonic components of galaxy formation and their implementation in simulations. Additionally, we describe a sample of feedback modes in galaxy formation models. As discussed in §1.1.3, unlike dark matter which its physics can be solved with gravitational instabilities alone, the hydrodynamical physics is far more complex to solve. In general, a well understood theory of baryonic feedback is non-existent. Part of the problem is the inability to resolve the physics at the resolution scales necessary, and thus “sub-grid” approximations are made to account for the physics we cannot resolve (e.g. Crain et al. 2015). Since there are multiple modes of feedback, we shall only discuss those that are referenced heavily in this thesis.

Physical prescriptions of physical baryonic feedback processes are described by free parameters. These typically include the rate of star formation, the threshold gas density for gas to begin to form stars and the efficiency of turning gas into stars (e.g. Davé et al. 2011). Additionally feedback models often include the rate at which supernova occur and the efficiency of energy injection into the interstellar medium (e.g. Martizzi et al. 2015) and the modelling of black holes or AGN (e.g. Wurster & Thacker 2013). The choice of values for the parameters are often motivated by their capability within galaxy formation models to reproduce a subset of available observational properties of galaxies from low redshift (nearby universe data) or from the observational properties of our own galaxy (e.g. Leroy et al. 2008; Stinson et al. 2012; Bergemann et al. 2014).

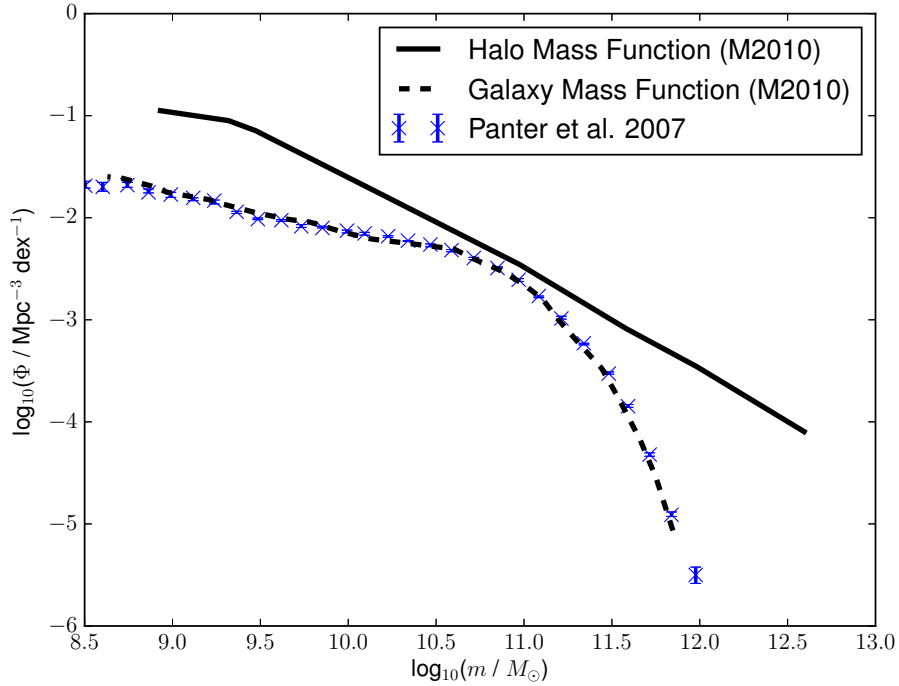


Figure 1.2: A comparison of the galaxy mass function with the halo mass function. We present the observed galaxy mass function (blue crosses and error bars, as seen in Panter et al. 2007) which is accompanied by a galaxy mass function (Presented as a dashed black black line in this figure. From Moster et al. 2010, and quoted in Figure 1 as the model with scatter in the referenced publication.). We compare this with the halo mass function (black solid line) as shown in Moster et al. (2010). The halo and gas mass functions are different shapes which implies that the stellar-to-halo mass ratio is not constant. This is due to the baryonic processes involved in galaxy formation (White & Rees 1978) with the lower mass end influenced by supernova feedback and the higher mass end by AGN feedback.

CHAPTER 1

Physical mechanisms of galaxy formation are required in order to solve for baryonic properties of galaxies, for example to produce the slope of the galaxy mass function (or galaxy luminosity function). White & Rees (1978) found that their prediction for the faint end of the luminosity function was steeper than the observational estimates, which thus requires some form of supernova feedback in order to make this slope flatter. The high mass and brighter end needs to be quenched by AGN feedback (e.g. Granato et al. 2004; Monaco & Fontanot 2005; Cattaneo et al. 2005; Di Matteo et al. 2005; Croton et al. 2006; Bower et al. 2006). See Figure 1.2 for an illustration of the differences between the halo mass function and the galaxy mass function. Figure 1.2 presents the observed galaxy mass function from Panter et al. (2007) as well as the galaxy and halo mass function models from Moster et al. (2010) (quoted as M2010). The actual implementation of supernova feedback varies from model to model but one commonly used implementation is the Sedov blast wave formalism (Sedov 1959) in which the shock velocity of the ejected matter increases linearly with radius i.e:

$$v_s(t) = \frac{dR}{dt} = \frac{2}{5} \frac{R(t)}{t}, \quad (1.1)$$

where $R(t)$ is the radius of the shock. More details of the Seldov formalism is outlined in Sedov (1959). It is often combined with the formalism in Taylor (1950) to make the Taylor-Seldov formalism. The ejecta expands freely subject to mass that is swept from the forward shock is smaller than the supernova ejecta. The reverse shock heats up the interior, which causes the hot gas temperature and pressure to rise, and thus expansion into the external medium proceeds with negligible radiative cooling. Upon expansion, the temperature drops and radiative cooling becomes important. This creates a thin dense shell on the outer edge of the supernova remnant (SNR) and here the temperature is at its lowest but its density is at its highest. This is known as the pressure-driven snowplow phase and the interior hot gas has a non-negligible

CHAPTER 1

pressure (Cox 1972; McKee & Ostriker 1977). The dense shell expands under its own momentum as the internal pressure is exhausted. This occurs until it merges with the surrounding interstellar medium. During its expansion, the shell sweeps up the ISM gas.

A detailed physical model is required to model the gas physics within simulations of galaxy formation. A physical model is required to consider how cold gas is heated and removed from the galactic disc, and how the rate of gas cooling from the hot halo is suppressed. Both these modes diminish the reservoir of available star forming cold gas. A detailed model should include a multiphase interstellar medium with hot and cold gas components, tracking collision between cold gas clouds, or giant molecular clouds, and their evaporation by supernova heating (McKee & Ostriker 1977; Efstathiou 2000; Monaco 2004). Since none of the models discussed in this thesis involves AGN feedback from a super-massive black hole, we shall focus this discussion on the feedback processes involved primarily in Milky Way-like galaxies. The motivation for invoking feedback in galaxy formation models is to reduce the star formation rates to ‘flatten the slop’ at the faint end of the predicted galaxy luminosity function, and to bring simulations in line with the observed galaxy luminosity function (Press & Schechter 1974; Cole 1991; White & Frenk 1991).

1.3.2 Gas Cooling

The cooling of gas is an important process in galaxy formation since it sets the rate at which star forming gas becomes available (Blumenthal et al. 1984). White & Rees (1978) were the first to theorise that dark matter halos enable the cooling of gas (White & Frenk 1991) (but additionally in Rees & Ostriker 1977; Silk 1977; Cole 1991; Lacey & Silk 1991). As dark matter density fluctuations enable its gravitational collapse, the gas is assumed to be heated by shocks as the gas falls into the potential well of the dark halo. The gas attains a virial temperature T_{vir}

CHAPTER 1

of the halo, which depends on the mass of the halo. Assuming an isothermal profile for the gas and dark halo;

$$T_{vir} = \frac{1}{2} \frac{\mu m_p}{k_b} V_c^2, \quad (1.2)$$

where μm_p is the mean molecular mass of the gas and k_b is the Boltzmann's constant.

The following equation:

$$V_c^2 = \frac{GM}{r_{vir}}, \quad (1.3)$$

describes the circular velocity V_c of the halo at the virial radius r_{vir} and G is the gravitational constant. Dark matter halos are supported against further gravitational collapse by pressure created by the thermalized velocities of dark matter particles.

Gas can cool through many other physical mechanisms (e.g. Kauffmann et al. 1993; Mo et al. 2010). The importance of these various mechanisms depends on the conditions in the universe at the time gas is cooling and the temperature, density and metal properties of the gas at that time. The net cooling rate is dependent on the properties of the gas density, the UV background (Haardt & Madau 1996) and approximate overall interstellar radiation field. Above 10^4 K cooling processes are dominated by the traditional atomic process such as those related to collisional ionization/excitation and at higher temperatures bremsstrahlung. Below 10^4 K either the properties of the cooling curve are extrapolated to cooler temperatures, or a fine-structure and molecular cooling model is implemented. In Chapter 2, we use a numerical simulation code that uses a fine structure cooling model based on Rosen & Bregman (1995) and in Chapter 3 we use another cooling model based on Robertson & Kravtsov (2008). We encourage the reader to view these refereed papers as a detailed discussion is beyond the scope of this thesis.

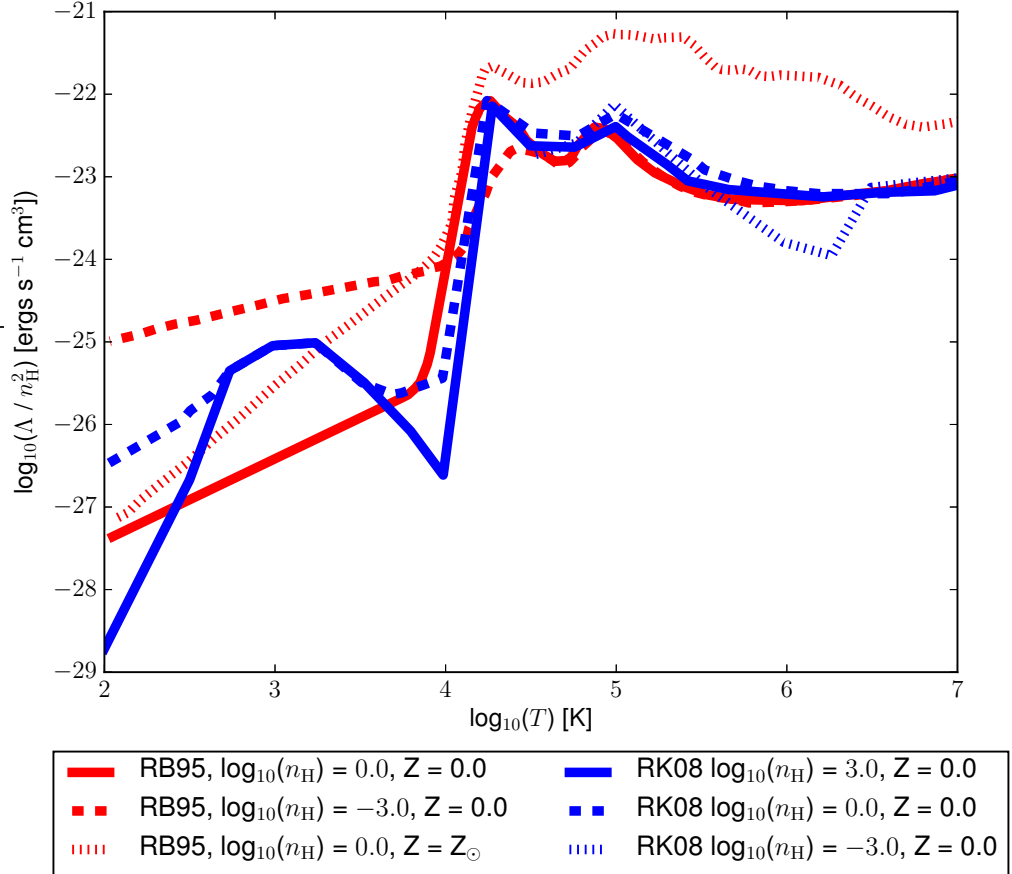


Figure 1.3: Cooling rates (Λ) for interstellar and intergalactic gas function gas temperature (T). The red functions (labelled RB95) are based on the work of Rosen & Bregman (1995) and the blue functions (labelled RK08) are presented in Robertson & Kravtsov (2008). For temperatures greater than 10^4 K cooling both models have similar cooling rates and derived from the use of the photoionisation code CLOUDY (Ferland et al. 1998). We include variations of the gas temperature, density (n_{H}) and metallicity (Z) which are labelled above. The data for the sharp decrease in cooling rate at 10^4 K is slightly spread out for clarity.

1.3.3 Mergers

In White & Rees (1978), dark halos grow through mergers and accretion, with dynamical relaxation effects erasing any traces of progenitor halos at each stage of the merging hierarchy (see Press & Schechter 1974). Galaxies survive the merger of their parent halos, which results in them being more concentrated than dark matter due to dissipative cooling of gas.

Mergers provide a rich source of gas for the more massive galaxy and are a typical occurrence in cosmological simulations of galaxies and the universe. As a satellite galaxy orbits its parent central galaxy in their host dark matter halo, it gradually loses energy through dynamical friction (Chandrasekhar 1943). The satellite galaxy accretes gas, stars and dark matter. The accreted material concentrates in the wake of the moving object, pulling it back, and slowing it down. The satellites orbital energy decays and experiences an infall towards the centre of the galaxy (Binney & Tremaine 1987). This is defined on a timescale which can be computed for the dynamical friction process to remove orbital energy of the satellite completely, of which if the timescale is shorter than the lifetime of the dark halo, then the satellite merges with the central galaxy, which accretes star forming gas into the galaxy. The impact of the galaxy merger is usually quantified by the ratio of the mass of the accreted satellite galaxy, to the central galaxy. Numerical works exist where satellites of different mass and gas content have been fired at central galaxies (e.g. Barnes & Hernquist 1991, 1992; Mihos & Hernquist 1994b, 1996; Walker et al. 1996). Depending on the nature of the merger, the disc of the central galaxy can be destroyed. A major merger (where the mass of the central galaxy is similar to the satellite) can bring in a burst of star formation, and change the morphology and properties of the stars in the central galaxy (Baugh et al. 1996; Somerville et al. 2001; Baugh et al. 2005).

1.3.4 Star Formation and Supernova Feedback

Star formation models in galaxy formation still rely on a significant number of free parameters (such as for example a gas threshold density for star formation to occur), and thus no functional form of star formation exists. Progress has been made in understanding the properties of the first generation of stars, when they formed and what mass they had (Smith 2007; Crosby et al. 2013). We also have some understanding of the distribution of stellar masses produced, which is quantified by the stellar initial mass function (IMF) (See §1.4.2), and an understanding for the conditions of star formation in galactic discs and starbursts. Overall the implementation of star formation and supernova feedback varies from model to model. The most frequently used implementations of the IMF are the Kroupa (2001) model and the model presented in Chabrier (2003). The former distribution takes the shape of a broken power law, and the latter is a log-normal distribution.

Cold gas ejection from a galactic disc by supernova driven wind is the most common form of feedback in galaxy formation models (e.g. Larson 1974; Dekel & Silk 1986). Cold gas is reheated and blown out of the disc to the hot gas halo, of which it can either re-cool back onto the disc (i.e. “retention feedback”), or be ejected altogether (i.e. ‘ejection feedback’). Both the “retention” and “ejection” modes of feedback have been shown to have a significant impact within galaxy formation models (e.g. Kauffmann et al. 1999; Somerville & Kolatt 1999; De Lucia et al. 2004).

Supernova driven winds reduce the number of faint galaxies to match the observational abundance. The strength of this feedback mode is not trivial to model. An excessive supernova feedback rate results in galactic discs that are larger than observed (Cole et al. 2000; de Jong & Lacey 2000) and introduce a deviation in the predicted Tully-Fisher relation ($L \propto V_c^4$ where L is the galaxy luminosity and V_c is the circular velocity of the galaxy) for spirals (Cole et al. 1994; Somerville &

CHAPTER 1

Primack 1999). Additionally, this would cause a mismatch in comparison with the predicted luminosity function. Strong supernova feedback would wipe out Milky Way-like galaxies and cause more gas to cool in more massive halos.

Overall, the physical implementation of supernova feedback varies from model to model. Commonly based on the injecting of energy into the interstellar medium over a specific period of time with some efficiency factor (Stinson et al. 2006; Woosley & Weaver 1995). Additionally, the dispersion of energy sometimes involves the use of a blast wave model (Stinson et al. 2006). However, with the inclusion of chemical evolution models, one can use nucleosynthesis models to better model supernova feedback and its impact on the temperature of the gas, and the chemical abundance ejected into the ISM (Kawata & Gibson 2003; Few et al. 2012a).

1.3.5 Gas Self Turbulence and Outflows

The effects of gravity on the ISM can also be considered as a gravitational feedback mechanism in its own right. The ISM is dominated by irregular/turbulent gas motions (e.g. Larson 1981; Elmegreen & Scalo 2004) where characteristic velocity dispersions are of the order of $\sigma \sim 10$ km/s for HI emission lines in most spiral galaxies. This exceeds the values expected from purely thermal effects such as supernova feedback. This velocity dispersion is typically at its strongest on the outer edges of the galaxy (Dickey et al. 1990), and as observed in NGC 1058, decreases towards the central parts of the galaxy and is uncorrelated with active star formation sites or spiral arms (Petric & Rupen 2007). The origin of the turbulence of the ISM, or the gas disc, is still subject to debate (Burkert 2006). Large-scale expanding outflows from high pressure HII regions (Kessel-Deynet & Burkert 2003), stellar winds or supernova are potential causes. Although supernova explosions dominate the energy input into the ISM (e.g. Mac Low & Klessen 2004; Dib et al. 2006) which can fuel turbulence (Vollmer & Beckert 2003), they cannot explain the broad HI

CHAPTER 1

lines in galaxies with low star formation rates.

Overall, the viscosity of the baryonic gas produced by self turbulence is not thought to have a strong influence on gas evolution, except in magnetized or hot environments such as a galaxy cluster (Sijacki & Springel 2006). The viscosities could impact disc evolution which take the form of large-scale instabilities (Gammie 2001; Rafikov 2009), or interactions between giant molecular clouds (Vollmer & Beckert 2002). Cloud interactions generate gas viscosities through gravitational scattering, which converts orbital energy into large-scale turbulence (Gammie et al. 1991; Fukunaga & Tosa 1989; Agertz et al. 2009a). Additionally, during inelastic collisions between clouds, shocks convert orbital energy into turbulence and heat within the colliding clouds (e.g. Gittins et al. 2003; Kitsionas & Whitworth 2007; Anathpindika 2009). Kinetic energy is dissipated through radiative processes during these collisions, along with turbulent energy which generates thermal energy. These processes are significant even in the absence of star formation as shown from simulations (Mac Low & Klessen 2004; Dib et al. 2006; Agertz et al. 2009a).

Another source of turbulence is the rotation of the galactic disc itself which is a huge reservoir of energy (Fleck 1981). Any mechanism able to generate random motions from ordered circular motion could sustain turbulence for many orbital times. Realistic models of galactic discs form complicated turbulent velocity fields from gravitational and thermal instabilities under the influence of galactic rotation (Wada et al. 2002; Wada & Norman 2007). Fukunaga & Tosa (1989) showed that rotational energy randomizes the motions of the cold cloud component of a galactic disc via gravitational scattering from their random epicyclic motions. This was later quantified by Gammie et al. (1991) who showed that the cloud velocity dispersion could reach 5 to 6 km/s in this way, in agreement with observations (Stark & Brand 1989).

These turbulent motions result in the creation of gas outflows in the galactic disc.

CHAPTER 1

Multi-wavelength observations reveal the existence of massive, galaxy-scale outflows of multiphase material, driven from rapidly star-forming galaxies (e.g. Heckman et al. 1990; Bomans et al. 1997; Pettini et al. 2001; Weiner et al. 2009; Martin et al. 2013). Gas outflows play a fundamental role in galaxy evolution due to enriching the intergalactic medium (IGM) (Songaila & Cowie 1996; Rauch et al. 1997; Simcoe et al. 2002; Pichon et al. 2003; Schaye et al. 2003; Adelberger et al. 2005, 2006; Ferrara et al. 2005; Steidel et al. 2010; Martin et al. 2010), shaping the mass-metallicity relation (Dekel & Silk 1986; Tremonti et al. 2004; Erb et al. 2006; Mannucci et al. 2010) and help eliminate small-scale random magnetic fields from galactic discs (Shukurov et al. 2006; Sur et al. 2007; Chamandy et al. 2014). Yet despite all of this, our understanding of the dynamical processes that influence the evolution of galaxy outflows remains challenging. We attempt to quantify some properties of galactic turbulence in a Milky Way-like galaxy in Chapter 3 as well as of giant molecular clouds.

1.4 Chemical Evolution

1.4.1 Chemical Evolution Models

A primary diagnostic tool used in galaxy formation is the determination of elemental abundance patterns. Galactic archaeological studies of a group stars with similar ages, kinematics and metal abundances could typically be used to trace a similar birth location at a similar point in time. Essentially the gas, the metal abundance (metallicity) of gas acts as a historic tracer of galaxy formation and additionally influence the evolution of the surrounding medium. Scannapieco et al. (2005) shows that the cooling rates of the gas phase result in differing internal stellar dynamics depending on the efficiency with which metals are diffused in the galaxy.

These properties within the context of galaxy formation have been widely studied

CHAPTER 1

(e.g. Lacey & Fall 1983; Woosley & Weaver 1995; Vilchez & Esteban 1996; Nordström et al. 2004; Bergemann et al. 2014; Kordopatis et al. 2015; Mollá et al. 2015). The galactic archaeological approach was used to discover the notion of ‘inside-out’ galaxy formation (White & Rees 1978; Fall & Efstathiou 1980; Lin & Pringle 1987; Clarke 1989). The inner regions of the galaxy formed first (i.e. the bulge) and then the outer regions formed or accreted later. Star formation in disc galaxies gradually radially migrated outwards in time. This creates a gradient in age and thus metallicity due to the continuing gas enrichment by metals. These trends guide and develop our understanding of the physical processes which undergo within galaxy formation models. The description of how elements evolve with time is described by a chemical evolution model (CEM), of which a well defined one should be able to recover the observed metallicity dispersion and growth rate (Meusinger et al. 1991; Edvardsson et al. 1993a; Bensby & Feltzing 2006; Ramírez et al. 2007). However there are large uncertainties associated with the derivation of stellar ages, thus age-metallicity relation a less reliable constraint than the α -iron relation. Where ‘ α -process elements’ are elements where the common isotope is formed through successively adding helium nuclei in nuclear reactions. These α -process elements are C, N, O, Ne, Mg, Si, S, Ar, Ca and Ti. The ‘iron-peak elements’ are the heaviest stable elements produced in stars (such as V, Cr, Mn, Fe, Co, and Ni). The dispersion of the iron abundance (Wyse & Gilmore 1995; Nordström et al. 2004) is an observation that may be used to understand the dispersion in metallicity. It is common to denote the element abundances as a ratio of two elements. The square bracket notation used for stating element abundance ratios is defined as,

$$[A/B] \equiv \log_{10}(N_A/N_B) - \log_{10}(N_{A,\odot}/N_{B,\odot}), \quad (1.4)$$

where N is the number of atoms of a particular element (in this case the number of element A or element B) and \odot is denoted as the solar abundance of a particular

CHAPTER 1

quantity, and thus in this case is the abundance of a particular element in the Sun. N can also be substituted by mass to attain the same value of $[A/B]$.

Tracing and studying element abundances of stars and gas provide valuable data in understanding the formation history of the host galaxy in addition to the stellar dynamics. Observations imply that α -process elements are produced on shorter timescales than iron-peak elements (Tomkin et al. 1985; Carbon et al. 1987; Edvardsson et al. 1993a; Reddy et al. 2006; Ramírez et al. 2007). This is theorised to be a consequence of varying nucleosynthetic processes in stars of different masses and different initial element abundances. Once a star's nuclear burning fuel is depleted, it is possible for it to erupt as a supernova. The two main types of supernova are SNII which has broad hydrogen lines in their spectra and SNIa which lacks hydrogen and has a strongly ionised Silicon (Si II) line. SNII are thought to represent the end-stage of the life cycle of a massive star after burning through its nuclear fuel, thus these stars have shorter lifespans than stars that undergo SNIa since massive stars burn through their nuclear material at a quicker rate. Additionally, SNII and other massive stars produce a larger quantity of α -elements relative to SNIa. SNIa are thought to originate in binary systems where a white dwarf accretes matter from its companion (Iben & Tutukov 1984; Whelan & Iben 1973). An additional mechanism involves two white dwarf stars merging after emission of gravitational energy (Iben & Tutukov 1984; Webbink 1984). Overall these scenarios take much more time than the lifespan of a massive star. In general, SNIa originate from long-lived low mass stars (and thus a long lived source of metal) and produce predominantly iron-peak elements but the exact nature of the SNIa progenitor is still subject to debate.

Mergers have a strong impact on chemical evolution since they disturb the distribution of metals and flatten existing gradients (Perez et al. 2011). Gas from the merging body is accreted into the central regions (Barnes & Hernquist 1992) and ignite bursts of star formation. The merger brings unenriched gas from the merging

CHAPTER 1

body but also pre-enriched stars and gas. Additional star formation occurs as the gas is accreted forming a new and younger disc structure in place of the disturbed older disc. Secular dynamical processes are also important because bar and spiral structures inspire radial migration to flatten metallicity gradients.

The first chemical evolution models assumed a chosen IMF and star formation history (SFH). Semi-numerical analysis techniques were used to calculate the metal content in spatial region as a result of stellar nucleosynthesis in that region (With examples found in Talbot & Arnett 1971; Pagel & Patchett 1975; Tinsley 1980; Matteucci & Francois 1989; Carigi 1994; Giovagnoli & Tosi 1995; Prantzos & Aubert 1995; Pagel 1997; Chiappini et al. 1997; Ramírez et al. 2007). These models are useful tools which allow for numerous realisations to be examined, but with the lack of a self-consistent dynamical component. Combining this technique with halo merger trees from cosmological simulations are used to create semi-analytical chemical evolution models (Lacey & Silk 1991; Devriendt & Guiderdoni 2000; Hatton et al. 2003; Pipino et al. 2009). These include analytical descriptions of the mergers to capture some dynamical behaviour whilst maintaining a low CPU cost.

Chemical evolution models can also be applied to sub-grid chemical evolution treatments in fully hydrodynamical simulation codes. The majority of these are SPH codes (Lia et al. 2002; Valdarnini 2003; Kawata & Gibson 2003; Kobayashi 2004; Tornatore et al. 2004; Romeo et al. 2005; Scannapieco et al. 2005; Martínez-Serrano et al. 2008; Oppenheimer & Davé 2008; Wiersma et al. 2009; Stinson et al. 2010; Rahimi et al. 2010; Shen et al. 2010) but these have also implemented in AMR codes too (Few et al. 2012a, 2014). These demonstrate that the cosmological nature of galaxy formation has an impact on the global metallicity and the distribution of metals in the gas and stellar populations. Studies show that SPH schemes however do not represent turbulent behaviour as accurately as AMR schemes do (O’Shea et al. 2005; Agertz et al. 2007; Tasker et al. 2008) and yet these codes represent the

CHAPTER 1

vast majority of cosmological CEMs. This is because traditional implementations of these codes within SPH codes fail to include any treatment of interparticle mixing. This hinders their ability to correctly trace the evolution of metal diffusion (Pilkington et al. 2012b). Mixing is relevant in recovering the metallicity distribution of the solar neighbourhood. Artificial mixing in SPH codes improves this (Shen et al. 2010) but the magnitude of this mixing remains as a free parameter.

CEMs are not without their flaws and a current ongoing one is that CEMs predict a greater number of long-lived metal-poor stars than observational surveys suggest (van den Bergh 1962; Pagel 1997). This is often referred to as the G dwarf problem. One solution to this suggests that the G dwarf problem could be due to a poor selection of stars (Bazan & Mathews 1990), but this does not provide enough of a correction to observations to fully explain the problem. Another possibility is that the mass function of stars in low metallicity gas skews away from the low mass end from the inclusion of massive Population III stars to reduce the number of G dwarves that may be observed today (Schmidt 1963; Larson 1998). The current successful solution to the G dwarf problem tackles shortcomings in the CEM itself. An additional gradual infall rate allows early enrichment without excessive star formation (Larson 1972) and this infall occurs naturally in hydrodynamical simulations.

1.4.2 Chemical Evolution Model Components

Nucleosynthetic processes and the stellar lifetimes of stars are mass dependent, and thus one of the main ingredients in CEMs is an initial mass function (IMF). The IMF $\psi(m)$ defines the total mass of stars, M of that are born with mass m in a given mass interval dm ,

$$\psi(m) \propto \frac{dM}{dm}. \quad (1.5)$$

A qualitative understanding of the form of the IMF was derived in the work of

CHAPTER 1

Salpeter (1955). A degree of uncertainty for the actual slope of the IMF is still large enough to result in significant variations in modelling galactic abundance patterns (e.g. $[\text{O}/\text{Fe}]$ can vary at the order of magnitude of 0.3 dex depending on the slope of the IMF (Few et al. 2012a, 2014)).

The earliest IMF proposed by Salpeter (1955) where luminosity function of stars determines the mass function of stars at the time they are formed. Further complex determinations of the IMF are proposed to capture the substellar regime. This has resulted in piecewise functions which generate multi-slope IMFs (Tinsley 1980; Scalo 1986; Kroupa et al. 1993; Scalo 1998; Kroupa 2001; Chabrier 2003) which predict a luminosity function closer to the observed value.

Stellar lifetimes define the time stars diverge off the main sequence and return gas which has undergone nucleosynthesis to the ISM. The lifetime of stars is a function of stellar mass and has a lesser dependence on metallicity. The duration of energetic contributions to the ISM is also controlled by theoretical stellar lifetimes. The choice of IMF and the lifetimes allow the number and mass of stars evolving from the main sequence to be calculated as a function of time. After this has occurred stars exist purely as remnants with no further mass or energy output to the ISM.

Different analytical stellar lifetimes of stars as a function of mass have been proposed by different groups (Tinsley 1980; Tosi 1982; Maeder & Meynet 1989), and differ significantly only in the substellar regime. In Romano et al. (2005) they find that 18 stellar lifetimes are generally in better agreement with observations if the substellar lifetimes are longer (Padovani & Matteucci 1993; Kodama & Arimoto 1997) and that deficiencies exist in the $[\text{O}/\text{Fe}]$ ratio of the model when the massive stars have shorter lifetimes (e.g. Tinsley 1980). Despite the differences in the substellar regimes, the order of the choice of stellar lifetimes does not have as much of an impact on the chemical evolution when compared with the IMF and with nucleosynthetic yields.

CHAPTER 1

Finally, Nucleosynthesis models describe the creation of massive elements via nuclear fusion. Nuclear fusion processes alters the abundance of elements by producing usually more massive elements. Nucleosynthetic processes occur through the lifetime of a star and during supernova explosions that cause mass to eject into the ISM are extremely complex. Some thought must also be given to mechanisms by which elements are ejected since the abundance of elements in ejected material and recycled into the ISM is the most important. Calculation of the nucleosynthetic yield of stars was first presented for low- and intermediate-mass stars in Iben & Truran (1978) and for massive stars in Arnett (1978); Chiosi & Caimmi (1979) and Maeder (1992). For a model of galactic chemical evolution, the yields of stars of all masses, metallicities and progenitor types must be considered.

1.4.3 The Solar Neighbourhood

The Solar neighbourhood is a benchmark region for models of the Galactic disc (Mollá et al. 2015; Nordström et al. 2004; Casagrande et al. 2011). The stars in the volume of space around the Sun enable a first estimate of the mass density of the Galactic disc near the plane of the galaxy. The distribution of age provides us with a record of the star formation history of the disc. Their element abundances as a function of age provide a fossil record of chemical evolution and enrichment history of the disc. Stellar motions as a function of age provide clues to the dynamical evolution of the galaxy and how mixing has occurred between stellar populations from different regions of the disc (see for example the review by Freeman & Bland-Hawthorn 2002). One advantage of studying stars in the solar neighbourhood is that measurements of stars - such as parallaxes or angular diameters - are more precisely obtained in the solar neighbourhood than anywhere else. This means that they are typically the best candidates for precise spectroscopic follow ups which aid the search for low-mass companions (stellar, brown dwarf or planetary), circumstellar

CHAPTER 1

discs, or solar-like cycles (Allende Prieto et al. 2004).

F- and G-type dwarf stars are typically used as tracer populations of the history of the disc. These stars are abundant long-lived stars which are capable of surviving the formation of the disc. They are regarded as snapshots of the stellar populations that are formed at different times and places over the history of our Galaxy. Their kinematics carry their dynamical histories and their atmospheres retain a fossil record of the elemental abundances of the interstellar medium at the time and place of their formation, thus their convective atmospheres reflect their initial chemical abundance. Therefore, F, G, and - to a lesser extent - K dwarfs have been traditionally used to study various aspects of the chemical evolution of the Milky Way.

The study of F and G dwarf stars is most easily achieved within the solar neighbourhood. Starting from pioneering works using spectra or ultraviolet and colour excess to estimate the metal abundance of stars in a Galactic context (Wallerstein 1962; van den Bergh 1962; Eggen et al. 1962; Schmidt 1963, e.g.), this endeavour has continued over the years with steadily improving spectroscopic and photometric studies of kinematic and chemical abundance properties. Examples of such surveys that study the Solar Neighbourhood are the Geneva-Copenhagen Survey (Nordström et al. 2004; Holmberg et al. 2007, 2009) and the Gaia-ESO survey (Gilmore et al. 2012). These observations allow us to derive and develop CEMs which can be applied to simulations of Milky Way-like galaxies to study Solar neighbourhood analogues. This enables us to develop a theoretical understanding of how the Milky Way evolved with time (Mollá et al. 2015, and references within).

1.5 Thesis Outline

In this thesis, we study aspects of the chemical and dynamical evolution of simulated late-type Milky Way-like galaxies. Galaxy formation is a broad field of study, with the chemical evolution of galaxies and the evolution of the gas disc being two components of the field. So far, we have covered the subject very broadly up this point, and we shall now focus our attention on the chemical evolution of stellar populations and the self turbulence of the gas disc. This is done using two different Milky Way-like galaxy simulations with the study of chemical evolution being undertaken in a cosmological context and the study of the gas disc in an isolated context.

In Chapter 2, we compare the chemical abundances of a chemodynamically simulated Milky Way-like galaxy directly with two different observational surveys. The surveys of choice are the Gaia-ESO survey and the RAVE survey, and we compare these surveys with a chemodynamically Milky Way-like galaxy ‘Selene-CH’ simulated using RAMSES-CH, a chemical evolution patch to RAMSES, in a cosmological context. The Gaia-ESO survey allows us to compare the solar neighbourhood of our Milky Way galaxy with an analogous region in Selene-CH and study a similar spatial region. We also compare with the RAVE survey which allows us to study the chemical properties of stars in an extended portion of the galactic disc and compare with a similar region and additionally different stellar population types. In this case we study the giants, main sequence and turnover region stars. We first perform a simple spatial comparison which tests the chemical evolution model we use in our own simulated galaxy model. We follow this up with the inclusion of observationally motivated errors from each survey, and compare our galaxy model like for like with the two surveys taking their observational errors into account. Finally we follow this up by applying observationally motivated selection functions to our simulated galaxy. We use theoretical isochrone data in order to compute observational properties of our simulated star particles, then apply similar survey selection functions

CHAPTER 1

and compare like for like. This also allows us to study different stellar populations within Selene-CH and compare that with the observational surveys like for like. The main motivation of this study is to build upon techniques of comparing observations and simulations in a more ‘like-for-like’ manner by mimicking observational effects into our simulation. This becomes increasingly important as observational surveys improve in both data volume and resolution and simulations improve in both spatial and mass resolution. Additionally we discuss the comparison of the chemical evolution model of choice with these two observational surveys and our galaxy and compare the metal abundances.

In Chapter 3, we study the turbulence, outflows and the giant molecular cloud populations of a simulated Milky Way-like galaxy in an isolated context. We generate a Milky Way-like galaxy from observational properties of the Milky Way and use the GALACTICS code to generate initial conditions for the galaxy. We run a simulation of the initial conditions of this galaxy using GIZMO and focus on the dynamics of the gas disc which undergoes optically thin cooling. In this sense we run our simulations without the occurrence of any star formation or supernova feedback and focus on the effects of the self-gravitating gas disc and its evolution. We additionally study the outflow rate of the galaxy disc with time and compare this with previous studies. We run the simulation using two different temperature floors and compare the two runs.

Chapter 4 draws together the conclusions of the work discussed here and raises avenues of future work that can be investigated from the work presented and discussed in this thesis.

Chapter 2

Comparing Chemo-Dynamical Simulations to Observations of the Milky Way

The typical methodology for comparing simulated galaxies with observational surveys is to apply a spatial selection to the simulation to mimic the region of interest covered by a comparable observational survey sample. In this work we compare this approach with a more sophisticated post-processing in which the observational uncertainties and selection effects (photometric, surface gravity and effective temperature) are taken into account. We compare a ‘solar neighbourhood analogue’ region in a model Milky Way-like galaxy simulated with RAMSES-CH with Gaia-ESO survey data. We find that a simple spatial cut alone is insufficient. The observational uncertainties must be accounted for in the comparison, particularly when the scale of the uncertainty is large compared to the dynamic range of the data, e.g. $[\text{Mg}/\text{Fe}]$ is significantly more affected than the more accurately determined $[\text{Fe}/\text{H}]$. In the case of the quite complete observational selection function - such as the Gaia-ESO survey - the selection function has a minimal impact on the distribution of observed

CHAPTER 2

age and metal abundances. However the impact of the choice of selection function will become more important for surveys with narrower selection functions such as shown with the RAVE survey that will be discussed here. This technique also allows for the study of stellar populations within computational simulation models. We find from using a selection function similar to RAVE that we observe an abundance of giants in the mid-plane of the galaxy towards, and a variety of different populations closer to the observer. This is akin to what is found in observational surveys. Overall the application of observationally motivated scatter to our simulation results produces reasonable agreement between the simulation and observations despite clear differences between the metal abundances of our simulated galaxy, the Gaia-ESO survey and the RAVE survey.

2.1 Introduction and Methodology

To aid the understanding of the evolutionary processes of the Milky Way, one needs to compare theoretical models of Milky Way-like simulations with observations. Studying the two hand in hand, one can better work towards an improved choice of free physical parameters to develop more accurate models. In short, one of the constraints of a physical model is to be able to reproduce observational survey results with good accuracy. In this chapter, we discuss methods of doing this with RAVE and the Gaia-ESO survey.

With the progression of time in astronomy, subsequent observational surveys and instrumentation, and the performance improvements of high performance computing, have lead to successive improvements in resolution and abundance of both survey and simulation datasets. This increasing performance in both observational and computational models have lead to an increased understanding of the Milky Way galaxy, its properties and the origins of the stars that reside within.

One of the primary diagnostic tools of galaxy formation is the determination of

CHAPTER 2

elemental abundance patterns. We use numerous comparisons of trends between stellar ages, metal abundance and spatial position relative to the galaxy. These trends are able to guide and develop an understanding of the physical processes which occur within galaxy formation models. Observations of various metal abundance ratios aid our understanding of the nuclear physics involved with α -element production, which are produced on shorter timescales than iron-peak elements (e.g. Carbon et al. 1987; Edvardsson et al. 1993b; Reddy et al. 2006; Ramírez et al. 2007).

The characteristic abundance ratios found in different stellar populations provide us with an opportunity to uncover the history of galaxy formation. Using what is known as galactic archaeology to link the chemistry, ages and dynamics of stars allows us to trace the origins of the components in the Milky Way (Feltzing & Chiba 2013) and its satellites (as reviewed in Tolstoy et al. 2009) including their Cepheids (Romaniello et al. 2008). Additionally we can use these techniques to trace red supergiants (Davies et al. 2015; Patrick et al. 2017) and A supergiants (Davies et al. 2015; Bresolin et al. 2016). We have learned a great deal about the processes associated with galaxy formation using the essential tools of chemical evolution models and simulations of galaxy formation (e.g. Scannapieco et al. 2005; Sommer-Larsen & Fynbo 2008; Roškar et al. 2008; Sánchez-Blázquez et al. 2009; Stinson et al. 2010; Kobayashi & Nakasato 2011; Wiersma et al. 2011; Calura et al. 2012; Pilkington et al. 2012a; Few et al. 2012b; Brook et al. 2012a; Few et al. 2014; Calura et al. 2012; Tissera et al. 2012; Miranda et al. 2016) and semi-analytical tools (Calura & Menci 2009; Yates et al. 2013). More recently, we have gone beyond tracing dynamics and global metallicity within simulations to include chemical evolution in such a way that individual elements and isotopes can be traced in combination with self-consistent galaxy formation scenarios (e.g. Steinmetz & Muller 1995; Mosconi et al. 2001; Lia et al. 2002; Kawata & Gibson 2003; Valdarnini 2003; Kobayashi 2004; Tornatore et al. 2004; Romeo et al. 2005; Scannapieco et al. 2005; Oppenheimer &

CHAPTER 2

Davé 2008; Martínez-Serrano et al. 2008; Wiersma et al. 2009; Few et al. 2012b, 2014).

Comparison of these chemical evolution models (with chemodynamical information to be tested in more detail in future work) with observed trends is fundamental to establishing the validity of the models and understanding the observations. Since a high precision and wealth of data is required from an observational perspective, testing chemical evolution models in this way is only achievable from within the Milky Way. Yet the way in which these comparisons are conducted has remained unaltered for decades despite improvements to the abundance of observational datasets and the improvement in simulation resolution. It is common, and indeed straight forward to simply take the results from the outputs of an observational survey and compare it like for like with simulation results of a Milky Way-Like galaxy. Typically, a spatial region in a simulation that is similar to the one covered by the observational data of interest is sampled and the stellar properties are directly compared (for example as done in Sahijpal 2013; Snaith et al. 2015, 2016). To a lesser extent, it is possible to compare with external galaxies by selecting stars for their dynamical properties in simulations and compare that with chemical properties of distant galaxies (e.g. Tissera et al. 2016).

One strong argument against this simple comparison method is that it ignores observational biases. Firstly, the observed datasets have inherent uncertainties, either systematic (for example due to stellar atmospheric models or instrumental) or random noise (such as signal to noise). Secondly, observational surveys usually observe stars within some range of stellar parameters or distances, which is usually dictated by the intention to study specific types of stars (low-mass or high-mass, low- or high-metallicity) in certain Galactic populations. This selection function (Stonkutė et al. 2016) creates biases in the distribution functions of the observed dataset. Most commonly, selection based on colour and apparent magnitude of stars

CHAPTER 2

is reflected in the shape of the metallicity and age distribution functions (Bergemann et al. 2014). This approach underpins the majority of analysis work of galaxy simulations, Additionally it takes the inherent assumption that the typical spatial selection of stellar data is completely analogous to that of galaxies in nature. As such that the physical and chemical properties of massive stellar-like particles can be directly compared with individual stars in observational surveys, despite the former being a consequence of resource and computational limitations.

In galaxy formation simulations, stellar properties are typically represented by “star particles”, which describe the combined properties of a coeval group of stars (a simple stellar population), its total stellar mass and metallicity¹. Thus one is limited primarily to the integrated luminosities and averaged chemical composition on the scale of open clusters within simulations, i.e. one star particle represents the mean properties of an open cluster. The ability to resolve stars in a galaxy at a mass like-for-like with fine spatial precision computationally challenging due to the lack of sufficient computational resources. The advantages of resolving star particles to mass scales similar to open clusters allows for computational simulations to run in a timely manner. Resolving more particles (less mass) increases the number of particles used, and thus increases the CPU resource requirement. On a galactic scale, mass resolutions at this scale are sufficient for studying global and large scale properties of galaxies in galaxy formation models. Thus simulation models try to take into account of the physics that is not being resolved at all, this is known as the sub-grid physics. The sub-grid physics typically includes the physical processes of star formation, supernova feedback, chemical evolution models. These sub-grid physics allow us to take into account physics that are not possible to resolve on spatial or time scales that the simulation code uses. We briefly explained this concept in §1.3, but we shall talk about it more in this section and in §2.3.1.

¹In this work, metallicity is defined as the iron abundance, $[\text{Fe}/\text{H}]$

CHAPTER 2

One could argue that the treatment of sub-grid physics aims to resolve the problems of mismatch of resolution between “star particles” and stars from observational surveys. However, spatial selection, along with treatment of the sub-grid physics - although both are quantitatively important - do not feature any inclusion of how one ‘observes’ the simulation. Typically in observational surveys, such as the Gaia-ESO survey (Gilmore et al. 2012; Randich et al. 2013), one would invoke an observational selection function which would consist of boundary conditions for individual stellar properties in addition to a spatial region for individual stars. In simulations, one is limited primarily to the integrated luminosities and chemical composition of the open cluster-scale simple stellar populations, which are used to represent “composite” stellar particles. As such, Miranda et al. (2014) concludes that the impact of how one observes a simulation, whether it be observationally motivated (e.g. from the point of view of a simulated observer), to even simple spatial cuts filtering out everything but the effective solar neighbourhood is as quantitatively important just as any of the sub-grid physics treatments within the simulations themselves.

As models improve, the detailed distribution of stellar ages and metallicities - in addition to their mean - become increasingly important. It is thus crucial that the approach to derive “observables” from the simulated data for comparison with real observations is as close as possible to the methodology employed by observers. This would allow for more direct comparisons between observational surveys with theoretical models on a self-consistent level. The Synthetic Colour-Magnitude Diagram (henceforth known as SYNCMD) Pasetto et al. (2012) is a tool that allows us to apply an observationally-motivated selection function upon the inferred age and metallicity distribution of an analogous region of space in a simulation. SYNCMD enables you to take the role of a survey designer within a simulated model. As such you can apply colour, magnitude and surface gravity boundary conditions and produce synthetic properties of ages and metal abundances by populating a colour

CHAPTER 2

magnitude diagram (CMD) for synthetic star particles, which is commonly done in observational surveys. Therefore allowing stellar samples to be drawn by an observer situated in a simulation using apparent magnitude and surface gravity criteria from an analogous “solar neighbourhood”.

In addition, one of the challenges faced by observational surveys is reducing the magnitude of, and number of sources of errors in observational surveys. Examples of such errors range from the measurement of the spectral line width for stellar spectral abundance measurements, errors on the precision of the measurement themselves or as result of the atmospheric physics for the case of a ground based observation. With simulation work, we are capable of measuring to a much finer precision various field data of “star particles”. As such the field data for “star particles” can be precisely measured and are computed as a result of the sub-grid physics, the hydrodynamical and chemodynamical mode employed and the resolution of position and particle number. With the right methodology, the errors on various fields of observational data can be replicated and implemented on fields in simulation data, so long as the errors are known precisely on an observational survey itself.

Kinematics and spatial distributions of Milky Way stars are studied to help define the galaxy that we live in. Kinematic and spatial information allow us to trace parts of the formation of the Milky Way. Spectroscopic surveys provide measurements of fundamental structural and dynamical parameters for statistical sample of Galactic stars. The Gaia-ESO survey (GES) (Gilmore et al. 2012; Randich et al. 2013) and The RAdial Velocity experiment (RAVE) (Steinmetz et al. 2006) are such spectroscopic survey studies which we shall compare with our “simulated observations”. There are other surveys such as the Sloan Extension for Galactic Understanding and Exploration (SEGUE) (Yanny et al. 2009), the APO Galactic Evolution Experiment (APOGEE) (Eisenstein et al. 2011) the LAMOST Experiment for Galactic Understanding (Zhao et al. 2012) and Exploration and the GALactic Archaeology

CHAPTER 2

with HERMES (GALAH) (Oliver et al. 2012; De Silva et al. 2015). In this work we shall focus our attention on both RAVE and GES for our comparisons.

We use the Synthetic Colour Magnitude Diagram (SYNCMD) (Pasetto et al. 2012) to generate colour-magnitude diagrams of our simulated galaxies, and thus also derive synthetic properties of our simulated galaxies such as the colours, observed magnitudes (from a simulated observer) and the surface gravity ($\log(g)$) of stars in simulations. The toolkit builds upon the work of Tantaló et al. (2010) which describes a technique to derive the integrated spectra, magnitudes and colours of the stellar content of simulated galaxies. However the techniques involved build upon this by using distribution functions and colour-magnitude diagrams. This toolkit allows us to sample our simulations in the same way that observers do, and thus are able to employ a similar selection criteria.

We first discuss and compare both a ‘solar neighbourhood analogue’ region in a model Milky Way-like galaxy simulated with the RAMSES-CH code (Teyssier 2002; Few et al. 2012a, 2014), which is post-processed using the SYNCMD toolkit based on the work of Pasetto et al. (2012) to mimic observational selection functions. The simulated data are compared with the Gaia-ESO spectroscopic stellar survey (Gilmore et al. 2012; Randich et al. 2013). The Gaia-ESO Survey is the largest ongoing high-resolution spectroscopic survey of stars in the Milky Way. In the high-resolution ($R \sim 47\,000$) mode, the goal is to acquire spectra for about 5 000 field stars, probing distances ~ 2 kpc from the Sun. Here we use the results from the fourth internal data release (iDR4) of the survey (hereafter, *GES-iDR4*), which includes all stellar spectra for the first 18 months of the survey from the iDR4 release. Our simulated solar neighbourhood analogue encapsulates a 2 kpc spherical region of space in our simulated galaxy.

Additionally, we discuss the comparison with a ‘wedge-like’ region of space with our model Milky Way-like galaxy. This region of space is similar to that covered by

CHAPTER 2

the RAVE survey (Steinmetz et al. 2006). We look at the fifth public data release (DR5) (Kunder et al. 2016) (hereafter, *RAVE-DR5*) and use all of the stellar data available to us in the publicly released catalogue². We use a similar photometric selection function as used in the DR5 release to post process our model Milky Way-like galaxy, using the SYNCMD toolkit (Pasetto et al. 2012) to mimic the observational selection functions to compare our model galaxy with the RAVE survey.

The motivation of this work is to demonstrate the effects of different degrees of post-processing on the simulated data to mimic observational effects. Within our simulation data, we sample a spatial region analogous to the solar neighbourhood region covered by the Gaia-ESO survey and discuss three different methods of transforming the simulated data into the ‘observer plane’. We additionally do the same with the region of space covered by the RAVE survey and compare this with the RAVE data.

This chapter is organised as follows. We describe the chemodynamical simulation code RAMSES-CH as well as the physics and chemical evolution model employed in the code in §2.3. Additionally in §2.3 we also talk about our simulated galaxy *Selene-CH*, its physical feedback parameters and describe the methodology undertaken to decide to use the chosen feedback parameters. In §2.4 we describe the SYNCMD toolkit in detail and how it is applied in the context of discussion here. We describe the observational surveys, *GES-iDR4* and *RAVE-DR5* in detail §2.5. We first discuss how we compare *Selene-CH* with *GES-iDR4* in §2.6 and the results of this in §2.7. We also briefly discuss what stellar populations one would expect to see upon choosing finer colour-magnitude bins in the selection function. Additionally we discuss how we compare *Selene-CH* with *RAVE-DR5* in §2.8 and the results of this in §2.9. We conclude the discussion laid out in this chapter in §2.10.

²see <http://rave-survey.org>

2.2 Adaptive Mesh Refinement and Galaxy Formation

In this section, we describe the underlying physics in the Adaptive Mesh Refinement (AMR) code used in RAMSES (Teyssier 2002). This discussion includes the implementation of the gravity and hydrodynamical solvers.

RAMSES is a three dimensional Eulerian hydrodynamical code with an N-body particle-mesh scheme to compute self-gravity. The adaptive mesh refines if it meets user defined refinement criteria, which for example can be chosen based on local particle density. Teyssier (2002) describes the details of the implementation of RAMSES. Additionally, Few et al. (2012a, 2014) describes the details of the chemical evolution patch. Overall RAMSES includes temperature, density and metallicity dependent radiative cooling rates whilst also assuming ionisation equilibrium with an ultra-violet radiative background (Haardt & Madau 1996). RAMSES-CH builds upon this framework by including a chemical evolution model.

2.2.1 Adaptive Grid

Extensive tests of the N-body and hydrodynamical components are described and discussed in Teyssier (2002). These tests include Sod’s shock tube test, Sedov blast waves in 1, 2 and 3 dimensions (Sedov 1959), the response to a shock moving from a coarse to a fine grid, the acceleration of particles in response to point masses, and Zel’dovich pancake (Zel’dovich 1970) (which is widely used as a benchmark in cosmological codes, see e.g. Cen 1992; Teyssier et al. 1998). These results are generally positive with minimal departures from analytical solutions as seen for the 3D blast wave tests and for shocks moving from coarser to finer grids (Khokhlov 1998). Although this is a very rare occurrence in cosmological contexts as pointed out in Teyssier (2002).

CHAPTER 2

The adaptive grid used in RAMSES increases the resolution of regions of interest with each refinement. The grid refinement scheme is based on the AMR technique used in Berger & Olinger (1984) to dynamically evolve a three dimensional grid. The refinement scheme statically refines nested regions, whilst cells outside of this region remain unrefined to reduce overall runtime. Cell refinement occurs only when specific user defined refinement criteria is achieved. The refinement criteria are usually density based which enables one to study e.g. a galaxy in high spatial resolution without the need to resolve the rest of the simulation. This reduces the amount of CPU resources required in comparison to resolving the entire simulation. The refinement criteria can be adjusted also according to the mass that a cell contains to resolve galaxies and dark matter halos and is thus important for gravitational interactions, which we do in the work presented here to resolve *Selene-CH* in detail with its surroundings unresolved. Additionally, the flexibility of choosing refinement criteria allows for the study of other astrophysical phenomena such as low density cosmological voids (Ricciardelli et al. 2013).

The basic element of a grid structure is an “oct”. An oct has 2^{dim} cells with a common vertex, where dim is the number of dimensions. Each individual oct is of a level, ℓ and by the links to its parent at level $\ell - 1$. Each oct has $2 \times dim$ octs before and after it. This essentially means octs are structured as a linked list and additionally if the entire grid was to refine, then there is a factor of $2 \times dim$ increase in cells. Elements in a linked list contain a data value, and a pointer to subsequent elements of ℓ . Thus each oct has knowledge of its parent and child octs. This creates a tree data structure called an octree since each oct has one parent and $3^{dim} - 1$ children. The refinement process is required to be smooth so that neighbouring cells are either of the same refinement level, or are at a refinement level which is one level above or below the refinement level of the current cell. Figure 2.1 illustrates the octree structure of an adaptive grid.

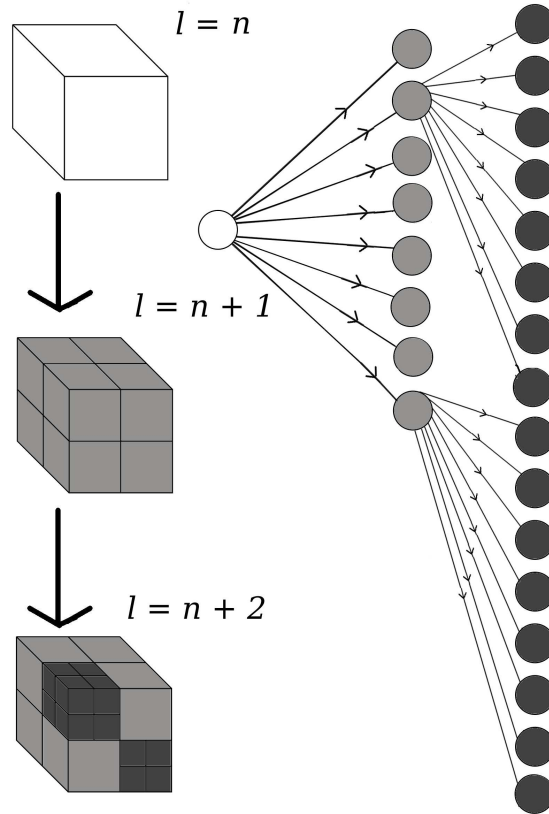


Figure 2.1: An illustration of adaptive mesh refinement of a three dimensional grid structure of cells/octs. The white octs represent a grid structure at a refinement level ℓ of n . The light grey octs represent a refinement level $\ell = n + 1$ and the dark grey cells represent a refinement level $\ell = n + 2$. The left hand side shows a visual representation of the grid, whilst the right hand side shows a visual representation. The right hand side presents the octree structure of the cell refinement structure from the left hand side.

2.2.2 N-body Physics

The N-body solver in RAMSES simulations uses the AMR technique of Berger & Olinger (1984) to evolve a three dimensional grid dynamically with time. The grid defines the local spatial resolution, so an increase in the number of cells correlates to an increase in spatial resolution which allows for overdensities to be better resolved. Upon establishing the grid resolution, cloud-in-cell interpolation (Hockney & Eastwood 1981) is used to compute the discretised mass distribution. The following equations describe the behaviour of collisionless particle dynamics in a gravitational potential:

$$\frac{d\mathbf{r}_i}{dt} = \mathbf{v}_i, \quad (2.1)$$

$$\frac{d\mathbf{v}_i}{dt} = -\nabla\Phi, \quad (2.2)$$

$$\frac{\partial^2}{\partial\mathbf{r}_i^2}\Phi = \nabla^2\Phi = 4\pi G\rho, \quad (2.3)$$

where \mathbf{r}_i and \mathbf{v}_i are position and velocity vectors of a particle i , Φ is the scalar gravitational potential, ρ is the density field, and G is Newtons gravitational constant. Equation 2.3 is Poisson's equation which describes the relation of the gravitational potential $\nabla^2\Phi$ - where $\nabla^2 = \partial^2/\partial\mathbf{r}_i^2$ - to the density distribution (ρ).

The N-body solver used in RAMSES has similarities (but not identical) to the ART code (Kravtsov et al. 1997) which is a standard Particle-Mesh (PM) scheme. The adaptive grid defines the local resolution, and allows overdensities to be resolved better. From the mass distribution, we then solve for the potential Φ in Equation 2.3 to calculate the gravitational potential field using the one-way interface scheme (Jessop et al. 1994; Kravtsov et al. 1997). For the coarse grid, which is unrefined and thus uniform, a fast Fourier transform is used to quickly solve Poisson's equation (Hockney & Eastwood 1981). On finer levels of the grid, the algorithms described

CHAPTER 2

in Kravtsov et al. (1997) and Teyssier (2002) are used to interpolate the potential to finer levels. Then we compute the acceleration on the mesh using a standard finite-difference approximation of the gradient and compute each particle acceleration using an inverse CIC interpolation scheme. From this we can update each particles velocity according to its acceleration, and then each particles position according to its velocity. This is achieved by using a second order midpoint scheme is used to advance the particle positions and velocities for which the Courant-Friedrich-Levy (CFL) condition must be satisfied (Courant et al. 1967). This is assisted by allowing variable time steps, i.e. the time resolution follows the local grid resolution for a given particle. We discuss this in more detail in §2.2.3.

Since we simulate our galaxy *Selene-CH* in a cosmological context, we thus need to transform these equations from Euclidean geometry into co-moving cosmological geometry. The transform between the two coordinate systems, one needs to convert position space into co-moving space $\mathbf{x} = \mathbf{r}/a(t)$ and time into conformal time $d\tau = dt/a(t)$. Here $a(t)$ is the cosmological expansion factor (Peebles 1980; Bertschinger 1998). Upon applying this transform, the collisionless motion of dark matter particles is now described by the following equations:

$$\frac{d\mathbf{x}_i}{d\tau} = \mathbf{v}_i, \quad (2.4)$$

$$\frac{d^2\mathbf{x}_i}{d\tau^2} + \frac{\dot{a}}{a} \left[\frac{d\mathbf{x}_i}{d\tau} \right] = -\nabla\Phi', \quad (2.5)$$

$$\nabla^2\Phi' = 4\pi G a^2 (\rho(\mathbf{x}, \tau) - \bar{\rho}\tau), \quad (2.6)$$

with ∇ being redefined as $\nabla = \partial/\partial\mathbf{x}$. $\rho(\mathbf{x}, \tau)$ represents the mass density in a region of co-moving space and time, and $\bar{\rho}\tau$ is the mean density of the Universe at co-moving time τ . The equations of motion are solved by numerical integration

CHAPTER 2

methods as described in more detail in e.g. Dehnen & Read (2011) and Trenti & Hut (2008) and thus we will not discuss this in further detail.

2.2.3 Time Evolution

Time steps are advanced using a midpoint method with time centred fluxes at cell boundaries used to update the hydrodynamical variables. The time centred fluxes are determined using a second-order Godunov method (otherwise known as the Piecewise Linear Method) (Godunov 1959; Toro 1997). The general CFL condition is:

$$C = \Delta t \sum_{i=1}^n \frac{u_i}{\Delta x_i} \leq C_{\max}, \quad (2.7)$$

where u_i is the velocity component in the x_i direction, n is the number of dimensions the system is in, Δt is the time step, and Δx_i is the size of the length interval (in this case the cell size). For an explicit (time-marching) solver $C_{\max} = 1$. Essentially this sets the restriction for the maximum time step in a computer simulation.

In RAMSES, we use a modified CFL condition such that the time step is:

$$\Delta t_{\text{CFL}} = \frac{\Delta x_\ell}{\sum_{i=1}^{N_{\text{dim}}} (|u_i| + c_s)} \frac{\sqrt{1 + 2C_{\text{CFL}}\epsilon_{\text{GSR}} - 1}}{\epsilon_{\text{GSR}}}, \quad (2.8)$$

where Δx_ℓ is the linear extent of a grid cell at level ℓ with $N_{\text{dim}} (=3)$ dimensional velocity \mathbf{u} and sound speed c_s . The right-hand part of equation 2.8 replaces the more traditional multiplication by the CFL factor, C_{CFL} . This is modified here in order to vary with the gravitational strength ratio,

$$\epsilon_{\text{GSR}} = \Delta x_\ell \frac{\sum_{i=1}^{N_{\text{dim}}} |g_i|}{\left(\sum_{i=1}^{N_{\text{dim}}} (|u_i| + c_s)\right)^2}, \quad (2.9)$$

where \mathbf{g} is the gravitational acceleration experienced by each grid cell. The right-hand part of equation 2.8 is equal to C_{CFL} for $\epsilon_{\text{GSR}} \rightarrow 0$ and is smaller (thus

CHAPTER 2

shortening the timestep) when the gravitational acceleration is large relative to the local gas velocity. The RAMSES runs presented here use $C_{\text{CFL}} = 0.8$.

To preserve the synchronisation between the time steps of different levels the time step at a level ℓ is half the timestep at level $\ell - 1$. The variation in time step introduces a source of error if a particle crosses from a grid cell to a new grid cell on a different level as it experiences a factor of two difference in the time step. This effect is fortunately very small and does not have a significant impact on a simulated system (Kravtsov & Klypin 1999; Yahagi & Yoshii 2001).

2.2.4 Hydrodynamics

The treatment of flow of gas in astrophysical simulations is achieved from solving the conservation laws of fluid dynamics by numerical integration. The first is the conservation of mass, which is valid in the absence of sources and sinks of mass in simulations. Since star formation and stellar feedback act as mass sinks and sources respectively this condition is not strictly enforced. Star formation takes a fraction of mass out of the baryonic gas the star particle is occupying. Some of this is later returned to the system stellar feedback processes. Overall the mass of the universe is kept conserved. These processes are computed separately in the simulation code to avoid conflict. The continuity equation which is derived from the assumption of mass conservation states,

$$\frac{\partial \rho_g}{\partial t} + \nabla \cdot (\rho_g \mathbf{u}) = 0, \quad (2.10)$$

with ρ_g representing the gas density and \mathbf{u} representing the flow velocity.

The second conservation law of fluid dynamics is the conservation of momentum. Essentially this is Newton's second law in the form of fluid dynamics. It is used to calculate the change of momentum of a fixed volume due to pressure (p) and gravitational forces as well as momentum flux through the volume surface.

CHAPTER 2

$$\rho_g \frac{\partial \mathbf{u}}{\partial t} + \rho_g \mathbf{u} \cdot \nabla \mathbf{u} = -\nabla p - \rho_g \nabla \Phi, \quad (2.11)$$

there is however no way of determining p on its own.

In general, the gas dynamics are computed with a second-order unsplit Godunov scheme (Godunov 1959; Toro 1997) and is based on Colella (1990) and Saltzman (1994) and is described as 'almost exact' by Teyssier (2002). The advantage of using a Godunov method is that it is inherently shock capturing with no need to invoke artificial viscosity. The exact details of the solver are beyond the scope of discussion in this thesis and we encourage the reader to look at the work we have cited here. In general it is a conservative finite-volume method which solves exact, or approximate Riemann problems at each inter-cell boundary. A Riemann problem is the initial value problem where the initial data consists of two states, separated by a discontinuity. In the case of an adaptive grid, this is the difference in properties between two cells. The Riemann solver (such as the Godunov scheme) is a method where time-averaged fluxes of all conserved quantities are calculated at cell interfaces. Essentially acts as a solver for conservation laws of fluid dynamics, which are partial differential equations across grid cells.

The conservation of mass and momentum equations are currently incomplete. A further constraint is needed from the first law of thermodynamics, which from adding a term to account for energy transportation, we can derive the energy equation,

$$\frac{\partial \epsilon}{\partial t} + \mathbf{u} \cdot \nabla \epsilon + \frac{p}{\rho} \nabla \cdot \mathbf{u} = \frac{\Gamma - \Lambda}{\rho}, \quad (2.12)$$

where ϵ is the specific internal energy of the gas, Γ is the heating rate and Λ is the cooling rate. We additionally require the equation of state of an ideal gas, which is:

$$p = \rho \epsilon (\gamma - 1), \quad (2.13)$$

where γ is a constant adiabatic index with a value depending of the physical nature

CHAPTER 2

of matter under consideration. Adiabatic processes do not cause the loss of thermal energy or matter of the system to its surroundings. Energy is however transferred to its surroundings as work. adiabatic cooling occurs when the pressure on an adiabatically isolated system decreases, which allows the system to expand and thus increase in volume. Typically for a monotomic gas, $\gamma = \frac{5}{3}$ and for diatomic gas $\gamma = \frac{7}{3}$.

Hydrodynamical cooling in these simulations is additionally metallicity- and density- dependent. On the physical scale of hundreds of parsecs, convection and conduction are less relevant and therefore are not required to be treated explicitly. Energy can either be lost or gained by the gas due to radiation and thus the cooling and heating of gas as a function of density, temperature and metallicity are considered. The cooling and heating rates are computed with the assumption of ionisation equilibrium in a uniform UV background as described in Haardt & Madau (1996). Haardt & Madau (1996) uses cooling curves which describe the nature of cooling in the absence of UV heating as a function of temperature for different metallicities and densities. Metal contribution for temperatures above 10^4 K is accounted for through the difference between cooling rates at solar metallicity and those at zero metallicity assuming ionisation equilibrium. The cooling and heating rates and the effects of physical properties are all derived from the use of the photoionisation code CLOUDY (Ferland et al. 1998). For gas cooler than 10^4 K, metal fine-structure cooling rates are taken from Rosen & Bregman (1995). However the polytropic equation of state that is used in simulations prevents the overwhelming majority of the gas from falling into this temperature regime. The net energy change, which is the difference in the heating and cooling rates ($\Gamma - \Lambda$) for each grid cell is calculated at each time step and is used in solving Equation 2.12. We present a sample of cooling curves (labelled RB95) with variations in the metallicity and density for RAMSES in Figure 1.3 with discussion in §1.3.2.

2.3 RAMSES

In this section, we discuss the implementation of baryonic feedback of star formation and cooling in RAMSES. Then the discussion focuses on the chemical evolution aspects as described in RAMSES-CH (Few et al. 2012a, 2014) which is a chemical evolution patch to the RAMSES v3.11 (Teyssier 2002). After discussing the physics of the code, we then go on to discuss the initial conditions for the galaxy *Selene-CH* which we simulate using *RAMSES-CH*. We conclude this section with a brief description of the physical parameters that were tested and outline our reasoning for the ones that we chose.

2.3.1 RAMSES: Cooling Physics and Star Formation

Due to limits upon spatial resolution, if the gas is poorly resolved in comparison to the scale of density perturbations, hydrodynamical simulations may undergo artificial fragmentation. This is an undesired consequence of the inability to easily resolve the Jeans length λ_J in high density regions (Jeans 1902). In the context of astrophysics, λ_J is the length of a gas cloud of a density ρ where if the size of the gas cloud is smaller than the λ_J , then gravitational attraction force is stronger than internal pressure forces, and thus the cloud proceeds to collapse to form a star. Since resolving the Jeans length of dense gas is impossible due to resolution limitations by technical constraints, we instead introduce the polytropic equation to prevent fragmentation by altering the gas temperature as a function of density to enforce a floor in the Jeans length. The polytropic equation of state is:

$$P \propto \rho_g^\gamma, \quad (2.14)$$

A suitably chosen value for γ prevents unphysical fragmentation of gas and thus the unphysical formation of stars. We apply this equation once the gas temperature drops below a chosen temperature T_{poly} and denser than chosen density n_{poly} (or

CHAPTER 2

ρ_{poly}). n_{poly} essentially represents the density threshold for star formation. The values of T_{poly} , n_{poly} and γ are chosen to make sure λ_J is resolvable by the simulation grid to prevent artificial fragmentation. The choice of values for T_{poly} , n_{poly} depends upon the maximum simulation resolution, but choosing $\gamma = 2.0$ allows the resolution of the Jeans length.

To tune T_{poly} , we wish to consider the lowest possible temperature $T_{\text{poly},\text{min}}$ that is capable of resolving the minimum Jeans length required for gravitational collapse:

$$\lambda_J = c_s \times \tau_{ff}, \quad (2.15)$$

$$c_s = \sqrt{\frac{P}{\rho}} = \sqrt{\frac{k_B T_{\text{poly},\text{min}}}{\mu m_H}}, \quad (2.16)$$

$$\tau_{ff} = \sqrt{\frac{\pi}{G\rho}} = \sqrt{\frac{\pi}{G\mu m_H n_H}}, \quad (2.17)$$

where c_s is the sound speed of the gas medium and τ_{ff} is the free-fall time, k_B is the Boltzmann constant, μ is the mean molecular weight of hydrogen and m_H is the mass of a hydrogen atom. We can thus define the Jeans length in terms of our free-parameters i.e:

$$\lambda_J = \sqrt{\frac{k_B \pi}{G(\mu m_H)^2}} \sqrt{\frac{T_{\text{poly},\text{min}}}{n_H}}, \quad (2.18)$$

which gives us:

$$\lambda_J = \sqrt{\frac{k_B \pi}{G(\mu m_H)^2}} \sqrt{\frac{T_{\text{poly}}}{n_H} \left(\frac{n_H}{n_{\text{poly}}} \right)^{\gamma-1}}. \quad (2.19)$$

We set $\gamma = 2$, which allows for the resolution of the Jean's length at all densities independent of resolution for the right choice of T_{poly} and n_{poly} as described above. This gives us:

CHAPTER 2

$$\lambda_J = \sqrt{\frac{k_B \pi}{G(\mu m_H)^2}} \sqrt{\frac{T_{poly}}{n_{poly}}} = N_J \Delta x, \quad (2.20)$$

where Δx is the minimum cell width, which is our maximum spatial resolution. N_J is the number of cells required to resolve the Jean's length. Spatial resolutions in adaptive mesh grids are discretised into ℓ_{\max} resolutions levels, is computed from rearranging the following formula,

$$\Delta x = \frac{L_{\text{box}}}{2^{\ell_{\max}}}, \quad (2.21)$$

where L_{box} is the size of the box in units of Mpc h^{-1} . By increasing/decreasing N_J , we are able to prevent the fragmentation of star forming gas and control the star formation rate which follows a Schmidt law (Schmidt 1959; Kennicutt 1998b) and Poisson random noise process for the number of stars. We choose $N_J = \frac{\lambda_J}{\Delta x} = 4$, i.e. we allow for the jeans length to be resolved in 4 cells in one dimension. This choice is motivated from discussion in Truelove et al. (1997). In order to avoid artificial fragmentation across isothermal density mediums in for example the isothermic collapse of perturbed Gaussian clouds (Burkert & Bodenheimer 1996) must maintain a minimum ratio of λ_J to Δx . from the work in Truelove et al. (1997) the best minimum value of the ratio $\frac{\lambda_J}{\Delta x}$ is 4.

Therefore, to compute $T_{poly,min}$, which is our ideal choice of T_{poly} for a given n_{poly} to minimise temperature-based fragmentation,

$$T_{poly,min} = n_{poly} (N_J \Delta x)^2 \frac{G(\mu m_H)^2}{k_B \pi}. \quad (2.22)$$

A carefully chosen T_{poly} is motivated by choosing a theoretical $T_{poly,min}$ which is calculated to remove the temperature-related contribution to Jeans fragmentation. Specifically, $T_{poly,min}$ is a necessary condition but not sufficient alone to prevent fragmentation.

In the context of galaxy formation, the lack of a theory of star formation means

CHAPTER 2

the best approach is to take a simple estimate of the global rate of star formation in a model galaxy, which can be simply treated as for example:

$$\dot{M}_* \propto \frac{M_{cold}}{\tau}, \quad (2.23)$$

where \dot{M}_* is the star formation rate which depends on the amount of cold gas available M_{cold} and some characteristic timescale τ . This timescale τ is also proportional to the dynamical time, the time for a uniform gas cloud with density ρ_g to collapse. In a simulation element (e.g. cell or particle) is treated as:

$$\tau_{dyn} = \sqrt{\frac{1}{C_g G \rho_g}}, \quad (2.24)$$

Where ρ_g is the density of a gas element, C_g is a constant which depends on how the hydrodynamical method of the simulation is handled (this value is typically 4π).

Thus the rate at which star particles are produced is:

$$\dot{\rho} = \epsilon \frac{\rho_g}{\tau_{ff}}, \quad (2.25)$$

Where ϵ is the star formation efficiency, which is a free parameter which governs the efficiency of conversion of gas mass to stellar mass within star forming regions. The maximum values for $\Delta x/\lambda_J$ at which the Jeans' length is resolved is described in Truelove et al. (1997). Additionally τ_{ff} is the free-fall time.

τ_{dyn} can also in hydrodynamical simulations have some fixed value with the motivation to reproduce empirical relations such as the Kennicutt-Schmidt (K-S) relation (Schmidt 1959; Kennicutt 1998b), as well as the fraction of stars to the mass of the halo, and the observed gas fraction in spiral galaxies as a function of their luminosity (e.g. Cole et al. 2000, 1994). In reality, due to feedback processes which deplete the reservoir of cold gas, as well as replenish it from material ejected from stars, the feedback timescale is effectively a modified version of this.

CHAPTER 2

The K-S law is an extension of the Schmidt law that was proposed in Schmidt (1959) where the star formation rate per unit area of a galaxy ($\dot{\Sigma}_*$) is proportional to a power of the surface density of the cold gas (Σ_g). I.e:

$$\dot{\Sigma}_* \propto \Sigma_g^n, \quad (2.26)$$

Kennicutt (1998b) showed from a large sample of spiral and starburst galaxies that $n \sim 1.4$ (see also Kennicutt 1998a). The Schmidt law can be rewritten similar to the analytical star formation equation,

$$\dot{\Sigma}_* \propto \frac{\Sigma_g^n}{\tau}, \quad (2.27)$$

where τ can be replaced with the dynamical time of the galaxy (Kennicutt 1998b). This therefore can be expressed as,

$$\frac{dM_*}{dt} = \epsilon \frac{M_{\text{gas}}}{\tau_{\text{dyn}}}, \quad (2.28)$$

with dt being some time between star formation events (assuming discretised bursts within the time dt). The technique here is to choose a value for ϵ in addition to the chosen n_{poly} value in order to reproduce the Kennicutt-Schmidt relation as closely as possible (Schmidt 1959; Kennicutt 1998b). Further details for the description of the star formation and feedback treatments can be found in Dubois & Teyssier (2008).

The stellar mass vs. halo mass (SHM) relation (Moster et al. 2010, 2013), in addition to the K-S law is typically used in determining whether the free parameters in star formation are successful. The SHM relation is an empirical function that parametrises the relation between the stellar mass and the halo mass, which here are labelled as m_* and M respectively. This is described by the power law:

$$\frac{m_*}{M} = 2 N \left[\left(\frac{M}{M_1} \right)^{-\beta} + \left(\frac{M}{M_1} \right)^{\gamma} \right]^{-1}, \quad (2.29)$$

CHAPTER 2

which has four free parameters. N represents the normalisation of the SHM ratio. M_1 represents a characteristic mass where the SHM ratio (m_*/M) is equal to N . β and γ indicate the behaviour of m/M at the low and high mass ends respectively. This empirical function implies a non-monotonic description of galaxy formation, in which the peak of this function (i.e. the peak of star formation efficiency for the mass of the system) is at the Milky Way mass, although this peak is typically only 20% of the mean baryon mass theorised to be in a Milky Way mass Halo. The functional form implies a lower efficiency at both high and low mass dark matter halos. This is due to feedback from stars in the form of stellar winds from hot young stars, and supernova from evolved stars at the low mass end, and supermassive blackholes at the high mass end (Guo et al. 2010).

Implementations and development of baryonic feedback processes are motivated by the goal of producing ‘realistic’ baryonic gas discs. Numerical simulations of galaxies have shown to produce baryonic gas discs with an angular momentum deficiency compared to real galaxies (Navarro & Benz 1991; Navarro & Steinmetz 2000) in addition to artificial losses from resolution and other numerical effects (Okamoto et al. 2003; Governato et al. 2004; Kaufmann et al. 2007). This causes cold baryons to sink to the centre of the proto-galaxy and form a spheroidal, rather than a disc (e.g. Maller & Dekel 2002). Energy injection from supernova (SNe) and evolving stars to prevent efficient gas cooling and removes low angular momentum material from the central part of the galaxy (e.g. Robertson et al. 2004; Governato et al. 2007; Scannapieco et al. 2009; Stinson et al. 2010; Piontek & Steinmetz 2011; Brooks et al. 2011). A consequence of some of these implementations results in centrally-concentrated systems, with rotation curves very steep towards the centre. This results with simulated disc galaxies that lie in the S0 or Sa category from the tuning fork shown discussed in §1.1.3 and in Figure 1.1. This causes numerical simulation to favour the production of galaxies with large bulges and smaller discs,

CHAPTER 2

unlike our own Milky Way.

One solution to this is to mimic the slow dissipation of non-thermal energy (Teyssier et al. 2013). A ‘delayed cooling’ implementation implicitly mimics the bottleneck of conversion of atomic gas into molecular. This is in contrast to the almost instantaneous dissipation of thermal energy through regular cooling mechanisms. This accounts for the unresolved multiphase nature of the gas and avoids the spurious loss of thermal energy following SN feedback. There is no universally defined implementation of delayed cooling (e.g. Guedes et al. 2011; Teyssier et al. 2013; Agertz et al. 2013).

We employ a delayed cooling feedback mechanism that is unique to RAMSES-CH, but it is similar to the implementation Agertz et al. (2013). In the implementation of delayed cooling presented here, upon the ejection of material from SNII of mass m_{ej} into the gas cell m_{gas} that it occupies, we increment a parameter ζ_{m} by the amount of mass that is ejected into the gas cell, i.e:

$$\zeta_{\text{m}} = \zeta_{\text{m}} + m_{\text{ej}}, \quad (2.30)$$

where m_{ej} is the mass ejected from the supernova into the cell, which increments ζ_{m} . In addition to this, we dampen ζ_{m} by a timescale t_{dis} over time Δt :

$$\zeta_{\text{m}} = \zeta_{\text{m}} \times \exp\left(-\frac{\Delta t}{t_{\text{dis}}}\right), \quad (2.31)$$

Should the ratio of this parameter and the mass of the gas cell be greater than a chosen ζ_{cool} :

$$\zeta_{\text{cool}} < \frac{\zeta_{\text{m}}}{m_{\text{gas}}}, \quad (2.32)$$

then gas cooling is disabled. Cooling is re-enabled when $\frac{\zeta_{\text{m}}}{m_{\text{gas}}}$ drops below ζ_{cool} . Our chosen parameters are $\zeta_{\text{cool}} = 0.001$ and $t_{\text{dis}} = 10$ Myr.

CHAPTER 2

The delayed cooling implemented here is not strictly related to the “overcooling problem”. However cooling does happen too quickly in RAMSES simulations if the delayed cooling scheme is not implemented (e.g. Teyssier et al. 2013; Agertz et al. 2013). The spatial scales and timescales do not capture cooling very well, and as a consequence, feedback methods excessively cool.

The energy injected by SNIa explosions into the ISM is:

$$E_{g,T} = \epsilon_{\text{SNIa}} E_{\text{SNIa}} N_{\text{SNIa}}, \quad (2.33)$$

and for SNII explosions:

$$E_{g,K} = \epsilon_{\text{SNII}} E_{\text{SNII}} N_{\text{SNII}}, \quad (2.34)$$

where $E_{\text{SNIa}} = E_{\text{SNII}} = 10^{51}$ erg as the energy per SN event and ϵ_{SNIa} and ϵ_{SNII} are the efficiency with which the energy couples to the ISM for SNIa and SNII respectively. Energy from SNII is kinetic whilst from SNIa is thermal.

RAMSES-CH also includes thermal and kinetic cooling schemes, with the latter being described in detail in Dubois & Teyssier (2008). The physical mechanism behind the kinetic cooling scheme is driven by the implementation of a self-consistent Sedov blast (Sedov 1959). This was discussed for the general case in §1.3. As a result of SNII explosion events, mass, momentum and energy into the ISM. In RAMSES, the impact of this is parameterised by two parameters f_k and f_w which occurs in a bubble over radius r_{blast} . These parameters concern the behaviour of the energy $E_{g,K}$ as a result of SNII events as described in Equation 2.34. f_k describes the fraction of energy that is ejected into the ISM kinetically over radius r_{blast} . In our work we set r_{blast} to be a 2-cell radius feedback-sphere centred on the star particle. The remaining $(1 - f_k)$ energy is injected thermally into the ISM. f_w controls the amount of gas that is swept up m_{swept} by the Sedov blast bubble which is described by,

$$m_{\text{swept}} = f_w m_{\text{ej}}, \quad (2.35)$$

where f_w is the wind loading parameter and m_{ej} is the mass of gas ejected by a SNII event. Thermal feedback modes do not incorporate any kinetic feedback at all, thus $f_w = 0.0$ and $f_k = 0.0$. Since our main focus of this study involves the use of the delayed cooling feedback mechanism, we shall not discuss. The choice of feedback parameters used are described and discussed in in §2.3.4.

2.3.2 RAMSES-CH: Chemical Evolution Supernova Feedback

To trace the chemical evolution of the simulated galaxy in a cosmological context, we employ a chemodynamical patch called RAMSES-CH (Few et al. 2012a, 2014) which is based on the AMR code RAMSES (TEYSSIER 2002). RAMSES-CH in addition to the physical prescription as described in RAMSES also includes the treatment of chemical enrichment. A key property of RAMSES-CH is its ability to capture metal mixing. This is extremely pertinent to this work as it directly affects the dispersion in the abundance ratios of the gas which becomes imprinted on the stars. Previous studies have found that adopting a grid-, rather than particle-based approach, in general allows for a better treatment diffusion of metals (e.g. Pilkington et al. 2012a; Revaz et al. 2016).

RAMSES-CH allows us to track the elements H, He, C, N, O, Ne, Mg, Si, and Fe from their dominant production sites into the ISM. The three dominant sources of metals are type-Ia and type-II supernovae (SNIa and SNII respectively) and lower mass stars entering their asymptotic giant branch (AGB) phase. The AGB phase is the result of a low mass star (not massive enough to undergo a Type II supernova) exhausts its supply of Hydrogen for nuclear fusion, and thus the star becomes a red giant. Once energy and metals are injected into the ISM they are advected with the gas flow and become imprinted on the stellar population particles. The details of RAMSES-CH are described fully in Few et al. (2014) but we briefly summarise

CHAPTER 2

the main components here and discuss them in this section.

One of the main ingredients of a chemical evolution model (CEM) is the initial mass function, since nucleosynthetic processes and lifetimes of stars are mass dependent. Equation 1.5 defines the IMF $\psi(m)$, which represents the number distribution of stars as a function of mass. The earliest IMF proposed by Salpeter (1955) in which the luminosity function of stars is used to determine the mass function of stars at the time they are formed. The degree of uncertainty of the actual slope of the IMF is still large enough to result in significant variations in modelling galactic abundance patterns (e.g. [O/Fe] can vary as much as 0.3 dex depending on the slope of the IMF) (Few et al. 2012a, 2014). The IMF in Salpeter (1955) is fitted as a simple power law in the form:

$$\psi(m) \propto M^{-1.35}, \quad (2.36)$$

within the range of $0.4 \leq \frac{M}{M_{\odot}} \leq 10$.

To this day, multiple studies have been undertaken on understanding the true nature of the IMF. More complex IMFs being proposed to capture the substellar regime, these include multislope IMFs which are piecewise functions (Tinsley 1980; Scalo 1986; Kroupa et al. 1993; Scalo 1998; Kroupa 2001; Chabrier 2003). These IMFs have had successes at predicting the stellar luminosity function closer to that observed.

However, it is common practice to perform the normalisation over a range of $0.1 - 100M_{\odot}$. Thus our IMF takes the functional form:

$$\psi(m) = AM^{-1.35}, \quad (2.37)$$

Where $A \approx 0.17$. It is worth noting that the theory of an IMF assumes that there must be some single function which universally describes the mass distribution of

CHAPTER 2

star forming regions under a variety of physical conditions. The rate of star formation is governed by many variables involving local density, metallicity, turbulence and feedback processes. Additionally the fact that many theoretical forms of the IMF exists (e.g. Kroupa 2001; Kroupa et al. 1993; Chabrier 2003) demonstrates the difficulty of quantifying the nature of the IMF including e.g. the impact of redshift. In literature, the Chabrier (2003) IMF is favoured for chemical evolution and galaxy modelling of e.g. Milky Way-like galaxies.

Nucleosynthesis is the process which describes how nuclear fusion capable gas alters the abundance of elements in stars or the Early Universe. This tends to create more massive elements. The resulting abundance patterns from nucleosynthetic processes is related to the conditions that give rise to them. Nucleosynthetic models are non-linear and depend a great deal on the mass and initial abundance patterns in the stars. Further complication is added from the distribution of elements within stars and how supernova and feedback schemes eject them. Models of the Nucleosynthetic yield of low- and intermediate-mass stars are found in Iben & Truran (1978); van den Hoek & Groenewegen (1997); Marigo (2001); Izzard et al. (2004); Karakas & Lattanzio (2007); Karakas (2010) and Doherty et al. (2010). Yields of massive stars are considered in Arnett (1978); Chiosi & Caimmi (1979); Maeder (1992); Woosley & Weaver (1995); Limongi & Chieffi (2003); Chieffi & Limongi (2004) and Kobayashi et al. (2006). CEMs need to consider the yields for stars of all masses, metallicities and progenitor types. These three processes undergo different internal physics and produce different abundances of metals. These also operate on different time scales with SNII peaking within the first 10^8 years as well as the production of α -elements (oxygen through to zinc). AGB and SNIa events favour times after the first 10^9 yr with AGB favouring the production of carbon and SNIa favouring the production of iron. Because of the different internal physical processes and variations in nucleosynthesis models, the yields of different sources in literature

CHAPTER 2

are often combined to make a single model despite inconsistencies between them, instead of using a single consistent model.

The CEM determines the relative rates of SNII, SNIa and AGB stars. Additionally the CEM defines the associated chemical enrichment for a stellar population by a given IMF. The relations between these variables are computed prior to the simulation being run from a ‘feedback table’. This is used as a lookup table in order to provide approximate values for SNII, SNIa, and isotopic return rates as a function of time for a range of Simple Stellar Population (SSP) metallicities. It is important to note that these SSP’s are essentially resolved as ‘stellar particles’ in the simulation, rather than as individual stars, of which the context of this distinction is discussed in more detail in §2.4. The feedback table itself covers a range of ages from 0.0 to beyond the Hubble time and a range of metallicities. Stepping through each metallicity entry in the table and for each age, a stellar lifetime model is consulted to determine the main sequence turnoff mass, $m_{\text{to}}(\tau, Z_{\text{sp},0})$ associated with the stellar populations current age (τ) and metallicity ($Z_{\text{sp},0}$). We use the stellar lifetime model as outlined in Kodama (1997).

We use the model B SNII yields from Woosley & Weaver (1995) with a correction applied to the yields after Timmes et al. (1995) which halves the Fe produced by massive stars. Timmes et al. (1995) discusses why the Fe produced by massive stars is halved in length. Essentially the uncertainty in the placement of the mass cut meant they provided error factors (+/–) of two variation in iron production (hence, why they always show multiple curves in their panels). As such this is mainly to reflect that iron over-production in CEM’s is problematic and we are mainly incorporating the uncertainties that this brings. This technique has been implemented in previous studies such as in GEtool (Renda et al. 2004) and GCD+ (Kawata & Gibson 2003).

The number of SNII associated with a star particle of initial mass M_0 can be

CHAPTER 2

calculated by integrating over the IMF by number $\psi(m)$ as:

$$N_{SNII}(\tau_*, Z_0) = M_0 \int_{MAX(m_{SNII,l}, m_{TO})}^{m_{SNII,u}} \phi(m) dm, \quad (2.38)$$

where m_{TO} is the main sequence turnoff mass, which depends on the main sequence lifetime τ_* and initial metallicity Z_0 . This equation is only applicable whilst $(m_{SNII,l}, m_{TO})$ is within the range of values for SNII progenitors $m_{SNII,l} = 8M_\odot$ to $m_{SNII,u}$ which in this simulation $m_{SNII,u} = 100M_\odot$.

The nature of SNII predominate α -process element production and short lifetimes causes produces an initial α -enhanced plateau. As time passes, lower mass stars eject their elements into the ISM as the outer layers of the star are thrown off during the AGB phase. This is dependent upon the stellar mass of the star. The most long-lived sources of metals in the Universe then begin to eject mass via SNIa.

AGB stars expel their outer layers during thermal pulsation via stellar winds. This occurs on a time-scale assumed to be shorter than a simulation time-step. The number of AGB stars ejecting their mass can be computed by:

$$N_{AGB}(\tau_*, Z_0) = M_0 \int_{MAX(m_{AGB,l}, m_{TO})}^{m_{AGB,u}} \phi(m) dm, \quad (2.39)$$

where m_{TO} is the range of AGB masses, $m_{AGB,l} = 0.5M_\odot$ to $m_{AGB,u} = 8.0M_\odot$. The turn-off mass as a function of stellar population is taken from (Kodama & Arimoto 1997), in which the stellar lifetime is a function of mass and Z_0 , the initial metallicity abundance. The yields produced from AGB stars are the same as from van den Hoek & Groenewegen (1997).

The contribution of SNIa to galactic CEMs is distinct from other sources and is well constrained (Nomoto et al. 1984; Iwamoto et al. 1999) predominantly produce iron-peak elements. Type Ia supernovae progenitors have a different treatment applied to them, as such the abundance of elements in the SNIa ejecta is taken as a constant. This SNIa model is based on (Hachisu et al. 1999) where the mass range of the SNIa progenitor is treated to be bimodal (Kobayashi et al. 2000; Kawata

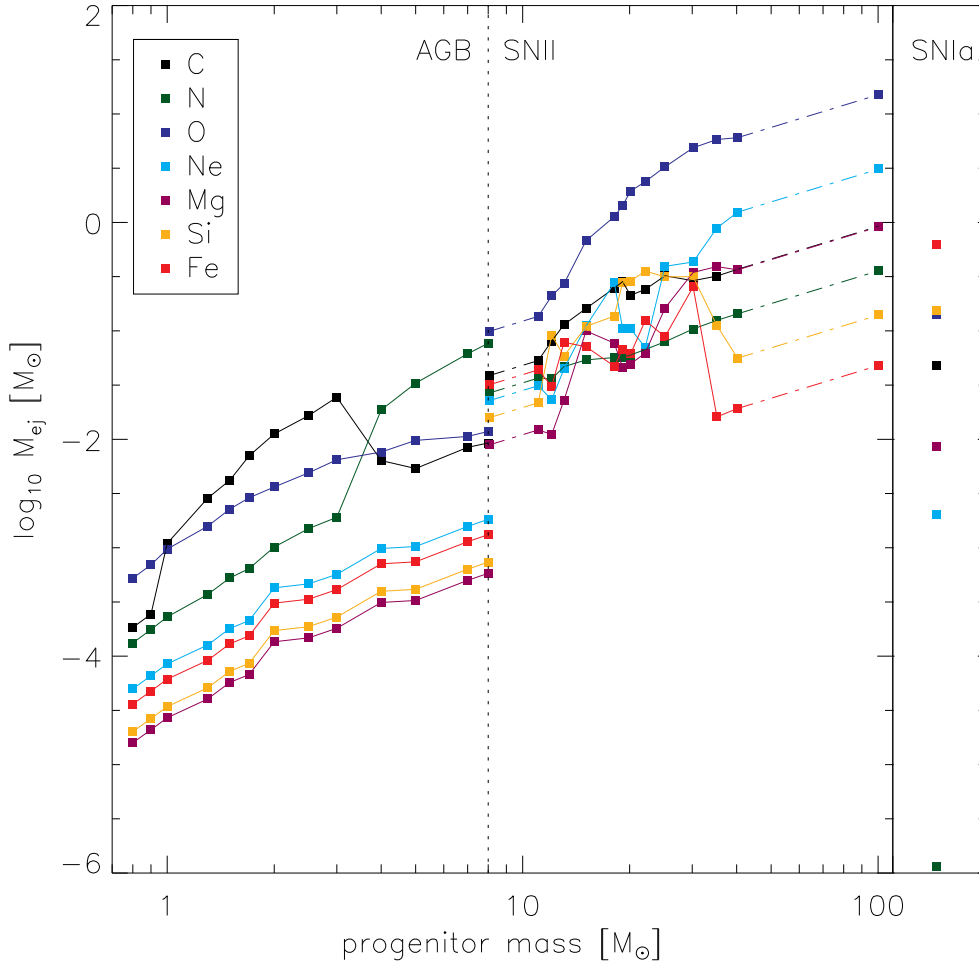


Figure 2.2: The mass of elements ejected by stellar processes as a function of initial mass in our nucleosynthesis model. Abundances for a single SNIa are shown for comparison on the right hand side. The mass limit between AGB stars and SNII progenitors is indicated at 8 M_{\odot} with a dotted line. Our AGB stellar data in our model is from van den Hoek & Groenewegen (1997). The yields for SNII from Woosley & Weaver (1995) and SNIa from Iwamoto et al. (1999). Solid lines indicate the original data whereas the dot-dash lines show adopted extrapolations to higher masses. The extrapolations are linear and scaled to the mass of the progenitor star. This plot was taken from Few et al. (2014) and reproduced with permission from the author.

CHAPTER 2

& Gibson 2003, similar to that as described in). The rate of SNIa in this case is computed by the double integration of the IMF and an assumed binary fraction of the two mass ranges i.e:

$$\begin{aligned}
 N_{SNIa}(\tau_*) &= M_0 \int_{m_{P,l}}^{m_{P,u}} \phi(m) dm \\
 &\times \left[b_{MS} \frac{\int_{MAX(m_{MS,l}, m_{TO})}^{m_{MS,u}} \phi(m) dm}{\int_{m_{MS,l}}^{m_{MS,u}} \phi(m) dm} \right. \\
 &\left. + b_{RG} \frac{\int_{MAX(m_{RG,l}, m_{TO})}^{m_{MS,u}} \phi(m) dm}{\int_{m_{RG,l}}^{m_{RG,u}} \phi(m) dm} \right].
 \end{aligned} \tag{2.40}$$

Here, SNIa systems are described as binary stellar systems with a primary mass range of $m_{P,l} = 3.0M_{\odot}$ to $m_{P,u} = 8.0M_{\odot}$. The primary star evolves into a white dwarf of which its mass is dominated by Carbon and Oxygen (C/O WD). The secondary star in a SNIa binary system is either a ‘main sequence’ (MS) or a red giant (RG). The mass ranges in this model for MS are $m_{MS,l} = 1.8M_{\odot}$ to $m_{MS,u} = 2.06M_{\odot}$, and for RG are $m_{RG,l} = 0.9M_{\odot}$ to $m_{RG,u} = 1.5M_{\odot}$. The binary fractions for each of the secondary types of stars in this model is $b_{MS} = 0.05$ and $b_{RG} = 0.02$ (the binary fractions for main sequence and red giants respectively) are taken from Kawata & Gibson (2003). This two-component SNIa model described here is similar to Mannucci et al. (2006) with the exception that the typical mass (and hence time-scale) of the two components are different, as such this model in particular has an onset time of 700 Myr.

In the regions of the galaxy with dense gas, star formation converts gas into collisionless star particles. Eventually some stars will return some of this gas to the ISM with more energy and momentum. This instantaneous return of matter emulates what happens from the feedback from SNII. Energetic feedback from both type-Ia and type-II supernovae (SNIa and SNII respectively) is included with each SN injecting 10^{51} erg as thermal energy into the local grid cell, AGB stars eject their mass passively into the enclosing grid cell.

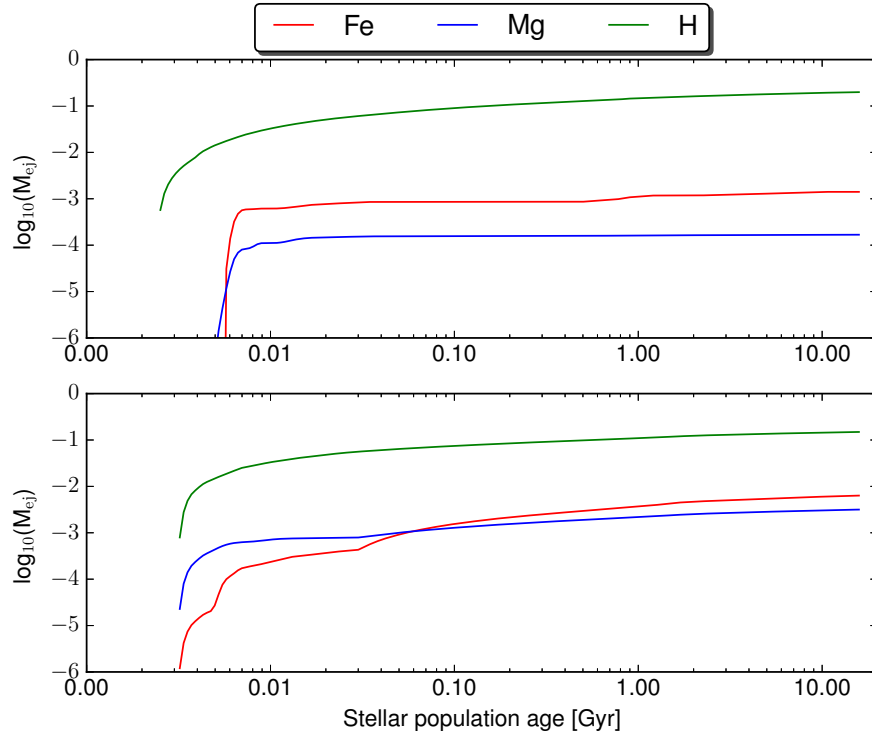


Figure 2.3: The ejection rate of isotopes per $1 M_{\odot}$ formed for stellar particle as a function of cosmic time. used in the study presented in this thesis. This is done per unit mass for the Salpeter (1955) IMF as a function of age which is a part of the chemical evolution model described in §2.3.2. The panel above represents that of a solar star metallicity and the one below for a Population III metallicity.

CHAPTER 2

In summary, we consider stars in the mass range $0.5\text{--}8 M_{\odot}$ to evolve along the AGB with the yields from van den Hoek & Groenewegen (1997). Stars with masses $8\text{--}100 M_{\odot}$ eject mass and energy as SNI and produce yields as described in Woosley & Weaver (1995) using a correction described in Timmes et al. (1995) to half the Fe production. The number of SNIa per unit initial stellar mass is also determined by the IMF via the number of stars with masses $3\text{--}8 M_{\odot}$ in binary systems with either a red giant or main sequence star whose secondary type binary fractions are $b_{MS} = 0.05$ and $b_{RG} = 0.02$. The lifetime of these systems is taken as the main sequence lifetime of the secondary star (Kodama & Arimoto 1997). Figure 2.2 shows the abundances of ejected metals as a function of the progenitor mass as a result of combining the nucleosynthesis models described here. We use the IMF from Salpeter (1955), where we treat the IMF as a single power law of slope -1.35 as shown in Equation 2.37 with lower and upper mass limits of 0.1 and $100 M_{\odot}$, respectively. This is commonly referred to as the Salpeter IMF. Figure 2.3 shows the abundances of elements H, Fe and Mg that ejected within our chemical evolution model. The implementation for SNeI, SNeII, and AGB stars and the physics of the chemodynamical patch are described in more detail in Few et al. (2012a) and Few et al. (2014, Section 2) as well as in Chapter 4 in (Few 2012). The impact of the choice of IMF in galactic chemical evolution models simulated in RAMSES-CH is discussed within Few et al. (2014).

This combination of theories produces a chemical evolution model with its parameters additionally described in Few et al. (2014) as model *S55-uM100-IaK*. The impact of the choice of IMF and SNIa model on simulations similar to that presented here is also discussed. The implemented IMF itself is not resolved in the simulation, but it is incorporated as a component of the chemical evolution model. A Kroupa 2001 IMF (Kroupa 2001), which bears similarities to a Chabrier IMF (Chabrier 2003) would for example increase the mean $[\text{Mg}/\text{Fe}]$ abundances by 0.1 dex and $[\text{Fe}/\text{H}]$ abundances by 0.2 dex compared to the Salpeter IMF. The theory

CHAPTER 2

above is combined to produce a CE model. We use the Salpeter (Salpeter 1955) IMF, with an upper mass limit of $100M_{\odot}$. In addition, we use the SNIa, SNII and AGB models described above to produce a CE model with the realisation name of *S55-uM100-IaH* (A change of name from *S55-uM100-IaK* in (Few et al. 2014), of which comparison with other CE models are discussed within). The SNIa model is henceforce denoted as IaH in our naming convention; However, unlike the works that inspired this model in particular (Kobayashi et al. 2000; Kawata & Gibson 2003), the IMF for the secondary stars is the same as for the primaries and we have not applied a metallicity floor.

2.3.3 Galaxy Initial Conditions: Selene-CH

We focus our study on a simulated galaxy called ‘Selene-CH’. This galaxy is the result of simulating the cosmological initial conditions that make up the galaxy Selene from the Ramses Disc Environment Simulations (RaDES) ‘Selene’ galaxy Few et al. (2012b) with RAMSES v3.11 and our chemodynamical patch RAMSES-CH.

We employ a cosmological ‘zoom-in’ simulation technique using RAMSES-CH to simulate the galaxy: ‘*Selene-CH*’. The initial conditions and local environment for Selene-CH is described in Few et al. (2012b) and the model used to create the realisation is described in §2.3.2 and (Few et al. 2014). The assembly history of the halo *Selene-CH* resides in is relatively quiescent (it was selected as such) with no major mergers after redshift $z = 1.0$. Additionally, this galaxy is sampled as such that there are no dark matter halos more massive than $3 \times 10^{11} M_{\odot}$ in a 3 Mpc radius. Although *Selene* is relatively isolated in comparison to the rest of the RaDES sample, this isolation does not make much difference on its physical properties as shown in Few et al. (2012b), for example the other half of the RaDES sample have neighbours the same mass as themselves but have relatively quiet merger histories.

CHAPTER 2

The assembly history of the original version of *Selene* is described in Few et al. (2012b) and more extensively with relation to the effect of its assembly on the metallicity and age distribution in Ruiz-Lara et al. (2016). We run the simulation to $z = 0$.

This galaxy exists in a box $20 h^{-1}$ Mpc in size created with cosmological parameters $(H_0, \Omega_m, \Omega_\Lambda, \Omega_b, \sigma_8) = (70 \text{ km s}^{-1}, 0.28, 0.72, 0.045, 0.8)$ of which these parameters are similar to those from Hinshaw et al. (2013). We run the simulation to $z = 0$. The adaptive grid can refine up to 17 levels corresponding to a maximum resolution of 218 pc with a dark matter particle mass resolution of $5.64 \times 10^6 M_\odot$ and a stellar population particle birth mass of $3.3 \times 10^4 M_\odot$. We describe our choice of feedback parameters in §2.3.4

The galaxy presented here is a chemodynamical resimulation of the *Selene* initial conditions first presented in Few et al. (2012b). The feedback scheme used in simulating *Selene-CH* is different to the original version and so, while the galaxy has roughly the same environment and assembly history, some differences are to be expected. The galaxy inhabits a dark matter halo with a mass of $5.245 \times 10^{11} M_\odot$ that is more than 3 Mpc distant from any other haloes more massive than $3 \times 10^{11} M_\odot$. The dark matter halo mass is somewhat lower than what is usually quoted from observations, which at the lower end of the possible mass range predicts a mass of $0.8_{-0.2}^{+1.2} \times 10^{12} M_\odot$ (Battaglia et al. 2005). The total mass of the stellar particles in the galaxy is $5.603 \times 10^{11} M_\odot$ which is lower than the quoted stellar mass of the Milky way around $6.43 \pm 0.63 \times 10^{10} M_\odot$ (McMillan 2011). The halo and its properties are identified using the AMIGA halo finder (AHF) (Knollmann & Knebe 2009; Gill et al. 2004). AHF uses adaptive mesh refinement of isodensity contours to resolve dark matter halos as well as its subhalos. The centre of a dark matter halo is a peak in the cosmological density field, and subhalos are peaks in each local halo density field. We align the galaxy by calculating the angular momentum of

CHAPTER 2

the cold gas with temperature $T \leq 10000$ K within 10% of the virial radius of the dark matter halo. Since *Selene-CH* is simulated using *RAMSES-CH* which is based on *RAMSES* v3.11 with a different gas cooling and feedback mechanisms, there are some subtle differences in the properties of the galaxy. Namely the mass of the dark halo in *Selene* is $5.09 \times 10^{11} M_{\odot}$ and the stellar mass is $6.71 \times 10^{10} M_{\odot}$. *Selene-CH* has a slightly more massive dark matter halo but with less mass converted into stars.

A gas surface density projection of *Selene-CH* is shown in Figure 2.4 demonstrating the presence and shape of the spiral arms. The cross at $x = 4.0$ kpc and $y = 6.93$ kpc is the region where we place our simulated observer as described in §2.6.3, 8 kpc from the galactic centre in a spiral arm. From repeated the analysis which follows with stars from different positions on a circle with a galactocentric radius of 8 kpc which shows our results are robust to changes in the position of the simulated observer. This is due to azimuthal homogeneity in the age and chemical abundances. Therefore keeping the radius consistent yields approximately homogeneous distribution of stellar age and metal abundances. The mean azimuthal variations at 8 kpc from the galactic centre for $[\text{Fe}/\text{H}]$ and $[\text{Mg}/\text{Fe}]$ are 0.02 dex and 0.005 dex respectively and the mean age variation is only 0.5 Gyr. This means that in this model, the choice of x and y as a function of $r = 8$ kpc makes little has little difference in terms of age or metal distribution, so picking a location inside or outside a spiral arm is irrelevant (other than spiral arms increase the abundance of stellar composite particles in the study).

We use stars from a spherical region 2 kpc in radius around this point which is treated as our simulated solar neighbourhood for the Gaia-ESO survey comparison and the wedge region for the RAVE comparison. The size of these regions are discussed in §2.6.3.

We further analyse *Selene-CH* in a similar way that an observer would do by filtering out stars from comparing the colours and effective temperatures of the

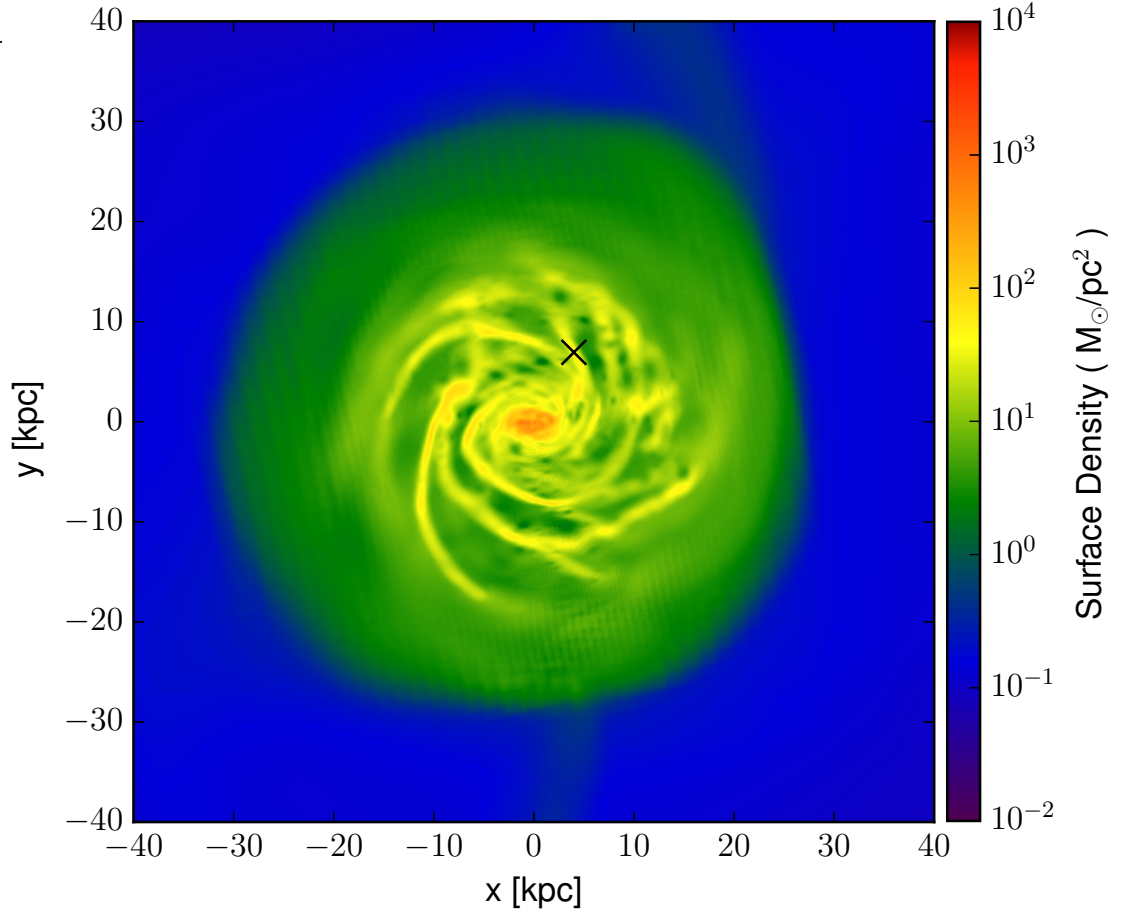


Figure 2.4: Face on gas surface density projection of the simulated galaxy Selene-CH. The galaxy was visualised using the YT visualisation toolkit (Turk et al. 2011) with a projection depth of 20 kpc. The black cross at $x = 4.0$ kpc and $y = 6.93$ kpc is the position of our simulated observer as described in §2.6.3. The region selected in this work is a 2 kpc sphere around the indicated position, similar to the coverage of the Gaia-ESO survey.

CHAPTER 2

stars to remove the contribution of stellar populations that we are not interested in (e.g. red giants). This is done using the Synthetic Colour-Magnitude Diagram tool (Pasetto et al. 2012) SYNCMD, in order to apply additional photometric cuts to the synthetic photometric stars. The choice of photometric cuts depend on the survey which the simulated galaxy is being compared with.

2.3.4 Choice of Galaxy Feedback Parameters

Our choice of physical feedback parameters for Selene-CH are a result of performing a simple parameter study. Our galaxy Selene-CH uses the parameters $n_{\text{poly}} = 0.1 \text{ cm}^{-3}$, $\epsilon_* = 0.01$, $\gamma = 2$, $T_{\text{poly}} = 188 \text{ K}$, $T_{\text{poly,min}} = 188 \text{ K}$ with delayed cooling (and thus the thermal and kinetic wind feedback off) are the result of performing a simple parameter study. Additionally our delayed cooling routine is described in §2.3.1 which uses the parameters $t_{\text{dis}} = 10 \text{ Myr}$ and $\zeta_{\text{cool}} = 0.001$. In our kinetic feedback model used, we set r_{blast} to be a 2-cell radius feedback-sphere centred on the star particle. The physical significance of these parameters has already been discussed in §2.3.1 so we shall focus on the choice of parameters and briefly discuss what impact they have.

Here we present a short parameter study to investigate the effects of the choice of feedback parameters in *RAMSES-CH*. We selected 12 different galaxy simulations with the same galaxy initial conditions used for the *Selene* galaxy in Few et al. (2012b) and we run each simulation to $z = 0$ keeping the chemical evolution model the same. However we vary the physical feedback parameters, feedback modes and the spatial resolutions. We keep chemical evolution model consistent throughout which is *S55-uM100-IaK* as described in Few et al. (2014). We use this model because it gives reasonable results in terms of the distribution (both the abundances and dispersion of those abundances) of elements.

CHAPTER 2

We shall briefly discuss the reasoning behind the choice of galaxy feedback parameters we have chosen for *Selene-CH*. Additionally we shall discuss the impact the choice of physical parameters appears to have on the chemical abundances of the galaxy. The visualisations presented here were made with the YT visualisation toolkit (Turk et al. 2011) to produce projection plots shown here.

There is a lot of ongoing work in the astrophysical community to understand the impact of feedback on galaxy formation models (Kim et al. 2014), as the resolution of simulated galaxies increase, the role of feedback becomes ever more important. Previous studies have discussed how the choice of chemical evolution model (i.e. your choice of IMF and supernova physics) have an effect on chemistry on an isolated galaxy which is discussed in Few et al. (2014) and briefly discussed in §2.3.2. However, since *RAMSES-CH* has only been used in a small sample of studies, the impact of the choice of physical feedback parameters (such as star formation threshold density and supernova feedback) on the kinematics and chemistry has not been studied in great detail. Additionally detailed analytical studies of the impact of the choice of parameters has not been undertaken due to time and resource constraints. Because of this, ϵ_* , t_{dis} and ζ_{cool} is not altered at all and additionally, we only present one kinetic feedback-based and one thermal feedback-based simulation runs. Additionally, we keep the chemical evolution model the same as described in §2.3.2.

Our galaxy of choice from Table 2.1 is *Selene-CH-10*. Any reference to *Selene-CH* in any other section is *Selene-CH-10* as presented here. For reference, we have also included the parameter choice used for the original *Selene* run. *Selene* differs from our runs from having a polytrope $\gamma = 5/3$ rather than 2. We shall now briefly discuss the differences between these galaxies. Our focus of this brief parameter study is to study the effects the variation of different physical parameters has on the star formation, SNII and SNIa history which is shown in Figure 2.6, the gas disc

Table 2.1: Physical parameters between the different versions of *Selene-CH*. Our galaxy of choice is Selene-CH-10 (in bold) and we also include the original Selene run from Few et al. (2012b). Here ℓ_{\max} is the maximum refinement level, ϵ_* is the star formation efficiency. The parameters n_{poly} is the threshold for star formation, T_{poly} is the polytropic temperature and $T_{\text{poly},\min}$ is the temperature floor. f_w is the fraction of stellar mass formed swept up in SNII wind and f_k represents the fraction of SNII energy that is ejected kinetically. dc determines whether delayed cooling is enabled not (with "y" representing true and "n" representing false). For delayed cooling runs, we use a $t_{\text{dis}} = 10$ Myr and $\zeta_{\text{cool}} = 0.001$.

Model	ℓ_{\max}	ϵ_*	n_{poly}	T_{poly}	$T_{\text{poly},\min}$	f_w	f_k	dc
Selene-CH-1	16	0.01	2.7	3000	20214.07138	0	0	y
Selene-CH-2	17	0.01	2.7	3000	5053.517846	0	0	y
Selene-CH-3	16	0.01	0.3	2900	2246.007931	10	1	n
Selene-CH-4	16	0.01	0.3	2900	2246.007931	0	0	n
Selene-CH-5	16	0.01	0.3	2900	2246.007931	0	0	y
Selene-CH-6	17	0.01	2.7	5000	5053.517846	0	0	y
Selene-CH-7	17	0.01	2.7	6000	5053.517846	0	0	y
Selene-CH-8	17	0.01	2.7	18700	5053.517846	0	0	y
Selene-CH-9	17	0.01	1	1872	1871.673276	0	0	y
Selene-CH-10	17	0.01	0.1	188	187.1673276	0	0	y
Selene-CH-11	17	0.01	5	9360	9358.366381	0	0	y
Selene-CH-12	17	0.01	1	3900	1871.673276	0	0	y
<i>Selene</i>	16	0.02	0.1	10000.0	9873.535436	10	1	n

CHAPTER 2

in Figure 2.5. Additionally we study the circular velocity profiles of the gas, stellar and dark matter distributions in Figure 2.7 as well as the rotation velocity of young stars and cold gas in the same figure. We look at the impact on the gas and star formation surface density in Figure 2.8 and finally the distribution of $[\text{Fe}/\text{H}]$ with age in Figure 2.9 and $[\text{Mg}/\text{Fe}]$ in Figure 2.10 within the galactocentric spatial region of galactic radius $5. \leq R \leq 11.$ kpc and height $-3. \leq z \leq 3.$ kpc similar as to the analysis done in Few et al. (2014).

We vary the maximum spatial resolution ℓ_{max} between levels 16 and 17, which corresponds to 436.0 pc and 218.0 pc respectively. We also discuss the variation between different feedback models, namely kinetic feedback ($f_w > 0.0, f_k > 0.0, dc = "n"$), thermal feedback ($f_w = 0.0, f_k = 0.0, dc = "n"$) and delayed cooling feedback ($f_w = 0.0, f_k = 0.0, dc = "y"$). Here dc represents the delayed cooling flag (with $dc = "y"$ for it being enabled). In all these instances SNIa feedback will always be treated on a thermal mode with or without delayed cooling, and SNII will be treated on a kinetic mode when $f_w > 0$, otherwise it will be treated on a thermal mode. We additionally vary the parameters $n_{\text{poly}}, T_{\text{poly}}$ and $T_{\text{poly,min}}$ and their physical relations are described in §2.3.1 and we assume that all of the energy ejected from SNII and SNIa is coupled to the energy at 100% efficiency.

The comparison between *Selene-CH-3*, *Selene-CH-4*, *Selene-CH-5* is that of different feedback mechanisms. Namely between kinetic (SNII) feedback which is a comparable feedback scheme with the original *Selene* run in Few et al. (2012b) and described in more detail in Few (2012). Although *Selene* was run on an older version of *RAMSES* (v3.01 to be precise) and *RAMSES-CH* is based on *RAMSES* v3.11. Additionally, for *Selene* $\epsilon_* = 0.02$, $T_{\text{poly}} = 10^4$ K and the differences in supernova implementation (where the Type II SNe efficiency is $\eta_{\text{sn}} = 10\%$). There is also the difference in choice of halo finder algorithms too as our work profiles the dark matter halo with AHF, whereas *Selene* is profiled using the adaptahop algorithm (Aubert

Table 2.2: The particle mass and mass resolution properties for each variant of *Selene-CH* in the parameter study. M_{dark} represents the total mass of dark matter with $M_{\text{dark,min}}$ representing the minimum dark matter particle mass, of which is found in the highest resolution regions. Likewise M_{star} and $M_{\text{star,min}}$ represent the same properties for the stellar mass distribution. Our galaxy of choice is Selene-CH-10 (in bold) and we reference the original Selene galaxy from from Few et al. (2012b).

Model	resolution (pc)	M_{dark} ($10^{10} M_{\odot}$)	$M_{\text{dark,min}}$ ($10^5 M_{\odot}$)	M_{star} ($10^{10} M_{\odot}$)	$M_{\text{star,min}}$ ($10^5 M_{\odot}$)	$\log(M_{\text{dark}})$ (dex)	$\log(M_{\text{star}}/M_{\text{dark}})$ (dex)
Selene-CH-1	436.	52.994	56.454	4.397	49.63	11.724	-1.0811
Selene-CH-2	218.	52.445	56.454	5.191	6.200	11.712	-1.0044
Selene-CH-3	436.	53.035	451.63	5.373	5.512	11.724	-0.9943
Selene-CH-4	436.	51.838	451.63	5.296	5.511	11.714	-0.9907
Selene-CH-5	436.	52.168	451.63	4.745	5.516	11.717	-1.0412
Selene-CH-6	218.	52.841	56.454	5.134	6.208	11.723	-1.0125
Selene-CH-7	218.	52.532	56.454	5.069	6.206	11.720	-1.0155
Selene-CH-8	218.	53.009	56.454	4.623	6.199	11.724	-1.0594
Selene-CH-9	218.	52.557	56.454	5.239	2.297	11.721	-1.0014
Selene-CH-10	218.	52.452	56.454	5.603	0.2295	11.720	-0.9713
Selene-CH-11	218.	52.890	56.454	4.940	11.481	11.723	-1.0297
Selene-CH-12	218.	52.685	56.454	4.111	2.294	11.722	-1.0132
Selene	436.	50.9	55.27	6.711	2.41	11.706	-0.8799

CHAPTER 2

et al. 2004; Colombi 2013) and the slight variation between the kinetic feedback implementations due to the different versions of RAMSES and the chemodynamical patch discussed here. Nevertheless *Selene-CH-3* is designed to mimic the original *Selene* run as closely as possible which is achieved to some extent with similar extent of young stars in the disc, but *Selene-CH-3* is cuspier than *Selene*, has a more extensive cold gas disc and has a higher peak in star formation, rotational velocities and rotation curves due to the cuspier halo. These differences can be accounted for the differences in the implementation of feedback. *Selene-CH-4* undergoes thermal feedback and *Selene-CH-5* undergoes the delayed cooling scheme. *Selene-CH-3* and *Selene-CH-4* are the most cuspy as seen in Figure 2.7 and a more centrally concentrated young stellar distribution in comparison to *Selene-CH-5*. There is in *Selene-CH-3* and *Selene-CH-4* a greater dispersion of $[\text{Fe}/\text{H}]$ abundances within the disc region as shown in Figure 2.9, but a narrower distribution of $[\text{Mg}/\text{Fe}]$ when compared to *Selene-CH-5*. *Selene-CH-4* has the least dense spiral arms as shown in Figure 2.5 as well as the most peaked amount of star formation. *Selene-CH-3* and *Selene-CH-4* have the steepest K-S law distribution as shown in Figure 2.8. The variation in SNe feedback is very minimal.

The next step in our parameter study is to increase the resolution. We wish to be able to resolve the solar neighbourhood region with a finer precision (in the order of 200 pc). The comparison between *Selene-CH-1* and *Selene-CH-2* demonstrate the impact of increasing the resolution. This increases the dispersion in both the $[\text{Fe}/\text{H}]$ and $[\text{Mg}/\text{Fe}]$ distributions as expected since we are able to resolve finer variations in the metal distributions. The increase in resolution increases the distribution of young stars whilst reducing the extent of the cold gas disc, increases the peak in star formation and Type II SNe feedback and maintains a similar density distribution. There is a slight shift in the star formation history to favour early times at higher resolution but nothing significant.

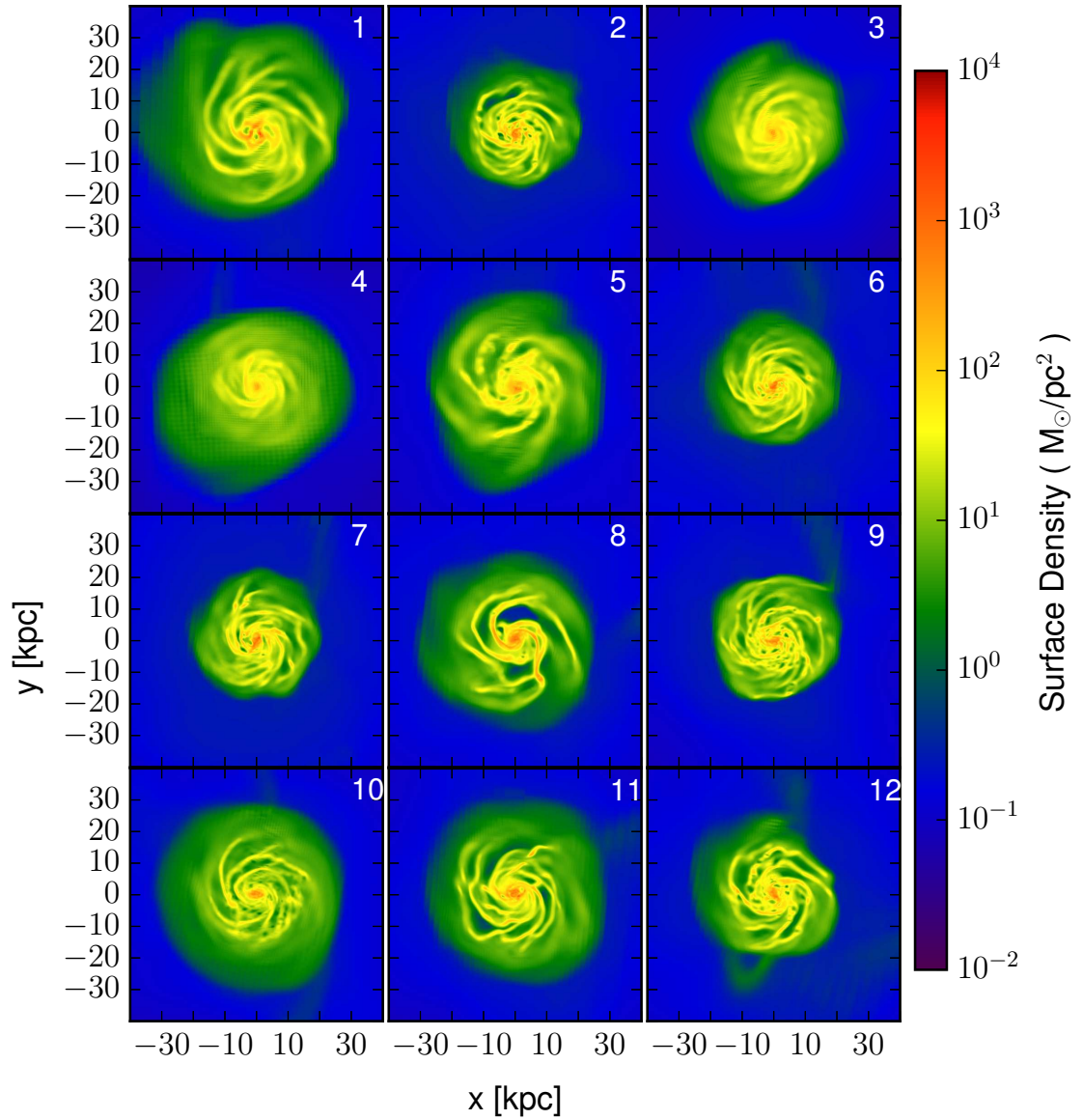


Figure 2.5: Plots of the surface density distribution of gas for the *Selene-CH* models labelled 1 to 12 from the parameter study. The change in colour from blue to red represents an increase in the gas surface density in M_{\odot} / pc^2 .

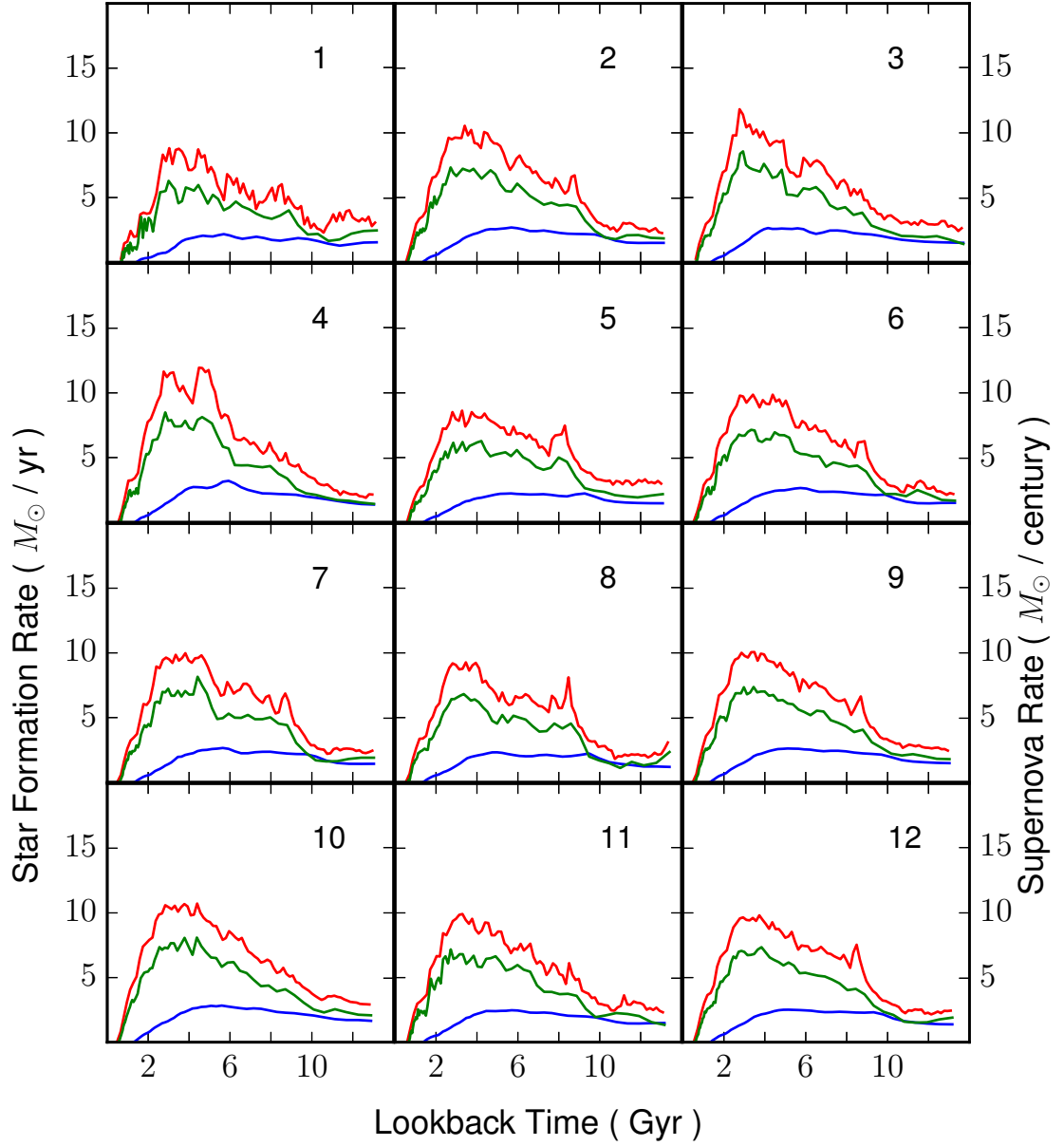


Figure 2.6: Plots of the star formation history, type SNIa and SNIi rates for the *Selene-CH* models labelled 1 to 12. The red line represents the star formation rate as a function of lookback time in M_{\odot} per yr. The green line represents the SNIi rate in units of M_{\odot} per century. The blue line represents $5\times$ the SNIa rate in units of M_{\odot} per century.

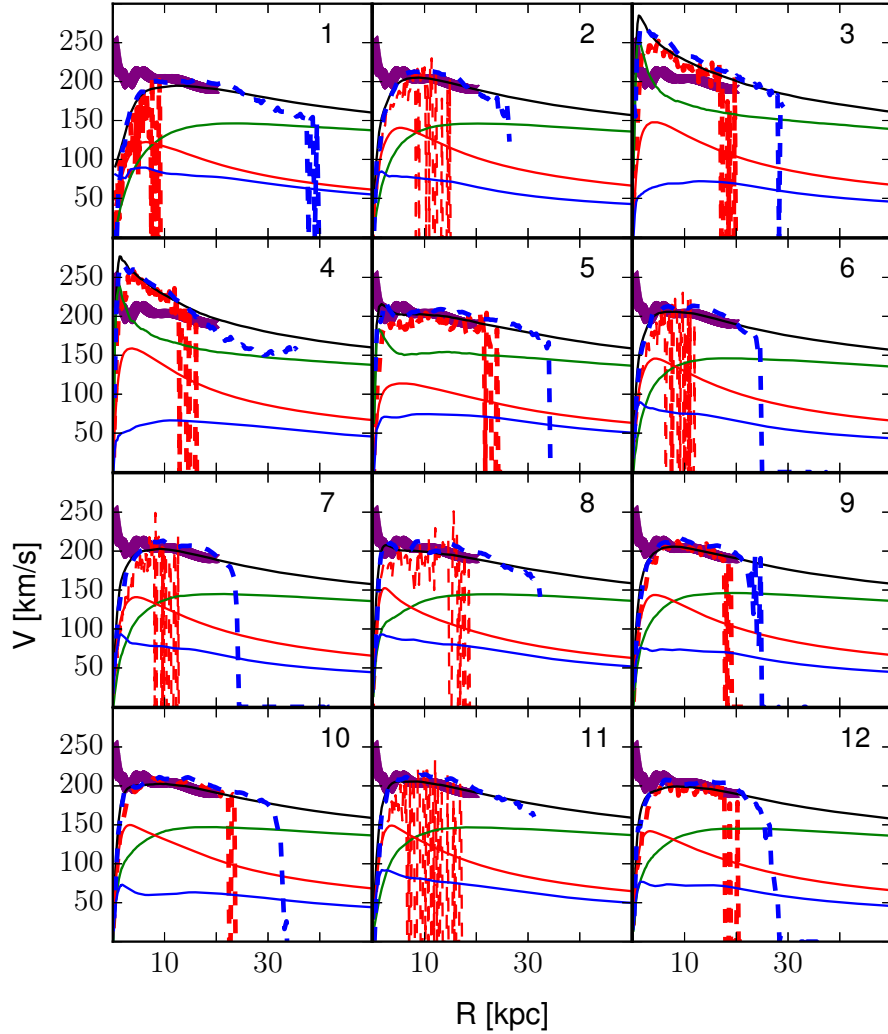


Figure 2.7: Circular and rotational velocity plots of the *Selene-CH* variants from the parameter study. The circular velocities V_{circ} are represented by the solid lines and the tangential velocities V_{rot} are represented by the dashed lines. The solid green line represents the dark matter V_{circ} profile. The solid red line represents the V_{circ} profile for all of the stars. The solid blue line represents the V_{circ} profile for the gas. The solid black line represents the rotation curve for all of the components of the galaxy. The dashed red line represents V_{rot} for stars with an age of 1 Gyr, and the dashed blue line represents V_{rot} for the gas with temperatures below 10^4 K. We also include the work of (Sofue et al. 2009) from observations of the Milky Way as shown by the purple line.

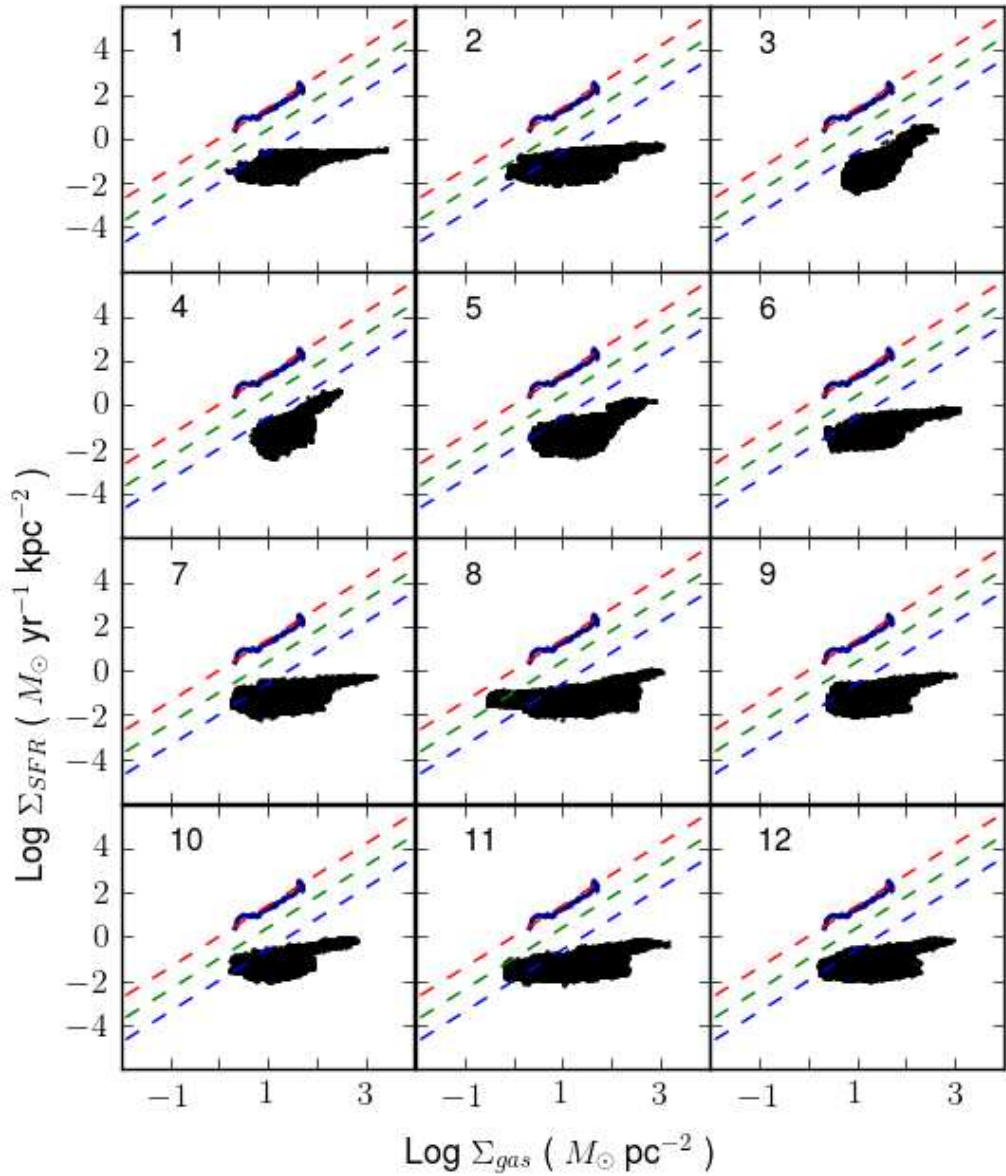


Figure 2.8: A scatter plot of the star formation rate per stellar surface density as a function of the gas surface density. This relation is often known as the Kennicutt-Schmidt law. The dashed blue line represents a star formation efficiency $\epsilon_* = 1\%$, the dashed green line $\epsilon_* = 10\%$ and the dashed red line $\epsilon_* = 100\%$. Selene-CH 3 and 4 follow the relation, but at lower efficiencies. This could be due to the choice of delayed vs. non-delayed cooling. We also include for comparison the equivalent plot for M51 as shown in Schuster et al. (2007) as the dark blue line.

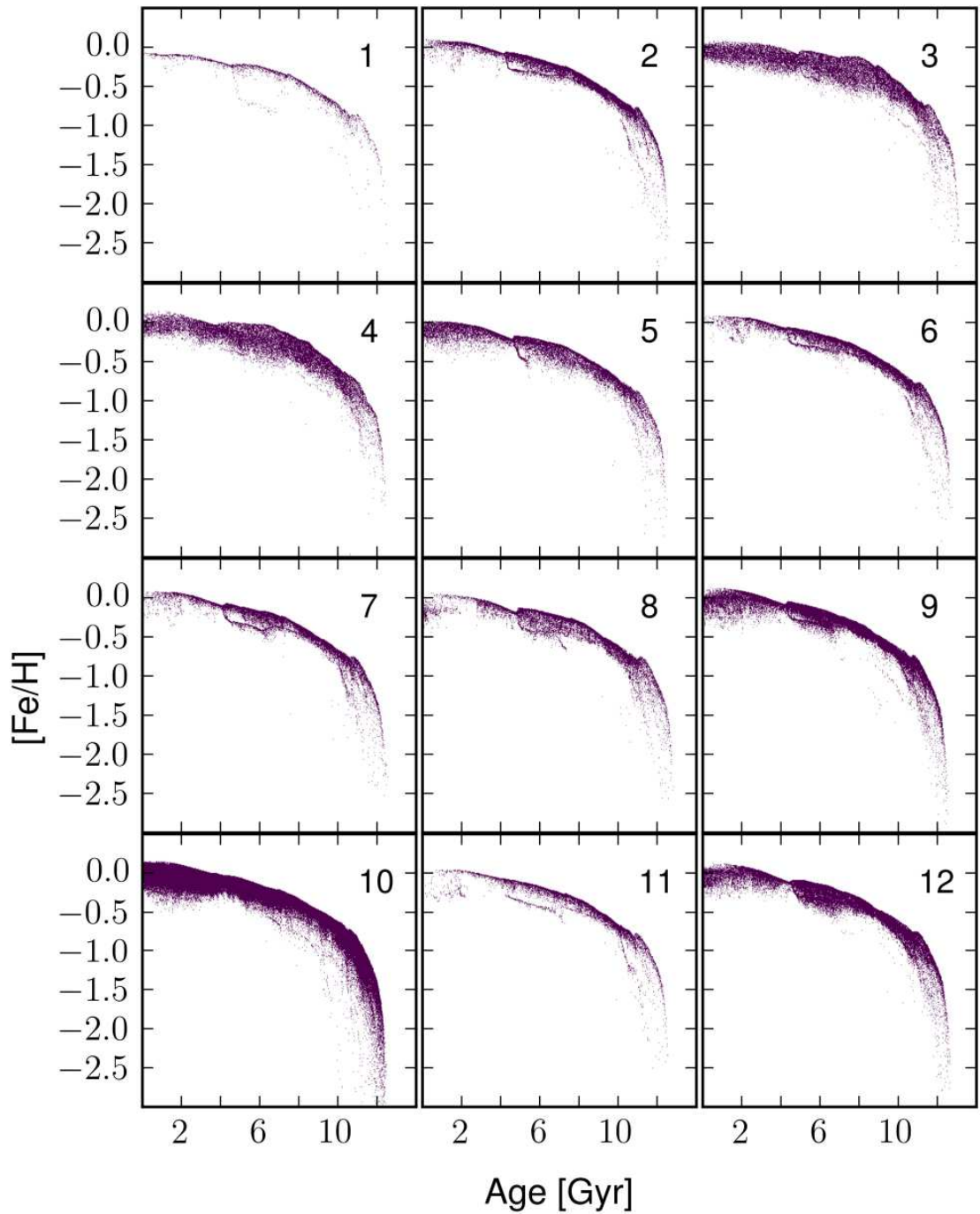


Figure 2.9: A scatter plot of the $[Fe/H]$ -age distribution for stars within the spatial region of $(5. \leq R \leq 11.)$ kpc and height $(-3. \leq z \leq 3.)$ for the the *Selene-CH* models labelled 1 to 12.

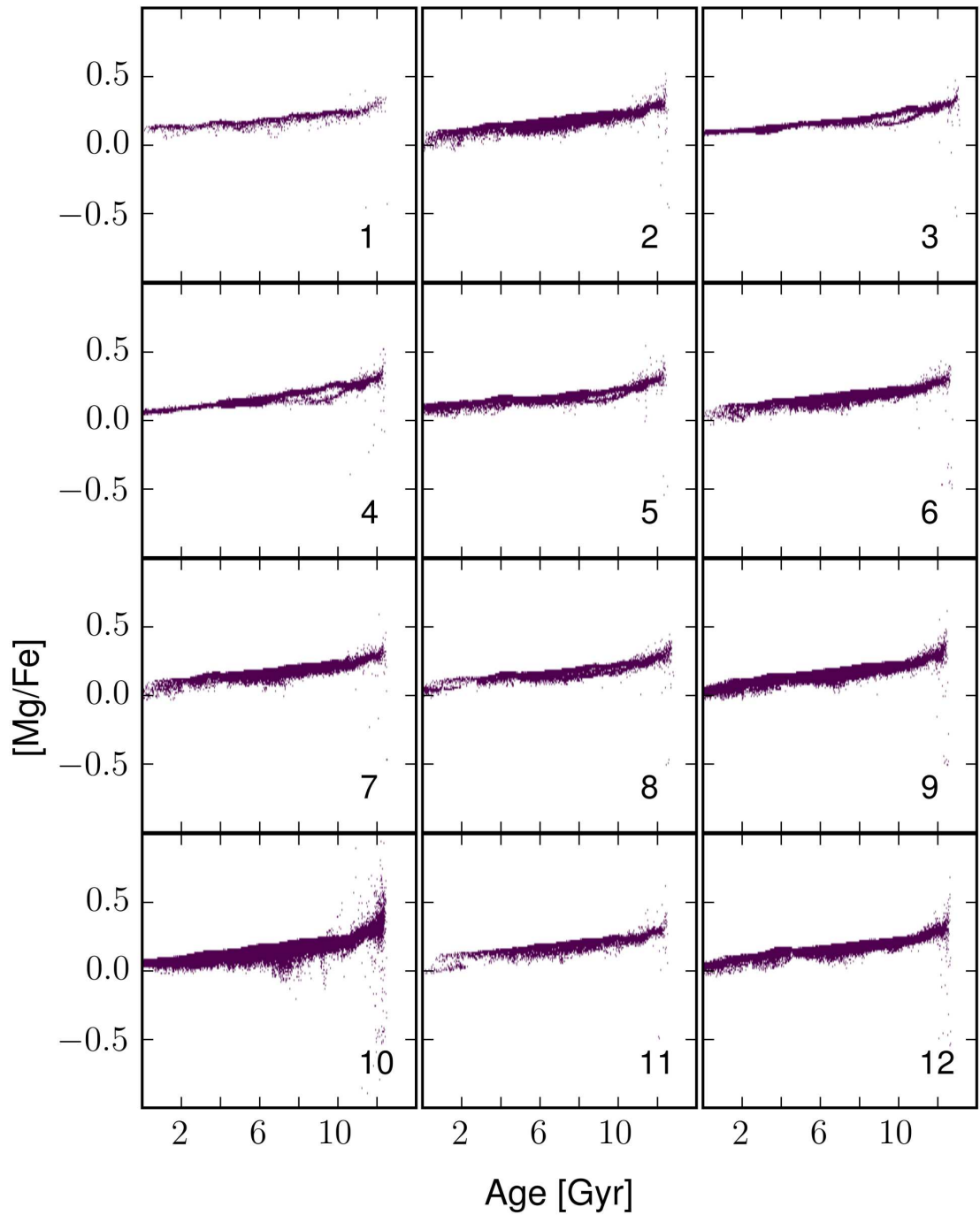


Figure 2.10: A scatter plot of the $[Mg/Fe]$ -age distribution for stars within the spatial region of $(5. \leq R \leq 11.)$ kpc and height $(-3. \leq z \leq 3.)$ for the the *Selene-CH* models labelled 1 to 12.

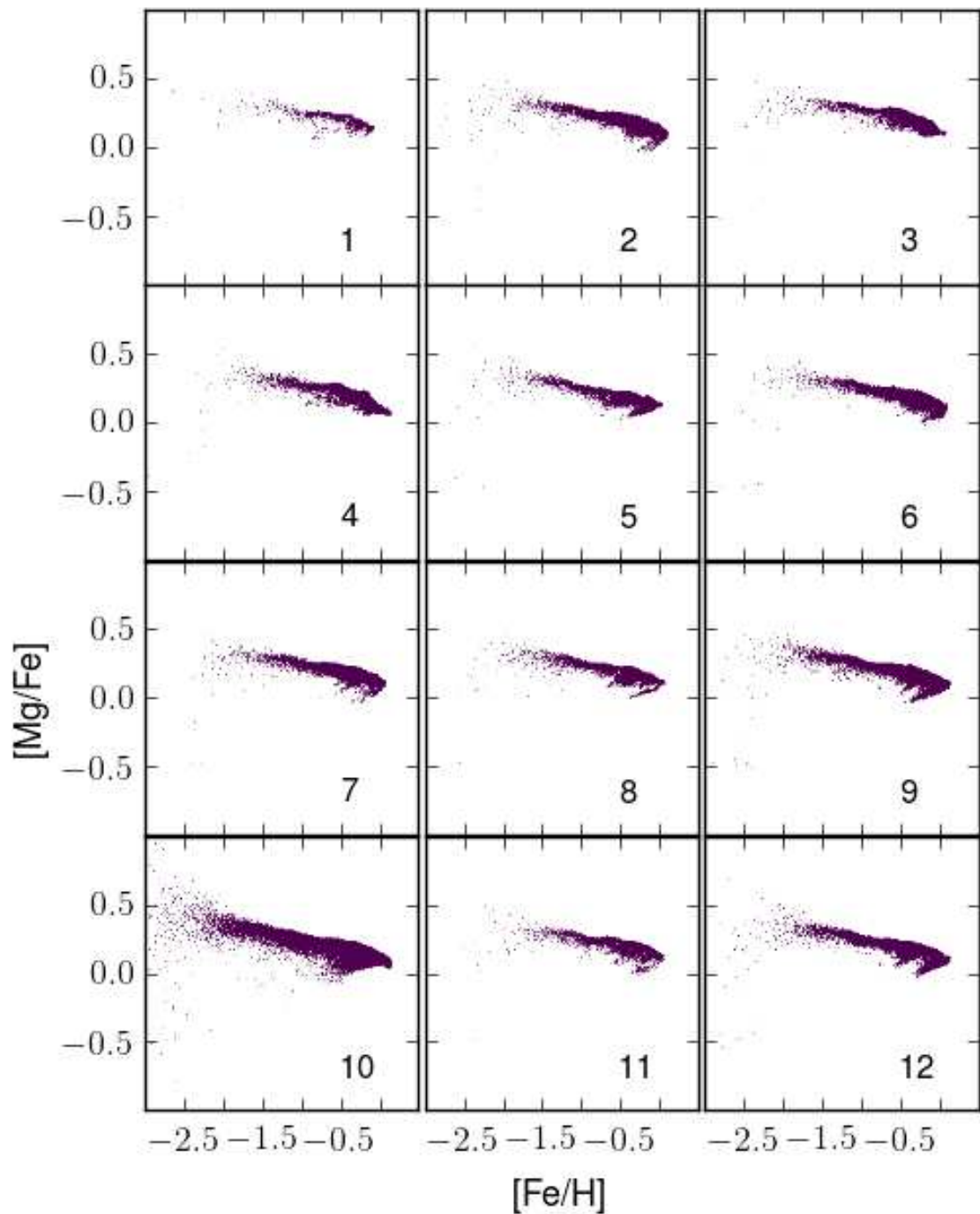


Figure 2.11: A scatter plot of the $[\text{Mg}/\text{Fe}]$ - $[\text{Fe}/\text{H}]$ distribution for stars within the spatial region of $(5. \leq R \leq 11.)$ kpc and height $(-3. \leq z \leq 3.)$ for the the *Selene-CH* models labelled 1 to 12.

CHAPTER 2

The comparison for the variation of T_{poly} is found from comparing *Selene-CH-2*, *Selene-CH-6*, *Selene-CH-7* and *Selene-CH-8*. The appearance of the gas disc goes from quite small and fairly similar to the extremely high value which has a more extended disc and ‘ropey’ arms with increasing T_{poly} . The metal distribution functions undergo minimal changes. The highest polytrope temperature (T_{poly}) in *Selene-CH-8* gives a more extended gas disc. The SFH is surprisingly robust to changes in the T_{poly} and even increases a little with the extreme value. Overall the biggest difference seems to be chiefly in the gas distribution which looks more ‘collapsed’ for the really low value with more extreme definition between the arm and inter-arm region. The rotation curve chiefly differs only for *Selene-CH-8* which has a more extended disc. This conclusion holds when comparing *Selene-CH-9* and *Selene-CH-12* which have a decreased star formation density threshold, the increase in T_{poly} extends the gas disc.

Our final comparison involves variations of n_{poly} . Variations in this parameter mostly appears to alter the dispersion of $[\text{Fe}/\text{H}]$ and $[\text{Mg}/\text{Fe}]$ abundances, but also the slope of the star formation history, with larger values of n_{poly} favouring the occurrence of star formation in earlier times. Additionally the reduction of n_{poly} generates star particles with a finer mass resolution as shown in Table 2.2. This is particularly useful in the study of small geometrical regions of a galaxy, such as the solar neighbourhood.

Overall from the short parameter study presented here, we choose *Selene-CH-10* as our galaxy of choice for the comparative studies with observational surveys. Our reasoning for this choice is due to the relatively high mass resolution of star particles which allows us to study stars in a finer spatial region, the larger dispersion in both the $[\text{Fe}/\text{H}]$ and $[\text{Mg}/\text{Fe}]$ abundance, the relatively smooth star formation history, good rotation curves and rotation velocity profiles. However we acknowledge that this parameter study is not rigorous and indeed there is most likely a choice of

CHAPTER 2

parameters that best replicates the properties of the Milky Way than those presented here. The motivation of this study however was to identify a reasonable galaxy for the purposes of comparing with the Gaia-ESO survey and the RAVE survey. If time was not a constraint, we would have varied the physical feedback parameters more finely and studied their effects on the properties of the galaxy over time. We leave a more detailed and rigorous analysis of the variation of the different feedback parameters to future work.

2.4 SynCMD

The SYNCMD synthetic stellar populations generation tool (Pasetto et al. 2012) is a toolkit designed to examine simulation data in a similar manner to how an observational survey would sample real life stellar populations. The toolkit is used to apply observationally-motivated selection functions to simulated stellar population particles. As discussed in §2.3, each such particle represents a coeval mono-abundance stellar population, its mass is simply the total stellar mass. The details of the SYNCMD code are given in Pasetto et al. (2012), and we summarise the process here and give details on how the code is used. A preliminary application of SYNCMD has been undertaken using a ‘RAVE-like’ selection function (Miranda et al. 2014).

In short, SYNCMD is capable of converting simulation parameters into the observational plane. The inputs required for this are the ages, metallicity and chemical abundances of stellar population particles as well as an observational selection function (including spatial, colour, Magnitude, surface gravity and effective temperature) and an IMF, as well as the location in the simulation for where the observer should be placed. The outputs of this process generates a colour-magnitude diagram (CMD), and an updated chemical abundance distribution based upon the observational selection function used for the simulation. This enables consistent comparison of Galactic

CHAPTER 2

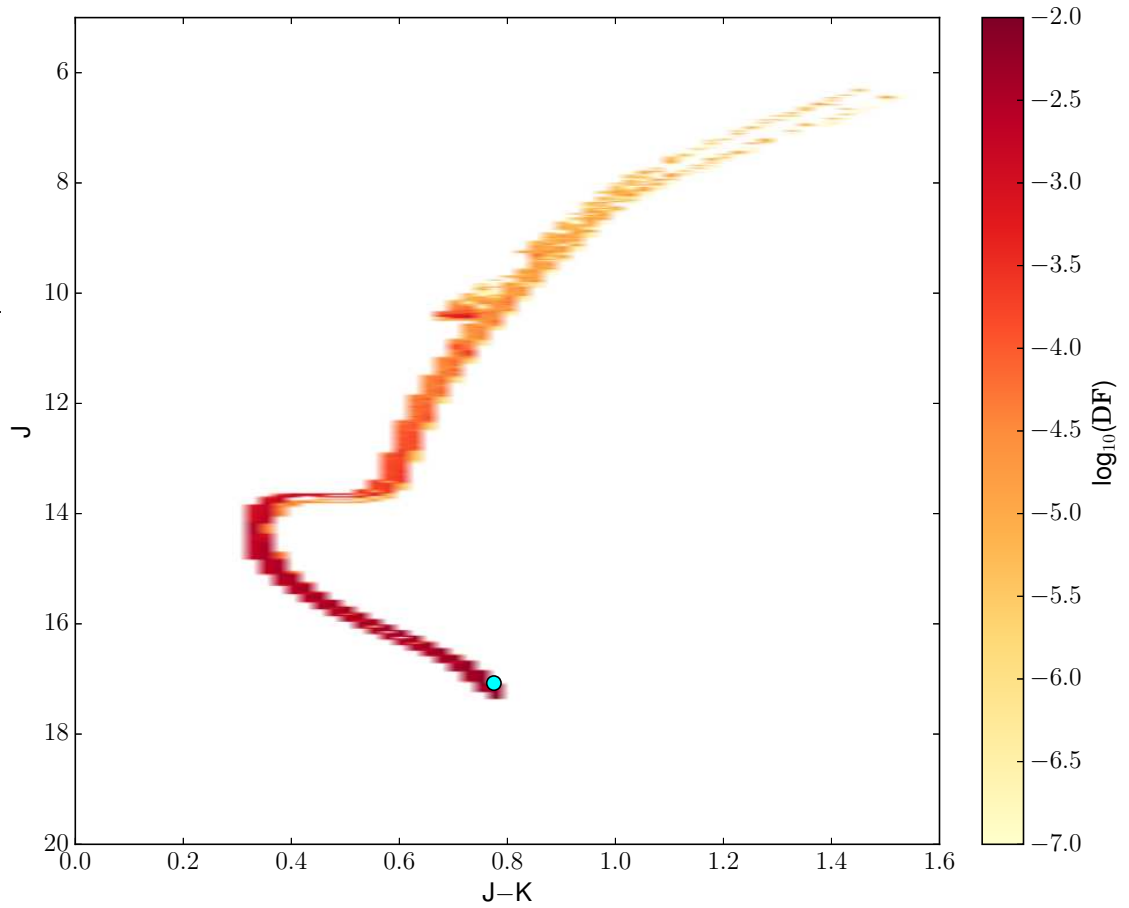


Figure 2.12: An example colour magnitude diagram of synthetic stellar particles generated through the application of SYNCMD. The cyan marker illustrates the single simulated composite stellar particle in which SYNCMD populates the presented CMD. The CMD is normalised to the total abundance of particles, the colour bar on the right from red to white shows the decrease in logarithmic abundance of normalised synthetic stars per CMD bin.

CHAPTER 2

chemical evolution models, and simulation results with observational surveys such as the Gaia-ESO survey and RAVE. The simplicity of the inputs for SYNCMD allow for a consistent treatment for different simulation methods (e.g. SPH vs. AMR, or chemical evolution model). The bulk of the code is written in FORTRAN and the mathematical principles and methodology behind the FORTRAN code were described in (Pasetto et al. 2012). We build upon this with pipeline for the code written in IDL which together makes SYNCMD. SYNCMD keeps to its original design criteria of being independent of a particular simulation software, not dependent on specific prescriptions used to generate the stellar models, handle the order of $\sim 10^{12}$ synthetic stellar particles and requires little computational power without requiring OpenMP or MPI. SYNCMD allows us to numerically split a stellar population particle from an N-body into individual stars by stochastically populating a CMD. Due to resolution limits in simulations, stellar population particles represent ‘averaged’ stellar populations rather than individual stars. Stellar population particles typically have a mass of $\sim 10^4\text{--}10^6 M_{\odot}$ and therefore a stochastic approach is valid. The usefulness of this toolkit is best demonstrated in Figure 2.4 in which demonstrates the difference the CMD a population of synthetic stellar particles and and a single stellar population particle both being the same mass.

A system of stellar population particles from a galaxy simulation has a distribution function of physical properties $f_{\text{SPP}}(\boldsymbol{\Omega})$. Here $f_{\text{SPP}}(\boldsymbol{\Omega}) = (\mathbf{X}, \mathbf{V}, m, Z, t_0, \beta)$ with \mathbf{X} and \mathbf{V} representing your position (x, y, z) and velocity (v_x, v_y, v_z) vectors respectively and m_0, Z, t_0 representing the particles birth mass, metallicity and age. In particular since we use the IMF as part of the computational process, the study here is best done using the birth masses of the stellar population particles. β represents any other physical properties (such as an array of metal abundances, or other properties of interest of study) one could associate within the simulation. In the case of this work $\beta = ([\text{Fe}/\text{H}], [\text{Mg}/\text{Fe}])$. Each stellar population particle is itself a distribution

CHAPTER 2

function of physical properties $f_{\text{SSP}}(\boldsymbol{\Omega}_{\text{SSP}}) = (\mathbf{X}_{\text{SSP}}, \mathbf{V}_{\text{SSP}}, m_{\text{SSP}}, Z_{\text{SSP}}, t_{0,\text{SSP}}, \beta_{\text{SSP}})$

The relation between $f_{\text{SPP}}(\boldsymbol{\Omega})$ and $f_{\text{SSP}}(\boldsymbol{\Omega})$ is:

$$f_{\text{SPP}}(\boldsymbol{\Omega}) = \sum_{i=1}^n f_{\text{SSP}}(\boldsymbol{\Omega}). \quad (2.41)$$

Where n is the number of stellar population particles in f_{SPP} (the simulation). We consider each stellar population particle to consist of 100,000 synthetic star particles in the mass range of 0.15 and 20.0 M_{\odot} . The number of stars is chosen to be large enough to sample the whole range of the IMF which is represented as a power law of index -1.35. The stellar mass of particles is indeed variable with mass lost from the stellar population via SN and stellar wind over the lifetime of the population.

The 100,000 synthetic star weighting is done using the initial mass of the particles and the appropriate amount of mass lost as the stars eject mass is accounted for after the 100,000 synthetic star particles are created from the stellar evolution models. With the correct weighting coming from the initial stellar population mass and with the SynCMD results being normalised for comparison with the observations the actual number doesn't matter except that it is sufficiently large to sample the IMF well. The stellar composite particle mass varies with time as mass is lost from the stellar population via SN and stellar wind over the lifetime of the population. However, the weighting is done using the initial mass of the particles and the appropriate amount of mass lost as the stars eject mass is accounted for after the 100,000 synthetic star particles are created. With the correct weighting coming from the initial stellar population mass and with the SYNCMD generated results being normalised for comparison with the observations the actual number doesn't matter except that it is sufficiently large to sample the IMF well. However a small minority ($< 5\%$) of the stars sampled have a birth mass a factor of 2 greater than the mass $3.3 \times 10^4 M_{\odot}$ (due to being born in a lower resolution region). What we did not have time to do in this study was to take this into account by e.g. doubling

CHAPTER 2

the contribution of stars to the synthetic CMD which have a birth mass double that of $3.3 \times 10^4 M_{\odot}$. However this is not an issue in this work since the majority of star particles have the same initial mass, and thus can all be weighted by the same number of synthetic stars. Additionally we assume that the 100,000 synthetic stars generated per composite star particle is at the same spatial position in the simulation. Thus all 100,000 stars generated are at the same distance from the observer as the composite star particle.

The physical properties of the synthetic stellar particles are based on theoretical stellar models. These properties are the effective temperature T_{eff} , log of the surface gravity $\log(g)$, magnitudes in different colour bands, ages, metal abundances and masses. Here we use the stellar isochrones presented in Bertelli et al. (2008, 2009), which cover a wide grid of helium (Y) and metal (Z) abundances, an enrichment ratio $\Delta Y/\Delta Z$, and include mass loss by stellar wind and the thermally pulsing AGB phase (Marigo & Girardi 2007). It is worth to briefly mention in this context that the metallicity Z is defined as the fraction of mass of a star (or gas) that is not in hydrogen (X) or helium (Y) i.e. if a star has $Z = 0.01$ then 1% of its mass is made up of metals. The isochrones are used to calculate a database of simple stellar populations using a modified version of YZVAR, which has been used in many studies (for instance Bertelli et al. 2003, and references therein). A detailed description of the properties of stellar libraries used to make the isochrones in SYNCMD are described on page 6 in Pasetto et al. (2012). These include bolometric corrections from Girardi et al. (2002) and the stellar spectral flux library ODFNEW ATLAS9 (Castelli & Kurucz 2003; Marigo & Girardi 2007), Additionally, the YZVAR isochrones³ features no alpha-enhancement. For this work, we place the observer in a region of the simulated galaxy analogous to the location of the Sun in the Milky Way. We study stars that lie within the region of choice as described in the relevant sections

³<http://stev.oapd.inaf.it/YZVAR/>

CHAPTER 2

comparing with *GES-iDR4* and *RAVE-DR5*. We only compare with similar spatial regions and distances as outlined within those surveys, studying stars beyond the survey selection regions yields diminishing returns since the majority of these stars will be too faint and thus fainter than the magnitude limit. For the regions within the survey boundaries we generate synthetic stars that trace a synthetic CMD by linearly interpolating in age and metallicity between isochrones of simple stellar populations. The interpolation is described in (Pasetto et al. 2012).

Essentially, the synthetic stellar population particles themselves are a result of 2D interpolation in age and metallicity. For a single stellar population particle p , the number of stars $d\nu_p(L, T_{\text{eff}})$ for the interval of luminosity L and T_{eff} over an interval $dT_{\text{eff}}dL$ is:

$$d\nu_p(T_{\text{eff}}, L) = f_{\text{SSP},p} \left[\left[\frac{d(\tau, Z)}{d(T_{\text{eff}}, L)} \right] \right] dT_{\text{eff}}dL, \quad (2.42)$$

where the Jacobian-matrix formalism, with $\left[\left[\frac{d(\tau, Z)}{d(T_{\text{eff}}, L)} \right] \right]$ can be applied to two physical properties in order to make a 2D histogram of the age-metallicity space, or [Fe/H]-[Mg/Fe] space, stellar distances or in order to make a synthetic colour magnitude diagram based on a chosen colour C and magnitude m (where these can be based off any colour system) i.e:

$$d\nu_p(C, m) = f_{\text{SSP},p} \left[\left[\frac{d(\tau, Z)}{d(T_{\text{eff}}, L)} \right] \right] \left[\left[\frac{d(T_{\text{eff}}, L)}{d(C, m)} \right] \right] dCdm. \quad (2.43)$$

In general there is no analytic formulation for the two matrices $\left[\left[\frac{d(\tau, Z)}{d(T_{\text{eff}}, L)} \right] \right]$ and $\left[\left[\frac{d(T_{\text{eff}}, L)}{d(C, m)} \right] \right]$. They are derived numerically from the tabulations of bolometric corrections, and in this work, the Johnson-Cousin-Glass system (Bessell 1990). This property has already been calculated in the form of the isochrone database described above.

This technique can be extended to the entire simulation of stellar population particles.

CHAPTER 2

$$\nu_p(C_{\alpha\beta}, m_\alpha) = \sum_p d\nu_p(C_{\alpha\beta}, m_\alpha). \quad (2.44)$$

This allows for an observable property, such as a CMD to be expressed in the form of a projected 2D distribution function with each element containing a relative quantity of synthetic stars. Additionally the magnitude for each synthetic star particle is modified by:

$$\begin{aligned} m'_\alpha(m) &= m_\alpha(m) - \left(\frac{1}{2} - r\right) \delta m_\alpha(m), \\ m'_\beta(m) &= m_\beta(m) - \left(\frac{1}{2} - s\right) \delta m_\beta(m), \end{aligned} \quad (2.45)$$

where m_α and m_β are two different magnitude pass bands (e.g. J and K) and δm_α and δm_β are their errors r and s are two randomly drawn numbers from a random number distribution (e.g. Gaussian) between 0 and 1. Additionally The synthetic stellar frequencies per elemental cell of the CMD are calculated after applying the correction for photometric errors. Initially we bin the entire isochrone database abundances (i.e. for each age and metallicity combination) into an initial array on its own without the consideration of the stellar population particles. The interpolation process involves a two point interpolation between the databases of ages above and below that of the star particle, then between metallicities above and below the star particle population, and then interpolate between the two results. We then increment the interpolated abundances and convolve these abundances with the initial array to produce the CMD. We apply our photometric selection function criteria within the interpolation process to remove synthetic star particles that fail to meet the selection function criteria. This of course means that the overall distribution functions will vary upon applying SYNCMD to all physical properties unless of course the selection function in SYNCMD is sufficiently broad that all of the stellar properties within the isochrone database are within the bounds of the

CHAPTER 2

selection function.

This methodology enables each individual stellar population particle to be mapped to 100,000 synthetic star particles. The mean stellar properties of age, metallicity and metal abundance are that of the parent stellar population particle. The synthetic star particles are allocated masses at random from the chosen IMF. The masses of these particles are then used to populate an isochrone using the metal abundance and age of the original stellar population particle from the simulation data. Properties of the synthetic star particles are calculated from the database and from the stellar population particle’s age, metallicity and distance from the observer. The synthetic star particle’s properties are the age, luminosity, T_{eff} , $\log(g)$, metal abundance, H abundance, He abundance and magnitudes in the UBVRIJHK bands. Photometric colours and magnitude values for each synthetic star will be adjusted according to the distance of the star to the simulated observer. The stars retain the age and chemical abundances of the simulation particle they are created from. We eliminate synthetic star particles from the sample that do not fall within the selection criteria. For comparison with an observational dataset, one can apply a selection function to the synthetic star particles of the observational survey that the user wishes to emulate. Since the magnitude of a star particle is related to the distance from the observer, with the application of colour or magnitude cuts, one can remove stellar population particles by for example removing synthetic star particles that do not meet your selection criteria (e.g. colour, magnitude). The remaining stars are used to analyse whatever physical property one wishes, having essentially removed the fraction of each stellar population particle that would not lie within the selection functions. The choice of a selection function is an important component of SYNCMD. If the selection function is too lenient (or non existent), then the chemical abundance properties of the synthetic star particles will as expected be the same as the stellar particle populations. This does enable one to study specific

CHAPTER 2

stellar populations within a simulation, such as giants, main sequence and turnoff stars. This is done by picking selection functions similar to what an observer would do to study those particular populations. The synthetic stellar particles produced by SynCMD are at the same distance from the observer than the stellar population particle that they originate from.

The following list details the procedure that SYN CMD undertakes to convert stellar population particles into synthetic star particles:

1. Select an Isochrone database, an IMF and a selection function (e.g. spatial, colour, magnitude and $\log(g)$).
2. Read in all of the Isochrone databases from which the composite particles are synthesised from.
3. Using IMF normalisation, determine the mass that is inherent within each isochrone.
4. Select which colour and magnitude bands the synthetic populations will utilise.
5. Read in the synthetic stellar population particle distribution.
6. For each particle, allocate the relevant isochrone database (depending on Age and Metallicity (Z)). The code interpolates the isochrone stellar distributions dependent on the composite particle age and Z . For particles with age/ Z outside of the restrictions, extrapolation is not carried out (and thus this method is limited to the Isochrone database available). The isochrone allocated is that of the relevant extremity. (For example if $Z_{\text{particle}} = 0.05$, then $Z_{\text{isochrone}} = 0.04$, as the limiting isochrone Z is 0.04. In our work, none of our stars have values outside of these extremes). Place these star particles at the same spatial position as the composite particle they originate from.

CHAPTER 2

7. From restrictions of spatial, colour, magnitude and $\log(g)$, restrict the synthetic population for each stellar population particle.
8. Using information of the restricted synthetic star particles, allocate the synthetic star particles to relevant colour-magnitude positions on the CMD. We use the apparent magnitude data to apply our selection criteria (SynCMD does produce absolute magnitude CMDs too)
9. Iterate over all of the stellar population particles, adding synthetic stars particles to colour-magnitude bins which satisfy the selection function criteria.

Specifically, for the Bertelli et al. (2008, 2009) isochrone database used in this work, interpolation makes use of the following Age and Z bins:

1. Age (Gyr) = (0.01, 0.02, 0.03, 0.04, 0.05, 0.06, 0.07, 0.08, 0.09, 0.1, 0.2, 0.3, 0.4, 0.5, 0.6, 0.7, 0.8, 0.9, 1.0, 2.0, 3.0, 4.0, 5.0, 6.0, 7.0, 8.0, 9.0, 10.0, 11.0, 12.0, 13.0).
2. Z (dex) = (0.0001, 0.0004, 0.004, 0.008, 0.02, 0.03, 0.04).

The initial mass function of a stellar distribution function which are represented as a power law as shown in Equation 1.5. To compute the normalization constant, and thus the total number of stars and mass of isochrone, we need to solve the Salpeter (1955) power law IMF between a lower mass limit M_l and an upper mass limit M_u . For the Salpeter IMF, one needs to solve the following equations for the mass spectrum function and the IMF:

$$N = A \int_{M_l}^{M_u} m^{-x-1} dm, \quad (2.46)$$

$$M = A \int_{M_l}^{M_u} m^{-x} dm, \quad (2.47)$$

CHAPTER 2

Where for the Salpeter IMF, $x = 1.15$, $M_l = 0.08$ and $M_u = 100$. A is the normalization constant which needs to be calculated. The normalisation constant A is:

$$A = \frac{N(M_l M_u)^{x+1} x}{(M_u^{x+1}) M_l - M_u M_l^{x+1}}, \quad (2.48)$$

N the number of stars between $0.15 M_\odot$ and $20.0 M_\odot$ is 100,000 since that is the number of stars in the Bertelli et al. (2008, 2009) isochrone database. The Bertelli et al. (2008, 2009) isochrones cover a mass range of $0.15 M_\odot$ to $20.0 M_\odot$. Therefore the minimum mass an SSP particle can be is $m = 0.15 M_\odot = M_{0.15}$. To compute A , we consider the number of stars in which their mass is below $M_{M_{0.15}}$ and above M_u , i.e. $N_{m < M_l}$ and $N_{m < M_u}$.

We need to know how many stars would be under i.e. $N_{m < M_{0.15}}$,

$$N_{m < M_{0.15}} = \frac{A}{-x + 1} (M_{0.15}^{-x+1} - M_l^{1-x}), \quad (2.49)$$

where $N_{m > M_{0.15}}$ is the total number of stars with a mass above $M_{0.15}$. Then we compute the mean mass above $M_{0.15}$ and below it, i.e. $M_{m > M_{0.15}}$ and $M_{m < M_{0.15}}$,

$$\bar{M}_{m < M_{0.15}} = \frac{\frac{1}{-x+1} (M_{0.15}^{-x+1} - M_l^{-x+1})}{\frac{1}{-x} (M_{0.15}^{-x} - M_l^{-x})}, \quad (2.50)$$

$$\bar{M}_{m > M_{0.15}} = \frac{\frac{1}{-x+1} (M_u^{-x+1} - M_{0.15}^{-x+1})}{\frac{1}{-x} (M_u^{-x} - M_{0.15}^{-x})}. \quad (2.51)$$

Then we use this information to compute the mean mass of the synthetic star particles (SSP) associated with a stellar population particle,

$$\bar{M}_{SSP} = \frac{N \bar{M}_{m > M_{0.15}} + N_{m < M_{0.15}} \bar{M}_{m < M_{0.15}}}{N + N_{m < M_{0.15}}}, \quad (2.52)$$

and finally compute the total mass of all of the synthetic star particles associated with a stellar population particle,

CHAPTER 2

$$M_{SSP} = N\bar{M}_{m>M_{0.15}} + N_{m<M_{0.15}}\bar{M}_{m>M_{0.15}}. \quad (2.53)$$

From this, we have the total mass of the synthetic stellar population particles within the CMD. The importance of this is to weight the contributions towards the CMD by that of the mass of the stellar populations that appear on the CMD (i.e. after being removed via the chosen selection function). Further details on how the numerical methodology employed within SYNCMD is found in Pasetto et al. (2012) Sections 2, 3 and 4.

With the advent of large scale and high resolution galactic archaeological surveys, the requirement to study simulations in this way for a more like-for-like comparison becomes ever more relevant. Indeed interest in these sort of techniques is growing. *SNAPDRAGONS* (Hunt et al. 2015) for example has properties similar to SYNCMD. It uses its own synthetic CMD generation tool, but convolved with Gaia uncertainties to put the synthetic stellar populations into the Gaia-plane. This toolkit is more specific than SYNCMD for the study of the Gaia region, but it is not as expandable and for instance is not suited at looking at the RAVE region whereas SYNCMD is a general synthetic CMD toolkit designed to work for any survey and simulation dataset.

In summary, each stellar population particle is split into 100,000 synthetic star particles (a number chosen to be large enough to sample the whole IMF). This number is applied because the stellar population particles mostly do have the same initial stellar mass. In comparison with similar survey spatial regions selected from *GES-iDR4* and *RAVE-DR5*, less than 2% of stellar population particles have a mass greater than the minimum stellar population particle mass resolution. This should have a minimal impact on our results and not account for any biases, however this may mean that we underestimate a smaller contribution from older stars, since older stars typically have a lower mass resolution. They are allocated masses at

random from a Salpeter IMF. These particles masses are then used to populate an isochrone using the helium and metal abundance as well as the age of the original stellar population particle from the simulation data. The synthetic star particle’s apparent magnitude in UBVRIJK bands, surface gravity and effective temperature are calculated and used to eliminate those synthetic stars that do not fall within the selection criteria for the observational dataset that the user wishes to emulate. The remaining stars are used to analyse whatever physical property one wishes, having essentially removed the fraction of each stellar population particle that would not lie within the selection functions.

2.5 Observational Surveys

2.5.1 The Gaia-ESO Survey

In this work, we focus on the high-resolution UVES data of the field stars. UVES is the ultraviolet and visual cross-dispersed echelle spectrograph installed at the second unit telescope of the VLT (Dekker et al. 2000). The stars were observed using the UVES U-580 setting, which covers the wavelength range from 480 to 680 nm, with a small beam-splitter gap at 590 nm. Most spectra have signal-to-noise ratio between 30 and 100 per pixel. For these stars, accurate effective temperatures T_{eff} , surface gravities $\log(g)$, $[\text{Fe}/\text{H}]$, and Mg abundances are available. These targets were chosen according to their colours to maximise the fraction of unevolved foreground (FG) stars within 2 kpc in the solar neighbourhood (see Stonkutė et al. 2016, for more details on target selection). The selection box was defined using the 2MASS photometry (Skrutskie et al. 2006; Huchra et al. 2012): $12 < J < 14$ and $0.23 < J-K < 0.45 + 0.5E(B-V)$; where $E(B-V)$ is the colour excess in the Johnson’s photometric system. The targets selected before April (2012) had a brightest cut on J of 11 instead of 12. If the number of objects in the field within the

CHAPTER 2

box was less than the number of UVES fibres, then the red-edge of the colourbox was shifted to have enough targets to fill the fibres. According to these selection criteria, the majority of stars are FG stars with magnitudes down to $V = 16.5$. The survey is limited to observing stars observable from the VLT, which is limited to $-70 < \text{DEC} < 20$ (mainly the southern hemisphere).

For the analysis of the spectra, several state-of-the-art spectrum analysis codes are used (Smiljanic et al. 2014). The observed spectra were processed by 13 research groups within the Gaia-ESO survey collaboration with the same model atmospheres and line lists (Heiter et al. 2014), but different analysis methods: full spectrum template matching, line formation on-the-fly, and the equivalent width method. The model atmospheres are 1D LTE spherically-symmetric ($\log(g) \leq 3.5$ dex) and plane-parallel ($\log(g) \geq 3.5$ dex) MARCS (Gustafsson et al. 2008). The final parameter homogenisation involves a multi-stage process, in which both internal and systematic errors of different datasets are carefully investigated. Various consistency tests, including the analysis of stellar clusters, benchmark stars with interferometric and asteroseismic data, have been used to assess each group's performance.

The final stellar parameters are medians of the multiple determinations, and the uncertainties of stellar parameters are median absolute deviations, which reflect the method-to-method dispersion. For most stars, the uncertainties are within 100 K in T_{eff} , 0.15 dex in $\log(g)$, and 0.1 dex in $[\text{Fe}/\text{H}]$ and Mg abundances. This accuracy could be achieved because of very careful selection of diagnostics features, very broad wavelength coverage and good signal-to-noise ratio of the observed spectra, and validation of the results on the accurate stellar parameters and NLTE estimates of chemical abundances of the Gaia Benchmark stars (Jofré et al. 2015).

The ages and masses were determined using the Bayesian code BeSPP (Serenelli et al. 2013). The age errors then depend on the shape of the posterior probability density function (PDF). This shape, in return, depends on the accuracy of the

CHAPTER 2

photometry, the uncertainties of the input spectroscopic parameters, evolutionary stage of the star. There is no one-to-one relationship between the derived age and its error. This is different to modelling that of stellar populations, or for modelling galaxy masses and ages, because they also account for hot massive (OBA) stars (which are very sensitive age diagnostic, when combined with low-mass cool stars), while we work only with FGK (low-mass cool) stars.

We use the grid of input stellar evolution models computed using the GARSTEC code (Weiss & Schlattl 2008); it covers a wide range of masses, $0.6 \leq M_{\odot} \leq 1.4 M_{\odot}$ in steps of $0.01 M_{\odot}$, and metallicities, $-5 \leq [\text{Fe}/\text{H}] \leq +0.5$ dex. The models more metal-poor than -0.6 dex assume α -enhancement of 0.4 dex. Distances were computed using the 2MASS photometry. The ages of the stars are computed from the mode of the posterior PDF. The uncertainties in age were determined as $\pm 34\%$ around the median value and the solar abundances from Asplund et al. (2009). Overall in the iDR4 release, there are 108994 stars. But only 1673 of those stars are suitable for this study. See §2.6.2 for more information.

2.5.2 The RAVE survey

The RAVE survey (Steinmetz et al. 2006) was the first designed spectroscopic survey to provide stellar parameters to complement missions that focus on astrometric data. Our attention shall focus on the DR5 release (Kunder et al. 2016).

RAVE is an ongoing large spectroscopic survey of the Milky Way in the southern hemisphere which uses the 1.2 m UK Schmidt Telescope of the Australian Astronomical Observatory (AAO) covering 20,000 square degrees of the night sky. It takes advantage of the emergence of wide field multi-object spectroscopy (MOS) fibre systems. Previous data releases have furthered our understanding of the disc of the Milky Way (see review by Kordopatis 2014). Examples of further understandings include the discovery of a wave-like pattern in the stellar velocity distribution

CHAPTER 2

(Williams et al. 2013) and the total mass of the Milky Way was measured using the RAVE extreme-velocity stars (Piffl et al. 2014b), and the local dark matter density (Bienaymé et al. 2014; Piffl et al. 2014a). Additionally, chemo-kinematical signatures of the dynamical effects of mergers on the Galactic disc (Minchev et al. 2014), and signatures of radial migration were detected (Kordopatis et al. 2013b; Wojno et al. 2016) as well as stars which have been tidally stripped from globular clusters (Kunder et al. 2014; Anguiano et al. 2015, 2016). RAVE allows for the creation of pseudo-3D maps of the diffuse interstellar band at 8260 \AA (Kos et al. 2014) and for high-velocity stars to be studied (Hawkins et al. 2015).

DR5 includes the final RAVE observations taken in 2013 (from the iDR4 dataset Kordopatis et al. 2013a). The overall dataset includes 520,629 stars. This also includes $\sim 30,000$ previously discarded observations recovered from previous data releases. DR5 is the first RAVE data release where the error spectrum was generated for each RAVE observation, so we can provide realistic uncertainties and probability distribution functions for the derived radial velocities and stellar parameters. The DR5 release preformed a recalibration of stellar metallicities, especially improving on stars more metal rich than the Sun. From the use of the Gaia benchmark stars (Jofré et al. 2014; Heiter et al. 2015) as well as 72 RAVE stars with Kepler-2 astrometric $\log g$ parameters (Valentini et al. 2016) the RAVE $\log g$ values have been recalibrated, resulting in more accurate gravities especially for the giant stars in RAVE.

We use the distance measurement pipeline as outlined in Binney et al. (2014) which has been improved and extended to process more accurately stars with low metallicities ($[M/H] < -0.9$ dex). We combine the optical photometry from APASS (Munari et al. 2014) with 2MASS (Skrutskie et al. 2006) to derive temperatures from the Infrared Flux Method (Casagrande et al. 2010).

RAVE DR5 stellar atmospheric parameters T_{eff} and $\log g$ and $[M/H]$ have been

CHAPTER 2

determined using the same stellar parameter pipeline as used in iDR4 (Kordopatis et al. 2013a) with the details being outlined here (Kordopatis et al. 2011) and the implementation in the DR5 paper (Kunder et al. 2016). The pipeline is based on the combination of a decision tree. It uses DEGAS (Bijaoui et al. 2012) to renormalise iteratively spectra and obtain stellar parameter estimations for low SNR (signal to noise) spectra, and a projection algorithm MATISSE (Recio-Blanco et al. 2006) to derive parameters for stars with high SNR. MATISSE is preferred to DEGAS at an SNR of 30 pixel^{-1} . The pipeline is run on the continuum normalised, radial-velocity corrected RAVE spectra using a soft conditional constraint based on the 2MASS J - Ks colour of each star. Once the spectra has been parameterised, the pipeline returns quality flags for each spectra. This is defined as *algoconv* and specifically we select stars where the normalization process converges, as did MATISSE (for high SNR spectra) or DEGAS (for low SNR spectra).

The chemical pipeline used to derive the elemental abundances for Al, Mg, Ni Si, Ti and Fe are determined for a number of RAVE stars using a dedicated pipeline introduced in (Boeche et al. 2011) and then improved upon in the iDR4 release (Kordopatis et al. 2013a). In short, equivalent widths are computed for a grid of stellar parameter values for T_{eff} , $\log g$, $[M/H]$ using solar abundances of (Grevesse & Sauval 1998). Using the calibrated RAVE effective temperatures, surface gravities and metallicities (see Kordopatis et al. 2013a; Kunder et al. 2016, for more details), the pipeline searches for the best-fitting model spectrum by minimizing the χ^2 between the models and observations.

The radial velocities (RV) for the stars are derived identically as to those in iDR4 (Kordopatis et al. 2013a). The velocity determination is explained in detail by Siebert et al. (2011) in DR3. First a subset of 10 template spectra is used to obtain preliminary RV results, which has an accuracy better than 5 km s^{-1} . A new template is constructed using the full template database described in DR2 paper (Zwitter

CHAPTER 2

et al. 2008) from which the final more precise RV (radial velocity) is obtained with an accuracy better than 2 km s^{-1} . An internal error in RV, $\sigma(\text{RV})$ comes from the *xcsao* tasks within IRAF⁴, thus describes the error on the determination of the maximum of the correlation function. Uncertainties derived from error spectra are useful for stars that have low SNR or high temperatures. Repeated RV measurements have been used to characterise the uncertainty in the RVs. The histogram of the RV scatter between repeat measurements peaks at 0.5 km s^{-1} and has a long tail at large scatter. This extended scatter is due to the variability from stellar binaries and problematic measurements. If stars are selected that have RV's. derived with high confidence, e.g. stars with $\text{CorrectionRV} < |10| \text{ km s}^{-1}$ and $\sigma(\text{RV}) < 8 \text{ km s}^{-1}$ (see Kordopatis et al. 2013a), the scatter of the repeat measurements peaks at 0.17 km s^{-1} and the tail of the scatter of RV is reduced by 90 %.

Due to its complex history, and owing to observational constraints and actual atmospheric conditions on the respective day, the input catalogue for RAVE carries some inhomogeneity, and it is therefore not straightforward to construct a valid parent sample from this variety of data sets. However, one data set in particular, 2MASS, offers complete coverage of both the survey area and the magnitude range of RAVE. Therefore, 2MASS photometry is adopted in order to compare RAVE targets with as homogeneous a sample as possible.

The accuracy of the RAVE abundances depends on many variables which can be inter-dependent in a non linear way which makes it non-trivial to provide one value to quantify the accuracy of the RAVE elemental abundances. DR5 does not also take into account the errors in abundance measurements from high resolution spectra (unlike the Gaia-ESO survey). In short for the purposes of this work, the DR5 dataset derives uncertainties for Mg and Fe to be 0.2 dex each for all stars.

⁴IRAF is distributed by the National Optical Astronomy Observatory, which is operated by the Association of Universities for Research in Astronomy (AURA) under a cooperative agreement with the National Science Foundation

Details as to why this is the case is described in the DR5 paper (Kunder et al. 2016).

2.6 Comparison Between the Gaia-ESO survey

In this section, we discuss the comparison methodology and the results between *Selene-CH* and the Gaia-ESO survey, the data sets related to the comparison and the results that are produced.

2.6.1 Analysing *Selene-CH* like an Observer

The aim of this work is to best examine how different ways of processing the same simulation data give variations in the results obtained for the distribution of chemical abundances in the solar neighbourhood analogue. A first-order approach that is commonly used is to simply take a spatial region within a simulation that matches the region of interest in a galaxy and compare that with observational data (e.g. Chiappini et al. 2001; Abadi et al. 2003; Stinson et al. 2010; Guedes et al. 2011; Few et al. 2012b; Pilkington et al. 2012b; Brook et al. 2012a; Calura et al. 2012; Aumer et al. 2013; Vogelsberger et al. 2014; Bird et al. 2014; Few et al. 2014; Hopkins et al. 2014; Agertz & Kravtsov 2015; Schaye et al. 2015; Crain et al. 2015). This approach samples the entire stellar population and requires volume completeness for each type of stars, something that no observational survey does. The fact that simulations are not subject to observational errors is also usually ignored. As a result, the observed and simulated distributions are not directly comparable.

In this work, we compare the Gaia-ESO survey results *GES-iDR4*, with the following variants of the simulated galaxy *Selene-CH* in order to demonstrate the influence of each component of the process used to mimic observational limits:

- *Selene-CH-G* is the unaltered and unmodified galaxy. We select all of the stellar population particles that reside within a 2 kpc sphere around the simulated

CHAPTER 2

observer, 15562 in total. These particles are compared directly with the *GES-iDR4* results. This kind of direct comparison demonstrates the methodology employed in the ‘traditional sense’, i.e. with spatial cuts alone.

- *Selene-SCA-G* is a modified version of *Selene-CH-G*. In this case we apply stochastic scattering to the ages and abundance ratios of the stellar population particles to emulate observational uncertainties. The magnitude of the scattering is based on the mean errors taken from the Gaia-ESO dataset. We do not stochastically scatter the distances in this work due to the distances not being the focus of our study.
- *Selene-SYN-G* is the result of applying the SYNCMD toolkit, as described in §2.4, to the scattered stellar population particles ages and metallicities in *SELENE-SCA-G* (i.e. the statistically scattered results of *Selene-CH*). This dataset includes the application of selection functions for $\log(g)$, T_{eff} , J-band magnitude, and J–K colour and is a more rigorous attempt to mimic the *GES-iDR4* data.

In short, *Selene-CH-G* represents a first-order analysis of the simulations similar to that found in the majority of the literature, *Selene-SCA-G* shows the effect of applying observational scatter, and *Selene-SYN-G* demonstrates the influence of selection effects. We now describe the post-processing used to create each of these datasets in detail. In theory, a similar result for *Selene-SYN-G* could be generated from applying stochastic scattering to the metal, age and other physical properties to the result of applying SYNCMD to *Selene-CH-G*, i.e. apply the scattering post-application of SYNCMD rather than before. However we did not have chance to investigate this due to time constraints, although the results presented here should not vary too much from that scenario.

2.6.2 GES-iDR4

We further post-process the *GES-iDR4* data for the analyses presented here. The *GES-iDR4* database has 108994 stars studied as of at the time these studies were under way. We only include field disc stars and remove bulge stars and stars in special fields, such as the asteroseismic (CoRoT) targets. This gives us a selection of 1673 stars. Stars with undefined age, Fe or Mg abundances and errors are also removed and 1557 stars remain within the sample.

Furthermore, we require that the observed stars must satisfy the following selection criteria for them to be included in the dataset:

1. Heliocentric radial distance of $r \leq 2.0$ kpc;
2. Surface gravity of $3.5 \leq \log(g) \leq 4.5$ dex;
3. Effective temperature of $5400 \leq T_{\text{eff}} \leq 6400$ K;
4. J-band magnitude $12.0 \leq J \leq 14.0$;
5. J–K colour of $0.23 \leq J-K \leq 0.45 + 0.5 E(B-V)$.

The $r \leq 2.0$ kpc filter is specifically chosen to best replicate the analogous 2 kpc sphere selection region that is used with the simulation datasets.

The T_{eff} and the $\log(g)$ fields of the selection function are chosen, because ages of stars with $T_{\text{eff}} \leq 5400$ may not be accurate. Likewise, stellar ages are not well determined for hotter stars with $T_{\text{eff}} \geq 6500$ K or $\log(g) \geq 4.5$ dex, and for more evolved stars on the red giant branch, $\log(g) \lesssim 3.5$ dex. Our selection would thus include subgiants and main-sequence dwarfs.

After applying the selection function as described, we have 1024 stars remaining and use this as the definitive *GES-iDR4* dataset. Subsequent datasets are compared against *Selene-CH*, *Selene-SCA-G* and *Selene-SYN-G*, and used to determine the

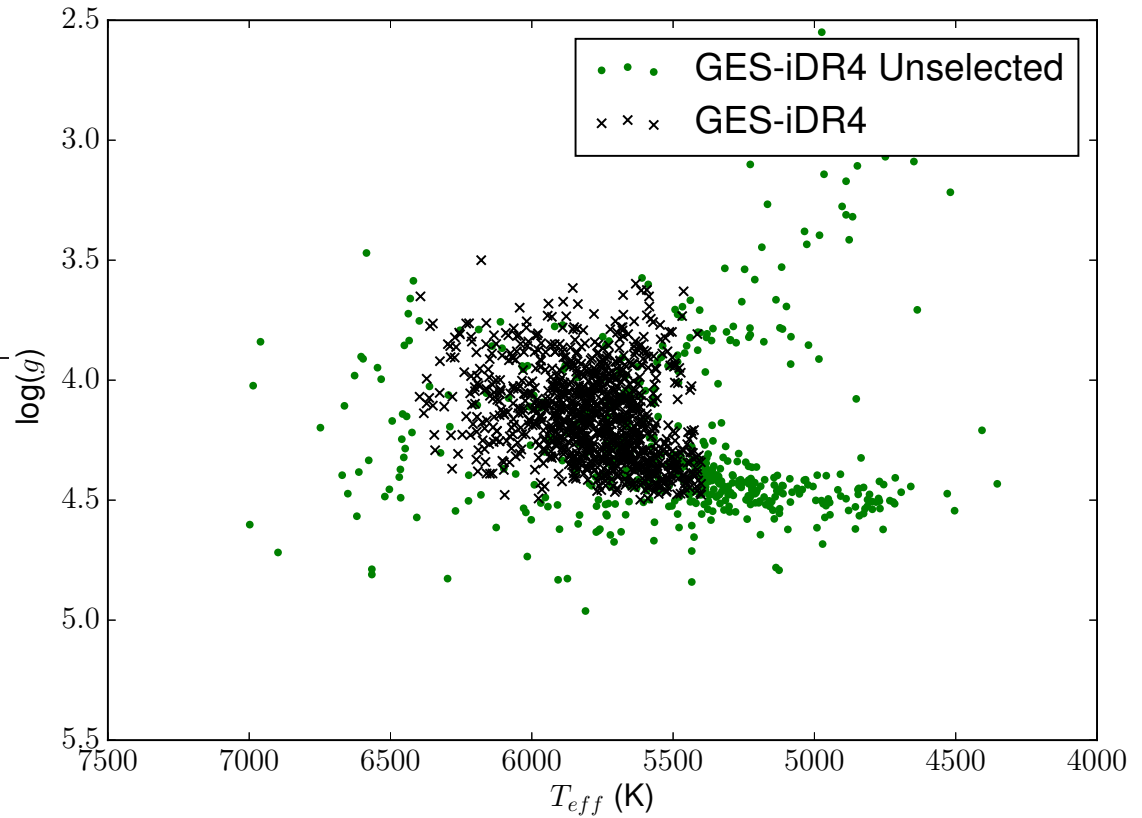


Figure 2.13: $\log(g)$ against T_{eff} for the *GES-iDR4* observed sample plotted as black crosses. For reference, we also include the stars which are removed *GES-iDR4* (labelled as *GES-iDR4 Unselected* dataset due to falling outside the selection criteria as green circles. The selection function is described in §2.6.2. There are 1557 stars in *GES-iDR4 Unselected* and 1028 stars in *GES-iDR4*.

scatter width for *Selene-SCA-G* as described in §2.6.4. The distribution of the *GES-iDR4* sample in the colour-magnitude plane is shown in Figure 2.14. The $T_{\text{eff}}\text{-}\log(g)$ diagram of the Gaia-ESO sample is shown in Figure 2.13.

2.6.3 Selene-CH: The ‘Standard’ Simulation Approach

We identify a solar neighbourhood analogue within the simulated galaxy *Selene-CH*, a position 8 kpc from the galactic centre on a spiral arm. This position is shown with a cross in Figure 2.4 at $(x,y) = (4.0, 6.93)$ kpc; the solar neighbourhood analogue is centred on this point relative to the galactic centre.

Element abundances are normalised to the Asplund et al. (2009) solar values. We additionally apply a shift to element abundance ratios with the magnitude of $[\text{Fe}/\text{H}] = -0.066$ dex and $[\text{Mg}/\text{Fe}] = 0.078$ dex. This is treated the same as an initial mass function renormalisation and is done to better match the stars in *GES-iDR4*. Previous works have applied different variations of *a posteriori* re-normalisations (e.g. Pagel & Tautvaisiene 1995; François et al. 2004; Henry et al. 2010) and/or employed GCE models to infer revised sets of stellar yields (François et al. 2004). This may seem arbitrary, however the amount by which we normalise is not very large compared to the width of the distribution and we are primarily concerned here with the dispersion of the element ratios. Furthermore it is demonstrated in Few et al. (2014) that variations in abundance ratios (particularly those of α -elements to Fe) are effectively shifted in the same way depending on the IMF. The need to apply such a shift implies that the sub-grid chemical evolution model is not quite correct which is hardly surprising given the uncertainties in the underlying yields and chemical evolution model. Therefore, while the renormalisation of abundance ratios introduces a slight inconsistency to the model it by no means negates our results.

2.6.4 Selene-SCA-G

This dataset extends the methodology described above to generate *Selene-CH* by applying a stochastic scattering based on the *GES-iDR4* error bars for age, metallicity, and [Mg/Fe] abundance ratio, to mimic the effect of the unavoidable uncertainties found in observations on the precisely known (but not necessary accurate) simulated values.

We degrade the precision of our simulated metallicity and [Mg/Fe] data on a particle-by-particle basis using a Gaussian distribution, centred on the original simulated value with a standard deviation equal to the mean error found in the *GES-iDR4* dataset: $\sigma_{[\text{Fe}/\text{H}]} = 0.101$ dex and $\sigma_{[\text{Mg}/\text{Fe}]} = 0.120$ dex. We use the normal distribution to compute new [Fe/H] and [Mg/Fe].

$$P(x) = \frac{1}{\sigma\sqrt{2\pi}} e^{-(x-\mu)^2/2\sigma^2}, \quad (2.54)$$

New abundance ratios for each stellar population particle are chosen randomly from this distribution.

The age value for each stellar population particle is also scattered this way except that the distribution from which the new value is chosen at random is not symmetric. The ages of the observed stars in the *GES-iDR4* dataset have a mean lower age error of $\sigma_{age,low} = 3.20$ Gyr and a mean upper age error of $\sigma_{age,high} = 2.37$ Gyr. We construct a piecewise function from two half-Gaussians with these standard deviations respectively to scatter the simulated ages. This process not only broadens the distributions but also makes stellar population particles slightly older. These equations are summarised here,

$$\beta + \gamma = 2.0, \quad (2.55)$$

where β and γ are normalization constants for the weighting of the two half-Gaussians to ensure non-discontinuity:

$$\frac{\beta}{\gamma} = \frac{\sigma_{age,low}}{\sigma_{age,high}}, \quad (2.56)$$

$$\gamma = 2.0 / \left(\frac{\sigma_{age,low}}{\sigma_{age,high}} + 1.0 \right). \quad (2.57)$$

Which when put together produces the following normalized continuous distribution function,

$$P(x) = \left\{ \begin{array}{ll} \frac{\gamma}{\sigma_{age,low}\sqrt{2\pi}} e^{-(x-\mu)^2/2\sigma_{age,low}^2} & x < 0 \\ \frac{\beta}{\sigma_{age,high}\sqrt{2\pi}} e^{-(x-\mu)^2/2\sigma_{age,high}^2} & x \geq 0 \end{array} \right\}, \quad (2.58)$$

in which we use to compute the new age values for *Selene-SCA-G*.

2.6.5 Selene-SYN-G

Our final version of *Selene* takes the scattered stellar population particles from *Selene-SCA-G* and inputs those particles to SYNCMD creating a third dataset referred to here as *Selene-SYN-G*. The mechanics of SYNCMD are described in §2.4 but the key here is to split the stellar population particles into individual synthetic star particles with a realistic distribution of star properties so that we can apply photometric, $\log(g)$ and T_{eff} cuts to exactly mimic the observed *GES-iDR4* dataset. The selection criteria are stated in §2.6.2 however we do not apply the dust extinction correction to the J–K upper limit, this is because the SyncMD toolkit does not feature correction for dust due to the abundance of gas between the simulated observer and the synthetic stars, thus we assume that synthetic star particles are unaffected by dust. The synthetic star particles that remain after this are used as our sample of stars analogous to the *GES-iDR4* dataset so that we can compare the simulations in a more like-for-like manner. The CMD for *Selene-SYN-G* is shown in figure 2.14.

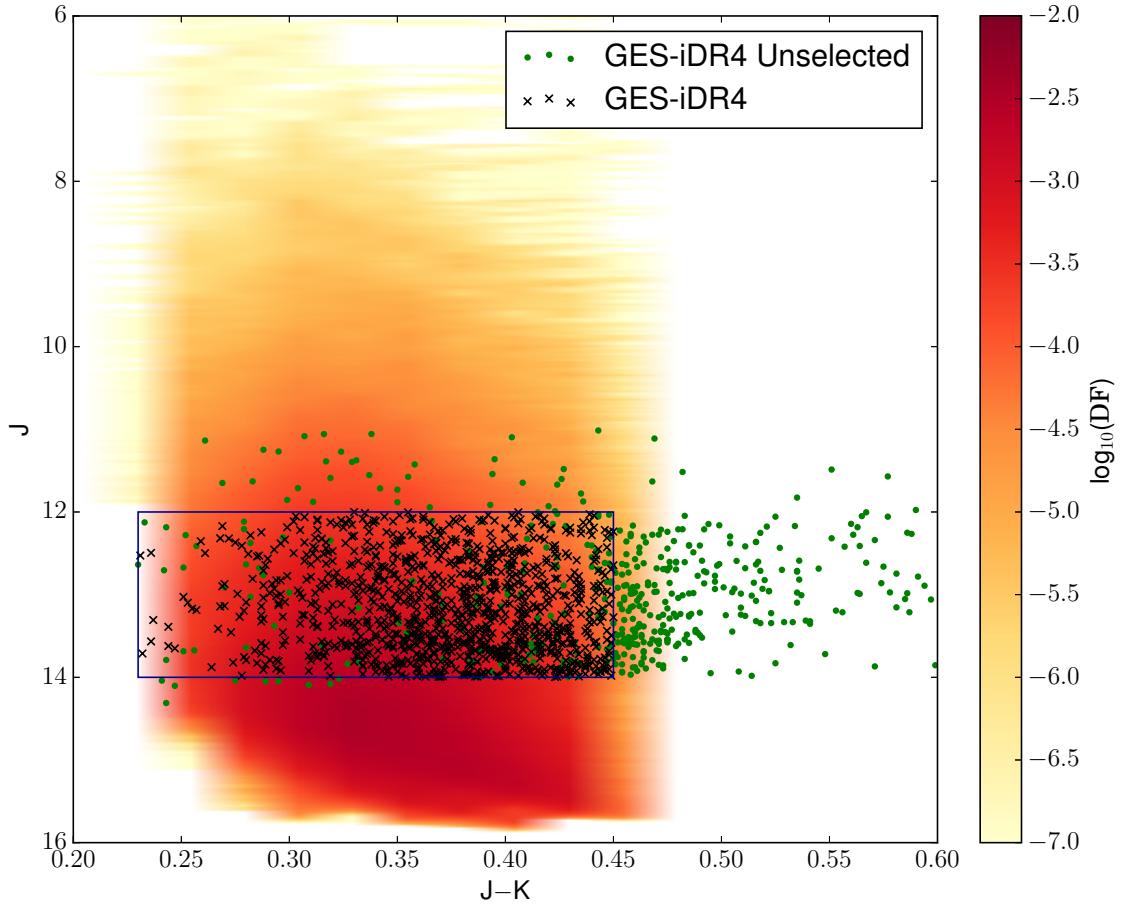


Figure 2.14: Synthetic CMD of J vs. $J-K$ in apparent magnitude space of the simulated solar neighbourhood analogue and of two sample of stars from Gaia-ESO iDR4. The red heatmap represents a normalised distribution function of the synthetic stellar populations from *Selene-SYN-G* which is derived from the simulated galaxy *Selene-CH* as shown in Figure 2.4. The black crosses represent stars selected from the *GES-iDR4* dataset whereas the stars labelled with green circles representing those removed from *GES-iDR4* by the selection function as described in §2.6.2. The blue rectangle highlights the J and $J-K$ region selection function boundary conditions of $12 < J < 14$ and $0.23 < J - K < 0.45$. Both datasets include the application of surface gravity and effective temperature filters of; $3.5 \leq \log(g) \leq 4.5$ dex and $5400 \leq T_{\text{eff}} \leq 6400$ K.

CHAPTER 2

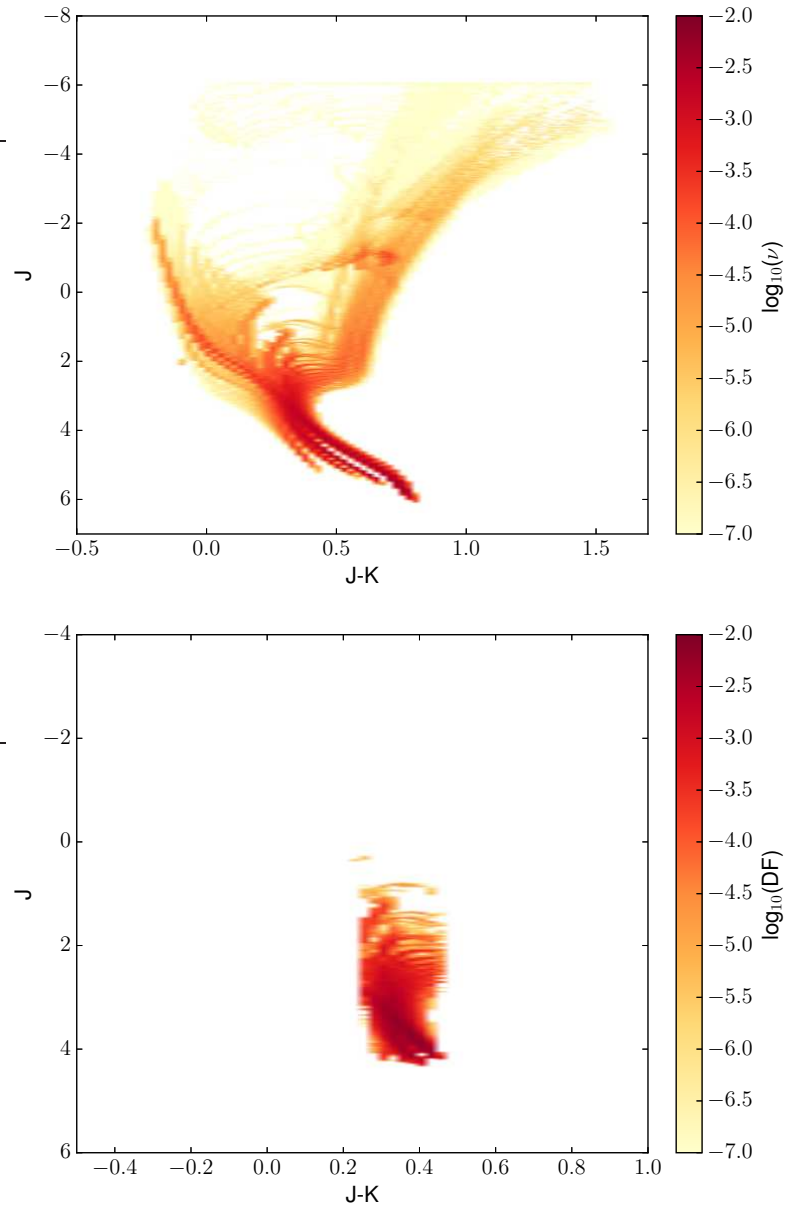


Figure 2.15: Synthetic CMD of J vs. J–K in absolute magnitude space of the simulated solar neighbourhood analogue. The top panel represents the absolute magnitude synthetic CMD of all of the isochrone data, the bottom panel shows what is left when we apply the selection criteria for *Selene-SYN-G* stated in §2.6.2. The red heatmap represents the normalised distribution function of the synthetic stellar populations from *Selene-SYN-G* which is derived from the simulated galaxy *Selene-CH* as shown in Figure 2.4.

As stellar population particles represent different masses of stars, the contribution of each one in terms of synthetic star particles is weighted by the initial mass of the stellar population particle to correctly account for the mass. The initial mass is used because any stars that have evolved and no longer form part of the stellar population are removed from the 100,000 synthetic star particles. The normalised distribution functions shown in this work are described as ‘mass-weighted’, this means that we have weighted the *Selene-CH-G* and *Selene-SCA-G* particles by their mass to be consistent with the *Selene-SYN-G* distribution function.

2.7 Gaia-ESO Comparison Results and Discussion

We now present and discuss the impact that ‘observing’ our simulations has on the distribution of selected stars in age, $[\text{Fe}/\text{H}]$, and $[\text{Mg}/\text{Fe}]$ in comparison with *GES-iDR4* data. The number of stars in *Selene-CH-G*, *Selene-SCA-G* is 15562 stars. In comparison in *GES-iDR4* there are 1024 and in *Selene-SYN-G* there are 61582452.64 synthetic stars in *Selene-SYN-G*. It is worth noting that due to the nature of the implementation algorithms, the number of synthetic stars is a non integer value.

Figure 2.16 shows the distance distribution function for the stars in the datasets *GES-iDR4*, *Selene-SCA-G*, *Selene-SYN-G* and *Selene-CH-G*. We do not include stochastic scattering for the distances since the errors on the distance scale are either similar or smaller than the spatial resolution. Therefore the distance distribution function for *Selene-CH-G* and *Selene-SCA-G* are the same. Within the first 0.5 kpc, we capture a similar relative abundance of stars, but this diverges. Due to spatial resolution limitations, the distribution of stellar population particles are roughly evenly spaced and increasing radial bins increases the spherical volume

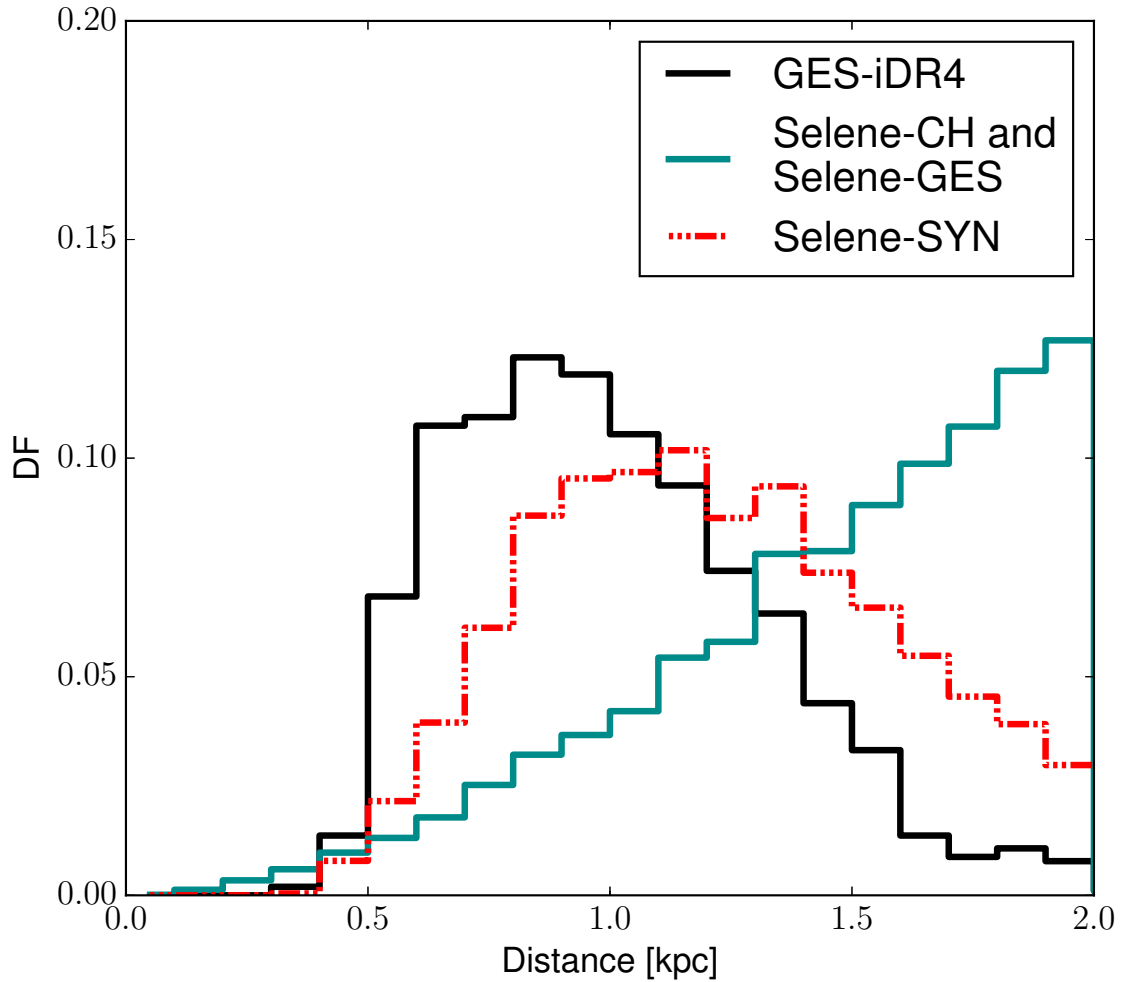


Figure 2.16: A plot of the present day normalised distance distribution functions for the datasets discussed in §2.7. The Gaia-ESO iDR4 data (*GES-iDR4*) is shown as a black line. The simulation datasets *Selene-CH* and *Selene-SCA-G* have the same distance distribution function and is shown by the cyan line (since distances are not stochastic scattered). *Selene-SYN-G* is represented by the red triple-dot-dashed lines respectively.

CHAPTER 2

covered, which in turn will hold a larger abundance of stars than at smaller radii. The application of the photometric selection function in *Selene-SYN* removes stars at larger radii due to being fainter than the photometric selection function. *Selene-SYN-G* therefore has a stellar radial distribution function more similar to *GES-iDR4* and therefore the application of SYNCMD allows for a more realistic selection of the distribution of stars than a simple spatial cut alone. Additionally, the stars nearer to the simulated observer in *Selene-SYN-G* are truncated due to being too bright.

2.7.1 Ages

We begin the discussion with the analysis of the age distribution in the observed and simulated Solar-neighbourhood datasets, however, we remind the reader that age determinations for the observed stars are notoriously difficult, because they rely on the knowledge of surface stellar parameters, metallicities, and α -element abundances (§2.5.1). Typically, ages of stars in *GES-iDR4* have an uncertainty of $\sim 30\%$, which is a statistical error and does not include any systematic component. Systematic errors cannot be easily quantified, because of the complex interdependence of different parameters and correlated errors (for example, the error in $[\text{Fe}/\text{H}]$ is correlated with the error in T_{eff} and in $\log(g)$). Therefore, some mismatch between the observed and model datasets is expected and should not be taken as the evidence of the failure of the galaxy simulations.

The age distributions of our three versions of *Selene* and the *GES-iDR4* stars are shown in Figure 2.17. Clearly, there is a systematic difference between the *GES-iDR4* and the simulation data, with an obvious offset to younger stars seen in the simulated data. The application of the stellar age scattering to the simulated data (*Selene-SCA-G*) has the effect of flattening the somewhat truncated older part of the age distribution, removing the peak at 8–10 Gyr and reducing the number of young stars which is entirely expected from the sharp edge of the underlying distribution.

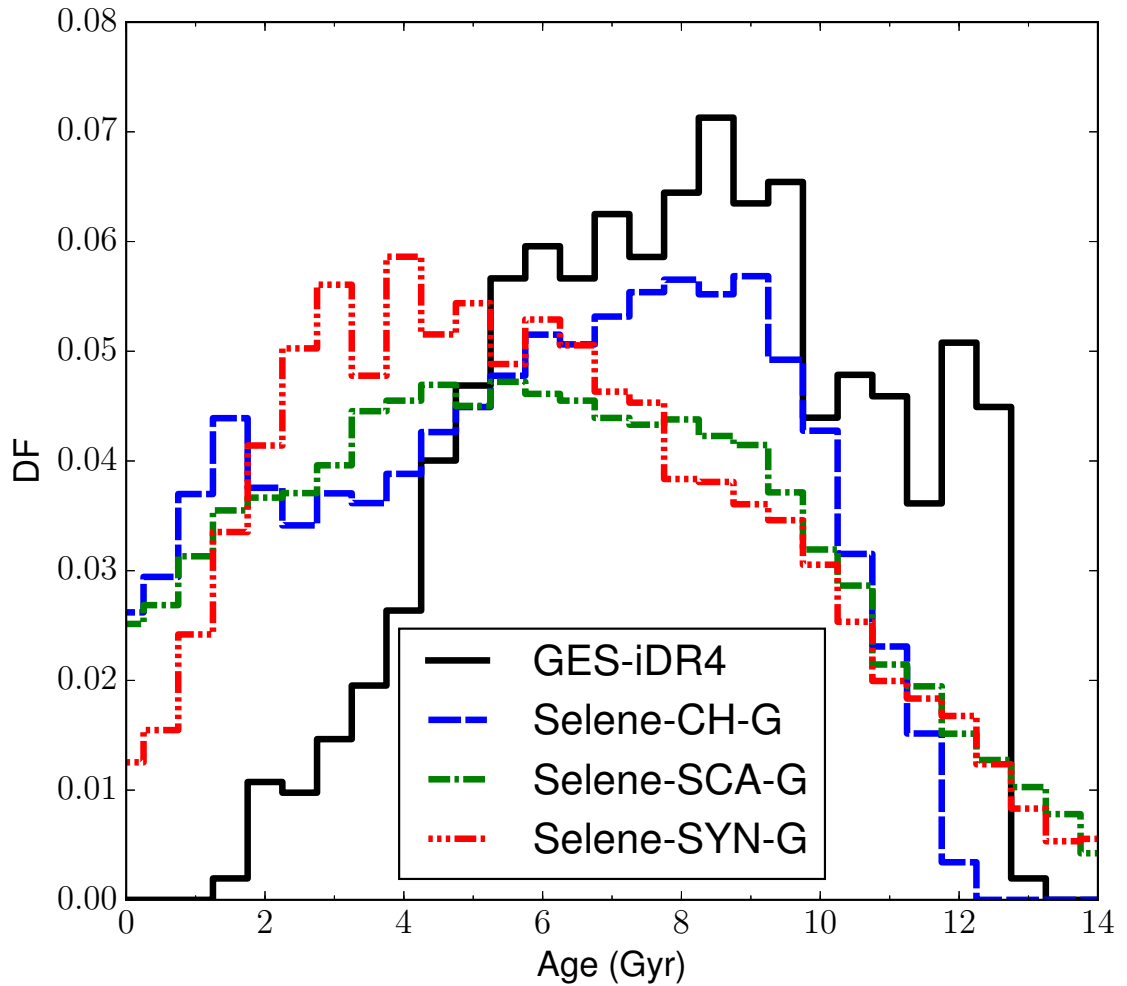


Figure 2.17: A plot of the present day normalised age distribution functions for the datasets discussed in §2.7.1. The Gaia-ESO iDR4 data ($GES-iDR4$) is shown as a black line. The simulation datasets $Selene-CH$, $Selene-SCA-G$ and $Selene-SYN-G$ are shown as blue dashed, green dot-dashed and red triple-dot-dashed lines respectively.

CHAPTER 2

Finally, when sampling the CMD of the stellar population particles and applying the *GES-iDR4* selection criteria to the scattered data (*Selene-SYN-G*) we find that the old end of the age distribution is unaffected, but that the GES photometric filters have the effect of producing a peak between 2–5 Gyr and removing many of the stars with ages below 1 Gyr from the distribution. The latter effect brings the young end of the distribution function closer to the observed distribution but there is still a significant discrepancy in both the shape and mean age.

The differences in the age distributions could be caused by several effects. Firstly, this could be due to the differences in the underlying distributions of stellar parameters in the observed and simulated samples. In particular, the combination of the SFH from *Selene-CH* and the SSPs database used in SYNCMD produce a temperature distribution with a ~ 400 K hotter mean T_{eff} value than our chosen *GES-iDR4* sample. This is a very significant difference and is most likely central to understanding of the discrepancy, but currently, we have no suitable framework to explore the effect. If the spectroscopic determinations of T_{eff} are biased, this could explain the deficiency in age for young stars in the *GES-iDR4* sample. Bergemann et al. (2014, Figure 2) showed that T_{eff} measurements, especially for stars with $T_{\text{eff}} > 6000$ K, appear to be over-estimated when compared to the more accurate methodology (infra-red flux method). If this also holds true for *GES-iDR4* datasets then by imposing a T_{eff} cut of 6500 K we actually remove stars, which may have even lower T_{eff} and this pushes the observed distribution towards colder (and older) stars. In SYNCMD we do not include any extinction correction. Perhaps in observations in *GES-iDR4* the young stars are more dust reddened by the local environment and therefore get removed in that way. Additionally the young stars are preferentially in the disc and thus susceptible to removal from the observations through reddening, and the young stars are in molecular clouds and so are more susceptible to removal through reddening. Both of these are dusty environments and therefore could be a

CHAPTER 2

contributing factor to the reduction of young stars too. It is interesting to note the relation between temperature, colour and age (Pecaut & Mamajek 2013) with bluer colours corresponding to hotter temperatures in young stars.

One should keep in mind that typically, the mean age of stars is a function of galactocentric radius. The age distribution of stars would shift to older values with decreasing radii, and thus a more appropriate solar neighbourhood analogue may exist for this galaxy, however given our uncertainty regarding the true distribution we have opted to select our region of interest based on the distance from the galactic centre. There is quite a substantial evidence that the galactic disc grows inside-out, both from observations of age-resolved abundance gradients for stars in the Galactic disc (Bergemann et al. 2014) and photometric and gas content observations of star forming galaxies (e.g. Wang et al. 2011). Theoretical studies have also explored the inside-out scenario, see for example (Schönrich & McMillan 2017) and references therein adding support to the observational evidence. Finally, the discrepancy in the age distributions could be due to the differences in the star formation history. Currently, we have no robust constraints on the star formation history of the Milky Way disc over the past 10 Gyr and a detailed analysis of this very complex problem is beyond the scope of this work.

2.7.2 Distribution Functions of $[\text{Fe}/\text{H}]$ and $[\text{Mg}/\text{Fe}]$

Figure 2.18 shows the normalised distribution functions of $[\text{Fe}/\text{H}]$ (top panel) and $[\text{Mg}/\text{Fe}]$ (bottom panel) for the simulated datasets compared with *GES-iDR4*. The unaltered simulated stellar population particles (*Selene-CH*, blue line) have a more

CHAPTER 2

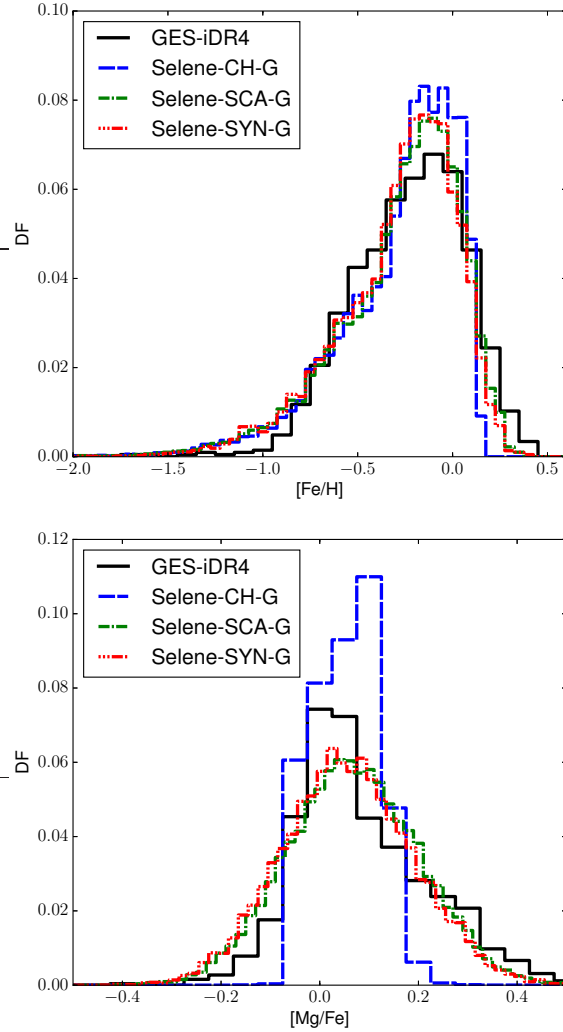


Figure 2.18: $[\text{Fe}/\text{H}]$ and $[\text{Mg}/\text{Fe}]$ normalised distribution functions in the solar neighbourhood analogues of the mass-weighted *Selene-CH* and *Selene-SCA-G* datasets, the synthetic observation dataset *Selene-SYN-G* and the observation dataset *GES-iDR4*. *Selene-CH*, *Selene-SCA-G* and *Selene-SYN-G* represented as blue dashed, green dot-dashed and red triple-dot-dashed lines respectively. The distribution functions of the *GES-iDR4* stars are shown in black. The bin widths for *Selene-CH*, *Selene-SCA-G* and *Selene-SYN-G* in $[\text{Fe}/\text{H}]$ is 0.05 dex, and for *GES-iDR4* this is 0.1 dex. The bin widths for *Selene-CH* and *GES-iDR4* in $[\text{Mg}/\text{Fe}]$ is 0.05 dex, for *Selene-SCA-G* and *Selene-SYN-G* is 0.02 dex.

CHAPTER 2

peaked $[\text{Fe}/\text{H}]$ distribution compared to the observations (black line), and an extremely narrow distribution in $[\text{Mg}/\text{Fe}]$. Furthermore, the mass-weighted⁵ *Selene-CH* distribution functions are truncated, at high- $[\text{Fe}/\text{H}]$ and at both low- and high- $[\text{Mg}/\text{Fe}]$. Table 2.3 shows the interquartile range (IQR), skewness (σ_3), and kurtosis⁶ (σ_4), which allow us to perform a quantitative analysis of the effect of the observationally motivated changes to the simulated data (see below).

The differences between the width of the *Selene-CH* distributions and the observations do not indicate a failure of the simulation. The simulated distribution is smoothed and broadened significantly when the observationally-motivated scattering with errors is applied (*Selene-SCA-G*, green line). This is seen as the increase in the IQR for both the $[\text{Fe}/\text{H}]$ and $[\text{Mg}/\text{Fe}]$ distributions. The effect is most pronounced for $[\text{Mg}/\text{Fe}]$ as it creates wings in the data on both sides of the distribution. For $[\text{Fe}/\text{H}]$, the change is only noticeable for higher $[\text{Fe}/\text{H}]$ values, with the low-metallicity tail being largely unaffected. The key result of Figure 2.18 is that the observational uncertainties in age, metallicity, and $[\text{Mg}/\text{Fe}]$ have a much greater effect on the resulting normalised distribution functions than do the photometric selection filters. This means, the observational errors place a fundamental limit on detection of any substructure and on our ability to quantify the slope of any astrophysical relevant relationship in the data.

As expected, scattering the data leads to an increase in the IQR for both the $[\text{Fe}/\text{H}]$ and $[\text{Mg}/\text{Fe}]$ distributions providing a good agreement with the observed IQR compared to the original values. When followed up by imposing selection functions we find that the distributions are slightly narrowed but not so much that the reasonable agreement in the spread of the distributions are lost. The simulated

⁵The metal abundance properties of *Selene-CH*, *Selene-SCA-G* and the synthetic stellar particles in *Selene-SYN-G* are weighted by the birth mass of the stellar population particles.

⁶We use the definition of kurtosis whereby a normal distribution has a kurtosis $\sigma_4 = 0$.

CHAPTER 2

[Fe/H] distribution is improved by both stages of our post-processing with the distribution becoming less skewed and reducing in kurtosis to approach the observed values largely due to the enhanced positive tail of the distribution. The [Mg/Fe] distribution is slightly more complicated in that the post-processing does not give a particularly good qualitative fit to the observations in terms of skewness and kurtosis despite the success of reproducing the IQR. As with the [Fe/H] distribution the scattering and selection effects make the initially negatively-skewed distribution more positive but does not go far enough to be in line with the positively-skewed, *GES-iDR4*, [Mg/Fe] data. The observed [Mg/Fe] kurtosis indicates a higher likelihood of outliers than found with a normal distribution, the even higher value of the *Selene-CH* distribution is due to the extremely narrow distribution (kurtosis is not a measure of peakedness). The post-processing greatly reduces the kurtosis to be much closer to zero which is entirely expected as the scattering in particular pushes the distribution to be almost normal. The conformity of the *Selene-SYN-G* distribution to a normal curve is because of the initially narrow distribution and the large scale of the scattering from the [Mg/Fe] uncertainty.

While the width of the observed DFs can be reproduced by application of observationally-motivated scattering, our simulations do not recover the detailed shape of the [Fe/H] or [Mg/Fe] normalised distribution functions. The shape of the simulated [Fe/H] distribution is promisingly close, but still defies similarity with an excess of abundance of stars between -0.4 and -0.2. But the mean values of [Fe/H] are too high in the simulations. In contrast, the simulated [Mg/Fe] are too low. The post-processing does not give a particularly good qualitative fit to the observations in terms of skewness and kurtosis. As with the [Fe/H] distribution the scattering and selection effects make the initially negatively-skewed distribution more positive but does not go far enough to be in line with the positively-skewed, *GES-iDR4*, [Mg/Fe] data. The implementation of the scattering *Selene-SCA-G* sufficiently incorporates

CHAPTER 2

the uncertainties within observational surveys, but more importantly without the scatter, *Selene-SYN-G* produces an $[\text{Fe}/\text{H}]$ abundance that has a larger abundance of stars around the median value peak.

The mismatch between observed and simulated data for $[\text{Mg}/\text{Fe}]$ could also hint a problem with the observations or with stellar yields in our chemical evolution model. In fact, our results confirm the earlier studies (Timmes et al. 1995; François et al. 2004; Andrews et al. 2016) that show that chemical evolution models of the solar neighbourhood systematically under-predict $[\text{Mg}/\text{Fe}]$ at any metallicity, also the solar values are too low compared to the observed $[\text{Mg}/\text{Fe}]$ in the solar photosphere. This could be either due to poorly understood stellar yields of SNIa or SNII (see François et al. 2004), or because of the systematic errors in the observed data. It is known that Mg lines in cool stars are affected by NLTE (Bergemann et al. 2015; Merle et al. 2011). In fact, Bergemann et al. (2016), show that the NLTE $[\text{Mg}/\text{Fe}]$ trend is lower than LTE trend, that would help to improve the agreement with the simulations. NLTE models show a larger abundance of low (magnesium poor) $[\text{Mg}/\text{Fe}]$ stars than LTE models.

2.7.3 Relationships Between $[\text{Fe}/\text{H}]$, $[\text{Mg}/\text{Fe}]$, and Stellar Ages in the Observed and Simulated Solar Neighbourhood

While the quantitative analysis of 1D normalised distribution functions is precise, it does not aid our understanding of which stars are responsible for the differences between the models and simulations. Greater insight can be provided by examining the evolution of $[\text{Fe}/\text{H}]$ and $[\text{Mg}/\text{Fe}]$ with age (shown in Figures 2.19 and 2.20 respectively) as well as by examining the distribution of $[\text{Mg}/\text{Fe}]$ as a function of metallicity (shown in Figure 2.21). In these figures we only show 1000 of the 15562 stars found within the 2 kpc sphere in the *Selene-CH* and *Selene-SCA-G* datasets for

CHAPTER 2

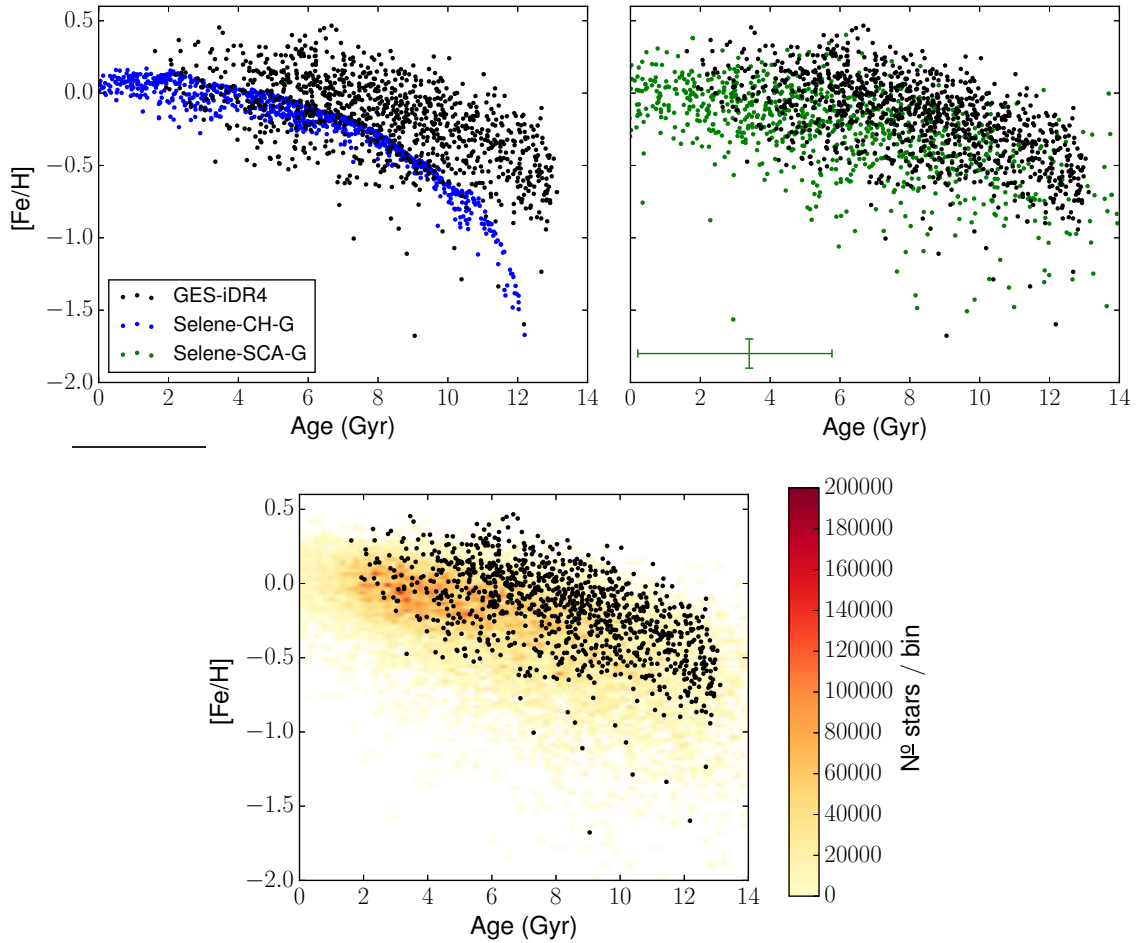


Figure 2.19: Age-metallicity relation for our various simulated datasets compared with the *GES-iDR4* distribution. The *GES-iDR4* stars are plotted as black points in each panel, *Selene-CH* is presented as blue points in the left-hand panel, *Selene-SCA-G* as green points in the middle panel and *Selene-SYN-G* as a heat map with increasingly red colours indicating an increase in the number of synthetic star particles in bins of 0.025 dex in $[\text{Mg}/\text{Fe}]$ and 0.2 Gyr in age. For clarity we show only 1000 random points from the *Selene-Ch* and *Selene-SCA-G* data and we also include a representative error bar showing the size of the scatter in $[\text{Fe}/\text{H}]$ and age between *Selene-CH* and *Selene-SCA-G* ($\sigma_{[\text{Fe}/\text{H}]} = 0.101$ dex, $\sigma_{\text{age},\text{low}} = 3.20$ Gyr and $\sigma_{\text{age},\text{high}} = 2.37$ Gyr, values which are computed from the mean of the errors of the *GES-iDR4* data).

CHAPTER 2

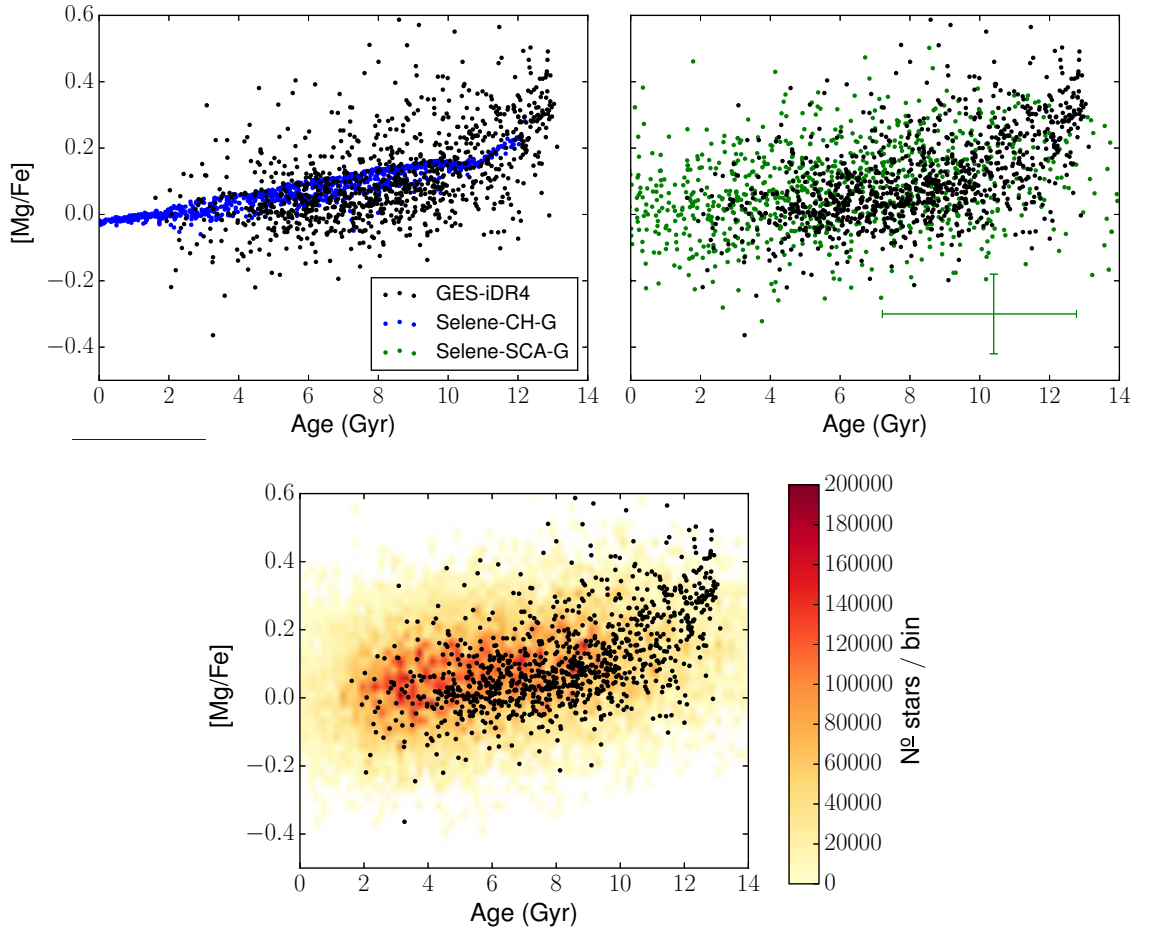


Figure 2.20: $[\text{Mg}/\text{Fe}]$ versus stellar age. The *GES-iDR4* stars are plotted as black points in each panel, *Selene-CH* is presented as blue points in the left-hand panel, *Selene-SCA-G* as green points in the middle panel and *Selene-SYN-G* as a heat map with increasingly red colours indicating an increase in the number of synthetic star particles in bins of 0.025 dex in $[\text{Mg}/\text{Fe}]$ and 0.2 Gyr in age. For clarity we show only 1000 random points from the *Selene-Ch* and *Selene-SCA-G* data and we also include a representative error bar showing the size of the scatter in $[\text{Fe}/\text{H}]$ and age between *Selene-CH* and *Selene-SCA-G* ($\sigma_{[\text{Mg}/\text{Fe}]} = 0.120$ dex, $\sigma_{age,low} = 3.20$ Gyr and $\sigma_{age,high} = 2.37$ Gyr, values which are computed from the mean of the errors of the *GES-iDR4* data).

CHAPTER 2

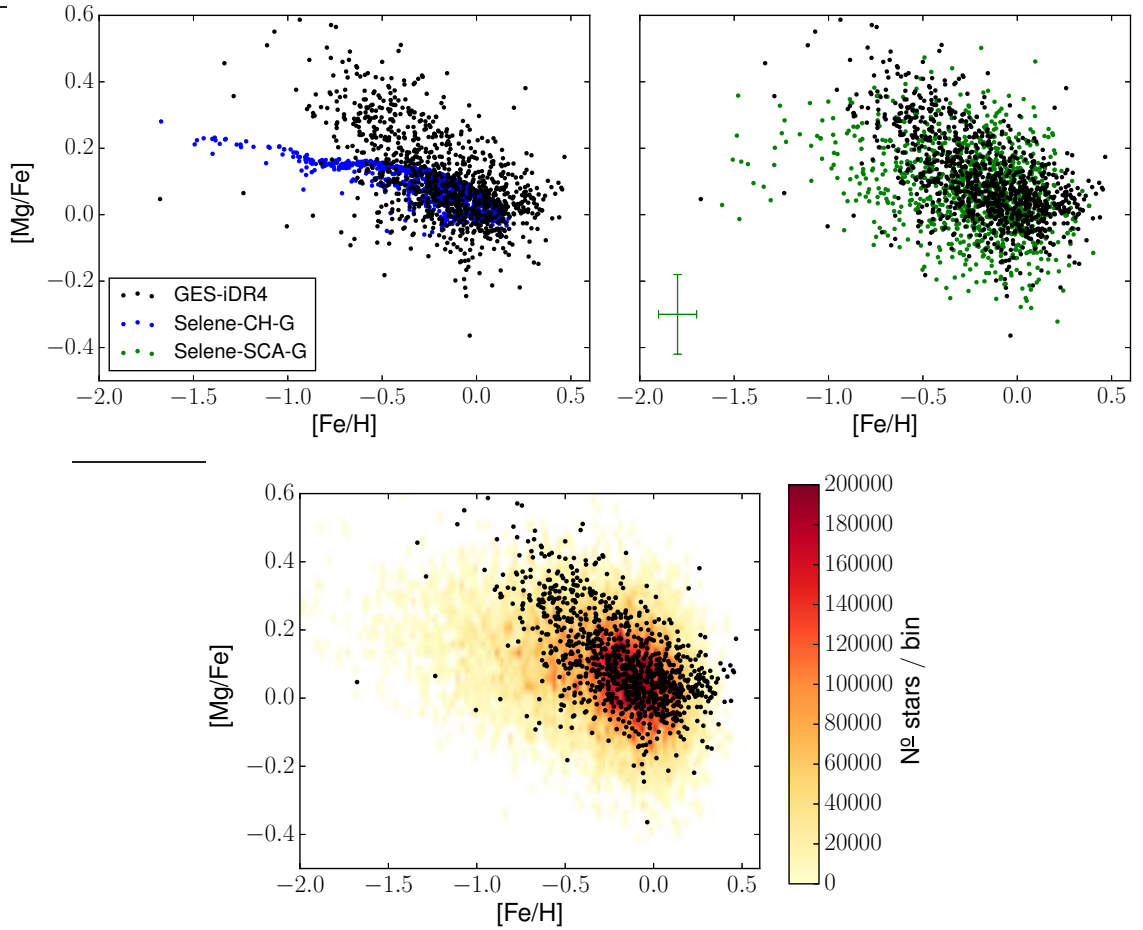


Figure 2.21: A plot of $[\text{Mg}/\text{Fe}]$ versus $[\text{Fe}/\text{H}]$. The *GES-iDR4* stars are plotted as black points in each panel, *Selene-CH* is presented as blue points in the left-hand panel, *Selene-SCA-G* as green points in the middle panel and *Selene-SYN-G* as a heat map with increasingly red colours indicating an increase in the number of synthetic star particles in bins of 0.025 dex in $[\text{Mg}/\text{Fe}]$ and 0.025 dex in $[\text{Fe}/\text{H}]$. For clarity we show only 1000 random points from the *Selene-Ch* and *Selene-SCA-G* data and we also include a representative error bar showing the size of the scatter in $[\text{Fe}/\text{H}]$ and age between *Selene-CH* and *Selene-SCA-G* ($\sigma_{[\text{Mg}/\text{Fe}]} = 0.120$ dex, $\sigma_{[\text{Fe}/\text{H}]} = 0.101$ dex, values which are computed from the mean of the errors of the *GES-iDR4* data).

CHAPTER 2

Name	[Fe/H]			[Mg/Fe]		
	IQR	σ_3	σ_4	IQR	σ_3	σ_4
<i>Selene-CH-G</i>	0.398	-1.47	3.52	0.113	-0.282	4.26
<i>Selene-SCA-G</i>	0.409	-1.28	2.98	0.180	-0.0165	0.358
<i>Selene-SYN-G</i>	0.350	-0.98	1.15	0.160	0.0416	0.099
<i>GES-iDR4</i>	0.414	-0.63	0.95	0.175	1.04	3.64

Table 2.3: [Fe/H] and [Mg/Fe] distribution function characteristics for the three simulation datasets (*Selene-CH-G*, *Selene-SCA-G* and *Selene-SYN-G*), and the observational dataset *GES-iDR4* in dex. The interquartile range (IQR), skewness (σ_3), and kurtosis (σ_4) values for the normalised distribution functions of [Fe/H] and [Mg/Fe] as shown in Figure 2.18. Column 1 gives the name of the dataset, columns 2, 3 and 4 are the IQR, σ_3 , and σ_4 of the [Fe/H] distribution. Columns 5, 6 and 7 are IQR, σ_3 , and σ_4 of the [Mg/Fe] distribution.

the sake of clarity; the *Selene-SYN-G* stars are shown as an abundance histogram.

The distribution of points as shown in Figure 2.19 for *Selene-CH* - the raw simulation data (with only a geographical cut to match the physical extent of the observed stars) - is significantly narrower than the observed distribution at all ages. The distribution of stellar population particles is particularly narrow for the oldest stars which are responsible for the low-metallicity tail in Figure 2.18. The distributions of the *Selene-CH* stellar population particles in both [Fe/H] and [Mg/Fe] are a result of the overall trend with age in contrast with the observed distribution for which the overall observational uncertainties dominate. As discussed in the previous section, when the scatter is applied in *Selene-SCA-G*, the initially narrow underlying distribution is no longer distinguishable in the simulated data. But the simulated age-metallicity relation is at least more similar to the observed data.

Synthetic star particles older than 8 Gyr as shown in Figure 2.19 appear to

CHAPTER 2

underestimate $[\text{Fe}/\text{H}]$ with their original, unscattered distribution in comparison with *Selene-CH-G*. This underestimation in the old stars is not so prominent in the *Selene-SCA-G* results (middle panel of Figure 2.18), because scattering with observational age errors brings some of the young metal-rich stars to greater apparent ages. Applying the SYNCMD tool to produce *Selene-SYN-G* does not lead to any significant improvement over *Selene-SCA-G* in terms of fitting the observations. While some of the youngest stars are removed (see Figure 2.17), it is not sufficient to match the dearth of young stars in *GES-iDR4*.

The trend of $[\text{Mg}/\text{Fe}]$ with age in Figure 2.20 for the unaltered simulation stellar population particles is a more or less linear increase with a very small up-turn seen in the oldest stars. Again the scattering broadens the distribution significantly, but the application of the selection function makes only small changes to the distribution of the simulated stars. The main difference between simulation and observation is in the stars older than 10 Gyr; the up-turn in the underlying *Selene-CH* is not as strong as the observed high $[\text{Mg}/\text{Fe}]$ stars in the old population. As discussed earlier, there are two possible explanations: a) neglect of NLTE effects in our observed $[\text{Mg}/\text{Fe}]$ distributions, and b) erroneous stellar yields in the chemical evolution model.

The relation between $[\text{Fe}/\text{H}]$ and $[\text{Mg}/\text{Fe}]$ is shown in Figure 2.21. Overall the scattering has more of an impact on the distribution of the simulated data. Applying the scatter matches the simulated relation more closely to the observations. Figure 2.19 shows that there is a systematic offset between the observed versus simulated $[\text{Fe}/\text{H}]$ - age plane, that cannot be seen in 1D normalised distribution functions in Figures 2.18 and 2.17. Figures 2.20 and 2.21 clearly illustrate the fundamental importance of observational errors. Observational errors wash out all sub-structure in the chemical abundance space, which is highly relevant to trace the assembly history of the Galactic disc, and make it impossible to detect and quantify it, thus strongly limiting our ability to constrain the simulations of galaxy formation. This

CHAPTER 2

means that varying the physics in your model, e.g. feedback or IMF, the effect on the $[\text{Mg}/\text{Fe}]$, $[\text{Fe}/\text{H}]$ and age distributions would be smaller than the effect of errors. These observational errors could be reduced from high resolution spectrographic surveys, of which technological advances will eventually make this possible. Figure 2.21 is important because this is the only figure illustrating ‘direct observables’, i.e. chemical abundances, from the Gaia-ESO survey. Other observed parameters, like ages, are not directly observable in stellar spectra (Bergemann et al. 2016) (although technically metal abundances require some form of spectral model). The determination of ages highly depend on stellar models, and through the use of the Bayesian pipeline, they also depend on other priors, like the IMF.

Finally, we should note that the GES high-resolution dataset does not show any evidence of the bimodal $[\text{Mg}/\text{Fe}]$ distribution with $[\text{Fe}/\text{H}]$, which have been proposed as a chemical separator of the thin and thick discs. This is also consistent with our simulations, which do not have any discontinuity in the SFH at ~ 1 Gyr.

2.7.4 Selection Function Subregions

Here we shall briefly discuss the impact different colour and magnitude bins have on the shape of the age and $[\text{Fe}/\text{H}]$ normalised distribution functions as well as their 2D abundance function. This allows us to examine what population of stars are occupying the colour and magnitude bins. The discussion presented here is more qualitative in comparison to the previous subsections, but the aim is more so to describe the contribution of finer components of the CMD have to the distribution functions of $[\text{Fe}/\text{H}]$ and the age of synthetic stellar particles.

A spherical region with a radius of 2 kpc was chosen in preference of other shapes/distributions. The motivation for this was to minimise the loss of stars via the photometric boundary conditions from running SYNCMD. Figure 2.7 demonstrates that the application of the Gaia-ESO selection function truncates stars that

CHAPTER 2

are further away. From the synthetic observers point of view, these stars further away are fainter than the lower limit on the magnitude selection. Discussion with the RAVE data in §2.9.2 also indicates that these stars are likely to be bright giants. Additionally, the Gaia-ESO survey targets foreground stars within 2 kpc from the earth and we wish to compare the *Selene-CH-G* with a similar like-for-like spatial region.

To demonstrate the impact of different bins on the colour magnitude diagram of different J and J–K within *Selene-SYN-G*. We study 12 different CMD bins and label these 1 through to 12 with the colour-magnitude bins defined in Table 2.4. These bins together cover the same photometric region for *Selene-SYN-G* and $0.23 \leq J-K \leq 0.45$ additionally use the selection function criteria as described in §2.6.2. The bins are ordered in increasing redness with incremental increases in J–K and decreasing magnitude with incremental increases in J. This includes the removal of the extinction correction to the J–K upper limit as described in §2.6.5. We shall now discuss the impact of these CMD bins in comparison to *Selene-SYN-G* and discuss the impact on the [Fe/H], age and distance distributions as well as the age-metallicity relation. Due to time constraints, our discussion here is limited and thus we mainly focus on the impact on the distribution functions within the different colour magnitude bins. It is worth noting that here we normalise each distribution to itself, i.e. the area under each distribution should be the same. We have stated the actual abundances of synthetic star particles in Table 2.4 for reference with the majority of the abundances of stars residing towards the centre of the CMD.

We chose a bin width of $J-K = 0.11$ on the blue edge of the CMD due to the deficiency of bluer stars as a result of the upper T_{eff} selection limit. This selection function component in particular removes younger (and bluer) stars with the impact discussed in §2.7.1. In general the abundance of stars increases with decreasing magnitude as shown in Table 2.4. This correlates with the distance distribution

CHAPTER 2

CMD Bin	J_{\min}	J_{\max}	J_{diff}	$(J-K)_{\min}$	$(J-K)_{\text{min}}$	$(J-K)_{\max}$	$N_{\text{SSP}} (10^5)$
1	12.0	12.5	0.5	0.23	0.34	0.11	32.9
2	12.0	12.5	0.5	0.34	0.395	0.055	14.7
3	12.0	12.5	0.5	0.395	0.45	0.055	4.93
4	12.5	13.0	0.5	0.23	0.34	0.11	60.9
5	12.5	13.0	0.5	0.34	0.395	0.055	27.7
6	12.5	13.0	0.5	0.395	0.45	0.055	9.67
7	13.0	13.5	0.5	0.23	0.34	0.11	102.0
8	13.0	13.5	0.5	0.34	0.395	0.055	54.8
9	13.0	13.5	0.5	0.395	0.45	0.055	18.3
10	14.5	14.0	0.5	0.23	0.34	0.11	163.6
11	14.5	14.0	0.5	0.34	0.395	0.055	97.0
12	14.5	14.0	0.5	0.395	0.45	0.055	29.2
<i>Selene-CH-G</i>	12.0	14.0	2.0	0.23	0.45	0.22	615.82

Table 2.4: The 12 different photometric regions studied on the synthetic CMD for *Selene-CH-G*. These regions are plotted on the synthetic CMD in Figure 2.22. J_{\min} , J_{\max} and J_{diff} columns show the minimum, maximum and difference (width) in the J magnitude. The $(J-K)_{\min}$, $(J-K)_{\text{min}}$ and $(J-K)_{\max}$ columns show the minimum, maximum and width of the $(J-K)$ bin. N_{SSP} is the number of stars in the CMD bin. We additionally use the selection function criteria as described in §2.6.2. Additionally we include *Selene-CH-G* as a reference.

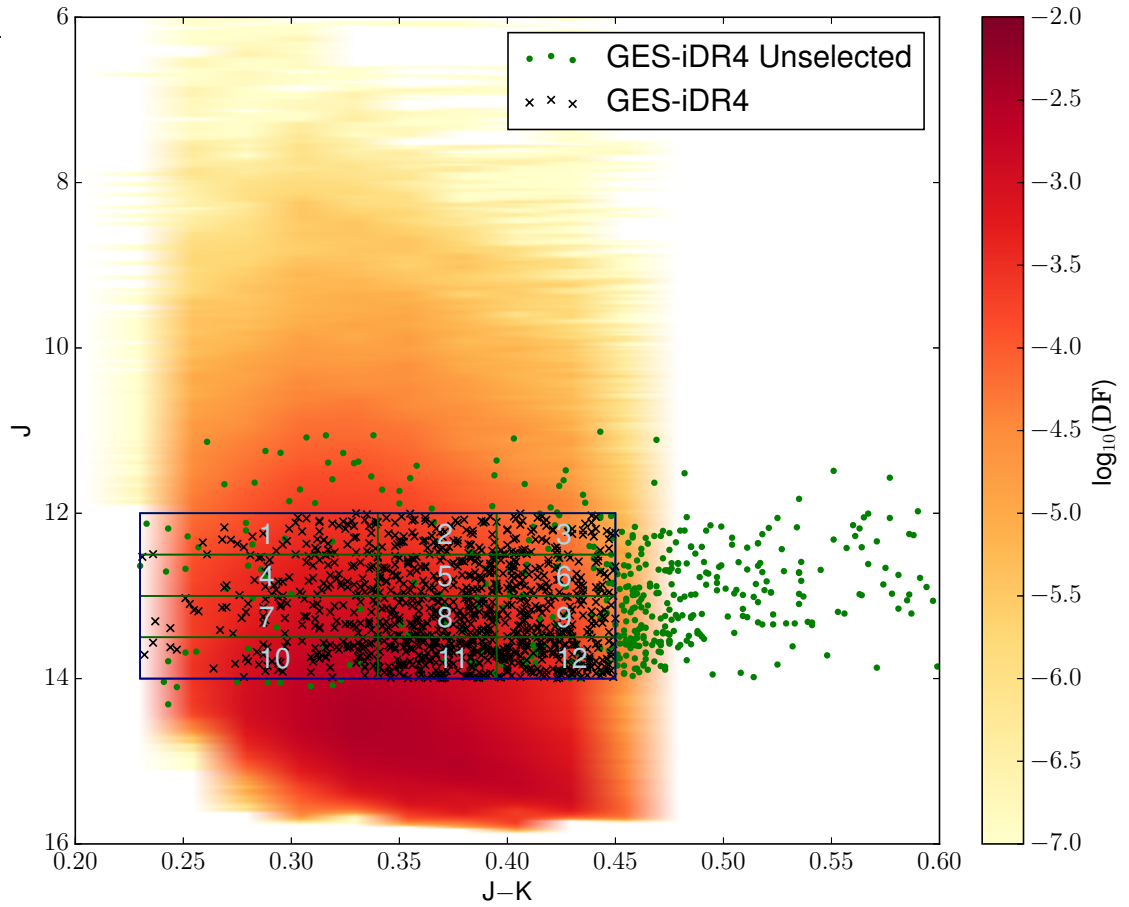


Figure 2.22: Synthetic CMD of J vs. $J-K$ in apparent magnitude space of the simulated solar neighbourhood analogue and *GES-iDR4* stars. The red heatmap represents the synthetic stellar populations from *Selene-SYN-G* which is derived from the simulated galaxy *Selene-CH* as shown in Figure 2.4. The black crosses represent stars selected from the *GES-iDR4* dataset. The blue rectangle highlights the J and $J-K$ region selection function boundary conditions of $12 < J < 14$ and $0.23 < J - K < 0.45$. Both datasets include the application of surface gravity and effective temperature filters of; $3.5 \leq \log(g) \leq 4.5$ dex and $5400 \leq T_{\text{eff}} \leq 6400$ K. We highlight 12 different subregions of the SYNCMD and label them 1 to 12. Each bin is of width $0.5 J$ and $0.055 J-K$, except for bins 1,4,7 and 10 which are of width $0.110 J-K$ and $0.5 J$.

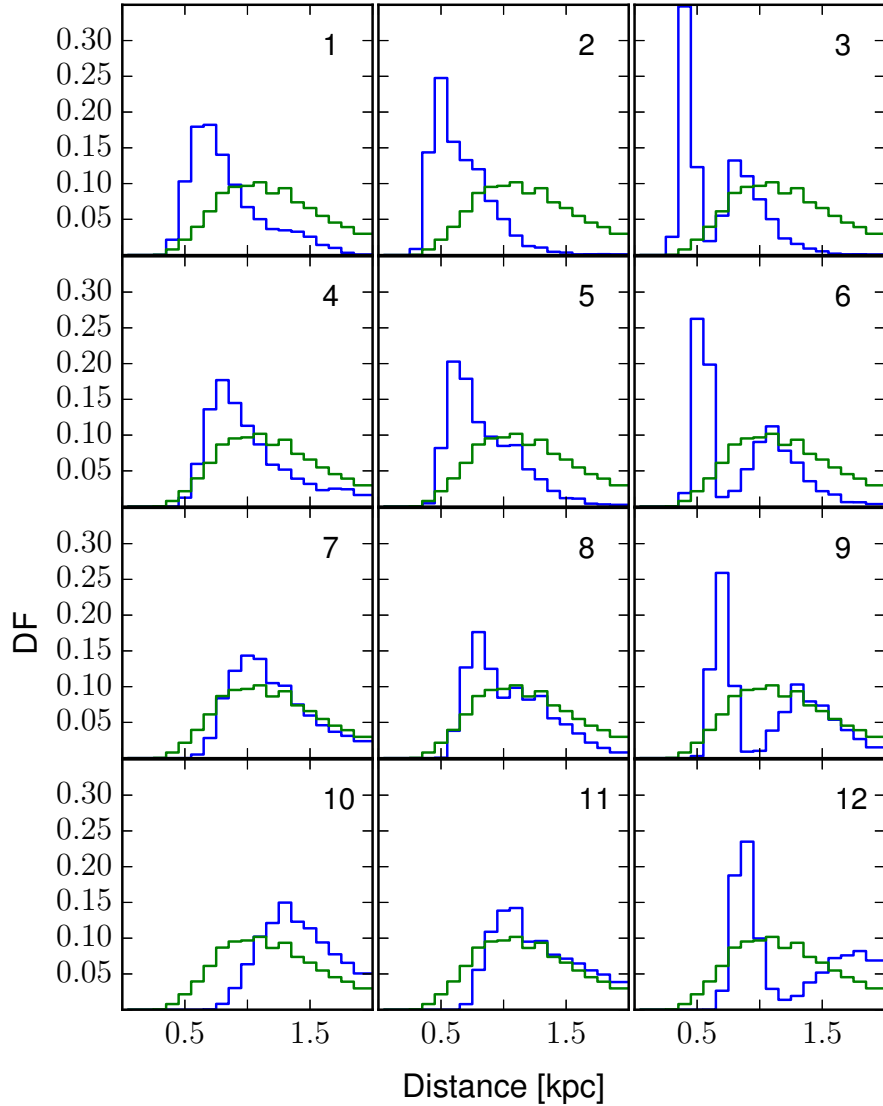


Figure 2.23: The distance distribution function for the synthetic star particles of photometric properties shown in Figure 2.22. The blue line represents the distribution function for the stars in the colour magnitude bin. The green line represents the results for *Selene-SYN-G* which covers the entire colour-magnitude selection region. The bins are chosen with $J-K$ from left to right and increasing J from top to bottom. Each bin is of width $0.5 J$ and $0.055 J-K$, except for bins 1,4,7 and 10 which are of width $0.110 J-K$ and $0.5 J$. The overall range is $12 < J < 14$ and $0.23 < J - K < 0.45$.

CHAPTER 2

function as shown in Figure 2.23 with the median of the distribution function of stars closer to the observer in brighter magnitudes than fainter magnitudes. The median in the distributions for redder stars is also more peaked and on average smaller in abundances than the other bins (even when taking into account the blue bin width is double the width). Additionally, a double peak starts to appear as well. This is likely due to the nearer peak being red faint main sequence stars and the second peak consists of giants.

Interestingly, Figure 2.24 shows that other than for the brightest and most blue CMD Bin (bin 1) as shown in Table 2.4, the $[\text{Fe}/\text{H}]$ abundance ratios remain for the most part relatively unchanged. However there is some subtle variation in the $[\text{Fe}/\text{H}]$ distribution. The reasoning for the narrow peak in CMD Bin 1 is due to the abundance of young stars as shown in Figure 2.25. Increasing $J-K$ in general increases the skewness of the $[\text{Fe}/\text{H}]$ distribution function, although this is a result of the more distinguishable differences between two stellar populations.

For the age distribution in Figure 2.25, increasing $J - K$ appears to shift the distribution from the younger stars to the older stars. Additionally selecting bins at larger $J - K$ tends the age distribution closer towards the resemblance of a normal distribution. The peak at the mean value for low $J - K$ decreases with increasing J (and thus fainter) since fainter regions lack younger stars. CMD Bin 10 closely represents *Selene-SYN-G* but also has the most synthetic stars. Figure 2.26 further supports the different stellar populations. There are multiple peaks in the age-metallicity relation in the higher $J-K$ bins.

The aim of the discussion here was to illustrate the impact of different regions of the CMD on the age and $[\text{Fe}/\text{H}]$ distribution functions and whether SYNCMD upholds this with simulation data. Indeed the figures presented here show the decrease in abundance of younger stars for decreasing magnitude and increasing “redness”. But overall, the impact on the $[\text{Fe}/\text{H}]$ distribution is relatively minimal, other than

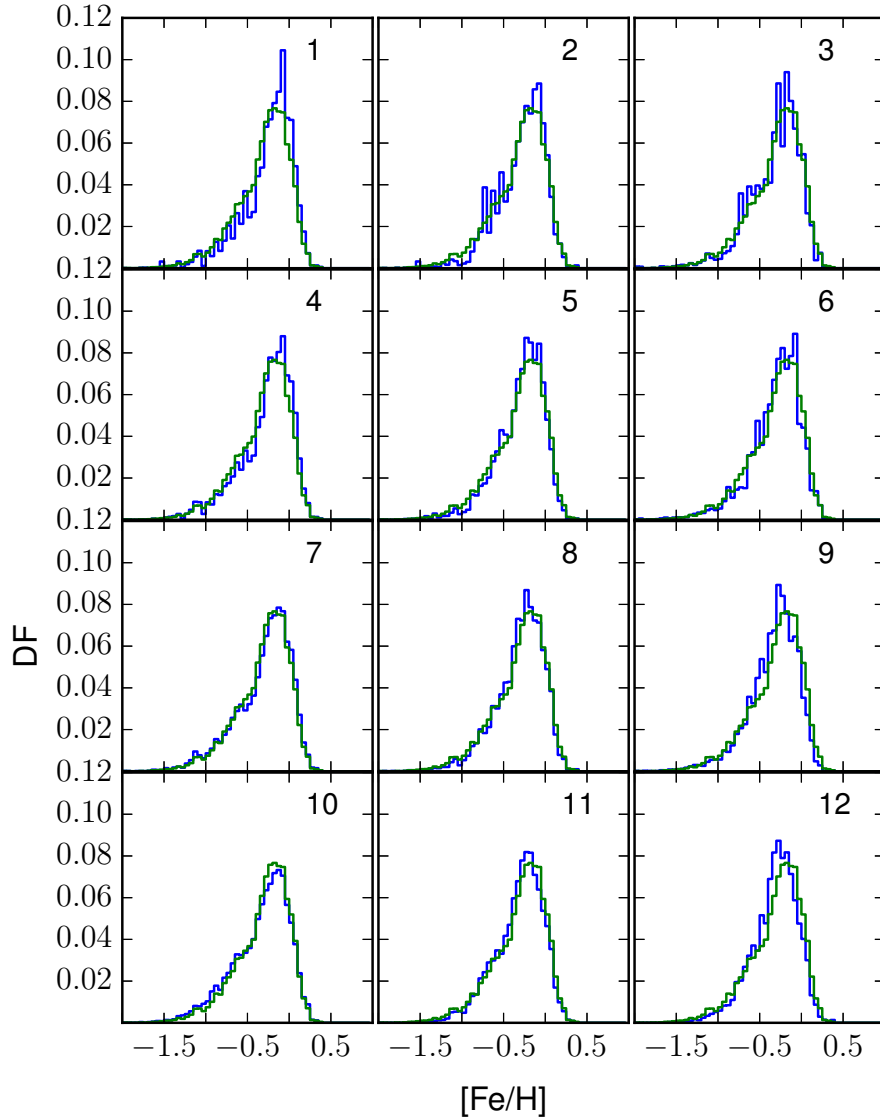


Figure 2.24: The $[\text{Fe}/\text{H}]$ distribution function for the synthetic star particles of photometric properties shown in Figure 2.22. The blue line represents the distribution function for the stars in the colour magnitude bin. The green line represents the results for *Selene-SYN-G* which covers the entire colour-magnitude selection region. The bins are chosen with $J-K$ from left to right and increasing J from top to bottom. Each bin is of width $0.5 J$ and $0.055 J-K$, except for bins 1,4,7 and 10 which are of width $0.110 J-K$ and $0.5 J$. The overall range is $12 < J < 14$ and $0.23 < J - K < 0.45$.

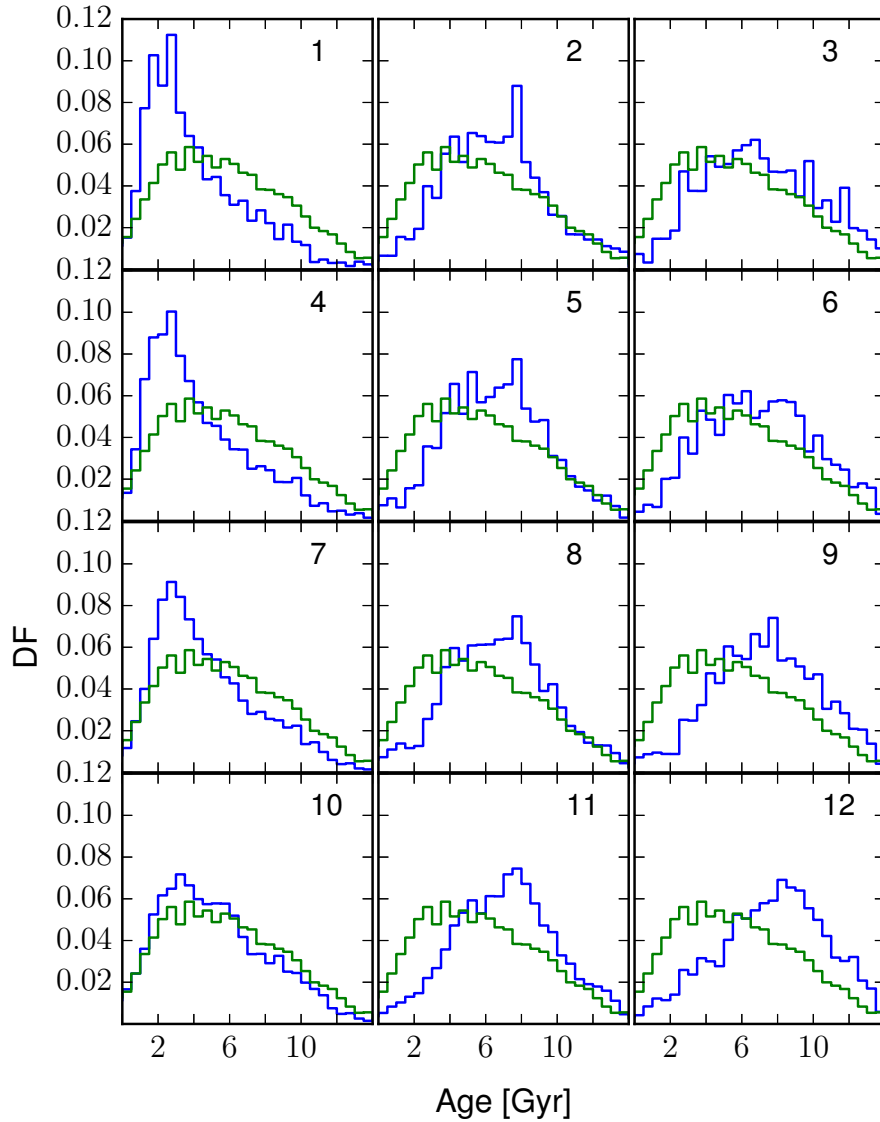


Figure 2.25: The age distribution function for the synthetic star particles of photometric properties shown in Figure 2.22. The blue line represents the distribution function for the stars in the colour magnitude bin. The green line represents the results for *Selene-SYN-G* which covers the entire colour-magnitude selection region. The bins are chosen with $J-K$ from left to right and increasing J from top to bottom. Each bin is of width $0.5 J$ and $0.055 J-K$, except for bins 1,4,7 and 10 which are of width $0.110 J-K$ and $0.5 J$. The overall range is $12 < J < 14$ and $0.23 < J - K < 0.45$.

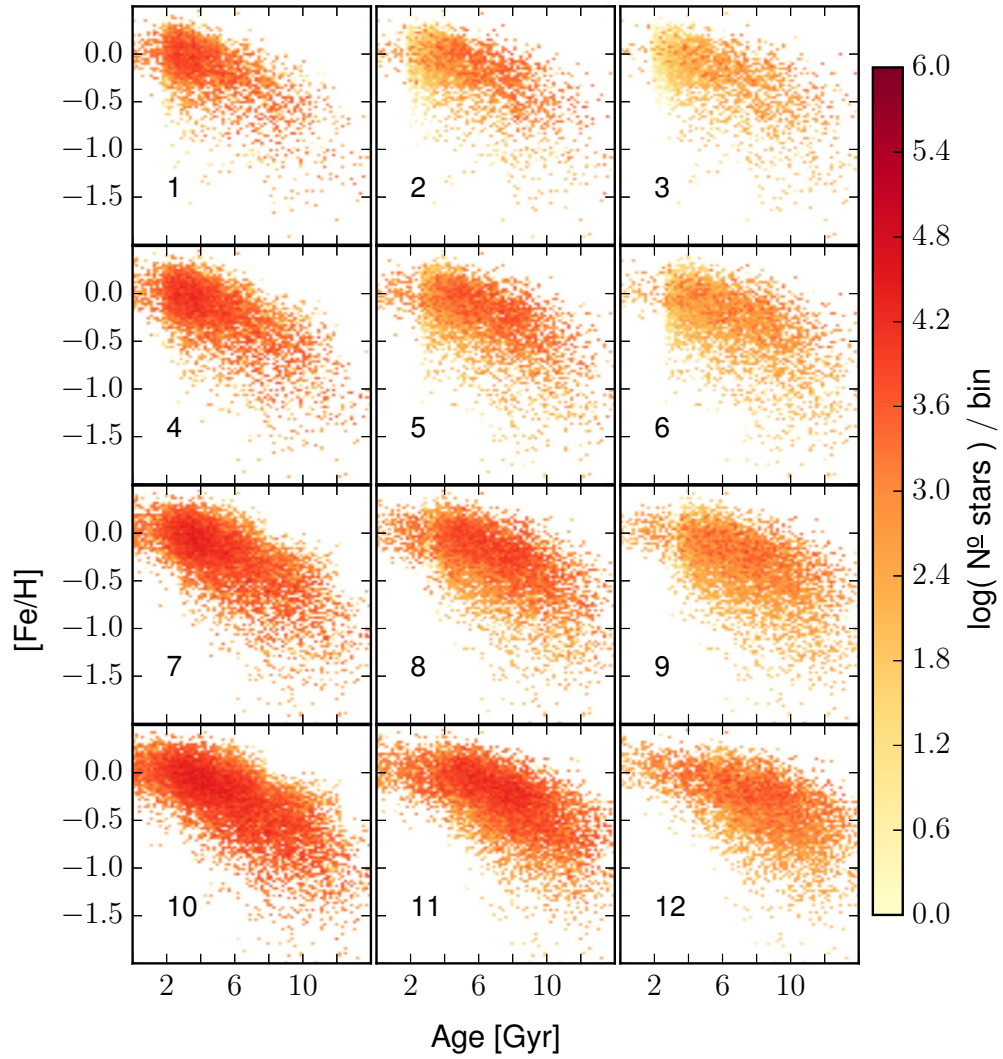


Figure 2.26: The age-metallicity relation for the synthetic star particles of photometric properties shown in Figure 2.22. The bins are chosen with $J-K$ from left to right and increasing J from top to bottom. Each bin is of width $0.5 J$ and $0.055 J-K$, except for bins 1,4,7 and 10 which are of width $0.110 J-K$ and $0.5 J$. The overall range is $12 < J < 14$ and $0.23 < J - K < 0.45$.

for the brighter and bluer region of the CMD in which is skewed towards younger and metal rich stars.

2.8 Comparison with RAVE

We now compare the RAVE DR5 dataset with Selene-CH using similar analysis methodology as used for the comparison with the Gaia-ESO Survey. We work with the same galaxy *Selene-CH*

We compare the RAVE-DR5 survey results *RAVE-DR5*, with the following variants of the simulated galaxy *Selene-CH*.

- *Selene-CH-R* is the the unaltered and unmodified galaxy. We select all of the stellar population particles that reside within the RAVE selection function around the simulated observer, 15562 in total. These particles are compared directly with the *GES-iDR4* results. This kind of direct comparison demonstrates the methodology employed in the ‘traditional sense’, i.e. with spatial cuts alone.
- *Selene-SCA-R* is a modified version of *Selene-CH-R*. In this case we apply stochastic scattering to the ages and abundance ratios of the stellar population particles to emulate observational uncertainties. The magnitude of the scattering is based on the mean errors taken from the Gaia-ESO dataset.
- *Selene-SYN-R* is the result of applying the SYNCMD toolkit, as described in §2.4, to the scattered stellar population particles ages and metallicities in *Selene-RAVE* (i.e. the statistically scattered results of *Selene-CH*). This dataset includes the application of selection functions for $\log(g)$, T_{eff} , J-band magnitude, and J–K colour and is a more rigorous attempt to mimic the *RAVE-DR5* data.

2.8.1 RAVE-DR5

We post-process further the *RAVE-DR5* (Kunder et al. 2016) data for analysis. We select initially the entire 520,629 stars from the DR5 database. The selection function is based off that discussed in (Wojno et al. 2017), but with some slight modifications to the temperature cut. We initially reduce this dataset down by filtering for high quality data:

1. $c1, c2, c3 = n$;
2. $\alpha_c \geq -3.0$;
3. $\chi^2 \leq 2000$;
4. $algoconv = 0$; i.e. we use the high quality dataset;
5. $SNR \geq 20$;
6. $CorrectionRV \leq |10|$;
7. $CorrelationCoeff \geq 10$.

Here *algoconv* is a flag in the stellar parameter pipeline used by RAVE and $= 0$ indicates the highest quality result. The analysis was carried out as desired. The renormalisation process converged, as did MATISSE (for high SNR spectra) or DE-GAS (for low SNR spectra). χ^2 quantifies the mismatch between the observed spectrum and the best-matching model used in the chemical pipeline. *CorrectionRV* and *CorrelationCoeff* (Tonry & Davis 1979, correlation coefficient) are parameters related to the accurate measurement of the radial velocity (RV). *c1*, *c2*, and *c3* are classification flags which indicate that the spectrum is normal (i.e. = "n") which Matijević et al. (2012) describes in detail. Finally α_c is the alpha-enhancement from chemical pipeline.

CHAPTER 2

This pipeline yields reliable results only in a restricted region in stellar parameter space (Kordopatis et al. 2013a). We explicitly select stars with the following selection criteria:

1. I-band magnitude $9 \leq I \leq 12$,
2. J–Ks colour of $J - K_s \geq 0.5$ for $|b| \leq 25^\circ$,
3. Galactocentric latitude $300 \leq l \leq 360$ and $0 \leq l \leq 150$,
4. $d \leq 8$ kpc,
5. $\sigma_{V,los} \leq 8.0$,
6. Surface gravity of $0.5 \leq \log(g) \leq 5.0$ dex,
7. Effective temperature of $4000 \leq T_{\text{eff}} \leq 8000$ K.

Where d is the distance of the star from the observer. No colour cut is applied for $|b| \geq 25^\circ$. The temperature and surface gravity limits are based on the range of parameters for the spectra used for the learning grid of the analysis pipeline (Kordopatis et al. 2011, 2013a). $\sigma_{V,los}$ is the error on the observed line of sight velocity V_{los} , also known as the heliocentric radial velocity. It is worth noting that there is no age field in this dataset. Additionally, since 2MASS provides accurate J, H and Ks photometry for nearly all RAVE targets and also for all other stars which could have potentially entered the input catalogue. However 2MASS does not provide I-band photometry which is needed to construct the selection function. To compute an approximate I_{2MASS} magnitude we use the following formula as used in Wojno et al. (2017):

$$I_{2MASS} - J = (J - K_s) + 0.2 \exp\left(\frac{(J - K_s) - 1.2}{0.2}\right) + 0.12. \quad (2.59)$$

CHAPTER 2

Since RAVE-DR5 dataset has over a factor of 100 more stars than GES-iDR4, as well as a larger spatial survey region within both the simulation and observations, we can look in more detail at the different stellar populations. We shall study the Giant branch stars (Gi), The Main sequence stars (MS) and the turnoff region stars (TO). Giant branch stars typically have a low surface gravity due to being large in radius. Main sequence stars typically have a large surface gravity and a colder surface temperature, whereas the turnoff region stars have larger surface gravities and are hot. The turnoff region is the region on the main branch where stars turn off the main sequence and transition onto becoming giants. The most massive stars leave the main sequence first to become giants, and then increasingly lower mass stars leave the main sequence with time. We describe the selection function of the three sub-datasets of *RAVE-DR5*:

1. *RAVE-DR5-Gi*: Giants (Gi): $\log(g) \leq 3.5$,
2. *RAVE-DR5-MS*: Main sequence (MS): $\log(g) \geq 4.0$ & $T_{\text{eff}} \leq 5500$ K,
3. *RAVE-DR5-TO*: Turnoff region (TO): $\log(g) \geq 3.5$ & $5500 \leq T_{\text{eff}} \leq 7000$ K.

We compare the above selection criteria with similar selection function parameters with *Selene-Syn-R* in §2.8.4. The boundaries for $\log(g)$ and T_{eff} were determined from studying the $T_{\text{eff}}\text{-}\log(g)$ plane (see bottom row of Figure 8 in Wojno et al. 2017). The additional selection function when applied to RAVE-DR5 creates the datasets *RAVE-DR5-Gi*, *RAVE-DR5-MS* and *RAVE-DR5-TO*.

2.8.2 Selene-CH-R

We select a region within the simulated galaxy *Selene-CH*, a position 8 kpc from the galactic centre on a spiral arm. This position is shown with a cross in Figure 2.4 at $(x,y) = (4.0, 6.93)$ kpc and we call this the location of the ‘Sun’. From here, we aim to mimic the spatial region used in *RAVE-DR5*. We select a spatial region with

CHAPTER 2

a Galactocentric longitude $300 \leq l \leq 360$ and $0 \leq l \leq 150$ and maximum distance from the sun of 8 kpc. This essentially leaves us with a semi-sphere selection region, in which we rotate this about the Cartesian Y axis by 20 degrees. By rotating this selection region, we are simulating the effects of the inclination of the earth with respect to the galactic centre, and allows us to capture some stars that are further from the galactic centre. In addition to this, we also include a Galactocentric latitude cut of $|b| > 10^\circ$. In short, we aim to best capture the spatial region selected in RAVE-DR5, although it is worth noting that we are limited by spatial resolution of ~ 217 pc, and thus this is mostly accurate to a first order. We normalise the Fe and Mg abundances to the Asplund et al. (2009) solar values and then apply the same shift as we did in §2.6.3 for consistency. The magnitude of the renormalisation is $[\text{Fe}/\text{H}] = -0.066$ dex and $[\text{Mg}/\text{Fe}] = 0.078$ dex and we justify the reasoning for this in §2.6.3. We do not adjust the stellar ages since there is no quantity associated with stellar ages in *RAVE-DR5*.

2.8.3 Selene-SCA-R

This dataset extends the methodology described above to generate *Selene-SCA-G* by applying a stochastic scattering based on the *RAVE-DR5* errors $[\text{Mg}/\text{Fe}]$, and $[\text{Mg}/\text{Fe}]$ abundance ratios.

RAVE-DR5 quotes the errors on $[\text{Mg}/\text{Fe}]$ and $[\text{Fe}/\text{H}]$ to be $\sigma_{[\text{Mg}/\text{Fe}]} = \sigma_{[\text{Fe}/\text{H}]} = 0.2$ dex. We degrade the precision of our simulated metallicity and $[\text{Mg}/\text{Fe}]$ data on a particle-by-particle basis using a Gaussian distribution, centred on the original simulated value with a standard deviation of either $\sigma_{[\text{Fe}/\text{H}]}$ or $\sigma_{[\text{Mg}/\text{Fe}]}$. We use the normal distribution to compute new $[\text{Fe}/\text{H}]$ and $[\text{Mg}/\text{Fe}]$. This methodology is similar as to that in §2.6.4.

2.8.4 Selene-SYN-R

Our final version of *Selene* takes the scattered stellar population particles from *Selene-SCA-R* and inputs those particles to SYNCMD creating *Selene-SYN-R* just like in §2.6.5. The mechanics of SYNCMD are described in §2.4 but the key here is to split the stellar population particles into individual synthetic star particles with a realistic distribution of star properties so that we can apply photometric, $\log(g)$ and T_{eff} cuts to exactly mimic the observed *GES-iDR4* dataset. The selection criteria are stated in §2.8.1 i.e. we use:

1. I-band magnitude $9 \leq I \leq 12$,
2. J–K colour of $J-K_s \geq 0.5$ for $|b| \leq 25^\circ$,
3. Effective temperature of $4000 \leq T_{\text{eff}} \leq 8000$ K,

Like for *RAVE-DR5*, we can apply subsequent photometric selection functions to produce

1. Selene-SYN-R-Gi: Giants (Gi): $\log(g) \leq 3.5$,
2. Selene-SYN-R-MS: Main Sequence (MS): $\log(g) \geq 4.0$ & $T_{\text{eff}} \leq 5500$ K,
3. Selene-SYN-R-TO: Turnoff region (TO): $\log(g) \geq 3.5$ & $5500 \leq T_{\text{eff}} \leq 7000$ K.

In which the photometric functions for Giants (Gi), Main Sequence Stars (MS) and turnoff region stars (TR) are applied to Selene-SYN to produce sub-datasets.

As stellar population particles represent different masses of stars, the contribution of each one in terms of synthetic star particles is weighted by the initial mass of the stellar population particle to correctly account for the mass. The initial mass is used because any stars that have evolved and no longer form part of the stellar population are removed from the 100,000 synthetic star particles. The normalised

distribution functions shown in this work are described as ‘mass-weighted’, this means that we have weighted the *Selene-CH-R* and *Selene-SCA-R* particles by their mass to be consistent with the *Selene-SYN-R* distribution function.

2.9 RAVE Comparison Results and Discussion

We now present and discuss the impact that ‘observing’ our simulations has on the distribution of selected stars in age, $[\text{Fe}/\text{H}]$, and $[\text{Mg}/\text{Fe}]$ in comparison with *RAVE-DR5* data, as well as the sub datasets featuring the giants, main sequence and turnoff stars (i.e. *RAVE-DR5-Gi*, *RAVE-DR5-MS* and *RAVE-DR5-TO* with *Selene-SYN-R-Gi*, *Selene-SYN-R-MS* and *Selene-SYN-R-TO* respectively).

The number of stars in each dataset after applying post *Selene-CH-R* = 212470 (same for *Selene-CH-SCA*), *RAVE-DR5* = 192274 and *Selene-SYN-R* = 212470 and thus conveniently we have a similar number of star particle data to compare with. For the subdatasets of RAVE-DR5, we have *RAVE-DR5-Gi* = 106785, *RAVE-DR5-MS* = 3567, *RAVE-DR5-TO* = 59099 stars which pass their selection function criteria. Number of Star Particle Populations that pass the initial selection function criteria are *Selene-SYN-R-GI* = 202095, *Selene-SYN-R-MS* = 37, *Selene-SYN-R-TO* = 582 which produce *Selene-SYN-R* = 19031604, *Selene-SYN-R* = 16877920, *Selene-SYN-R* = 167111 and *Selene-SYN-R* = 1612888 synthetic star particles. The information about the number of stars is also in Table. 2.5. The lower abundance of initial stellar population particles for the synthetic MS and TO means that we will have an abundance of stars with similar chemical properties which we demonstrate in the discussion in §2.9.1.

Figure 2.27 shows the synthetic CMDs for *Selene-SYN-R*, *Selene-SYN-R-Gi*, *Selene-SYN-MS* and *Selene-SYN-TO*. Figure 2.28 shows the CMDs for *RAVE-DR5*, *RAVE-DR5-Gi*, *RAVE-DR5-MS* and *RAVE-DR5-TO*. There are a factor of 100 fewer stellar population particles which contribute towards synthetic CMD for the

CHAPTER 2

MS and the TO subdatasets which have magnitudes of $9 \leq I \leq 12$. Additionally, the $9 \leq I \leq 12$ region has bins containing $\sim 10^{-6}$ of the overall synthetic stars which pass the other selection function components. The main reason for the differences in the shape of the CMD can be accounted from the normalised distance distribution function in Figure 2.30. Since 70% of the *RAVE-DR5* stars are within a distance of 1 kpc from the sun, there will be a larger abundance of brighter stars in the I band. *Selene-SYN-R* has a larger spatial distribution range of stars, as such stars that are further away which reside within the $9 \leq I \leq 12$ magnitude cut are large bright giants. Additional factors that could shape the differences in the CMDs is the choice of isochrone databases which we use.

Figure 2.30 shows the normalised distance distribution function for the the datasets *Selene-CH-R*, *Selene-SCA-R*, *RAVE-DR5* and *Selene-SYN-R*. The stars in *Selene-CH-R*, *Selene-SCA-R* are more evenly distributed, and thus with increasing distance causes an increase in volume, and thus an increase in the number of stars. *Selene-SYN-R* distance function is truncated with the application of SYNCMD since stars further away are fainter, and thus lie outside the I colour band selection. The majority of stars for *Selene-SYN-R* are within 3 kpc from the simulated observer, whereas *RAVE-DR5* shows that the majority of stars are within 1.2 kpc of the observer with a small fraction of stars at further distances.

2.9.1 Distribution Functions of [Fe/H] and [Mg/Fe]

We first consider the datasets *RAVE-DR5* in comparison with *Selene-CH-R*, *Selene-SCA-R* and *Selene-SYN-R*. Figure 2.31 shows the normalised distribution function of [Fe/H] (top panel) and [Mg/Fe] (bottom panel) for the datasets as described. Additionally, the IQR, σ_3 and σ_4 results from Table 2.5 give valuable insights in the difference in shape of the normalised distribution functions.

CHAPTER 2

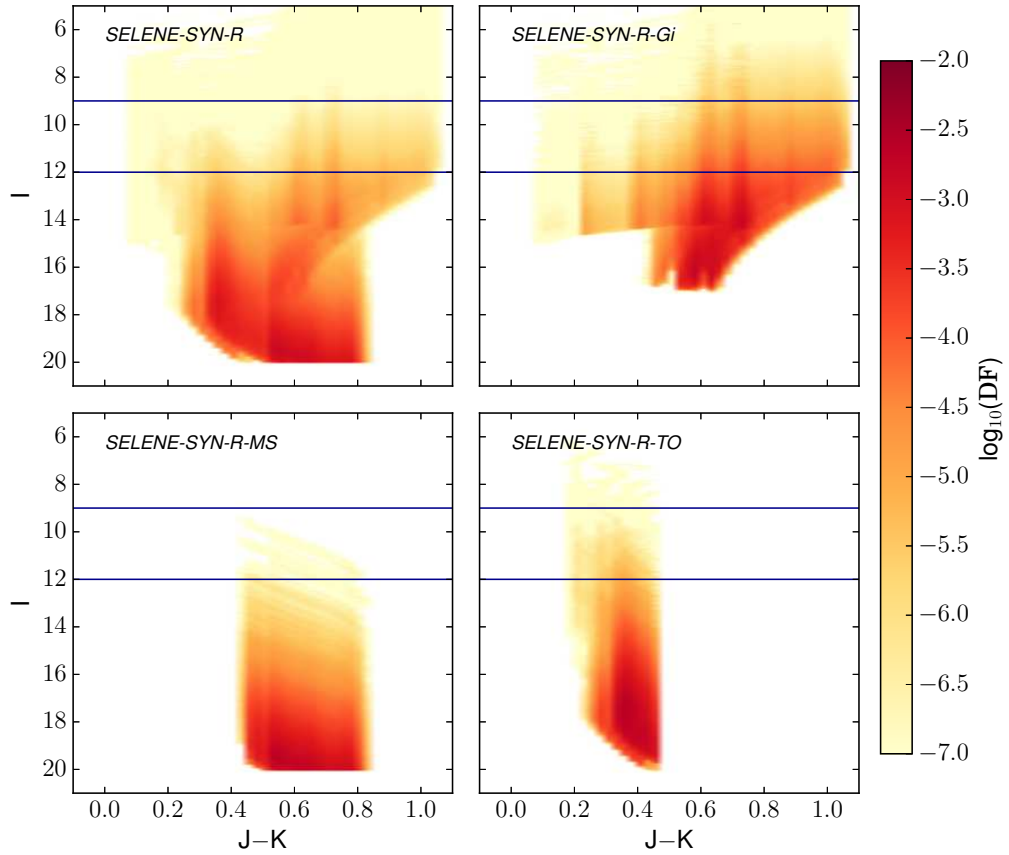


Figure 2.27: Synthetic CMD of I vs. $J-K$ in apparent magnitude space of the simulated ‘RAVE-like’ spatial region analogue *Selene-SYN-R*, and its subdatasets. The giants subdataset *Selene-SYN-R-Gi* is shown in the top right. The main sequence subset *Selene-SYN-R-MS* is shown in the bottom left. Finally the turnoff region *Selene-SYN-R-TO* is shown in the bottom right. The red heatmap represents the synthetic stellar populations from *Selene-SYN-R* which is derived from the simulated galaxy *Selene-CH* as shown in Figure 2.4. The blue rectangle highlights the J and $J-K$ region selection function boundary conditions of $9 < I < 12$. Also included is the application of surface gravity and effective temperature filters of; $0.5 \leq \log(g) \leq 5.0$ dex and $4000 \leq T_{\text{eff}} \leq 8000$ K as well as a $J-K$ colour cut for $J-Ks \geq 0.5$ when $|b| < 25^\circ$. Each data subset also includes additional selection function criteria for T_{eff} and $\log(g)$ as outlined in §2.8.4.

CHAPTER 2

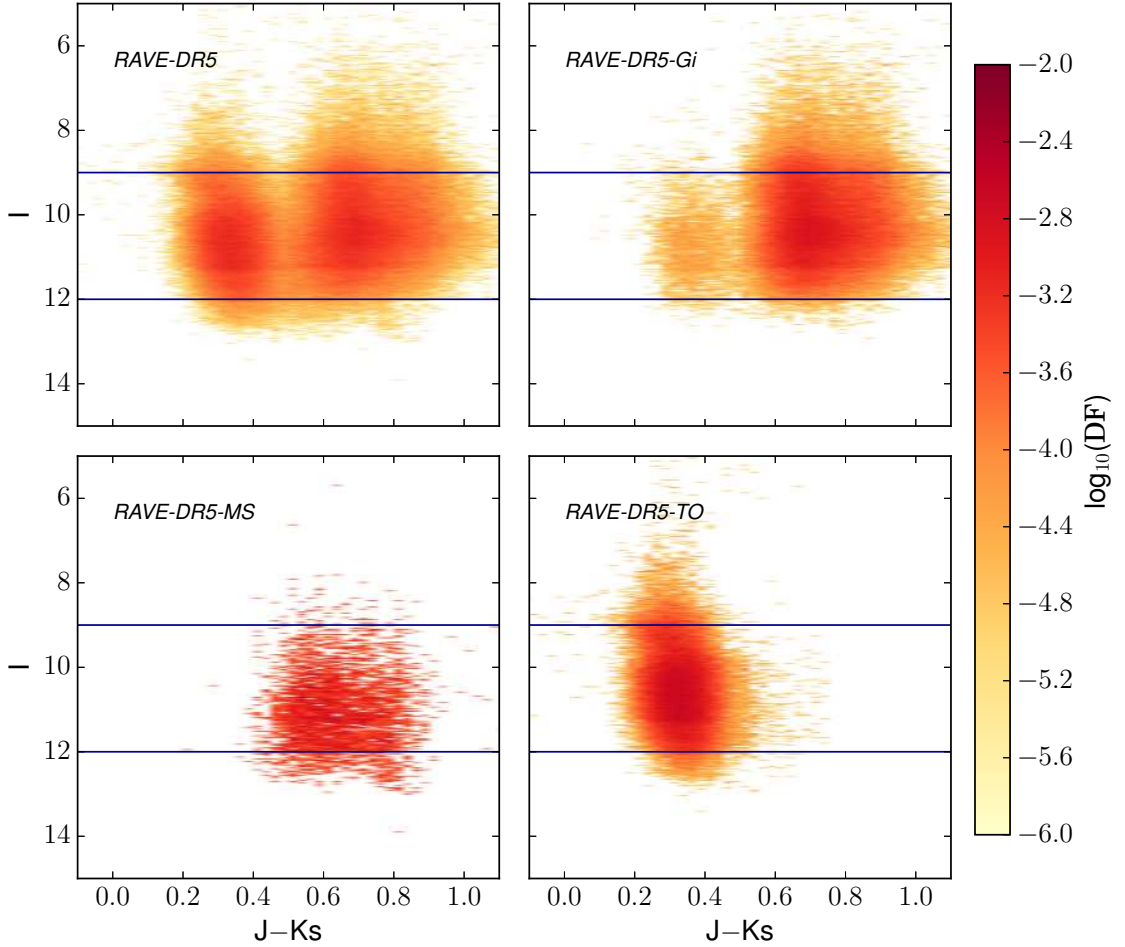


Figure 2.28: CMD of I vs. $J-K$ in apparent magnitude space of *RAVE-DR5* and the subdatasets. The giants subdataset *RAVE-DR5-Gi* is shown in the top right. The main sequence subset *RAVE-DR5-MS* is shown in the bottom left. Finally the turnoff region *RAVE-DR5-TO* is shown in the bottom right. The red heatmap represents the synthetic stellar populations from *RAVE-DR5-R* which is derived from the simulated galaxy *Selene-CH* as shown in Figure 2.4. The blue rectangle highlights the I and $J-K$ region selection function boundary conditions of $9 < I < 12$. Also included is the application of surface gravity and effective temperature filters of; $0.5 \leq \log(g) \leq 5.0$ dex and $4000 \leq T_{\text{eff}} \leq 8000$ K as well as a $J-K$ colour cut for $J-K_s \geq 0.5$ when $|b| < 25^\circ$. Each data subset also includes additional selection function criteria for T_{eff} and $\log(g)$ as outlined in §2.8.1.

CHAPTER 2

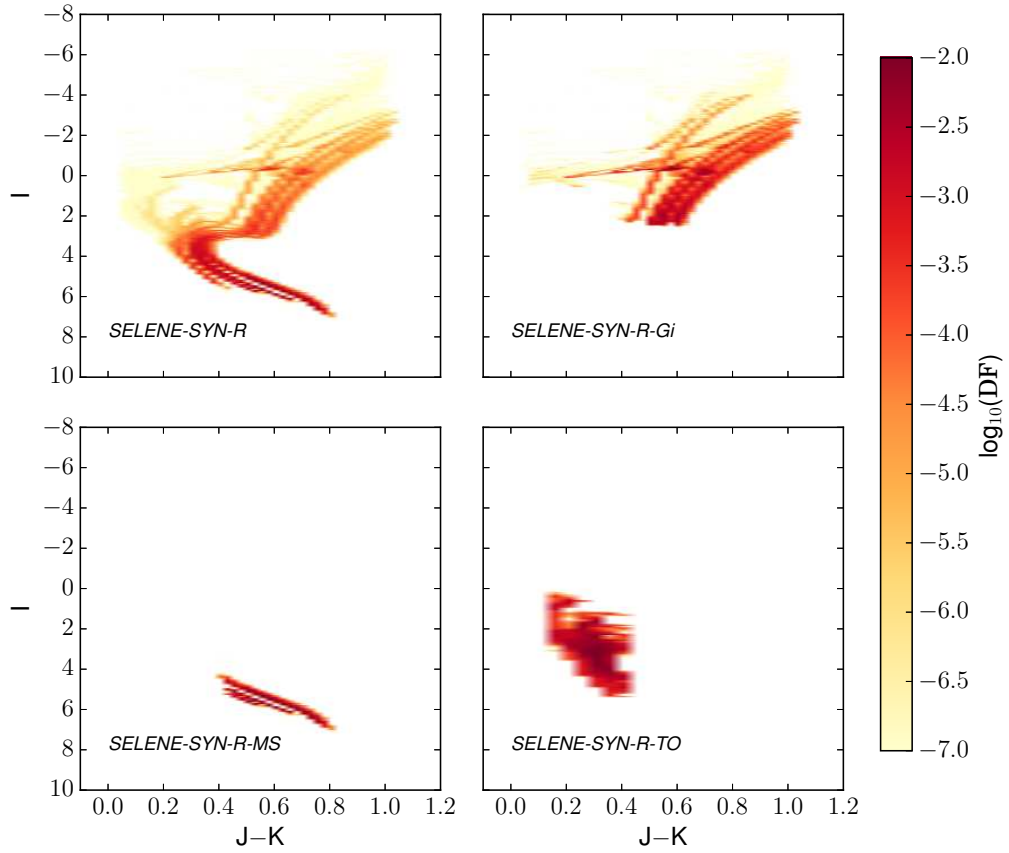


Figure 2.29: Synthetic CMD of I vs. $J-K$ in absolute magnitude space of the simulated ‘RAVE-like’ spatial region analogue *Selene-SYN-R*, and its subdatasets. The giants subdataset *Selene-SYN-R-Gi* is shown in the top right. The main sequence subset *Selene-SYN-R-MS* is shown in the bottom left. Finally the turnoff region *Selene-SYN-R-TO* is shown in the bottom right. The red heatmap represents the synthetic stellar populations from *Selene-SYN-R* which is derived from the simulated galaxy *Selene-CH* as shown in Figure 2.4. This does not include the photometric selection filter of $9 < I < 12$. This does include is the application of surface gravity and effective temperature filters of; $0.5 \leq \log(g) \leq 5.0$ dex and $4000 \leq T_{\text{eff}} \leq 8000$ K as well as a $J-K$ colour cut for $J-Ks \geq 0.5$ when $|b| < 25^\circ$. Each data subset also includes additional selection function criteria for T_{eff} and $\log(g)$ as outlined in §2.8.4.

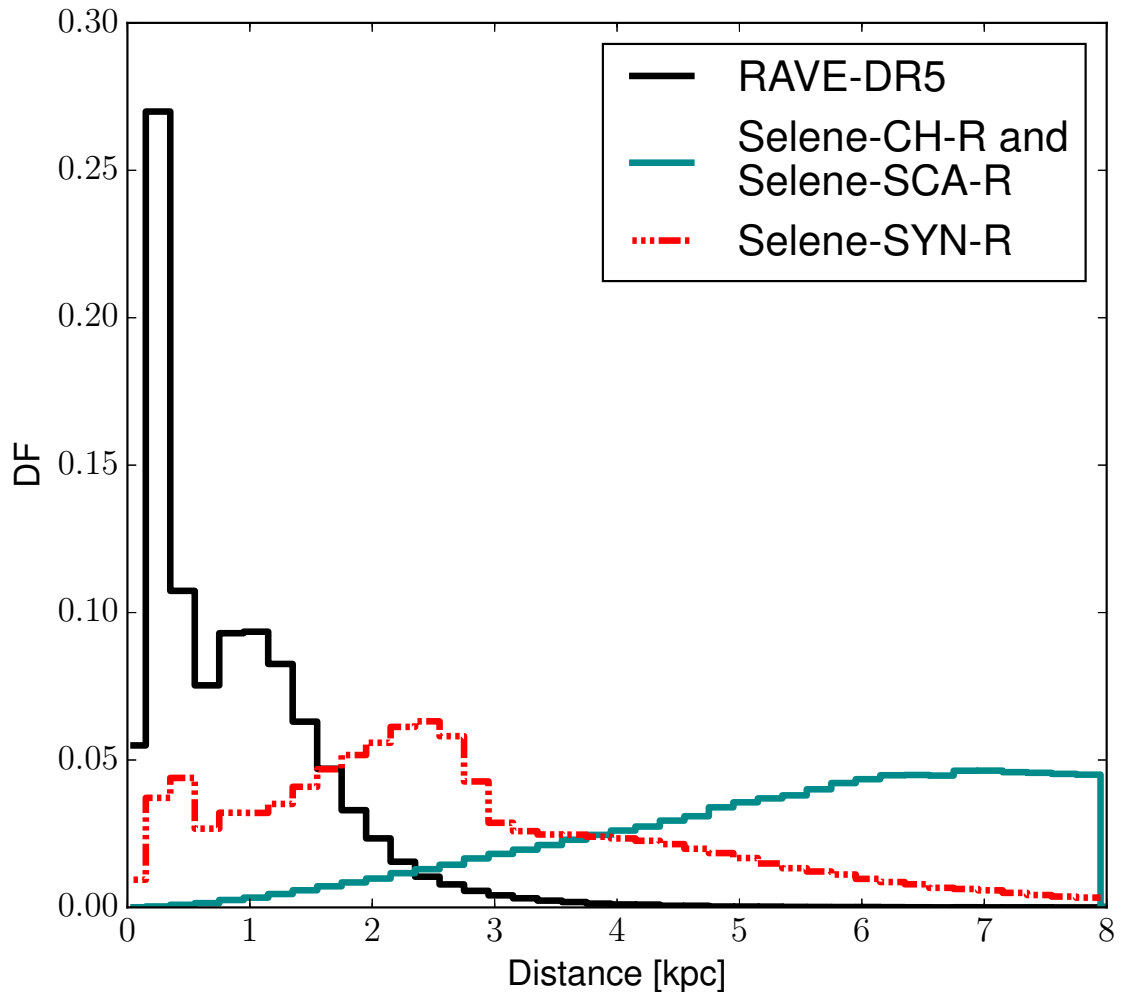


Figure 2.30: The normalised distance distribution function for *RAVE-DR5* (black) and *Selene-SYN-R* (red). The simulation datasets *Selene-CH-R* and *Selene-SCA-R* distance normalised distribution functions are the same and is shown by the cyan line (since distances are not stochastic scattered) *RAVE-DR5* stars within 1 kpc, or 70% of the stars in *RAVE-DR5*. The distance function is truncated with the application of SYNCMD since stars further away are fainter, and thus lie outside the I colour band selection. This accounts for the difference in CMD shapes and brightnesses between Figure 2.8.1. and Figure 2.27 since the overall CMDs for *RAVE-DR5* are brighter.

Name	N_{star}	N_{SSP}	[Fe/H]			[Mg/Fe]		
			IQR	σ_3	σ_4	IQR	σ_3	σ_4
<i>Selene-CH-R</i>	212470	-	0.441	-0.340	3.582	0.0678	-0.343	5.42
<i>Selene-SCA-R</i>	212470	-	0.503	-0.862	2.037	0.277	-0.00290	0.0225
<i>Selene-SYN-R</i>	202885	19031604	0.5	-0.611	0.293	0.200	0.0212	0.0632
<i>RAVE-DR5</i>	192274	-	0.4	-1.324	0.347	0.34	0.0377	0.217
<i>Selene-CH-R-Gi</i>	202095	16877920	0.20	-0.609	0.340	0.10	-0.00721	0.0734
<i>Selene-SCA-R-MS</i>	37	167110	0.150	-0.791	0.202	0.10	0.511	0.318
<i>Selene-SYN-R-TO</i>	582	1612888	0.150	-0.860	0.258	0.10	0.117	0.0693
<i>RAVE-DR5-Gi</i>	106785	-	0.390	-0.481	0.294	0.280	-0.351	0.293
<i>RAVE-DR5-MS</i>	3567	-	0.420	-0.583	0.181	0.390	-0.233	-0.0618
<i>RAVE-DR5-TO</i>	59099	-	0.350	-0.0401	0.253	0.32	-0.0538	0.219

Table 2.5: [Fe/H] and [Mg/Fe] distribution function characteristics for the *RAVE-DR5* and *Selene-CH-R* based datasets. and the observational dataset *RAVE-DR5* in dex. The interquartile range (IQR), skewness (σ_3), and kurtosis (σ_4) values for the normalised distribution functions of [Fe/H] and [Mg/Fe] as shown in Figure 2.18. Column 1 gives the name of the dataset. Column 2 shows N_{star} , the number of simulation star particles for the simulations based on *Selene-CH-R*, or the number of stars in the observational survey datasets based on *RAVE-DR5*. Column 3 shows the number of synthetic stellar particles produced from running SYNCMD on the same dataset. Columns 4, 5 and 6 are the IQR, σ_3 , and σ_4 of the [Fe/H] distribution. Columns 7, 8 and 9 are IQR, σ_3 , and σ_4 of the [Mg/Fe] distribution.

CHAPTER 2

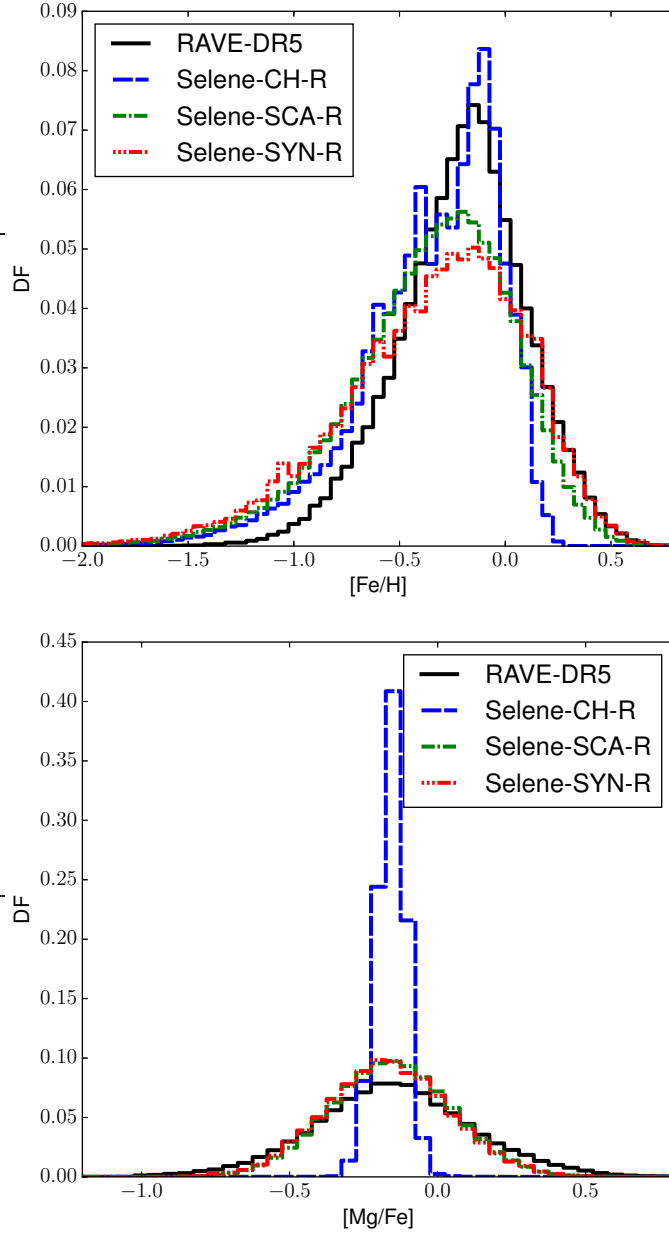


Figure 2.31: $[\text{Fe}/\text{H}]$ and $[\text{Mg}/\text{Fe}]$ normalised distribution functions in the ‘RAVE-like’ spatial regions of the mass-weighted *Selene-CH-R* and *Selene-SCA-R* datasets, the synthetic observation dataset *Selene-SYN-R* and the observation dataset *RAVE-DR5*. *Selene-CH*, *Selene-SCA-G* and *Selene-SYN-R* represented as blue dashed, green dot-dashed and red triple-dot-dashed lines respectively. The normalised distribution functions of the *RAVE-DR5* stars are shown in black. The bin widths for the data in $[\text{Fe}/\text{H}]$ and $[\text{Mg}/\text{Fe}]$ are 0.05 dex.

CHAPTER 2

The application of observationally motivated scattering in *Selene-SCA-R* produces an $[\text{Fe}/\text{H}]$ distribution function shape that is closer to a normal distribution as shown in Figure 2.31. This can be shown in Table 2.5 where σ_4 drops by ~ 1.5 . Since *Selene-CH-R* covers a larger spatial region in comparison to the Gaia-ESO equivalent *Selene-CH-G* we are able to capture a wider distribution of $[\text{Fe}/\text{H}]$ abundances. The additional application of SYNCMD in *Selene-SYN-R* further reduces the height of the peak of the distribution function, but also captures more of the high $[\text{Fe}/\text{H}]$ tail end of the distribution function, as evidenced with the reduced skewness. The overall application of observational motivated scattering shifts the shape of the distribution function away from *RAVE-DR5*.

However, the importance of observationally motivated analysis for the distribution function of $[\text{Mg}/\text{Fe}]$ becomes more apparent. Like in *Selene-CH-G*, *Selene-CH-R* has a narrow $[\text{Mg}/\text{Fe}]$ distribution which upon observationally motivated scatter in *Selene-SCA-R* produces an $[\text{Mg}/\text{Fe}]$ distribution function similar to *RAVE-DR5*. Additionally *Selene-SYN-R* does not show much of a greater deviation from *Selene-SCA-R* which is shown upon comparison of σ_3 and σ_4 in Table 2.5.

Similar to the comparison with the Gaia-ESO survey in §2.7.2, the differences between the width of the *Selene-CH-G* distributions and the observations don't indicate a failure of the simulation. On the contrary, a spatial cut alone as shown in *Selene-CH-R* returns an $[\text{Fe}/\text{H}]$ distribution not too dissimilar to *RAVE-DR5*. The application of observationally-motivated scattering over-smooths the $[\text{Fe}/\text{H}]$ distribution function in *Selene-SCA-R* does little to change the lower- $[\text{Fe}/\text{H}]$ tail, but does a good job for accounting for the lack of high $[\text{Fe}/\text{H}]$ stars in the upper-tail of the distribution, which *Selene-CH-R* fails to do. Either the stellar yields in our chemical evolution model are not generating enough metal-rich stars, or the mixing of gas prevents high $[\text{Fe}/\text{H}]$ stars from forming. The application of observationally motivated scattering increases the IQR for both the $[\text{Fe}/\text{H}]$ and $[\text{Mg}/\text{Fe}]$ distributions

CHAPTER 2

as expected. The effect is most pronounced for $[\text{Mg}/\text{Fe}]$ as it creates wings in the data on both sides of the distribution, which produces a much better fit to the *RAVE-DR5* abundance. Like in §2.7.2 the change is only noticeable for higher $[\text{Fe}/\text{H}]$ values, with the low-metallicity tail being largely unaffected.

Scattering the data leads to an increase in the IQR for both the $[\text{Fe}/\text{H}]$ and $[\text{Mg}/\text{Fe}]$ distributions. The IQR in *Selene-CH-R* already provides a good agreement with the observed IQR compared to the original values and the application of observationally motivated analysis diverges the IQR away from *RAVE-DR5*. The inverse is true for the $[\text{Mg}/\text{Fe}]$ distribution but the CEM produces a very narrow initial distribution initially in comparison to *RAVE-DR5* which is much broader than *GES-iDR4*. However the skewness and kurtosis properties are improved with both stages of the post-processing. Unlike the *GES-iDR4* comparison, both stages of the post-processing gives increasingly better better qualitative fit with each stage to the observational survey.

While the width of the observed DFs can be reproduced by application of observationally-motivated scattering, our simulations do not recover the detailed shape of the $[\text{Fe}/\text{H}]$. However, the observationally-motivated scattering provides us with a $[\text{Mg}/\text{Fe}]$ distribution function much more similar to observations. The shape of the simulated $[\text{Fe}/\text{H}]$ distribution in *Selene-CH-R* is promisingly close, but still defies similarity with an excess of stars below -0.5 and a deficiency of stars beyond 0.0. Additionally as discussed before, The mismatch between observed and simulated data for $[\text{Mg}/\text{Fe}]$ could also hint at the problem with the observations or with stellar yields in our chemical evolution model.

2.9.2 Comparison of Giants, Main Sequence and Turnoff Stars

We now consider the analysis of different regions of the colour magnitude diagram within *RAVE-DR5* and *Selene-CH-R*. This is achievable due to the greater abundance of stars in *RAVE-DR5* in comparison to e.g. *GES-iDR4* and sufficient quantity of stars cover different regions of the CMD for analysis to occur. This enables us to take full advantage of SYNCMD and study different stellar populations in simulations in a way that an observer would do which enables one to study whether chemical evolution models are capable of reproducing additional observational properties of the Milky Way.

The selection function criteria for Giants, Main Sequence and Turnoff regions of the CMD are described in §2.8.4. For each dataset, we obtain the following number of star particles: *Selene-CH-R* = 212470, *RAVE-DR5* = 192274, *RAVE-DR5-Gi* = 106785, *RAVE-DR5-MS* = 3567, *RAVE-DR5-TO* = 59099. For the synthetic data, the number of star population particles that pass the initial selection function criteria *Selene-SYN-R* = 202885, *Selene-SYN-R-GI* = 202095, *Selene-SYN-R-MS* = 37, *Selene-SYN-R-TO* = 582 Which returns 19031604 synthetic stars for *Selene-SYN-R*, 16877920 stars for *Selene-SYN-R-GI*, 167110 stars for *Selene-SYN-R-MS* and 1612888 stars for *Selene-SYN-R-TO*. This data is also in Table 2.5.

Figure 2.33 shows the distance normalised distribution function for the synthetic and rave stellar population datasets. The majority of stars that reside in the main sequence and the turnoff regions that are observed are within 1 kpc from the observer. Giants can be observed further away due to being brighter stars, but additionally there is a deficiency of giants within the first 0.5 kpc. This is because the giants that are nearer appear bright. The truncation further away could also be due to the selection function requirement $J-K_s \geq 0.5$ for $|b| \leq 25^\circ$ of which at further

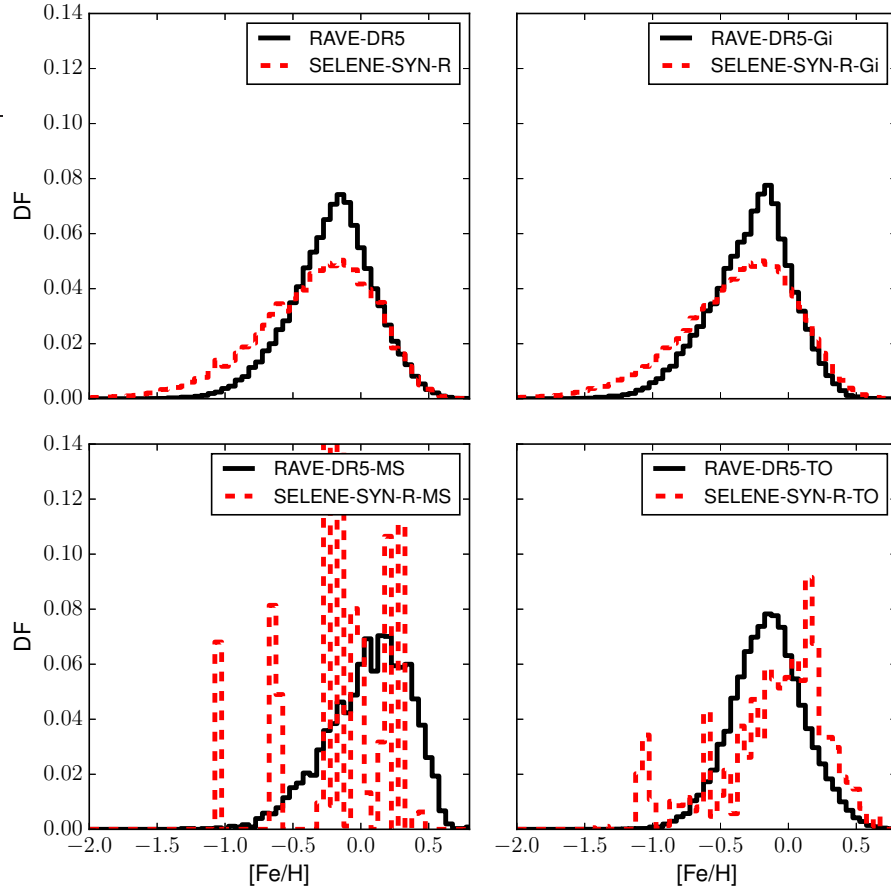


Figure 2.32: The $[\text{Fe}/\text{H}]$ normalised distribution function (DF) for the RAVE datasets. The observation dataset RAVE presented as a solid black line whereas the Synthetic star particle data generated from the application of SYNCMD to *Selene-CH-R* as a red dashed line. The top left plot shows the DF for the entire *RAVE-DR5* dataset and our model galaxy synthetic star particle data generated from *Selene-SYN-R*. The top right plot presents the giant stellar data subsets, *RAVE-DR5-Gi* and *Selene-SYN-R-Gi*. The bottom left presents the main sequence stellar data subsets, *RAVE-DR5-MS* and *Selene-SYN-R-MS*. The bottom right presents the turnoff region on the CMD for the stellar data subsets, *RAVE-DR5-TO* and *Selene-SYN-R-TO*. The bin width for all of the datasets is 0.05 dex.

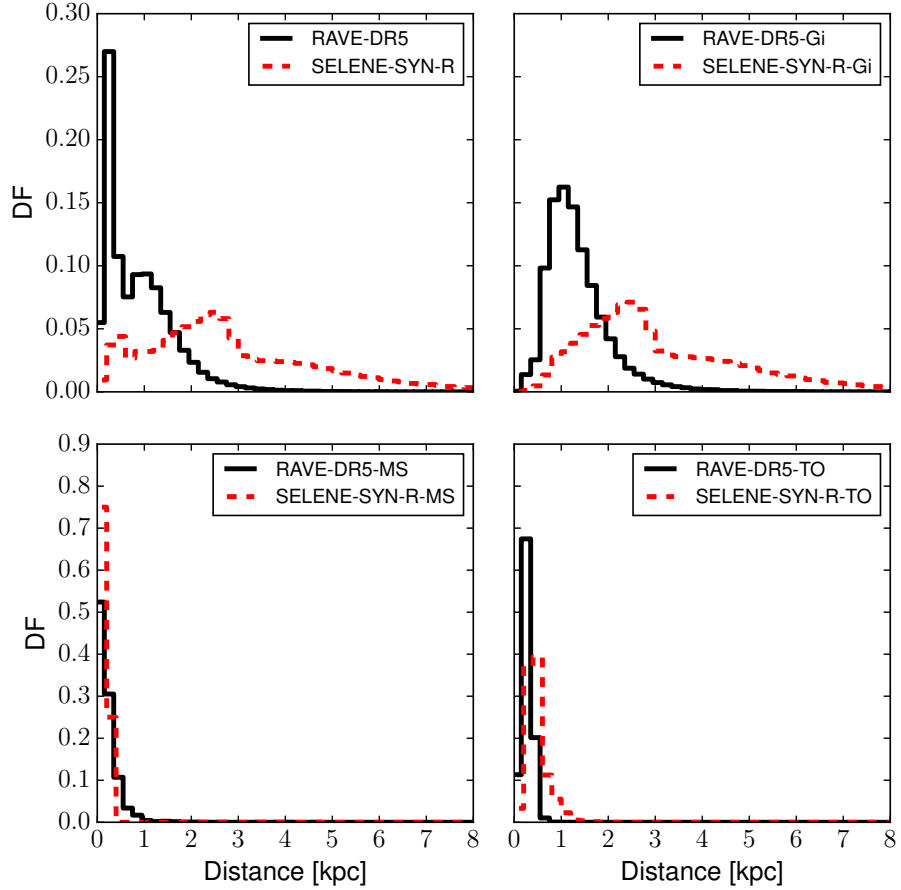


Figure 2.33: The distance normalised distribution function (DF) for the RAVE datasets. The observation dataset RAVE presented as a solid black line whereas the Synthetic star particle data generated from the application of SYNCMD to *Selene-CH-R* as a red dashed line. The top left plot shows the DF for the entire *RAVE-DR5* dataset and our model galaxy synthetic star particle data generated from *Selene-SYN-R*. The top right plot presents the giant stellar data subsets, *RAVE-DR5-Gi* and *Selene-SYN-R-Gi*. The bottom left presents the main sequence stellar data subsets, *RAVE-DR5-MS* and *Selene-SYN-R-MS*. The bottom right presents the turnoff region on the CMD for the stellar data subsets, *RAVE-DR5-TO* and *Selene-SYN-R-TO*. The bin width for all of the datasets is 0.05 dex.

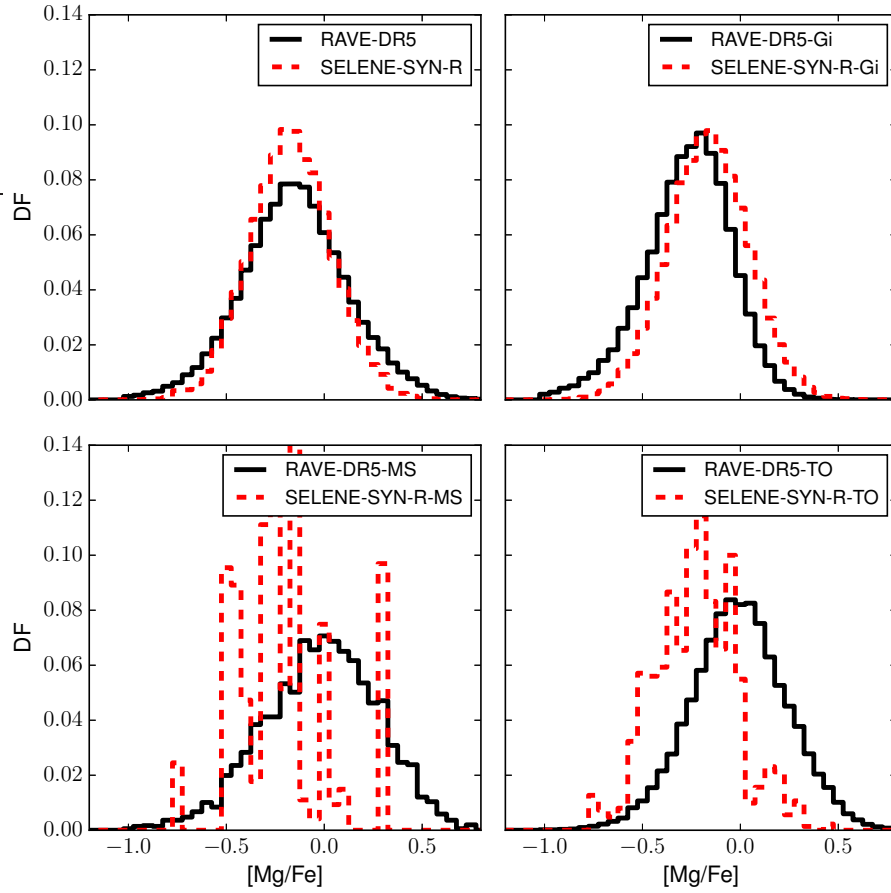


Figure 2.34: The $[\text{Mg}/\text{Fe}]$ normalised distribution function (DF) for the RAVE datasets. The observation dataset RAVE presented as a solid black line whereas the Synthetic star particle data generated from the application of SYNCMD to *Selene-CH-R* as a red dashed line. The top left plot shows the DF for the entire *RAVE-DR5* dataset and our model galaxy synthetic star particle data generated from *Selene-SYN-R*. The top right plot presents the giant stellar data subsets, *RAVE-DR5-Gi* and *Selene-SYN-R-Gi*. The bottom left presents the main sequence stellar data subsets, *RAVE-DR5-MS* and *Selene-SYN-R-MS*. The bottom right presents the turnoff region on the CMD for the stellar data subsets, *RAVE-DR5-TO* and *Selene-SYN-R-TO*. The bin width for all of the data is 0.05 dex. The noisy distribution functions for *Selene-SYN-R-Gi* and *Selene-SYN-R-TO* is due to small number statistics from the lack of composite stellar particles that meet the selection function criteria.

CHAPTER 2

distances, you start to cut out the midplane of the disc. In general we fit the TO and MS stars better than the giants in terms of distance distribution.

More importantly though is the number of stellar population particles that have a sample of synthetic stars which meet the selection function criteria. This becomes apparent when looking at the normalised $[\text{Fe}/\text{H}]$ distribution function in Figure 2.32. The $[\text{Fe}/\text{H}]$ distribution function is essentially derived from 37 individual stellar population particles in *Selene-SYN-R-MS*. This does not give a broad diversity of $[\text{Fe}/\text{H}]$ abundances, and thus the shape of the DF remains very peaked around the $[\text{Fe}/\text{H}]$ abundances of the 37 stellar population particles. Essentially there is a problem with small number statistics. This is similar for the $[\text{Mg}/\text{Fe}]$ distribution function as shown in Figure 2.34.

In both *Selene-SYN-R* and *RAVE-DR5*, the majority of stars are giant branch stars. This can be shown by both the relatively small change in abundance of stars in the datasets as well as the shape of the CMDs as shown in Figures 2.27 and 2.28 with comparing the overall datasets and their synthetic counterparts (i.e. between *Selene-SYN-R* and *Selene-SYN-R-Gi* and between *RAVE-DR5* and *RAVE-DR5-Gi*). Additionally the overall shape of the $[\text{Fe}/\text{H}]$ and $[\text{Mg}/\text{Fe}]$ distribution functions as shown in the skewness and kurtosis profiles are similar, although the reduction in the IQR implies a narrower distribution around the mean. The DF in both the simulation and observational cases narrows as shown by the reduction of the IQR. One must note the strong fit between the distribution function shapes of *RAVE-DR5-Gi* and *Selene-SYN-R-Gi* which almost overlap with each other.

The comparison between the the Main Sequence and Turnoff regions is harder to quantify. The difference in distance distribution functions as shown in Figure 2.30 with the stars in *Selene-SYN-R* being more dispersed and further away from

CHAPTER 2

the observer on average results in a small abundance of stellar population particles in main sequence and turnoff region stars in *Selene-SYN-R* (*Selene-SYN-R-MS* and *Selene-SYN-R-TO*) than in comparison with *RAVE-DR5* (*RAVE-DR5-MS* and *RAVE-DR5-TO*). This reduces the diversity of the possible [Fe/H] and [Mg/Fe] abundances that synthetic stars can take on, as demonstrated by the multiple peaks in *Selene-SYN-R-MS* in both [Fe/H] and [Mg/Fe]. However this is not as profound in *Selene-SYN-R-TO*. The spread of possible abundance values for [Fe/H] and [Mg/Fe] is more profound in the synthetic results than the observational results, but this could be an artefact of a lower abundance of stars in the dataset relative to their observational counterparts. The turnoff region is easier to quantify, and indeed there are similarities in the shape of the [Mg/Fe] distribution functions between the synthetic star particles and the observations. The peaks for *Selene-SYN-R-TO* are shifted towards higher [Fe/H] and lower [Mg/Fe] respectively.

2.10 Conclusions

We compare the results of a Milky Way-like galaxy simulation created using RAMSES-CH (Few et al. 2014) and the galaxy *Selene-CH-10* with the fourth data release of the Gaia-ESO survey considering the 1D normalised distribution functions of age, [Fe/H], and [Mg/Fe] as well as the age evolution of the latter two properties. The comparison is conducted in three stages:

1. The simulated stellar population particles are compared directly with the observed distributions.
2. Typical observational errors (from GES-iDR4) as the standard deviation of a Gaussian function used to stochastically scatter the simulated data to mimic observational uncertainty.
3. The simulated stellar population particles are stochastically scattered as above

CHAPTER 2

and are then split into individual stars based on stellar population models and only those accepted by the GES-iDR4 selection functions are retained for comparison.

We subsequently do a similar comparison with the fifth data release of the Rave Survey (RAVE-DR5).

Each of these stages mimics the effects found in observations as a way of placing the simulated data ‘in the observer frame’. The application of stochastic scattering based on the errors of an observational survey has the effect of smoothing out the age distribution function. The further application of the *GES-iDR4* selection function has the effect of removing young stars (< 1 Gyr). Additionally it increases the amount of stars with ages 2-5 Gyrs. Despite both these effects bringing the simulated age distribution closer to the observed one there is still a significant offset between the distributions. This is simply because of placing the simulated observer the same distance from the galactic centre as the sun but in a galaxy with a different assembly history. *Selene* is not constrained to be identical to the Milky Way and determining the location in the Selene which is the best analogue to the solar neighbourhood is somewhat open to interpretation. We stress that the focus of this study has been to demonstrate the effects of different observational motivated analysis techniques, rather than how to best fit the overall data. It is clear in Figure 2.17 that one should hope to replicate a solar neighbourhood age distribution that somewhat over produces older stars, such that once the post-processing described here is applied, concordance is achieved with observations. We note however that the age distribution is not as dramatically altered as the $[\text{Mg}/\text{Fe}]$ distribution or age- $[\text{Fe}/\text{H}]$ or $-\text{[Mg/Fe]}$ distributions by post-processing.

Our key finding is that chemical evolution models should attempt to replicate a dispersion in metallicity that is narrower than observations so that once the observationally motivated scattering has been applied, that the simulation follows the

CHAPTER 2

empirical distribution in age and abundance space. This is somewhat dependent on the abundance ratio in question as the post-processing has a far lesser effect on $[\text{Fe}/\text{H}]$ than on $[\text{Mg}/\text{Fe}]$ distributions because of the fundamental scale of the uncertainty relative to the dynamic range of the observations. This is because measurements of $[\text{Fe}/\text{H}]$ are more robust, in standard spectroscopic analysis one first determines T_{eff} , $\log(g)$ and metallicity ($[\text{Fe}/\text{H}]$, using iron as a proxy for metallicity) and then computes abundances of the other elements. So any error in $[\text{Fe}/\text{H}]$ propagates in the error in $[\text{Mg}/\text{Fe}]$. Fe is represented, by far, with the largest number of spectral lines - mostly those of neutral or singly-ionized iron - in the spectra FGK stars (typically, many thousands Smiljanic et al. 2014). So, the stellar iron abundance (metallicity) is usually much more accurate, because one can check the abundances derived from the optical, infrared, near-UV, low-excitation lines, or lines from neutral or singly-ionised iron. This richness of information is not available for any other element. For example, for Mg, we have only two spectral lines in the Gaia-ESO high-resolution spectra (Gilmore et al. 2012).

We find that our actual simulated $[\text{Fe}/\text{H}]$ is narrow and our $[\text{Mg}/\text{Fe}]$ distributions more so when compared with *GES-iDR4*. Although this is not the case when comparing the simulated $[\text{Fe}/\text{H}]$ with *RAVE-DR5*, but in the *RAVE-DR5* comparison, a broader distribution of stars is selected. However once we apply a random scattering to the data the simulated distribution is broadened sufficiently to match the observations despite offsets in the mean value. Scattering spreads the $[\text{Fe}/\text{H}]$ distribution towards larger values which creates a high-metallicity tail that is not present in the raw simulation data. The scattering produces wings on both sides of the $[\text{Mg}/\text{Fe}]$ distribution which greatly improves the fit to the observational data. In both examples the scattering according to observational uncertainties does exactly as one should expect, that is the IQR of the distributions are broadened significantly to be more in line with the observed distributions. The application of an

CHAPTER 2

observational selection function to the simulated data then acts to slightly reduce the IQR by culling a number of outliers in the distributions. Indeed it is possible for observers to reverse this process, i.e. from the observational survey and its errors deduce a narrower metal distribution function. This has been done in previous work, for example in the SEGUE large spectroscopic survey (Bovy et al. 2012).

Subsequent application of the scattering and observational selection function improves the fit of the skewness of the simulated $[\text{Fe}/\text{H}]$ distribution to the Gaia-ESO data and the RAVE data. This is simply because the scattering swamps the excessive negative skewness of the simulated distributions, driving the distributions toward a normal curve. The skewness is further reduced by the selection functions because they tend to remove the extreme outliers from the distribution tails. In this work the $[\text{Mg}/\text{Fe}]$ distribution is given a small positive skew by the selection functions, despite this is it unlikely that with conventional selection functions any kind of large skew will be introduced to the distribution functions. The kurtosis of both $[\text{Fe}/\text{H}]$ and $[\text{Mg}/\text{Fe}]$ distribution functions is reduced by both stages in our post-processing. Again, this is because the normal scattering function drives the distributions to conform more closely to a normal curve which has a kurtosis of zero (under the definition used in this work, sometimes called the *excess kurtosis*). The selection effects also tend to remove stars from the tails of the distribution (which are most likely to be the oldest and youngest stars) which further reduces the kurtosis.

For the $[\text{Fe}/\text{H}]$ distribution function and comparison with the Gaia-ESO data, these changes lead to an overall improvement in skewness and kurtosis for which the observed values are smaller than the simulated distribution (*Selene-CH*). However, due to the broader distribution of stellar populations captured from covering a larger spatial region populated with giants, the simulation on its own is able to capture a similar $[\text{Fe}/\text{H}]$ distribution function when compared with RAVE-DR5, with

CHAPTER 2

the exception of the metal rich region The IQR in all of the comparisons are actually worsened by the application of selection functions from its initially reasonable agreement. The simulated $[\text{Mg}/\text{Fe}]$ IQR is improved by the post-processing from its initially very narrow distribution however the other shape parameters are somewhat more challenging to reproduce due to the positive skew in the observations (which will be difficult to induce in the simulations given the large uncertainty on the observed values which must be applied to the simulated particles). The kurtosis in the unaltered simulation data are in reasonable agreement with the observations but is significantly reduced by post-processing. Nevertheless the overall similarity to the observed distribution is much improved by the wider spread of the data. It is worth mentioning that our model of the Milky Way is slightly lower than suggested mass of the Milky Way galaxy which results in a lower mean $[\text{Fe}/\text{H}]$ abundance due to the mass-metallicity relation (e.g. Tremonti et al. 2004).

In the *Selene-CH* model presented, we produce $[\text{Fe}/\text{H}]$ -age and $[\text{Mg}/\text{Fe}]$ -age distributions which are too narrow, but match the observations far better once scattering is applied. The $[\text{Fe}/\text{H}]$ -age distribution of *Selene* underestimates $[\text{Fe}/\text{H}]$ for stars older than 8 Gyr but one should be aware that the scattering of younger simulated stars to older ages compensates somewhat for this discrepancy. The effect of the application of observational selection functions is smaller but does decrease the number of stars in the lower age bins. Stochastic scattering has a larger effect on the $[\text{Mg}/\text{Fe}]$ -age distribution because of the very narrow simulated distribution and larger uncertainties relative to the spread of the distribution but, as with the $[\text{Fe}/\text{H}]$ -age distribution, the application of selection functions does little to improve upon the overall result.

The key conclusion of this work is that the most significant change in *observing* the simulations in a way that is consistent with the survey is introduced by scattering the data in accordance with the uncertainties. The broader distribution of the

CHAPTER 2

simulated data when such scattering is included bring the simulated distributions of $[\text{Fe}/\text{H}]$ and $[\text{Mg}/\text{Fe}]$ much closer to the observed distributions demonstrating a degree of success in the underlying models. The application of selection functions does influence the analysis but due to the broadness of the GES-iDR4 selections the effect is extremely small in comparison to the observationally motivated scattering from the inclusion of observational errors. Running SYNCMD on its own does little to broaden the $[\text{Fe}/\text{H}]$ distribution function, but instead reveals how different stellar populations contribute towards the metal distribution function. In general our model shows that there are an abundance of giants in comparison to other populations. This holds true when comparing with observational surveys with the comparison of *RAVE-DR5* in §2.8 which reveals the contribution of different stellar populations to the overall metal distribution. The easiest component to model are giant branch stars, since there is both an abundance of them in theory and observations. Modelling main sequence, subgiants and turnoff region stars is a challenge due to there being a relatively small abundance compared to the overall survey and theoretical population. Overall upon examining different stellar components as we do in comparison with RAVE, we find significant variations in the metallicity distribution functions with various, more exclusive, selection functions. For this reason one should certainly consider applying the star selection step of the post-processing to simulation data.

While the actual agreement found between the simulation and observations used in this work is not the main focus of our discussion, we find a reasonable degree of concordance overall and are particularly satisfied with the improvement of the post-processed (scatter and SYNCMD) $[\text{Mg}/\text{Fe}]$ distribution over the narrow, unaltered simulated distribution (*Selene-CH*) which might be considered a significant failing when directly compared. The Selene-CH simulation is quite capable of matching observational metallicity trends, however there are some discrepancies that remain

CHAPTER 2

visible even in the the scattered data, e.g. the dearth of old, high-[Mg/Fe] stars and the consequent differing skewness and kurtosis characteristics of the [Mg/Fe] distribution function. Further work is required to improve the relations between different stellar components of observational surveys with theory.

From the comparison with our observational surveys, especially the Gaia-ESO survey which has a strict set of selection functions, we find that mimicking selection effects is not very impactful on the analysis of simulations (as would be the case with a more strict set of selections). The introduction of observational uncertainties to the simulated data does however have a large impact on the interpretation of age-metallicity trends found in simulated data particularly in the case of [Mg/Fe] ratios where the uncertainties are quite large compared to the dynamic range of the data while having a smaller but still significant effect on the more precisely known [Fe/H] distribution. SYNCMD importance comes where one wishes to compare different stellar populations (of which the greatest success is with comparison of giants) between observational surveys and simulations. Of which is impossible to do without stellar population synthesis tools since simulations do not store colour, magnitude, surface gravity and other observational fields within themselves. When observational motivated scatter and SYNCMD is used in conjunction with eachother, one can successfully transform from the simulation plane to the observational plane, and undertake realistic comparisons with observational surveys (which are growing in importance and wealth of data today) and additionally compare the stellar population abundance and properties.

In general, observational errors can be systematic or random. Systematic errors include imperfect stellar models (physics of stellar atmospheres, that should, in ideal world, include convection, 3D geometry, NLTE (non-local thermodynamic equilibrium, winds, chromospheres e.t.c. - everything that is known from multi-wavelength

CHAPTER 2

diagnostics in cool stars) and systematic error component due to the data reduction (correlated errors). Random errors can be reduced by taking higher resolution, higher signal-to-noise spectra (i.e. observing with larger telescopes results in more light exposure and a stronger signal), observing with very narrow slit results in a higher resolving power. Finally, a careful data reduction pipeline, which takes care of various artefacts (like contamination by the earth's atmosphere, sky lines, continuum normalisation), is still an issue for many surveys. Additionally, various sources of uncertainty relevant to modelling the chemical evolution of different elements has been outlined in Côté et al. (2017).

To conclude, it is fundamentally important to reduce the uncertainty of the observed datasets in order to constrain the models of Galaxy formation. The typical observational errors of 0.1 dex in chemical abundances and $\sim 30\%$ in ages are too large to provide meaningful information on the substructure in the age-chemical abundance space, which is relevant to the interpretation of the evolution of the Galactic disc. Survey selection functions, like the colour-magnitude selection in the Gaia-ESO survey, may or may not have a sizeable effect on the results, however for the Gaia-ESO, this effect is extremely small compared to the effect of observational uncertainties. Surveys such as the *Gaia-ESO* survey and *RAVE* are really limited by the observational errors, but on the other hand, of all other surveys, *Gaia-ESO* provides the highest-resolution spectra in the wavelength range, which is best understood from the perspective of stellar atmosphere models. Additionally future surveys will improve upon the ones that are present today.

Chapter 3

Investigation of Halo Inflow and Disc Outflow via Disc-Driven Turbulence

Galaxy formation and evolution involves a complex interplay between a number of factors, perhaps most notably accretion and regulation of star formation. While feedback mechanisms are broadly viewed as regulating the state of the ISM, they also play a role in driving outflows. However, recent research on idealized small-scale simulations of the ISM has shown that turbulence is capable of driving outflows. Initial investigations, which we not conducted in a truly self-gravitating environment, suggest horizontal velocity dispersions above 35 km s^{-1} are needed to drive significant outflows. Scaling arguments derived from this research suggests that in evolved disc galaxies, such as the Milky Way, these outflows should be very weak or non-existent. However, given the number of assumptions in the initial investigations, we investigate disc models using the GIZMO gravitohydrodynamic solver. The key goal is to examine how far material can be driven above the equatorial regions of the disc in the absence of feedback. Moreover, rather than amplifying the effect we

CHAPTER 3

make assumptions that place a lower bound on outflow driving to establish a minimum impact. In this context we include a hot halo which adds a cooling flow on to the galaxy. Perhaps surprisingly, we find that weak outflows are still driven with some disc material rising more than 1.5 kpc above the disc plane, although none of this material reaches the halo escape velocity. The vertical velocity dispersion that results is also very close to that observed in other studies, even including those with feedback. This is an unexpected result and highlights the significant anisotropy in the velocity dispersion arising for turbulence. As would be expected, outflows from higher surface density regions are suppressed by the cooling flow from the halo.

3.1 Introduction

In the overview of galaxy formation, as discussed in §1.3, feedback from baryonic processes was noted as having the largest impact on the observable properties of galaxy formation (e.g. McKee & Ostriker 1977; Thacker & Couchman 2000; Okamoto et al. 2005; Kereš et al. 2009; Harikane et al. 2014; Faucher-Giguere 2016, amongst many others). Baryons play a role in both driving galaxy formation and regulating it. The continuous inflow of gas from the intergalactic medium (IGM) is required to sustain the observed star formation rates over cosmic time (e.g. Erb 2008; Prochaska & Wolfe 2009; Bauermeister et al. 2010). However, if efficient conversion of gas into stars is assumed, there is a discrepancy in the observed stellar masses vs. those predicated by theory (White & Frenk 1991; Navarro et al. 1995; Kereš et al. 2009).

Feedback manifests on large scales via gas outflows. Consequently, observations of gas inflows, representing supplying fuel, and outflows, representing some feedback processes, are critical to test and inform galaxy formation theories. Observations of gas inflows and outflows within galaxy evolution is critical to test and inform galaxy formation theories. Observational techniques for probing inflows and outflows of gas generally provide limited information about their nature due to limitations as

CHAPTER 3

a result of the lack of suitable high quality outflow tracers, of which are sometimes obscured by material in the host galaxy or (Martin 2005; Tacconi et al. 2006; Engel et al. 2010; Chisholm et al. 2015). Or have motions that are perpendicular to our line of sight, which leads to small projected velocity components. Outflow velocities are easiest to measure when observing galaxies face on (de Avillez & Breitschwerdt 2004a). Simulations of galaxy evolution and comparing with observations plays a central role in disentangling these processes (Faucher-Giguere 2016; Chisholm et al. 2015).

One of the main effects of stellar feedback in the galactic disc is to shape the evolution of the galaxy. Energetic events such as supernova, stellar winds and radiation pressure inject energy and momentum into the gas both in and around the galaxy. The result of this is the formation of multiphase gas structure in the interstellar medium (ISM) (McKee & Ostriker 1977; Governato et al. 2007; Hopkins et al. 2012b). Through heating the densest gas in the ISM, the rate of collapse of star forming gas decreases (e.g. Bigiel et al. 2008; Leroy et al. 2008), which delays the buildup of stellar mass (Katz et al. 1996; Springel & Hernquist 2003; Hopkins et al. 2012b). This additionally leads to characteristically different behaviour between the dark matter halo mass function and the baryonic mass function (Larson 1974; Kereš et al. 2009; Moster et al. 2010; Nelson et al. 2015). This additionally effects the mass-metallicity relationship due to the enrichment of metals within the galaxy (Tremonti et al. 2004) and also enriches the intergalactic medium (Tremonti et al. 2004; Erb et al. 2006; Finlator & Davé 2008; Andrews & Martini 2013). Figure 1.2 illustrates the difference between the halo mass function and baryonic (galaxy) mass function.

Galaxy outflows occur in rapidly star-forming galaxies over a range of masses and redshifts. They play a central role in the history of galaxy formation (e.g. Scannapieco et al. 2001; Bomans et al. 1997; Franx et al. 1997; Pettini et al. 2001; Frye et al.

CHAPTER 3

2002; Rupke et al. 2005; Veilleux et al. 2005; Weiner et al. 2009; Martin et al. 2013). Outflows are required to reconcile the number density and morphology of observed galaxies in comparison to cosmological models (e.g. Somerville & Primack 1999; Cole et al. 2000; Scannapieco et al. 2002; Benson et al. 2003) and they are essential to the enrichment of the IGM (Tytler et al. 1995; Songaila & Cowie 1996; Rauch et al. 1997; Simcoe et al. 2002; Pichon et al. 2003; Schaye et al. 2003; Adelberger et al. 2005, 2006; Ferrara et al. 2005; Steidel et al. 2010; Martin et al. 2010). Yet, despite the central importance of galaxy outflows, the processes that control their evolution are exceptionally difficult to constrain both theoretically and observationally. Theoretical predictions for inflows and outflows are furthermore complicated by the fact that inflows and outflows inevitably interact with each other (Kereš et al. 2009; van de Voort et al. 2011; Faucher-Giguère et al. 2015; Nelson et al. 2015). The difficulty of understanding the physics of outflows primarily stems from the complexities of the ISM and the variation in the spatial ranges from the feedback source (Mpc scales) to the scale it eventually manifests on (kpc scales). Heating of the ISM by UV photons, cosmic rays and supernova shocks operate in addition to radiative cooling processes resulting in multiphase, supersonic medium.

From an observational perspective, the most problematic issue is measuring and interpreting the evolution of wide range of multiphase material found in galaxy outflows. The temperatures of the multiphase material ranges include 10^7 – 10^8 K plasma observed in X-rays (Martin 1999; Strickland & Heckman 2007, 2009), 10^4 K material observed at optical and near-UV wavelengths (Pettini et al. 2001; Tremonti et al. 2004; Martin et al. 2012; Soto et al. 2012) and 10 – 10^3 K molecular gas observed at radio wavelengths (Walter et al. 2002; Sturm et al. 2011; Bolatto et al. 2013). The X-ray emitting medium is the easiest phase to interpret due to being consistently energetic events from supernova explosions, of which can be modelled trivially (Heckman et al. 1990). Additionally, the temperature, surface brightness,

CHAPTER 3

ambient material and other properties of the X-ray emitting medium is consistent over a wide variety of galaxies (Grimes et al. 2005) that is shock heated out to large distances (e.g. Suchkov et al. 1994; Strickland & Stevens 2000). However X-ray emitting mediums are the most difficult to observe, for example a 10^8 K medium is so hot that it is only detectable in deep Chandra and XMM imaging in very nearby galaxies (Strickland & Heckman 2007; Wang et al. 2014) and best measured in M82. In these nearby galaxies, X-ray emitting material can be nicely fit by a simple analytic model (Chevalier & Clegg 1985; Heckman et al. 1990). Below 10^7 K, the X-ray emitting medium is detectable in a larger number of galaxies since the X-ray luminosity is proportional to $T^{1/2}\rho^2$, and thus the local stellar density dominates. The X-ray emitting medium is shock heated by the wind fluid as it flows out to large distances (Suchkov et al. 1994; Strickland & Stevens 2000). Given the high temperatures of the X-ray emitting plasma, it will always escape the gravitational potential of the host galaxy.

Colder phases of gas can be observed from the ground and studied at many redshifts, but they are poorly understood theoretically. Unlike the X-ray emitting medium, low-ionization state material is observed to have complex velocity profiles (Westmoquette et al. 2009b,a) that are strongly correlated with the overall host luminosity (Martin 2005), circular velocity (Martin et al. 2012), star formation rate per unit area (Heckman 2014), and the star formation rate per stellar mass (Chen et al. 2010). However because it is often visible only through absorption lines and resonant Ly α emission (Pettini et al. 2001), the total mass in this phase is poorly constrained. It could either be the primary avenue for baryon and metal ejection, or make up only a small fraction of the ejected material. Equally poorly understood is the final fate of this material, as its position along the line of sight is unknown and it is often moving at velocities that are similar to the escape velocity of the host. In fact, even the presence of this medium is surprising as simple theoretical estimates

CHAPTER 3

predict that it should be disrupted by interactions with the hot wind fluid well before it is accelerated to significant velocities (e.g. Scannapieco 2013; Scannapieco & Brüggén 2015).

In galaxy formation models, one of the key problems is the ability to model the ISM at resolution scales sufficient enough to resolve physical phenomena in the interstellar medium. This is because of the range of physical scales that is involved with modelling the ISM in galaxy formation models. Very short cooling times and physical scales that resolve to the order ~ 1 pc are required to model multiphase gas distribution and the expansion of supernova remnants directly (e.g. de Avillez & Breitschwerdt 2004b; Hill et al. 2012; Hennebelle & Iffrig 2014; Walch et al. 2015; Kim & Ostriker 2015; Girichidis et al. 2016). Neither the correct momentum injected into the ISM by supernova, or the mass of hot gas can be captured unless the Sedov and shell formation stages are sufficiently well resolved (Kim & Ostriker 2015). Additionally, simulations of galaxy evolution often model the galaxy on the order of ~ 1 kpc resolution scales. This means that it is computational challenging to directly model supernova in the galactic ISM even in modern isolated galaxy simulations (e.g. Scannapieco 2013; Scannapieco & Brüggén 2015; Hopkins et al. 2014; Martizzi et al. 2015; Williamson et al. 2014).

Arguably the most uncertain issue is the coupling of energy return from type II supernovae and stellar winds to the surrounding ISM. This is because the highly efficient cooling within the ISM makes it impossible to model energy input from supernovae in the ISM on large scales. As a result, studies have been forced to adopt a number of unsatisfactory approximations, including: temporarily lowering the densities of heated particles or delaying their cooling (e.g. Gerritsen & Icke 1997; Mori et al. 1997; Thacker & Couchman 2000; Stinson et al. 2006), imposing a minimum temperature floor (Suchkov et al. 1994; Tenorio-Tagle & Muñoz-Tuñón 1998; Strickland & Stevens 2000; Fujita et al. 2004), using an empirical heating function

CHAPTER 3

to mitigate cooling (Mac Low et al. 1989; Mac Low & Ferrara 1999), implementing exaggerated momentum kicks (Navarro & White 1993; Mihos & Hernquist 1994a; Scannapieco et al. 2001) and temporarily decoupling particles from their neighbours (Springel & Hernquist 2003; Scannapieco et al. 2006b,a; Dalla Vecchia & Schaye 2008). Indeed, the most resolved cosmological zoom-in simulations (Gnedin et al. 2009; Agertz et al. 2009b; Ceverino et al. 2010; Governato et al. 2010; Shen et al. 2012) are faced with excessive cooling since supernova often occur within giant molecular clouds, which thus must be pre-conditioned by ionization fronts (e.g. Matzner 2002) and radiation pressure (e.g. Murray et al. 2010) to be modelled accurately. Attempts have been made to couple stars with the ISM in greater detail (e.g. Hopkins et al. 2011, 2012a,b), but these rely strongly on tuning against observations to achieve good results. Additionally, it is not yet possible to model galactic winds in large volume cosmological simulations due to the resolution scales required and that it is not computationally feasible to model galaxy evolution in a volume sufficiently large enough to encompass large scale wind evolution. So in these instances, galactic winds are tuned in simulations to match observational properties such as the galaxy stellar mass function (Davé et al. 2011; Vogelsberger et al. 2014; Schaye et al. 2015).

Furthermore, the uncertainties of modelling cold material in a hot medium is somewhat surprising given that simulations of cold clouds interacting with a hot high-velocity medium have been frequently carried out. Our understanding of the physics here is limited to distant observations and computational modelling since it is not possible to study these effects in a laboratory due to the physical nature of the medium. Additionally codes exhibit different asymptotic behaviours depending on the numerical method used since there are multiple different means of shock capturing. Neither of these shock capturing methods produce consistent results.

CHAPTER 3

Groups have carried out two- and three-dimensional simulations which either neglect radiative cooling (Nittmann et al. 1982; Klein et al. 1994), including radiative cooling (Woodward 1976; Mellema et al. 2002; Fragile et al. 2005; Melioli et al. 2005; Cooper et al. 2009; Marinacci et al. 2010, 2011), including both radiative cooling and thermal conduction (Marcolini et al. 2005; Orlando et al. 2005, 2006, 2008; Recchi & Hensler 2007), including the impact of magnetic fields (Mac Low & Zahnle 1994; Gregori et al. 1999, 2000; Fragile et al. 2005; Orlando et al. 2008; Shin et al. 2008), and including non-equilibrium chemistry effects (Kwak et al. 2011; Henley & Shelton 2012). Yet despite the usefulness of these studies in elucidating the physics of cold clouds in a hot medium, none of them has spanned the range of parameters and timescales necessary to study galaxy outflows. Studies in two-dimensional simulations are capable of resolving the spatial resolution that is necessary, but at a compromise of geometry since we're unable to resolve similar spatial resolutions in 3 dimensional space.

The relation to observations is becoming more complicated. Recent claims have been made that outflows could rather be driven by physical mechanisms other than primarily by supernova. One of the key physical mechanisms is the impact of radiation pressure on dust, (Thompson et al. 2005; Murray et al. 2011; Hopkins et al. 2011, 2012a) or by cosmic rays which generate non-thermal pressure (e.g. Socrates et al. 2008; Samui et al. 2010; Uhlig et al. 2012; Booth et al. 2013; Hanasz et al. 2013; Salem & Bryan 2014). Additionally, the Reynolds number (the ratio of inertial forces to viscous forces) in the ISM is typically high at the value of $Re \approx 10^5$ or greater. In addition to being computationally challenging to model, this implies that a complete understanding of massive outflows cannot be obtained by ignoring small-scale turbulences in the disc. Numerical sub-grid models for unresolved turbulent velocities and length scales show the possibility to produce outflows of multiphase material from simultaneous turbulent heating and radiative cooling in the disc (Scannapieco

CHAPTER 3

& Brüggen 2010) and thus galaxy scale outflows can be produced from the turbulent disc.

Recent studies suggest that the physics of gas outflows may be related to the global properties of the galaxies that host them (Bordoloi et al. 2014; Sur et al. 2016). In general although galaxy scale outflows have been observed in a wide range of galaxy masses, the range of the surface densities of these galaxies is small. Thus the impact of the surface density of galaxies have not been studied in great detail. Strong and abundant outflows in observational surveys seem to correlate with large star formation densities per unit area (Mulchaey & Stocke 2002; Heckman 2003) where the outflows have high velocity dispersions (Swinbank et al. 2011; Genzel et al. 2011). Galaxies with a star formation rate density per unit area below the critical value $\dot{\Sigma}_*^{\text{cr}} \approx 0.1 \text{ M}_\odot \text{ yr}^{-1} \text{ kpc}^{-2}$ have smaller and less frequent outflows (Chen et al. 2010). Additionally the velocity dispersion of these strong outflows have a value of $\sigma_v^{\text{1D}} \approx 50 - 100 \text{ km s}^{-1}$. Supernova explosions have only been shown to drive velocities to $\sigma_v^{\text{1D}} \approx 10 - 20 \text{ km s}^{-1}$ (Dib et al. 2006; Joung & Mac Low 2006; Kim et al. 2011, 2013; Shetty & Ostriker 2012; Hennebelle & Iffrig 2014; Gatto et al. 2015; Martizzi et al. 2015), therefore supernova explosions cannot account for the high velocity outflows in galactic discs.

Recent work (e.g. Sur et al. 2016) suggests that the self-gravitational motions in high surface density discs could be the cause of high velocity outflows i.e. related to the internal dynamics of the galaxy. The Toomre stability criterion as stated in Toomre (1964) relates the total disc surface density Σ , the epicyclic frequency κ , and the sound speed c_s in infinitesimally thin discs. These thin discs are marginally unstable to axisymmetric modes as,

$$Q \equiv \kappa c_s / \pi G \Sigma, \quad (3.1)$$

where G is the gravitational constant and Q is the Toomre stability criterion. Thick

CHAPTER 3

disc effects decrease the Q value whereas non-axisymmetric instabilities, magnetic fields, and interaction with a stellar disc increases it (e.g. Romeo 1992; Kim & Ostriker 2001; Kim et al. 2002; Kim & Ostriker 2007; Romeo & Falstad 2013). Turbulent velocities are related to the thermal sound speed of the warm gas medium in the ISM. Additionally these turbulent velocities are greater than the thermal sound speed of the cold medium. Because of this, any calculation of Q should depend on the total velocity dispersion i.e. the sum of the thermal and scale-dependent turbulent velocity dispersion (Romeo et al. 2010; Hoffmann & Romeo 2012).

Based upon these initial investigations, we can use new computational methods made possible by the GIZMO code (Hopkins 2015) to investigate turbulent driven outflows in full galactic disc models. In Sur et al. (2016), turbulent driven outflows were studied from the perspective of examining the physical dependence on various parameters such as driving velocity dispersion, local density and outflow rates without an additional inflow. Our investigation specifically examines this behaviour in an evolved Milky Way analogue, that does include an accreting halo reservoir, so as to put a lower limit on the anticipated behaviour. At the same time the variation in gas density and local velocity dispersion that naturally happens across a galactic disc also allows us to examine variation in the derived outflow rates for different parameters. Additionally, our model includes the treatment of self-gravity. One particularly challenging issue in reproducing giant molecular cloud populations is that much of the key physics is missing in simplified models, such as we simulate here. Therefore, erring on the side of lower limits, we have taken the unusual step of allowing some of the disc material to collapse beyond its Jeans limit. The result is less interactions again, driving down the overall outflow rates. We also include two separate temperature floors to investigate differences in behaviour.

In this work, we are going to focus on galactic disc dynamics of Milky Way-like

CHAPTER 3

galaxies and specifically on galactic outflows caused by galactic disc self-turbulence and the formation of giant molecular clouds (GMCs) in the absence of feedback, to establish the contribution of turbulent driven outflows. This is achieved using the hydrodynamical simulation code GIZMO (Hopkins 2015) of which we describe the code and briefly discuss the physics of it in §3.2. We then discuss derived physical formula relating to the outflow of gas in §3.3. We describe the simulation we run, including it's initial conditions, implementation and GMC identification in §3.4. We describe the morphological evolution of the galaxy model and giant molecular clouds in §3.5. Finally we discuss the physics of gas outflows for our galaxy model in §3.5.4 and state our conclusions in §3.6.

The work presented here is motivated by the work presented in Sur et al. (2016). The main difference to earlier work is we can establish behaviour at different surface densities, but the underlying turbulence is set by the physics of the local gas instability. Whereas the simulation setup in Sur et al. (2016) was designed with the variation of physical parameters in mind, such as the velocity dispersion of the gas. Although their goal was to study the parameter space in detail, the motivation here is to apply their findings to a galaxy simulation. We have additionally included gas infall from a hot halo, arguably a cooling flow, which is not included in the earlier work. This is a somewhat important point. The lack of feedback in our simulations should not be any cause for concern. For example Shetty & Ostriker (2008) showed that properties of large clouds are not sensitive to baryonic feedback processes at all.

3.2 Simulation Methodology with Gizmo

3.2.1 Hydrodynamical Simulations Schemes

The majority of galaxy formation simulation codes are based on Lagrangian (follows the fluid) SPH schemes (e.g. Gingold & Monaghan 1977; Lucy 1977; Monaghan 1992; Katz et al. 1996; Springel 2010b). In SPH the flow of a gaseous fluid is represented with fluid elements, which are called particles. Gas is followed throughout the simulation with the conserved quantities discretized into particles (like an N-body code), and a kernel function is used to “smooth” their volumetric distribution to determine the equations of motion. SPH is numerically stable (perhaps overly so) and the Lagrangian methodology allows for a locally adaptive resolution, includes truncation errors which are independent of the fluid velocity, couples trivially to N-body gravity schemes, exactly solves the particle continuity equation and the equations of motion can be exactly derived from the particle Lagrangian (Springel & Hernquist 2002). Overall, over the last few decades, the two dominant and most popular hydrodynamic schemes were smooth particle hydrodynamics (SPH) and grid - often Adaptive Mesh Refinement (AMR) - based schemes. We have already discussed the theory of adaptive mesh schemes in detail in §2.2.

Recently, however, new techniques have begun to emerge, which focus on using an unstructured mesh, such as ‘moving-mesh’ technique. This is distinct from the AMR technique which typically has a static stationary mesh which subdivides into sub-cells depending on resolution criteria. ‘Moving-mesh’ techniques use a method which hybridises Lagrangian and Eulerian schemes. It evolves using a finite-volume Godunov method (Godunov 1959), but partitions the volume into non-regular unstructured cells using for example, a Voronoi tessellation. This allows the cells to move and deform continuously depending on the physical flow of the fluid. The

CHAPTER 3

moving-mesh approach retains the ability of Eulerian codes to resolve shocks by employing a Riemann solver across each boundary between cells. Moving-mesh schemes are Galilean invariant, less noisy and less diffusive than standard SPH codes. This technique is used in AREPO (Springel 2010a).

Moving-mesh techniques retain the advantages of the SPH and AMR methods. Like SPH it can be Lagrangian and adapt resolution continuously, features velocity-independent truncation errors, avoids preferred directions and couples well with gravity. Additionally like AMR, it is capable of treating shocks, fluid instabilities and shear flows with high accuracy and eliminates low-order errors, artificial diffusion terms and noise. AREPO has been applied to both problems of cosmic structure formation (Vogelsberger et al. 2012) as well as isolated galaxy simulations (Pakmor & Springel 2013; Smith et al. 2014).

Another method that hybridises the SPH and grid schemes is the ‘meshless’ scheme. The particle ensemble is topologically similar to moving-mesh method but differentiates between it due to lacking a sharply defined boundary between the resolution element domains. Lanson & Vila (2008a,b) implemented a new, mesh-free finite-volume method which is both consistent and fully conservative. This method shares similarities with the moving-mesh method above, but the discrete operators traditionally found in an SPH-like method are rederived from a consistent mathematical basis. An implementation of this method in an astrophysical context was presented in Gaburov & Nitadori (2011) which produced encouraging results for hydrodynamic and magnetodynamic test problems.

An implementation of the meshless concept was presented in Hopkins (2015). The meshless scheme is based on a kernel discretization of the volume which is coupled to a high-order matrix gradient. For the volume overlap between cells a Riemann solver acts to resolve the physics in this regime. GIZMO has a number of solvers built into the code, the two quasi-Lagrangian meshless schemes are the

CHAPTER 3

meshless finite volume (MFV) and meshless finite mass (MFM). These solvers ensure the conservation of either mass or volume with cells. The MFM method allows for the advantages of mass tracking and being fully adaptive without re-meshing. These methods appear to differ only slightly within the test problems as demonstrated in Hopkins (2015). In either of these contexts each fluid cell element can be analysed as though it is a "particle", although strictly speaking it actually represents a meshless node.

GIZMO is capable of exact mass, energy and momentum conservation. Additionally, GIZMO is much better at conserving angular momentum in comparison to the other methods since it, for example, does not require 'artificial diffusion' terms which is a flaw of SPH schemes (Shen et al. 2010). Since SPH schemes do not traditionally include any treatment of interparticle mixing, physical properties of two different gas particles do not diffuse amongst each other unless artificially driven to do so. In practice, meshless codes are much closer to SPH codes than moving-mesh techniques which similarly employ a Riemann solver across the interfaces between resolution elements which enables for shock capturing. Although like the moving mesh methods, these advanced meshless methods are still comparatively in their infancy, and are thus not as well tested in comparison to SPH and AMR codes. We illustrate the differences in the SPH, moving Mesh and Meshless schemes in Figure 3.1.

Meshless methods avoid many known problems with SPH methods, and thus give more accurate results in the isolated tests and eliminate the need for artificial dissipation terms. Meshless methods capture sharper shocks and discontinuities and reduce the 'noise', and thus the method can be reliably extended to smaller Mach numbers. There is no need for artificial diffusion terms to manage fluid instabilities, mixing and there is no zeroth or first order errors unlike in SPH. These new methods are able to obtain much greater accuracy with ~ 32 neighbours than in SPH with

CHAPTER 3

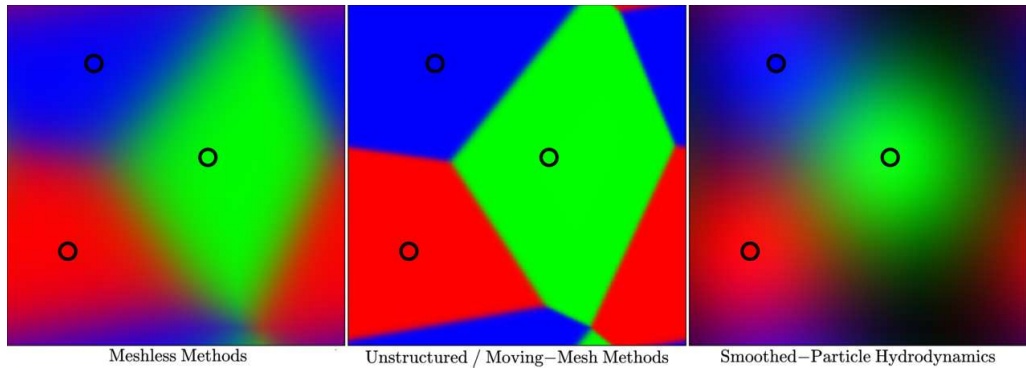


Figure 3.1: An illustration of the key differences between the hydrodynamical methods discussed here. Black circles represent the particles or ‘grid points’ with a location \mathbf{x}_i . The coloured regions represent the fraction of the volume occupied by each particle. The meshless methods volume partition is given by the weighted kernel at each point and is a Voronoi tessellation with smoothed boundaries and thus entire volume is represented. The unstructured/moving-mesh partition are a strict step function at the faces given by the tessellation, this is the limit of the meshless method for an infinitely sharply-peaked kernel function. The contribution to volume integrals behaves as the kernel in SPH, centred on each particle location and the whole volume is considered only when the kernel size is infinitely large compared to the inter-particle spacing This figure is taken from Hopkins (2015) which discusses in detail the different methodologies and is reproduced here with permission.

~ 400 neighbours without performance degeneration.

In comparison to grid methods, meshless methods avoid the disadvantages of stationary grids (preferred velocity direction, convection, angular momentum conservation). Moving with the flow minimises advection errors and thus leads to sharper and more accurate capturing of contact discontinuities and shocks and reduces over-mixing. Most importantly, errors are independent of velocity, thus can follow the motion of a fluid with an arbitrary ‘boost’ which is important for multiphase fluids where advection errors in grid methods can rapidly diffuse away self-gravitating

CHAPTER 3

clouds, or structures moving relative to the grid. Hopkins (2015) and Springel (2010a) show that this is important for fluid mixing instabilities as the velocity dependent errors in grid methods artificially slows down and eventually wipes out the growth of Kelvin-Helmholtz and Rayleigh-Taylor instabilities. If the fluid is moving at sufficient bulk velocities at finite resolution; effectively, the simulation resolution is downgraded. Since meshless methods have no grid alignment effect, the carbuncle instability does not appear and thus discs are not forcibly torqued into alignment with a coordinate axis, and shocks do not preferentially propagate along the grid.

There are contexts where grid codes are particularly useful, especially in the context of chemical evolution. Adaptive mesh methods can be given any particular refinement scheme and can adapt in regions where high resolution is desired in low-density regions for example in a void (Ricciardelli et al. 2013) or around the reverse shock inside an explosion (Zhang & MacFadyen 2006). This is because Lagrangian methods do not follow physics through lower density regions as well in comparison to Eulerian methods. The differences between meshless methods and moving-mesh methods are more subtle, and more work is needed to be done to determine the real advantages and disadvantages. Moving-mesh methods with the exact volume partition and simple faces reduce ‘partition’ and ‘mesh deformation’ noise from irregular particle motion in strong shear flows. Thus moving mesh methods allow for more accurate tracing of sub-sonic pressure dominated rotation. But symmetry and angular momentum are more strongly conserved in meshless methods than moving mesh, particular in gas gravitational orbits (galaxy discs). This may partly be due to a trade off with the known mesh deformation errors which arise due to mapping a spherical kernel functions to partition the volume. This angular momentum can be well defined and conserved whereas moving mesh methods cannot define angular momentum beyond the second-order quadrature and integration accuracy (see e.g. Duffell & MacFadyen 2012). Finally meshless methods are symmetry maintaining

CHAPTER 3

whereas moving-mesh methods with irregular cell shapes may lead to symmetry breaking ‘mesh-bending’ instabilities (Springel 2010a).

3.2.2 GIZMO

With acknowledgement to the code author Dr. Phil Hopkins; we use the code GIZMO (Hopkins 2015) to simulate our isolated galaxies using the meshless finite volume (MFM) scheme provided in GIZMO for this study. As noted, GIZMO (Hopkins 2015) is a multi-method code which can be run with one of several hydro solvers built upon the domain decomposition and N-body framework of GADGET-3 (Springel 2005; Wiersma et al. 2009). One of the methods included is the ‘meshless’ hydrodynamics method which is a moving mesh-like Godunov code, but the ‘mesh’ is defined by a deformable kernel.

GIZMO provides the following solvers: ‘Traditional SPH’ method comparable to *GADGET* (Springel 2005) and *TREE-SPH* (Katz et al. 1996). A ‘Modern SPH’ scheme is included which is analogous to *PSPH* used in the *FIRE* simulations (Hopkins 2013; Hopkins et al. 2014). The differences between the two are that the lower noise in *PSPH* allows for better shock capturing, but this occurs at slower rates computationally since *PSPH* considers more nearest neighbours. A stationary grid method is also included Stone et al. (2008) which is similar to *ATHENA* but also comparable to RAMSES. It also includes a Moving Mesh scheme similar to *AREPO* (Springel 2010a) and additionally includes the implementation of two meshless methods given here.

Hopkins (2015) involves a multitude of tests which vary both the simulation scheme and the test scenario. It is important to test your code in smooth equilibrium regions. These include modelling a sound wave in 1D, 2D and 3D (Stone et al. 2008). Modern SPH undergoes problems due to its dependency on the sensitivity on the start-up conditions as per Springel (2010b), however meshless schemes model

CHAPTER 3

it accurately. Another involves modelling the fluid in a shape of a square to test advection and surface tension errors, which is common in SPH comparisons, although grid codes can handle this perfectly.

Hopkins (2015) also presents tests for sub-sonic turbulence and angular momentum via The Gresho Vortex (Gresho & Chan 1990). Angular momentum conservation and alignment via Keplarian Discs (e.g. Maddison et al. 1996; Imaeda & Inutsuka 2002), Sod Shock Tube (Hernquist & Katz 1989), Interacting blast waves involving interaction of two strong blast waves (Woodward & Colella 1984). Conservation, stability and symmetry of Sedov (Sedov-Taylor) blast wave (Sedov 1959) (see (See Saitoh & Makino 2013, for the importance of stability). The Noh Test (spherical collapse / implosion) (Noh 1987). The work also considers fluid mixing with Kelvin-Helmholtz Instabilities (McNally et al. 2012). Rayleigh-Taylor instabilities (Springel 2010a; Abel 2011), the blob test (Kelven-Helmhotz and Rayleigh-Taylor instabilities in a supersonic astrophysical medium, see Agertz et al. (2007)). Finally Hopkins (2015) tests GIZMO under self gravity conditions, namely the The Evrard Test (spherical collapse) (Evrard 1988), the Zeldovic Pancake (anisotropic geometries and entropy conservation, see Zel’dovich 1970)) and finally test it on the formation of the “Santa Barbara Cluster” from the comparison project in Frenk et al. (1999) as well as isolated galaxy simulations (e.g. Hopkins et al. 2011, 2014; van de Voort et al. 2015; Faucher-Giguère et al. 2015; Few et al. 2016). Overall, our method of choice, the MFM method does exceptionally well under these tests and because of this, it is a suitable method for solving gas disc instabilities and turbulence. GIZMO has gone under extensive testing and is a suitable code for simulations of galaxy evolution and indeed GIZMO has already been applied in astrophysical simulations to investigate the evolution of galaxies in a cosmological context (e.g. Hopkins et al. 2014; Davé et al. 2016), as well as isolated context (e.g. Lupi et al. 2016; Few et al. 2016).

3.2.3 Meshless Methodology

We shall now outline the hydrodynamical equations in the meshless finite volume (MFM) scheme. This will closely follow Gaburov & Nitadori (2011) and the full derivations are described in Hopkins (2015). A fully rigorous mathematical formulation of the method, with proofs of various consistency, conservation, and convergence theorems, is presented in Lanson & Vila (2008a,b) and Ivanova et al. (2013).

The conservation laws for mass, momentum and energy moving in a frame with velocity $\mathbf{v}_{\text{frame}}$ are contained within the following hyperbolic partial differential equation:

$$\frac{\partial \mathbf{U}}{\partial t} + \nabla \cdot (\mathbf{F} - \mathbf{v}_{\text{frame}} \otimes \mathbf{U}) = 0, \quad (3.2)$$

with $\nabla \cdot \mathbf{F}$ as the the inner product between the gradient operator and tensor \mathbf{F} , \otimes is the outer product, \mathbf{U} is the state vector. A state vector is a vector of conserved (in the absence of sources) variables,

$$\mathbf{U} = \begin{pmatrix} \rho \\ \rho \mathbf{v} \\ \rho e \end{pmatrix} = \begin{pmatrix} \rho \\ \rho \mathbf{v} \\ \rho u + \frac{1}{2} \rho |\mathbf{v}|^2 \end{pmatrix} = \begin{pmatrix} \rho \\ \rho v_x \\ \rho v_y \\ \rho v_z \\ \rho u + \frac{1}{2} \rho |\mathbf{v}|^2 \end{pmatrix}. \quad (3.3)$$

Here ρ is mass density, e is the total specific energy, u the specific internal energy, and the last equality expands the compact form of the vector \mathbf{v} in 3 dimensions). Additionally the tensor \mathbf{F} is the flux of conserved variables,

$$\mathbf{F} = \begin{pmatrix} \rho \mathbf{v} \\ \rho \mathbf{v} \otimes \mathbf{v} + P \mathcal{I} \\ (\rho e + P) \mathbf{v} \end{pmatrix}, \quad (3.4)$$

CHAPTER 3

where \mathcal{I} is the identity tensor and P is a pressure scalar.

The key difference between the MFV method and the MVM method is found when computing the projection of states to the “face” of the cell. since we boosted to a frame which moves with the velocity of the quadrature point assuming the time-variation in kernel lengths are second-order, the face is exactly $\mathbf{v}_{\text{eff}}^{\text{frame}} = 0$ in this frame. This is the what you would expect for a MFV method. In MFV methods, the faces of the volume of the particle are locally flat planes of arbitrary extent. For MFM methods, $\mathbf{v}_{\text{eff}}^{\text{frame}} = S_*$, where S_* is the speed of the contact wave in the Riemann problem on either side of which the mass is conserved. This means that there is no mass flux between any particles. Both of these methods have different finite numerical methods and the errors only arise from the study of second-order motions at discontinuities. More details of the MFV method are found in Hopkins (2015) and its earlier implementation in Gaburov & Nitadori (2011) and the MFM method in Hopkins (2015). The MFM and the MFV method uses a Harten-Lax-van Leer-Contact (HLLC) Riemann solver (Miyoshi & Kusano 2005; Toro 1999) as the default method. In the cases where the HLLC solver returns a non-physical result, the code automatically falls back to the slower but more accurate solver described in Toro (1997). The use of this solver eliminates the need for artificial viscosity (which in some SPH models is required in order to capture shocks Hopkins et al. 2014) . But also to evolve the fluid in a way that conserved the mass within each fluid element.

To deal with non-linear and discontinuous flows in the Galerkin-type method, we multiply Equation 3.2 by a test function $\phi = \phi(\mathbf{x}, t)$ which is taken to be arbitrarily differential Lagrangian function. We integrate the test function over the domain Ω in space such that $d\Omega = d^\nu \mathbf{x}$, where ν is the number of spatial dimensions in the system. Assuming fluxes (or ϕ) vanishes at infinity we can produce, as shown in Luo et al. (2008),

CHAPTER 3

$$0 = \frac{d}{dt} \int_{\Omega} \mathbf{U}(\mathbf{x}, t) \phi \, d^{\nu} \mathbf{x} - \int_{\Omega} \mathbf{F}(\mathbf{U}, \mathbf{x}, t) \cdot \nabla \phi \, d^{\nu} \mathbf{x}, \quad (3.5)$$

in which this integral is discretized in the same manner as the discretization of the domain volume onto a set of a volume element (either points, cells or particles) i with coordinates \mathbf{x}_i . In the meshless methods (and moving mesh methods) we partition the volume occupied by \mathbf{x}_i with a Voronoi mesh.

We partition a differential volume $d^{\nu} \mathbf{x}$, at arbitrary coordinates \mathbf{x} fractionally among the nearest particle/cell. The terms particles and ‘cells’ are used interchangeably in this work as each particle acts as a cell-generating point (or mesh generating point). This defines the volume domain where the mean fluid properties are represented by the particle/cell-carried quantities. The advantage of also doing this is that we can make simulation outputs into a form that is easily read with by a lot of analysis toolkits today. This can include analysis toolkits that would typically be used to read SPH data such as those used to study GADGET-2 outputs.

The weighting function W associates $\psi_i(\mathbf{x})$ with a volume $d^{\nu} \mathbf{x}$ with particle i according to a function $W(\mathbf{x} - \mathbf{x}_i, h(\mathbf{x}))$ i.e:

$$\psi_i(\mathbf{x}) \equiv \frac{1}{\omega(\mathbf{x})} W(\mathbf{x} - \mathbf{x}_i, h(\mathbf{x})), \quad (3.6)$$

$$\omega(\mathbf{x}) \equiv \sum_j W(\mathbf{x} - \mathbf{x}_j, h(\mathbf{x})), \quad (3.7)$$

with $h(\mathbf{x})$ is some “kernel size” that enters W . This means the weighting function determines how a volume at any point \mathbf{x} is partitioned among other volume associated with the tracer points i . Additionally, W can be any arbitrary function. This is because the term $\omega(\mathbf{x})^{-1}$ normalizes the weights such that the total volume always sums correctly. This means that the sum of fractional weights must always be unity at every point. However the second-order accuracy of the method must be maintained in order to maintain the conservation of linear and angular

CHAPTER 3

momentum, and additionally the locality of the hydrodynamic operations. Therefore the function $W(\mathbf{x} - \mathbf{x}_i, h(\mathbf{x}))$ must be continuous. Additionally we must have $W = 0$ for sufficiently large $|\mathbf{x} - \mathbf{x}_i| \gg h(\mathbf{x})$ in order to have compact support (since $|\mathbf{x} - \mathbf{x}_i| \sim \mathcal{O}(h(\mathbf{x}_i))$ where $W \neq 0$) and W also needs to be symmetric. The symmetry of W requires only on the absolute value of the coordinate differences $|x - x_i|, |y - y_i|$. Since we normalize by $\omega(\mathbf{x})$, the absolute normalization of W is irrelevant. This means that without loss of generality we take the normalization to be $1 = \int W(\mathbf{x} - \mathbf{x}', h(\mathbf{x})) d^{\nu} \mathbf{x}'$. The impact of the choice of kernel size is shown in Figure 3.2 which is taken from Hopkins (2015). Here Hopkins (2015) shows the meshless kernel on the left panel and a moving-mesh kernel in the central panel and additionally an SPH kernel in the right panel for reference. In general, the edges between particles are smoothed as particles move. This allows for the avoidance of discontinuities in mesh deformation. Mesh deformation occurs in which the shape of the volume element for an associated particle changes. Voronoi-based moving-mesh kernel is essentially the result of taking W to the limit of a delta function and 100% of the weight will be associated with the nearest particle.

From the volume partition function as described in Equation 3.6, we Taylor-expand all terms to second order accuracy (e.g. $f(\mathbf{x}) = f_i(\mathbf{x}_i) + h(\mathbf{x}_i) \nabla f(\mathbf{x} = \mathbf{x}_i) \cdot (\mathbf{x} - \mathbf{x}_i)/h(\mathbf{x}_i) + \mathcal{O}(h(\mathbf{x}_i)^2)$). Additionally we require $1 = \sum_i \psi_i(\mathbf{x})$ from the compact support requirement. Applying $\int f(\mathbf{x}) d^{\nu} \mathbf{x} = \sum_i f_i V_i + \mathcal{O}(h_i^2)$ and dropping the $\mathcal{O}(h_i^2)$ term to Equation 3.2 we get:

$$0 = \sum_i \left[\phi_i \frac{d}{dt} (V_i \mathbf{U}_i) - V_i \mathbf{F}_i \cdot (\nabla \phi)_{\mathbf{x}=\mathbf{x}_i} \right], \quad (3.8)$$

where $\mathbf{F}_i \cdot (\nabla \phi)_{\mathbf{x}=\mathbf{x}_i}$ refers to the product of the tensor \mathbf{F} with the gradient of ϕ evaluated at \mathbf{x}_i . The derivation process is described in more detail in Hopkins (2015).

CHAPTER 3

To proceed further, we require a second-order discrete distance gradient estimator. We use locally-centres least-squares matrix gradient operators. These operators have been described in previous numerical studies (e.g. Dilts 1999; Kuhnert 2003; Maron & Howes 2003; Luo et al. 2008; Lanson & Vila 2008a,b; Maron et al. 2012). In summary, for any instance of configuration of points, the use of weighted moments defines a least-square best fit to Taylor expansions of any fluid quantity. We can thus define the second order expansion parameters,

$$(\nabla f)_i^\alpha = \sum_j (f_j - f_i) \tilde{\psi}_j^\alpha(\mathbf{x}_i), \quad (3.9)$$

$$\tilde{\psi}_j^\alpha(\mathbf{x}_i) \equiv \mathbf{B}_i^{\alpha\beta} (\mathbf{x}_j - \mathbf{x}_i)^\beta \psi_j(\mathbf{x}_i),$$

with the use of the Einstein summation convention over β i.e. the matrices \mathbf{B}_i and \mathbf{B}_i^{-1} are:

$$\mathbf{B}_i \equiv \mathbf{E}_i^{-1} \quad (3.10)$$

$$\mathbf{E}_i^{\alpha\beta} \equiv \sum_j (\mathbf{x}_j - \mathbf{x}_i)^\alpha (\mathbf{x}_j - \mathbf{x}_i)^\beta \psi_j(\mathbf{x}_i). \quad (3.11)$$

Putting this into Equation 3.8 and noting that:

$$\sum_i V_i \mathbf{F}_i^\alpha (\nabla \phi)_i^\alpha = - \sum_i \phi_i \sum_j (V_i \mathbf{F}_i^\alpha \tilde{\psi}_j^\alpha(\mathbf{x}_i) - V_j \mathbf{F}_j^\alpha \tilde{\psi}_i^\alpha(\mathbf{x}_j)), \quad (3.12)$$

gives us;

$$0 = \sum_i \phi_i \left(\frac{d}{dt} (V_i \mathbf{U}_i) + \sum_j [V_i \mathbf{F}_i^\alpha \tilde{\psi}_j^\alpha(\mathbf{x}_i) - V_j \mathbf{F}_j^\alpha \tilde{\psi}_i^\alpha(\mathbf{x}_j)] \right), \quad (3.13)$$

and holding this for any unknown test function ϕ gives us;

$$\frac{d}{dt}(V_i \mathbf{U}_i) + \sum_j [V_i \mathbf{F}_i^\alpha \tilde{\psi}_j^\alpha(\mathbf{x}_i) - V_j \mathbf{F}_j^\alpha \tilde{\psi}_i^\alpha(\mathbf{x}_j)] = 0, \quad (3.14)$$

Finally replacing the flux functions \mathbf{F} with a time-centred Riemann solver between the particles i and j automatically includes dissipation terms. We can use the following relations $\mathbf{A}_{ij} = |A|_{ij} \hat{A}_{ij}$ where $\mathbf{A}_{ij}^\alpha \equiv V_i \tilde{\psi}_j^\alpha(\mathbf{x}_i) - V_j \tilde{\psi}_i^\alpha(\mathbf{x}_j)$ to redefine the flux as $\tilde{\mathbf{F}}_{ij}$ to give us:

$$\frac{d}{dt}(V_i \mathbf{U}_i) + \sum_j \tilde{\mathbf{F}}_{ij} \cdot \mathbf{A}_{ij} = 0, \quad (3.15)$$

Which is a Godunov-type finite-volume equation, but this is strictly not that since we calculate the “effective face” from solving a volume integral, rather than transforming a volume integral into a surface integral for flux calculations. The term $V_i \mathbf{U}_i$ is the particle-volume integrated value of the conserved quantity to be carried with particle i . This quantity can be for example the total mass $m_i = V_i \rho_i$, associated with the particle i , or its energy or momentum. The rate of change of time is given by the sum of the fluxes $\tilde{\mathbf{F}}_{ij}$ through an “effective face area” \mathbf{A}_{ij} . Since the fluxes of conserved quantities are calculated between particles, the quantities that they possess will be conserved to machine accuracy independently of the time-step, integration accuracy, and particle distribution. Additionally, the fluxes are antisymmetric i.e. the flux from i to j is always the negative of the flux from j to i at the same point in time i.e. $\mathbf{A}_{ij} = -\mathbf{A}_{ji}$. This means the discrete equations are therefore conserved.

The method of solving 3.15 is well studied and the same methods used in grid-based Godunov methods are used. In particular the second-order MUSCL-Hancock type scheme is used (van Leer 1984; Toro 1997) which is also used in RAMSES (Teyssier 2002) and AREPO (Springel 2010a). A slope-limited linear reconstruction of face-centred quantities from each particle and a first order prediction step for

CHAPTER 3

evolution over half of a time step. The application of a Riemann solver estimates the time-averaged interparticle fluxes for each timestep. A more detailed explanation is found in in (Hopkins 2015). A slope-limiting procedure is required to avoid numerical errors near discontinuities (see e.g. Barth 1989) and have been implemented in previous studies (Gaburov & Nitadori 2011). But Mocz et al. (2014), notes improvements are required, of which Hopkins (2015) provides a general form of discontinuity handling between two particles i and j . The Riemann solver we use is the HLLC Riemann solver (Toro 1999) with the Roe-averaged wave-speed estimates as our default Riemann solver (Roe 1981).

The time integration scheme follows (Springel 2010a) to maintain conservation of mass, momentum and energy even when using adaptive timesteps. Timesteps are discretized into bins of the power of 2 (see e.g. Hernquist & Katz 1989) and fluxes of conserved quantities are synchronised over each timestep to individual interparticle faces. Allowing for the variation of timesteps for different particles allows us to resolve finer structure within a simulation with more precision. For a vector of some conserved quantities $\mathbf{Q}_i = (V \mathbf{U})_i$,

$$\mathbf{Q}_i^{(n+1)} = \mathbf{Q}_i^{(n)} + \Delta t \left\langle \frac{d\mathbf{Q}_i}{dt} \right\rangle \equiv \mathbf{Q}_i^{(n)} + \Delta t \frac{d\mathbf{Q}_i^{(n+1/2)}}{dt}, \quad (3.16)$$

$$= \mathbf{Q}_i^{(n)} - \Delta t \sum_j \mathbf{A}_{ij} \cdot \tilde{\mathbf{F}}_{ij}^{(n+1/2)}. \quad (3.17)$$

Additionally we use a local Courant-Friedrich-Levy (CFL) (Courant et al. 1967) timestep criterion for the hydrodynamics (see §2.2.3) for more detail. For GIZMO the CFL condition takes the form:

$$\Delta t_{\text{CFL},i} = 2 C_{\text{CFL}} \frac{h_i}{|v_{\text{sig},i}|}, \quad (3.18)$$

$$v_{\text{sig},i} = \text{MAX}_j \left[c_{s,i} + c_{s,j} - \text{MIN} \left(0, \frac{(\mathbf{v}_i - \mathbf{v}_j) \cdot (\mathbf{x}_i - \mathbf{x}_j)}{|\mathbf{x}_i - \mathbf{x}_j|} \right) \right], \quad (3.19)$$

CHAPTER 3

with h_i as the kernel length, MAX_j is the the maximum over all interacting neighbours j of i , and $|v_{\text{sig}}|$ is the signal velocity (Whitehurst 1995) and $C_{\text{CFL}} = 0.2$. Previous SPH related work have $C_{\text{CFL}} = 0.2$ (e.g. Katz et al. 1996). This is combined with a timestep limiter based on Saitoh & Makino (2009) to prevent neighbouring particles from having very different timesteps.

The implementation of Gravity is similar to that of GADGET-3. Following Springel (2010a), the gravity is coupled to the hydrodynamics via operator splitting. The kernel lengths change and thus extra care is required to maintain the conserved quantities. Price & Monaghan (2007) shows how these are conserved. By defining the gravitational self-energy of a system of gas cells:

$$E_{\text{grav}} = \frac{1}{2} \sum_{i,j} G m_i m_j \phi(r_{ij}, h_j), \quad (3.20)$$

and then following the derivation in Price & Monaghan (2007) and our kernel length h :

$$\begin{aligned} m_i \frac{d\mathbf{v}_i}{dt} &= -\nabla_i E_{\text{grav}} \\ &= -\sum_j \frac{G m_i m_j}{2} \left(\frac{\partial \phi(r, h_i)}{\partial r} \Big|_{r_{ij}} + \frac{\partial \phi(r, h_j)}{\partial r} \Big|_{r_{ij}} \right) \frac{\mathbf{r}_{ij}}{r_{ij}} \\ &\quad - \sum_j \frac{G}{2} \left(\zeta_i \frac{\partial W(r, h_i)}{\partial r} \Big|_{r_{ij}} + \zeta_j \frac{\partial W(r, h_j)}{\partial r} \Big|_{r_{ij}} \right) \frac{\mathbf{r}_{ij}}{r_{ij}}, \end{aligned} \quad (3.21)$$

$$\zeta_a \equiv m_a \frac{h_a}{n_a \nu} \frac{1}{\Omega_a} \sum_b m_b \frac{\partial \phi(r_{ab}, h)}{\partial h} \Big|_{h=h_a}, \quad (3.22)$$

$$\begin{aligned} \Omega_a &\equiv 1 + \frac{h_a}{n_a \nu} \frac{\partial n_i}{\partial h_i} \\ &= 1 - \frac{h_a}{n_a \nu} \sum_b \left(\frac{r_{ab}}{h_a} \frac{\partial W(r, h_a)}{\partial r} \Big|_{r_{ab}} + \frac{\nu}{h_a} W(r_{ab}, h_a) \right), \end{aligned} \quad (3.23)$$

where $\mathbf{r}_{ij} = \mathbf{x}_i - \mathbf{x}_j$ (so $\partial \phi / \partial r = h^{-1} \partial \phi / \partial q$). The first term of the gravity equation assumes h is fixed and the forces between each particle is equal and opposite. The second term (the ζ terms in $\partial W / \partial r$) accounts the variations in h .

3.3 Galaxy Outflow Physics

We shall now discuss the relevant physics used in our study to model gas outflows in a simulated galaxy disc. In §3.1, specifically Equation 3.1, showed that the surface density of the disc is able to drive gravitational instabilities. An increase in frequency and abundance of gravitational instabilities drives an increase in velocity dispersion, and thus larger outflows. We shall now elucidate the physics in more detail.

Our aim is to understand how the varying surface density environments in galaxies drive galaxy-scale gas outflows as well as quantifying the magnitude of these variations. In Scannapieco et al. (2012) and summarised in §3.1, the gas density of $\Sigma_g \approx 100 M_\odot \text{pc}^{-2}$ leads to a velocity dispersion of $\sigma \approx 35 \text{ km s}^{-1}$ to have $Q_{\text{eff}} \approx 1$. Additionally large-scale gravitational instabilities maintain a turbulence where $Q_{\text{eff}} \approx 1$ in which the instabilities primarily are in-plane motions. Additionally using the assumption that $c_s^2 \ll \sigma^2$ for large scale instabilities turbulences which gives rise to a horizontal velocity dispersion;

$$\sigma_H \approx \pi G \Sigma / \kappa. \quad (3.24)$$

here σ_H is the velocity dispersion in the horizontal plane, or the velocity dispersion in the r direction in a spherical polar co-ordinate system of the galaxy. Sur et al. (2016) shows that horizontally-driven turbulence results in vertical motions. Shocks from both the horizontal and vertical motions heat the gas. This creates a thermal pressure gradient and combined with a vertical turbulence drives the outflow of gas from the disc. Our study focuses on the turbulence purely driven by gravitational instabilities with the inclusion of molecular cooling. We do not include any supernova feedback or any other source of feedback. As emphasised in §3.1, we are also taking a conservative approach of to put a lower limit on this effect.

Characterising the impact of the feedback in addition to the stability of the disc is a complicated task (Agertz et al. 2015). However, large scale gravitational

CHAPTER 3

instabilities promotes an increase of the velocity dispersion, σ , until;

$$Q_{\text{eff}} \equiv [\sigma^2 + c_s^2]^{1/2} \kappa / \pi G \Sigma \approx 1.0, \quad (3.25)$$

which implies high surface density discs must develop significant turbulent motions even if stars are unable to stir the discs sufficiently to stabilize them. This is due to the fact that gravitational instabilities will lead to the formation of clumps moving at typical velocities $\sigma \approx \pi G \Sigma / \kappa$. This occurs in both Milky Way-like galaxy simulations (e.g. Wada et al. 2002; Agertz et al. 2009a, 2015) and high-redshift galaxy simulations (e.g. Immeli et al. 2004; Ceverino et al. 2010; Genel et al. 2012a,b).

Scannapieco et al. (2012) simulated a local patch of the ISM in a galaxy that was turbulently stirred and radiatively cooled. Turbulences were driven at a rate to match the overall cooling rate. However the critical gas surface density for galaxy outflows corresponds to a gas surface density of $\Sigma_g \approx 100 M_\odot \text{pc}^{-2}$, which assuming typical values of $\Sigma \approx 2 \Sigma_g$, $c_s \approx 10 \text{ km s}^{-1}$, and $\kappa^{-1} \approx 15 \text{ Myr}$. This gives rise to a one-dimensional turbulent velocity dispersion of $\sigma \approx 35 \text{ km s}^{-1}$ to have $Q_{\text{eff}} \approx 1$. For high velocity dispersions, there is a thermally driven runaway which causes multiphase material to escape from the surface of the disc. This implies the absence of a stability equilibrium beyond this value, and thus gas outflows occur.

A disc that is self-gravitating with a velocity dispersion σ_z in the z plane has a scale height;

$$H = \sigma_z^2 / (\pi G \Sigma_b), \quad (3.26)$$

Where Σ_b is the surface density of the baryons (stars and gas). Assuming that the Toomre parameter Q is unity so that velocity dispersion in the radial direction is described by Eq. 3.24, we have;

$$\lambda_f \approx R_{\text{turb}} \equiv \pi G \Sigma / \kappa^2, \quad (3.27)$$

CHAPTER 3

with R_{turb} being the turbulent stirring scale. From assuming an axisymmetric potential (i.e. independent of the angular co-ordinate θ) in a cylindrical coordinate system (R, θ, z) with potential $\Phi = \Phi(R, z)$ and effective potential;

$$\Phi_{\text{eff}} = \Phi(R, z) + \frac{L_z^2}{2R^2}, \quad (3.28)$$

with the $\frac{L_z^2}{2R^2}$ as the centrifugal barrier. From this, one can compute an approximation for the epicycle frequency (Binney & Tremaine 1987). The epicycle frequency κ is the frequency of which a star in the disc will oscillate and return to its original position in a co-ordinate system with the rest frame rotating around the galaxy at a speed of v_{rot} i.e. the rotational velocity of stars in the galaxy. From computing the angular momentum of the gas $L_z = V_{\text{circ}}r$ where V_{circ} is;

$$V_{\text{circ}} = GM(< R)/R, \quad (3.29)$$

with $M(< R)$ as the total enclosed spherical mass at a point R. Furthermore, one can relate the rotational velocity to the angular velocity. The angular acceleration is:

$$\frac{d\Omega^2}{dR} = \frac{1}{R} \frac{d^2\theta}{dR^2} \frac{v_{\text{rot}}^2}{R^3}, \quad (3.30)$$

with Ω is the angular frequency and for circular velocity $v_{\text{rot}} = R\Omega$. In an axisymmetric potential, Ω is also related to the z component of the angular momentum vector L_z ,

$$\Omega = \frac{2\pi}{t} = \frac{L_z}{R^2}, \quad (3.31)$$

Finally, one can compute the epicycle frequency κ from the angular frequency Ω

$$\kappa = R \frac{d\Omega^2}{dR} + 4\Omega^2 = \frac{v_{\text{rot}}^2}{R} + 4 \left(\frac{L_z}{R^2} \right)^2, \quad (3.32)$$

Which is computed at a radius of choice, typically that of the galaxy.

CHAPTER 3

From the epicycle frequency and the turbulent stirring scale, we can define a vertical height z_{\max} which defines whether a gas particle that originates in the disc is outflowing from the disc. This height is defined as:

$$z_{\max} = 3R_{\text{turb}} \equiv 3\pi G\Sigma/\kappa^2, \quad (3.33)$$

And for a disc originating gas particle to be consider as part of the outflowing gas per unit area per unit time $\dot{\Sigma}_g$ at radius R , the disc gas particle i is required to have a position $|z_i| \geq z_{\max}$.

Comparatively very few disc originating gas is expected to reach halo escape velocities. So instead we calculated the theoretical escape velocity from the plane of the disc $v_{\text{es,disc}}$.

$$v_{\text{es}} = \sqrt{2g z_{\max}} \approx \left(\frac{103}{\text{km s}^{-1}} \right) \left(\frac{\Sigma_g}{100 \text{ M}_{\odot} \text{ pc}^{-2}} \right)^{1/2} \left(\frac{z}{\text{kpc}} \right)^{1/2}, \quad (3.34)$$

where $g = 4\pi G \Sigma_g$ is the acceleration due to gravity (assuming $\Sigma = 2\Sigma_g$).

From the physics described here, we shall model the relations of these properties as a function of time and surface density. These derived relationships and quantities thus give the key physical parameters to be investigated in our models. Through following the disc evolution with time we can also check their evolutionary behaviour as well as any instantaneous relationships. We sample 1 kpc radial bins in order to study outflow physics different surface density environments within the galaxy. We track this physics with the time evolution of the galaxy and we track the evolution of these environments with time.

3.4 Methodology

In this section, we outline the generation of initial conditions, the simulation properties of two galaxies with different temperature floors, *Giz-A* and *Giz-B* and describe our method of identifying giant molecular clouds.

3.4.1 Initial Conditions

The initial conditions of isolated galaxy models consist of its bulge, disc, dark matter halo, and gas contents. There are numerous variations, from modelling only selected components of the galaxy and setting the others as rigid potentials whilst making simplified approximations about the nature of the distribution function of those components (e.g. Toomre & Toomre 1972; Hernquist & Quinn 1988). Or by sequentially considering the potential of each component whilst subsequently adding in new galactic components i.e. growing the disc mass distribution in a self-consistent halo/bulge model (Barnes 1988, 1992). Or by treating the halo and bulge as a static background (e.g. Sellwood & Merritt 1994; Quinn et al. 1993). Or directly solving the Jeans equations (under a suitable ansatz) for the complete system of the disc, bulge and halo to find the Velocity dispersions (Hernquist 1993), and realizing these dispersions with (typically) Gaussian distributions. In general the optimal procedure for constructing galaxies that are already formed is problematic. If the distribution function was already known then creating individual galaxies would be trivial. Isolated galaxy initial conditions are typically derived from equilibrium solutions to the collisionless Boltzmann and Poisson equations. Additionally, these models typically include multiple input parameters where one can use observation results of an observed galaxy (for example line of sight velocity) to determine the probability distribution function of the model in full multi-dimensional parameter space with the aid of Bayesian statistics and Markov Chain Monte Carlo (MCMC) techniques (Kuijken & Dubinski 1995; Widrow et al. 2008; Widrow & Dubinski 2005;

CHAPTER 3

Widrow 2008).

We generate our isolated Milky Way model using the GALACTICS package (Kuijken & Dubinski 1995; Widrow & Dubinski 2005; Widrow et al. 2008), of which the input parameters names and values are shown in Table. 1. Using an iterative process, this package produces a self consistent system in equilibrium consisting of an exponential stellar disc, a stellar bulge and a dark matter halo. The physical parameters we use in GALACTICS is similar to that used in Williamson & Thacker (2012) which were based on Widrow et al. (2008) which originate observations of the Milky Way. These parameters are described in Table 3.4.1. For completeness, we shall discuss in detail the creation of the galaxy initial conditions here.

The dark matter halo density profile ρ_h follows:

$$\rho_h = \frac{2^{2-\gamma}\sigma_h^2}{4\pi a^2 + h} \frac{1}{(r/a_h)^\gamma(1+r/a_h)^{3-\gamma}} C(r; r_h, \delta r_h), \quad (3.35)$$

where a_h is the halo scale length, r_h is the cutoff radius, γ is the central cusp strength (equal to unity for a NFW profile) and σ_h is a (line of sight) velocity scale that sets the mass of the halo (Widrow 2008). The truncation function:

$$C(r; r_h, \delta r_h) = \frac{1}{2} \operatorname{erfc} \left(\frac{r - r_h}{\sqrt{2}\delta r_h} \right), \quad (3.36)$$

which smoothly goes from $C(r; r_h, \delta r_h) = 1$ at $r = 0$ kpc to $C(r; r_h, \delta r_h) = 0$ at $r = r_h$ over width δr_h there by avoiding distributions that are unnecessarily large.

The stellar bulge density profile $\tilde{\rho}_b(r)$ is given by:

$$\tilde{\rho}_b(r) = \rho_b \left(\frac{r}{R_e} \right)^p e^{-b(r/R_e)^{1/n}}, \quad (3.37)$$

which yields the Sérsic Law,

$$\Sigma(r) = \Sigma_0 e^{-b(r/R_e)^{1/n}}, \quad (3.38)$$

CHAPTER 3

Table 3.1: The parameters that are used within GalactICS initial conditions generator to produce our model galaxy. These are similar to those used in Williamson & Thacker (2012) which were based on Widrow et al. (2008).

Component	name	parameter	value
bulge	scale radius	R_e	0.64 kpc
bulge	stream fraction	f_{stream}	0.5
bulge	Sérsic index	n	1.31
bulge	bulge velocity scale	σ_b	272 km/s
bulge	bulge mass	M_b	$1.19 \cdot 10^{10}$
stellar disc	disc scale radius	R_d	2.81 kpc
stellar disc	disc scale height	z_d	0.36 kpc
stellar disc	truncation radius	R_{trunc}	30.0 kpc
stellar disc	truncation width	$R_{\text{trunc,width}}$	0.1 kpc
stellar disc	central radial velocity dispersion	σ_{R0}	119.0 km/s
dark halo	halo cutoff radius	r_h	275.0 kpc
dark halo	stream fraction	f_{stream}	0.5
dark halo	line of sight velocity scale	σ_h	330.0 km/s
dark halo	halo scale length	a_h	13.6 kpc
dark halo	truncation width	δr_h	25.0 kpc
dark halo	cuspidity parameter	γ	0.81

CHAPTER 3

for a projected mass density profile if $p = 1 - 0.6097/n + 0.05563/n^2$ where n is the Sérsic index (Prugniel & Simien 1997; Terzić & Graham 2005). R_e is a radial scale parameter, which is a free parameter. The constant b is adjusted so that R_e encloses half the total projected stellar mass. The constant ρ_b in GALACTICS is parameterized by the velocity parameter:

$$\sigma_b \equiv \sqrt{4\pi n b^{n(p-2)} \Gamma[n(2-p)] R_e^2 \rho_b}, \quad (3.39)$$

where σ_b^2 is the depth of the gravitational potential associated with the bulge.

The stellar disc has a truncated density profile that falls off approximately exponential radially and follows sech^2 vertically (Kuijken & Dubinski 1995),

$$\tilde{\rho}_d(r, z) = \rho_{d,0} e^{-(r/R_d)} \text{sech}^2(z/Z_d) \times \text{erfc}\left(\frac{R - R_{\text{trunc}}}{R_{\text{trunc,width}}}\right), \quad (3.40)$$

with the parameters R_d , z_d as the radial and vertical scale heights, R_{trunc} as the truncation radius which represents the radius of which truncation occurs over a width of $R_{\text{trunc,width}}$. $\rho_{d,0}$ is a constant which is parameterized by the radial velocity dispersion profile, which is given as follows:

$$\sigma_R^2(R) = \sigma_{R0}^2 \exp(-R/R_\sigma), \quad (3.41)$$

where we set $R_\sigma = R_d$ for simplicity and σ_{R0} is the central radial velocity dispersion. Details of these parameters can be found in Table 3.4.1.

The GALACTICS code does not include any methodology to generate both the gas disc or hot gas halo components of the galaxy. To conserve the overall density profiles described above, additional calculations are required to generate the gas components. Essentially this is done by transferring mass from the dark matter component to the hot gas halo component, but also some of the stellar disc mass into gas disc mass. We shall next describe this process in more detail.

CHAPTER 3

We generate the gas disc by initially copying the stellar disc particle positions and velocities to initialise gas disc particles. Then we flip these gas disc particles across the $x = y$ plane position $v_x = v_y$ plane in velocity space to prevent the gas particles/cells having coincident positions with the stellar disc particles. This also conserves the disc rotational velocity magnitude (velocity in the z plane for the disc gas is set to 0). Bulge stellar particles are not copied in this way at all. We then transfer 10% of the initial stellar disc mass to the gas disc particles to conserve the total mass of the system. This means that the stellar disc mass is reduced from the initial setup of $5.28 \times 10^{10} M_{\odot}$ to $4.75 \times 10^{10} M_{\odot}$. The reasoning for these transformations are due to the context in which the disc was set-up. GALACTICS sets up the halo bulge and stellar disc. Since the Milky Way-mass disc is more massive in stars if we had just converted the required number of stars particles into gas, we would lose significant spatial sampling. So copying the stars, reducing the mass and then flipping to avoid coincident positions was used. We then reduce the spatial separation from the $z = 0$ plane for all of the gas particles by a factor of $z_{d,gas} = 0.36$ kpc. The motivation of this is to dampen strong ring-shaped shocks which propagate outwards as a consequence of the cold collapse as discussed in Williamson & Thacker (2012). The adopted process was shown therein to significantly reduce initial ringing. Bulge particles are not copied or manipulated in this manner and thus there is no bulge gas component. The gas disc is initially isothermal at $T_{\text{initial}} = 10^4$ K. For generation of the hot gas halo (hgh) we assign particles that are distributed by a density profile which is motivated by the observationally motivated β -profile (e.g. Cavaliere & Fusco-Femiano 1976) given by:

$$\rho_{hgh} = \rho_0 \left[1 + \left(\frac{r}{r_c} \right)^2 \right]^{-\frac{3}{2}\beta} C(r; r_h, \delta r_h), \quad (3.42)$$

where ρ_0 is the central density, r_c is the core radius and β is the outer slope parameter and the truncation width $\delta r_h = 25$ kpc. We set $r_c = 1.75$ kpc and $\beta=2/3$ (Moster

CHAPTER 3

et al. 2011). ρ_0 is set by choosing the mass of the hot gas within 40 kpc (Rasmussen et al. 2009). The mass of individual hot gas halo particles is set to be the same as the particle mass of the disc gas. Overall we convert 1.04% of the dark matter halo mass into hot halo gas mass, giving a mass of $0.73 \times 10^{10} M_\odot$. Additionally, we truncate the hot gas halo,

$$C(r; r_{\text{hgh}}, \delta r_{\text{hgh}}) \frac{1}{2} \operatorname{erfc} \left(\frac{r - r_{\text{hgh}}}{\sqrt{2} \delta r_{\text{hgh}}} \right), \quad (3.43)$$

where $r_{\text{hgh}} = 275$ kpc, and $\delta r_{\text{hgh}} = 25$ kpc are the radius of the hot gas halo and the truncation widths respectively. The mass of the gas, stellar and dark matter contents, number of particles and softening length used can be found in table 3.2.

To evaluate the temperature of the hot gas halo particles, we assume isotropy and solve the equation of hydrostatic equilibrium of an ideal gas inside a dark matter halo as done in Mastropietro et al. (2005). We assume spherical symmetry and the radial dependants by the formulation also used in Kaufmann et al. (2007),

$$T_{\text{hgh}}(r) = \mu \frac{m_p}{k_B} \frac{1}{\rho_{\text{hgh}}(r)} \int_r^\infty \rho_{\text{hgh}}(r) \frac{GM(r)}{r^2} dr, \quad (3.44)$$

where $m_p = 1.6726 \times 10^{-24}$ g is the proton mass, $k_b = 1.38 \times 10^{-16}$ erg.K⁻¹ is the Boltzmann constant, and $M(r)$ is the cumulative mass distribution as a function of r of the dark matter and baryonic components interior to r . μ is the mean molecular weight of an ionized mixture of hydrogen and helium in the primordial ratio.

The angular momentum of the hot gas halo is set to 0 with the halo gas particles having no initial rotational velocity or velocity in the Z direction. Whereas the dark matter halo velocity profile remains unchanged. We also convert from internal energy units into temperature units using the following conversion,

$$\hat{K} = \hat{U} \times (\gamma - 1.0) \frac{\mu}{k_b}, \quad (3.45)$$

here, γ is the index for the ideal gas equation, which is 5/3.

CHAPTER 3

Table 3.2: The number of particles, masses and softening lengths (ℓ_{soft}) for the different particle populations of the galaxy simulated in this work.

Model Component	Total Mass ($10^{10} M_{\odot}$)	Particle Mass (M_{\odot})	Number of particles	ℓ_{soft} (pc)
Dark matter halo	69.16	350027.47	1975948	150.0
Hot gas halo	0.73	13215	553488	50.0
Stellar bulge	1.01	118939	84722	100.0
Stellar disc	4.75	118939	400000	100.0
Gas disc	0.529	13215	400000	50.0

3.4.2 Simulation of an Isolated Galaxy

We now discuss the evolution of the initial conditions with the MFM method. We run simulations of two galaxies which we shall henceforth refer to as *Giz-A* and *Giz-B*. The only differential condition between *Giz-A* and *Giz-B* is the temperature floor of the simulation, which is set to 1000 K for *Giz-A* and 1500 K for *Giz-B*. They are both simulated for $t = 600$ Myr from the same initial conditions. Table 3.2 describes the total mass, the number of particles, the particle masses and the softening lengths for the different components of the initial conditions of the galaxy. We choose to have the finest softening length in the gas since that is the main focus of our study. Our simulations are run in absence of baryonic feedback physics (such as star formation feedback and supernova feedback) since the primary interest in this study is of how the ISM dynamically evolves from the self-turbulence of the gas disc alone.

GIZMO assigns each particle into timestep bins depending on the abundance of particles within fine scale regions. This is described in more detail in §3.2.3. In our simulations, cold gas gravitationally collapses into giant molecular clouds. As these clouds get denser, the timestep bin for each of those particles gets smaller. In our

CHAPTER 3

study we are only required to resolve the location and an approximate size for the clouds, we do not need to resolve the finer structure of each cold gas cloud which are known to be incorrect, then we can use a less accurate time stepping scheme to reduce the amount of CPU time required. We force a minimum timestep bin to $t_{\text{min,bin}} = 2861.0$ yr and we briefly demonstrate the impact of this in §3.5.1. Overall this choice of timestep does not have any significant impact on the structure of the galaxy. As such less than 2% of the gas particles would have resided in finer time bins in the simulation. Forcing a minimum timestep bin is not new to hydrodynamical simulations (e.g. Katz et al. 1996), and indeed the motivation to do so is to reduce the amount of CPU time required to complete the simulation. This does bring about a loss of accuracy, but we argue this only occurs in the central regions of giant molecular clouds and the centre of the galaxy, of which are no interest in this study. Indeed separating the relative forces in outflow physics is an interesting problem for the future.

We use the optically-thin cooling module that was originally part of the GADGET3 code (Springel 2005; Wiersma et al. 2009). This cooling module is based the standard cooling curve from Katz et al. (1996), supplemented with approximate molecular cooling for H_2 . The optically-thin radiative cooling includes heating from H and He ionization and cooling from their recombination. It also includes cooling from collisional, free-free and Compton effects. The ionization and recombination requires a UV background. Additioanl thermal heating and cooling processes used in the mode include local radiative heating, photo-electric heating, molecular, dust, and fine structure heating/cooling, metal line cooling. Specifically the the cooling methodology used here treats the gas primarily as molecular hydrogen.

In particular, we use the Robertson & Kravtsov (2008) implementation of radiative cooling with takes inputs of gas density, the UV background (Haardt & Madau 1996) plus and assumption about the overall interstellar radiation field. We

CHAPTER 3

present cooling rate functions that are of relevance to this work in Figure 1.3 (as model RK08) in §1.3.2. Above 10^4 K cooling processes are dominated by the traditional atomic process such as those related to collisional ionization/excitation and at higher temperatures bremsstrahlung. Continuing our conservative approach we assume no interstellar radiation field leaving the only source of heating the UV background which has comparatively little impact on the net cooling rates within the disc primarily because of the high densities of the gas. The only notable impact is an increase in the cooling rate at low temperatures, around 100 K, by a factor of two as the local density is increased from $\log_{10}(n_{\text{H}}) = 0.$ to $\log_{10}(n_{\text{H}}) = 3.0$. In practice this has comparatively little impact in dense regions and, temperature-wise, the gas in the disc tends to separate between the 10^4 K end of atomic processes, down to a few hundred K where the cooling curve rises slightly. It is clear, however, that the low temperature cooling is still considerably more inefficient (by about 1.5 orders of magnitude) than atomic processes at the 10^4 K and higher temperatures. The overall stratification that the cooling curve produces in the gas temperatures is clearly visible in the temperature-density phase plots in Figure 3.11.

In this work, we do not trace the evolution of metals in these simulations. As a consequence of this, less cooling will occur than in Sur et al. (2016) since the dominant low temperature cooling is from molecular hydrogen. We note that this is one aspect of this study that is not entirely consistent with minimising the creation of outflows, however it was a necessary compromise given the absence of metals in our simulation model. One could consider enforcing a metallicity gradient on the gas disc in an ad-hoc manner, however lacking a plausible representation of the UV background within the galaxy itself, it is thus not clear that representing a metallicity gradient would have produced significantly improved results.

3.4.3 Identifying Giant Molecular Clouds

A Giant Molecular Cloud (GMC) is large structures of molecular gas. These typically have a radius of approximately 100 pc and have a hydrogen number density of $n = 1 \text{ cm}^{-3}$ (Murray 2011). The interior of a GMC is host to a complex substructure of filaments, bubbles, sheets and irregular clumps (Williams et al. 2000). We do not resolve this structure in our simulations since our choice of gas minimum resolution is too large.

There is no universally consistent method in the literature to identify giant molecular clouds in galaxy simulations. What is common however is the inclusion of a density based cloud identification algorithm. Examples of this include setting a minimum density threshold to remove gas particles not belonging to any dense structure, and then follow this up with a group finding algorithm (e.g. Williamson & Thacker 2012), or to look for peaks of gas density within the simulations themselves (e.g. Tasker & Tan 2009). Our methodology to identify GMCs is loosely based off of the former approach. First, we need to identify where in the galaxy GMCs are located which mainly makes use of a group finding algorithm, and then we need to refine the physical properties of the GMCs based on energy conservation.

We first select a cylindrical region centred on the centre of the galaxy within $R = 30 \text{ kpc}$, and a vertical restriction $-1.5 \leq z \leq 1.5 \text{ kpc}$ from which we select all of the disc originating and hot halo originating gas particles. From there, because the hot gas halo gas particles and the disc gas particles have the same mass, we use the DBSCAN clustering algorithm (Ester et al. 1996) to identify GMCs and group the associated particles with a maximum distance (also known as linking length) between two particles to be 22 pc. DBSCAN is a particle density-based clustering algorithm and from a set of points in 3D space is able to group together points that are closely packed together. Each GMC must also have a minimum of 60 particles, otherwise the GMC shall be rejected from the algorithm. This generates our initial

CHAPTER 3

GMC catalogue and computes the centroid of the GMC.

From the GMC catalogue that we have generated so far, we further refine the properties of the GMCs. Although DBSCAN is suitable for grouping together points of data spatially, the grouping method does not take into account of any other physical properties of the gas particles. GMCs are gravitationally bound structures which although DBSCAN is capable of quickly identifying where these groups are, does not check for whether the structure is gravitationally bound. For a structure to be gravitationally bound, the kinetic energy of a particle must not exceed the gravitational potential acted upon the particle. i.e. for a gas particle i to be bound;

$$\frac{1}{2}\mathbf{V}_i^2 \leq G \sum_{j \neq i}^n \frac{m_j}{\mathbf{r}_j}, \quad (3.46)$$

where \mathbf{V}_i is the velocity vector of the gas particle i of which we are checking is bound or not. Additionally, m_j and \mathbf{r}_j are the masses of particle j and the distance between particle i and particle j respectively and n is the number of particles. From the centroid of the GMC;

- We select a 100 pc sphere of gas, dark matter and star particles and assume that the GMC cannot be greater than 100 pc in size.
- From the selected particles, we compute the bulk velocity of the system so we can shift the velocities of all the particles to the reference frame of the GMC.
- We then compare the kinetic energy of individual gas particles to the potential energy acting upon the gas particle.
- If the particle has a kinetic energy less than or equal to the potential energy (see equation 3.46) accept it. Otherwise reject it. This allows us to remove gas particles that are within the 100 pc sphere but not gravitationally bound to it.

CHAPTER 3

- From the accepted particles for each GMC, we update our GMC catalogue by computing the new centre of mass and velocity for each GMC.
- We remove any GMC with a single particle within the cylinder of $r = 1$ kpc and $-0.5 \leq z \leq 0.5$ kpc. We assume that any GMC within this spatial region is likely to be accreted into the central bulge. This means we focus our attention on the disc region, where GMCs are most likely to form and avoid any complication of GMC particles intersecting with bulge particles.

For a gas particle inside a giant molecular cloud to become star forming, the Jeans mass of the gas particle must be less than that of the gas particle itself (Jeans 1902, 1928). We discussed the Jeans length in §*physdesc* for the context of an adaptive mesh refinement simulation, but here since particle densities are already defined, we use that to define the Jean’s mass of the particle,

$$M_J = \frac{\pi}{6} \lambda_{Jg}^3 \rho_g = \frac{5}{2} \sqrt{\frac{15}{8\pi}} \left(\frac{k_b}{G} \right)^{\frac{3}{2}} m_H^{-2} T^{\frac{3}{2}} n^{-\frac{1}{2}}, \quad (3.47)$$

where m_H is the mass of a hydrogen atom, k_b is the Boltzmann constant, (Jeans 1902, 1928). Setting this density criterion allows us to minimise artificial fragmentation, although some of the most dense particles in our simulation which reside at the centre of giant molecular clouds have a jeans mass greater than the particle mass. We discuss this in more detail in §3.5.4.

3.5 Morphological Evolution

In this section, we describe the morphological evolution of the galaxy model. We first describe the impact of the choice of minimum timestep, then describe the global morphological properties, such as the rotation curve, and finally we describe the evolution of the properties of giant molecular clouds. To study our galaxy, we assign GIZMO to produce GADGET2 Type-2 snapshots and we read in the data using PYGADGETREADER (Thompson 2014). We use the YT visualisation toolkit (Turk et al. 2011) to produce projection plots shown here. At the time of studying the simulations, YT had no native frontend for GADGET2 Type-2 snapshots, so we instead used PYGADGETREADER to read the data and export the particle data into YT. YT is capable of studying multiple different astrophysical simulation codes within a consistent framework. We used YT in our study of our simulated galaxy with RAMSES in Chapter 2. Since YT places particles into an octree in which each oct refines when $n_{\text{refine}} = 512$ (the minimum number of particles required to refine the cell). It is worth noting that YT visualizations are not consistent with the actual GIZMO fields, but are a reasonable proxy for them.

3.5.1 Minimum Timestep Bin and Timestep Evolution.

In our simulations, we force a minimum timestep bin of $t_{\text{min,bin}} = 2861.0$ yr. From our initial tests, we find that this timestep bin is fine enough to resolve the overall location and sizes of internal structure in the galaxy itself as measured by visually comparing the distribution on the ~ 100 pc scale. However this will fail to resolve accurately the accurately densest regions inside internal structures, but this does not impact any of our studies since we are not studying the internal physics of giant molecular clouds, or the central region of the galaxy. To motivate why we chose a minimum timestep, we ran a variation of the simulation *Giz-B* to $t = 200$ Myr without a minimum timestep bin at all (effectively $t_{\text{min,bin}} \approx 0.0$ yr).

CHAPTER 3

The timebins in the simulation in [yr] are 5.85×10^6 , 2.92×10^6 , 1.46×10^6 , 7.32×10^5 , 3.66×10^5 , 1.83×10^5 , 9.16×10^4 , 4.58×10^4 , 2.28×10^4 , 1.15×10^4 , 5.72×10^3 and 2.86×10^3 . The simulation that has no timestep bin additionally has bins 1.43×10^3 yr and 7.15×10^2 yr. We study the impact of this from simulation *Giz-B* with and without a minimum timestep bin on the same machine up to $t = 200$ Myrs. In Figure 3.2 we illustrate the differences between the gas cell distributions amongst the timestep bins with and without the choice of the minimum timestep bin. The cells that occupy the finest timebins typically are the most dense and with small theoretical Jean's mass, these are not of interest to our study and thus we can justify the minimum timestep bin.

Additionally the differences in the structure of the galaxy, including the giant molecular clouds and other dense structures in the simulation is extremely small. Figure 3.3 illustrates the overall structural differences at $t = 200$ Myr between *Giz-B* without a minimum timestep bin of $t_{\text{bin}} = 2861.0$ yr. One can conclude from observing this figure that the differences between the two mainly reside in the denser regions of the galaxy, of which are not of any interest in this study.

3.5.2 Evolution of Global Properties

Because both the 1000 K and 1500 K (*Giz-A* and *Giz-B*) runs evolve similarly, we shift the focus towards a single run, specifically *Giz-B*. Unless there is any explicit mention of *Giz-A* and *Giz-B*, the reader should assume that we are infact referring to *Giz-B*.

We present the initial conditions of *Giz-B* in Figure 3.5 and the galaxy after the 600 Myr duration of the simulation. The evolution of the gas density distribution of the galaxy is shown in Figure 3.6. The galaxy gas density distribution starts off uniformly, until self gravity results in the collapse of internal structure and the

CHAPTER 3

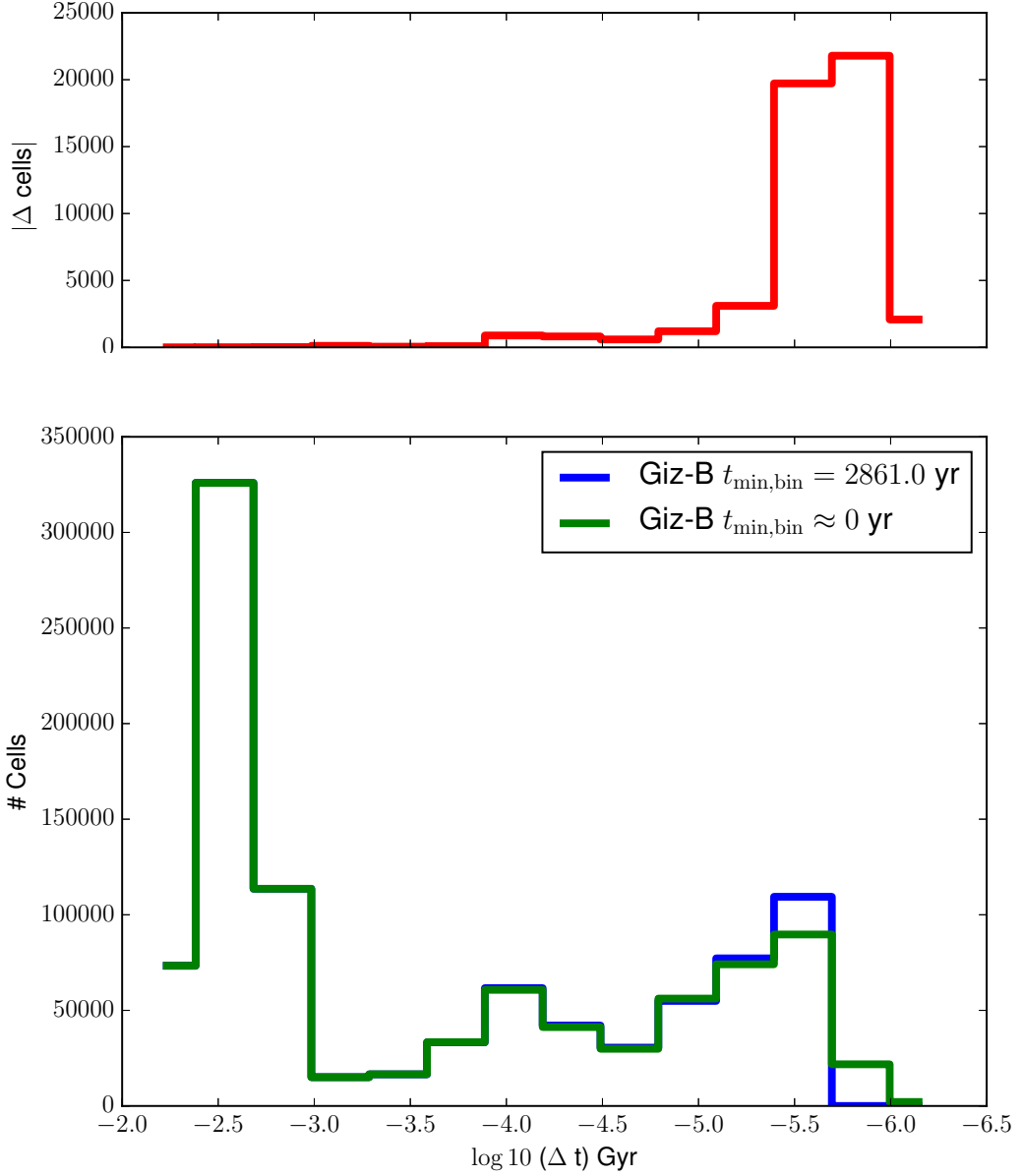


Figure 3.2: The distribution of gas cells across different timebins for time $t = 200$ Myr. On the bottom panel, we show the distribution of gas cells in timebins with each line centred on $\log_{10}(t_{\text{bin}})$ in Gyr. We show the distribution of gas cells for galaxy simulation *Giz-B* with (blue) and without (green) a forced minimum timestep of $t_{\text{min,bin}} = 2861.0$ yr. On the top panel, we show the absolute difference between the number of cells of these distributions.

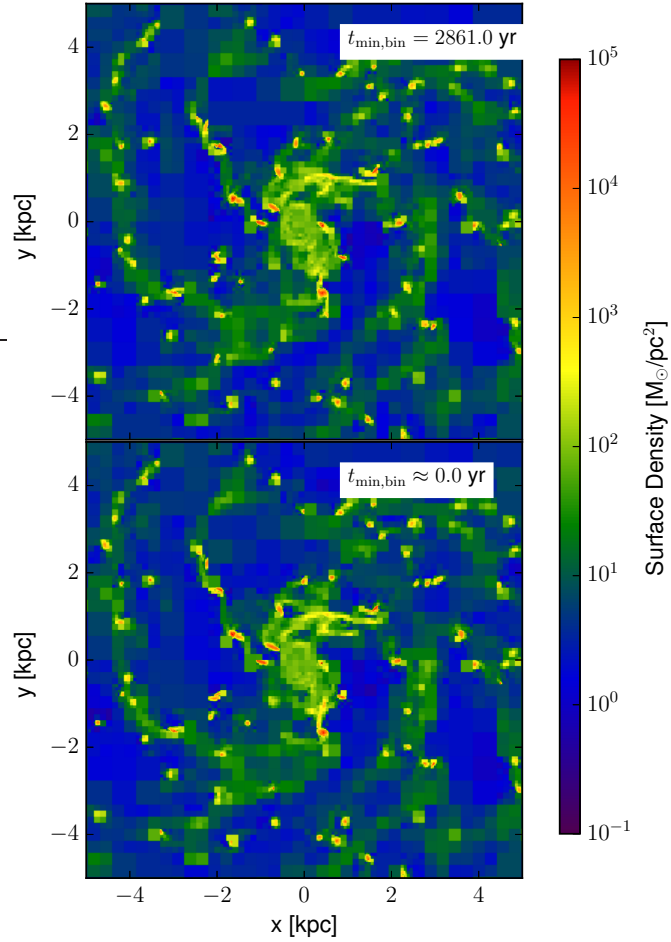


Figure 3.3: A projection of the gas surface density of *Giz-B* at $t = 200$ Myr of width 10 kpc at the centre of the galaxy. The top panel is the simulation with the minimum timebin of $t_{\text{bin}} = 2861.0$ yr and the bottom panel is the simulation without it ($t_{\text{bin}} = 0$ yr). The differences between the two galaxies are in the denser regions, of which could equally be explained from a simulation with choosing a different seed in the initial conditions.

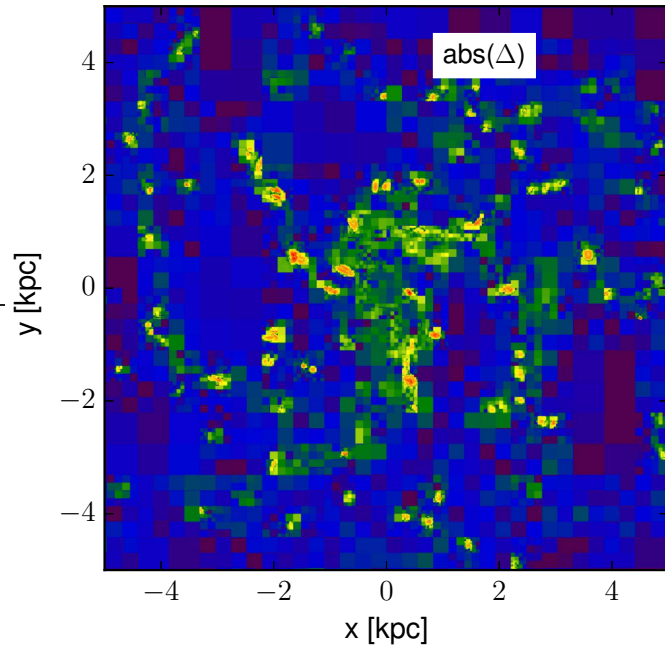


Figure 3.4: Following on from Figure 3.3. A projection of the absolute difference of the gas surface density between the $t_{\text{bin}} = 2861.0$ yr and $t_{\text{bin}} = 0$ yr runs for *Giz-B* at $t = 200$ Myr. Other than the exact positioning of the high density regions, of which will have a slightly different motion due to not having access to the finer timesteps, the two galaxies looks exactly the same and any differences that occur could also be generated with a different initial condition generation seed. The difference between the number of cells occupying different timestep bins can be found in Figure 3.2.

CHAPTER 3

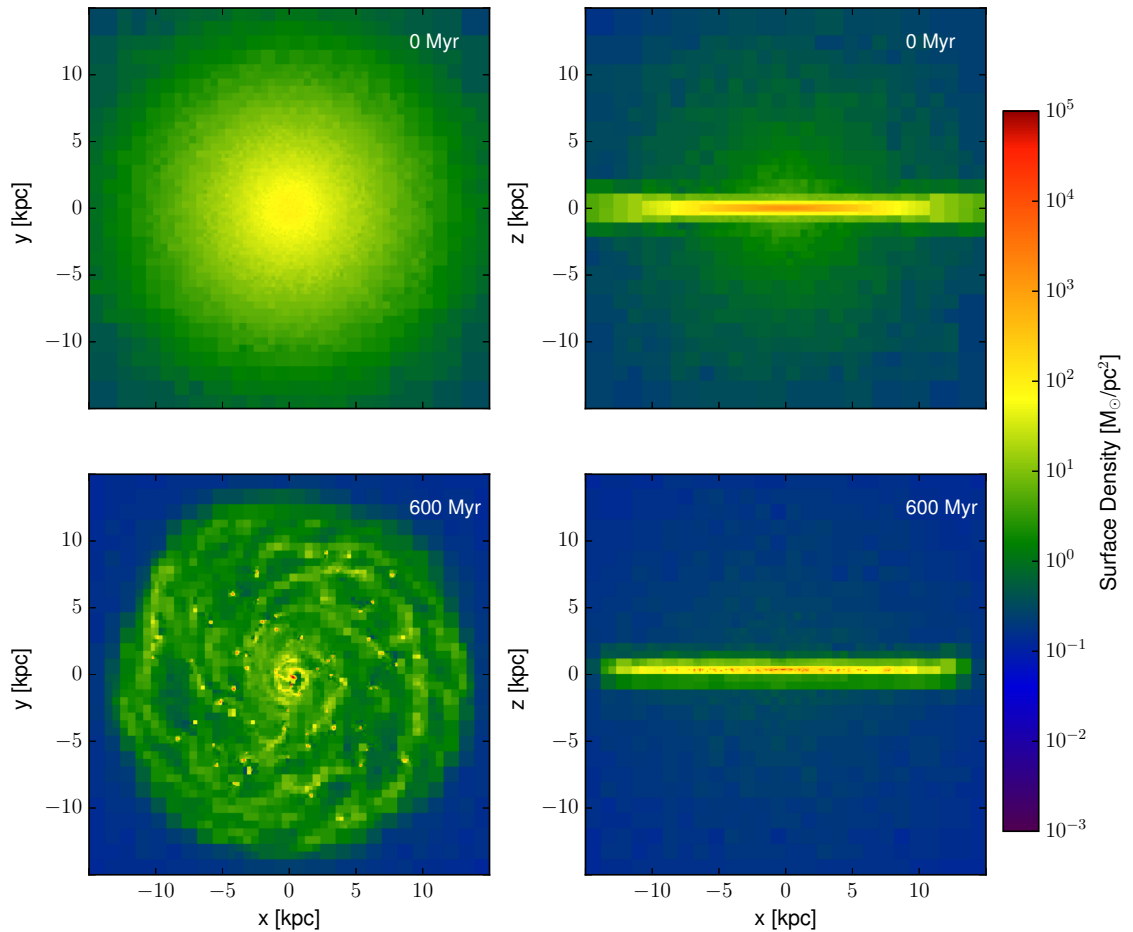


Figure 3.5: A 2 kpc-deep projection of the gas density distribution of *Giz-B*. The left hand panels show the galaxy face on and the right hand panels show the galaxy edge on. The top panels show the galaxy initial conditions and the bottom panels shows the galaxy after running the full 600 Myr of the simulation.

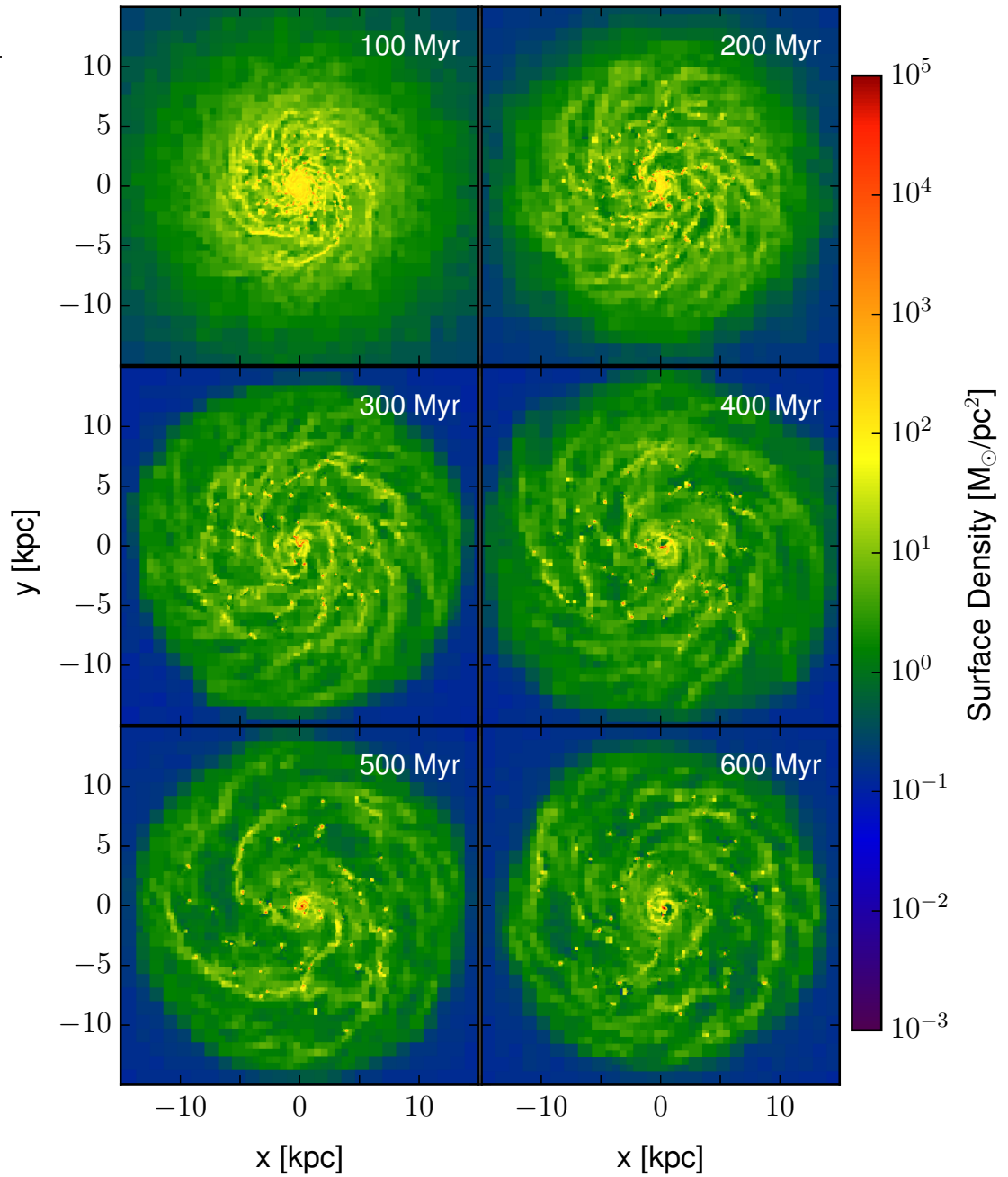


Figure 3.6: The time evolution of the gas density projection of the galaxy model *Giz-B* at six timesteps throughout its evolution. Self-gravity results in the collapse of internal structures and thus the formation of GMCs. The depth of this projection is 2 kpc.

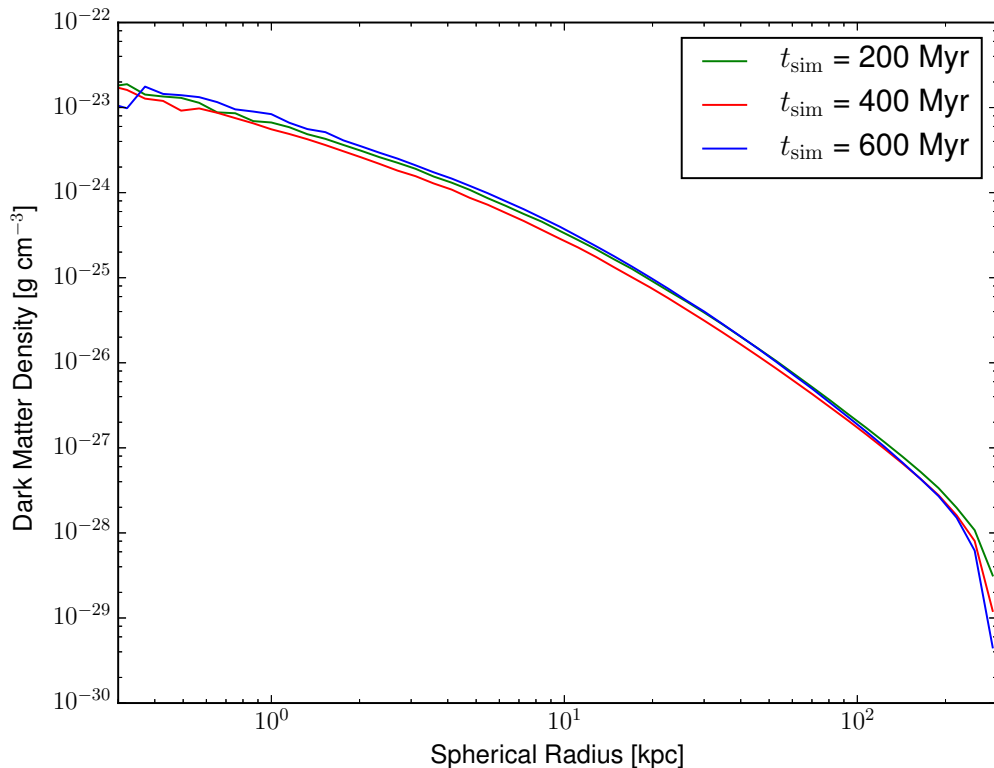


Figure 3.7: The density profile of the dark matter halo. The density profile stays relatively unchanged with time for simulation model *Giz-B*. The green line represents the timestep of $t = 200$ Myr, red for $t = 400$ Myr and blue for $t = 600$ Myr.

formation of giant molecular clouds which peak in the 200 Myr snapshot. Additionally the gas disc decreases in radius as the gas core scatters stellar particles. The depth of the projection in these figures is 2 kpc.

The dark matter halo density distribution remains relatively unchanged with time as shown in Figure 3.7. One of the reasons that the density distribution is relatively unchanged is due to the galaxy is not undergoing any physical feedback processes which are known to influence the structure of the halo (e.g. Read et al. 2016) as well as lacking any merger activity. However its stable nature means that we can rule out any significant influence of dark matter on the physics of galactic

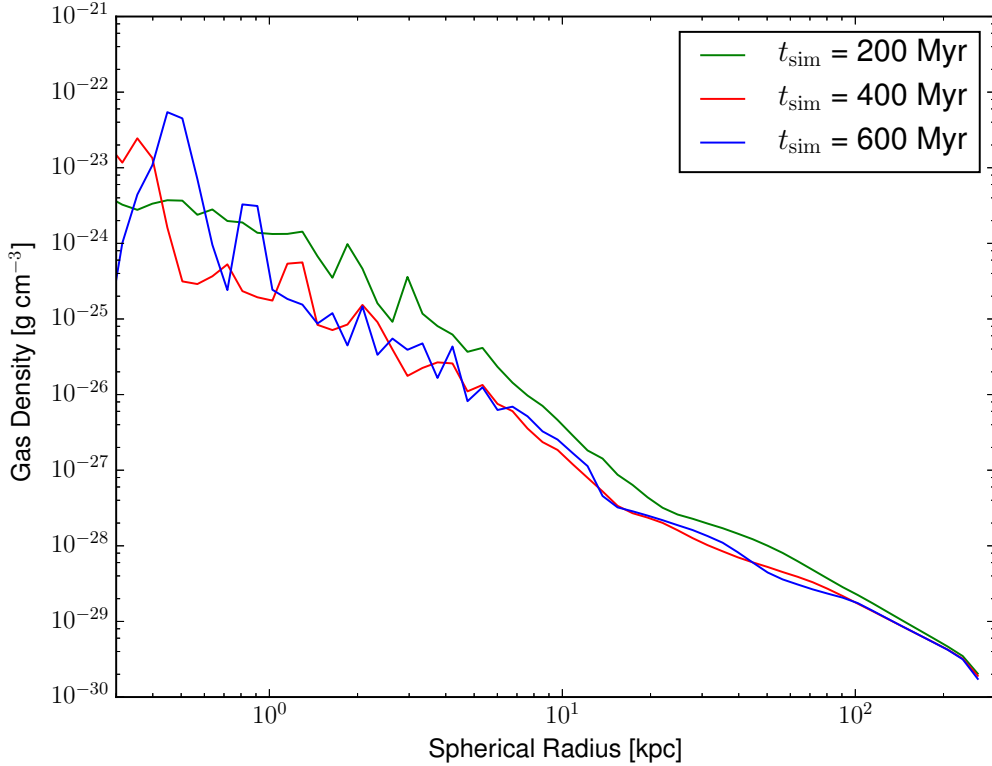


Figure 3.8: The density profile of the gas halo of *Giz-B*. The green line represents the simulation timestep of $t = 200$ Myr, red for $t = 400$ Myr and blue for $t = 600$ Myr.

outflows. We should note that a halo with substructure would have an impact on spiral structure (e.g. Widrow & Dubinski 2005; Dubinski et al. 2008).

Figure 3.8 shows the density profile of the hot gas halo originating particles with time. The initial density profile of the halo at $t = 0$ Myr is a result of solving Equation 3.42. Outer regions of the gas halo beyond 10 kpc remain relatively unchanged although there are evidence of small density perturbations (perhaps slight ringing) fluctuating around the initial density. For $r_g < 10$ kpc, gravitational collapse combined with cooling, results in an increase in density towards the central regions of the galaxy.

The cooling flow of hot gas halo particles into the central region deposits mass

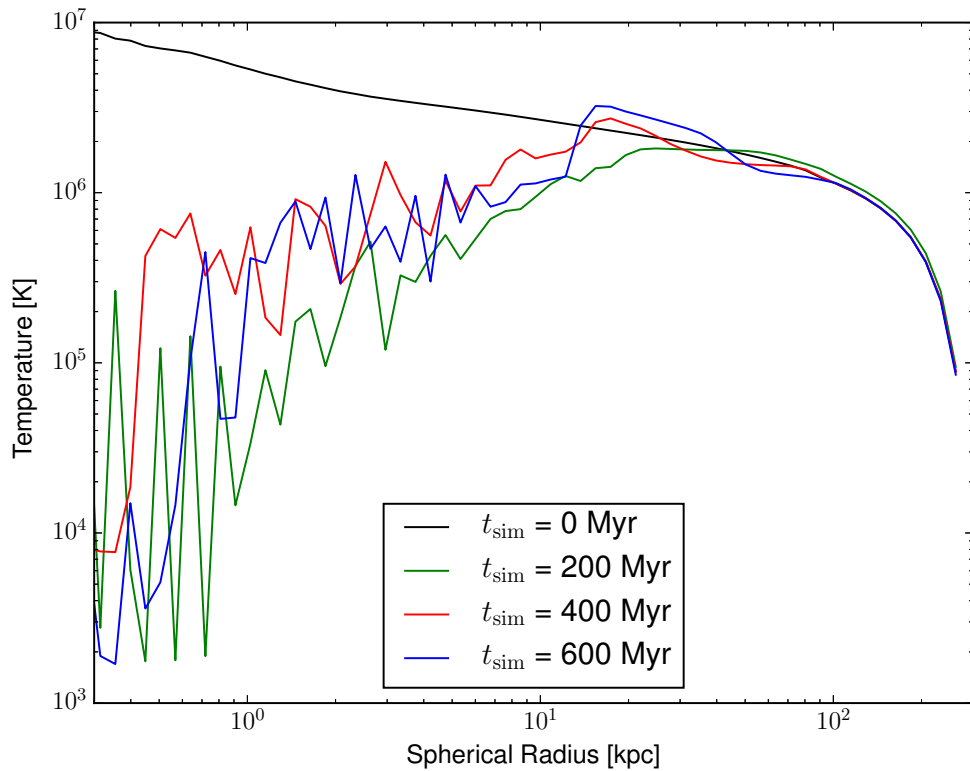


Figure 3.9: The temperature profile of the gas which has its origins as part of the hot gas halo. The black line represents the simulation *Giz-B* at $t = 0$ Myr, green for $t = 200$ Myr, red for $t = 400$ Myr and blue for $t = 600$ Myr. The central region (< 10 kpc) of the gas halo is gravitationally cooled.

CHAPTER 3

whilst at the same time changing the gas temperature profile. Figure 3.9 shows the temperature profile of the hot gas halo originating particles. The temperature profile at $t = 0$ Myr is generated from solving Equation 3.44 and evolves from that profile over time. The inclusion of the cooling which is not accounted for in the kaufmann equation (Springel 2005; Wiersma et al. 2009) leads to the decrease in temperature within the inner regions which grows with time corresponding to the cooling radius. The only cooling that is of relevance in this model is H, He and H_2 . and our cooling is thus less efficient than in Sur et al. (2016).

Figure 3.10 shows the relation between particle density and the Jeans mass. The Jeans mass is computed from Equation 3.47. The distribution of gas amongst the disc and halo components is obvious in the top left panel which shows the initial conditions (0 Myr). The disc gas population occupies the straight line of material in the bottom of the image, whereas the halo gas material occupies the top left region. As time evolves the gas disc becomes denser, and thus this region starts to slide to denser and lower Jeans mass regions. Additionally, the hot gas halo collapses and becomes denser. In some cases, flows onto the galaxy create a bridge between the distribution of hot and cold gas. The collapse of the hot gas decreases the temperature and increases the density, which decreases its Jeans Mass. The dashed line in Figure 3.10 represents the region in which any gas particle below it is dense enough to collapse and form stars. These particles are however found in the most dense regions of giant molecular clouds, and the central regions of the galaxy. However, our goal is to study how the ISM stirred, and not the collapse of individual objects. Since gas particles in these dense clumps are locked into them gravitationally, this fact does not impact our study.

The distinction between the disc and halo gas particles in the initial conditions is obvious with the halo gas occupying hot and dense regions, and the outer edges of the halo cold and sparse regions. The disc gas is set to 10000 K in the initial

CHAPTER 3

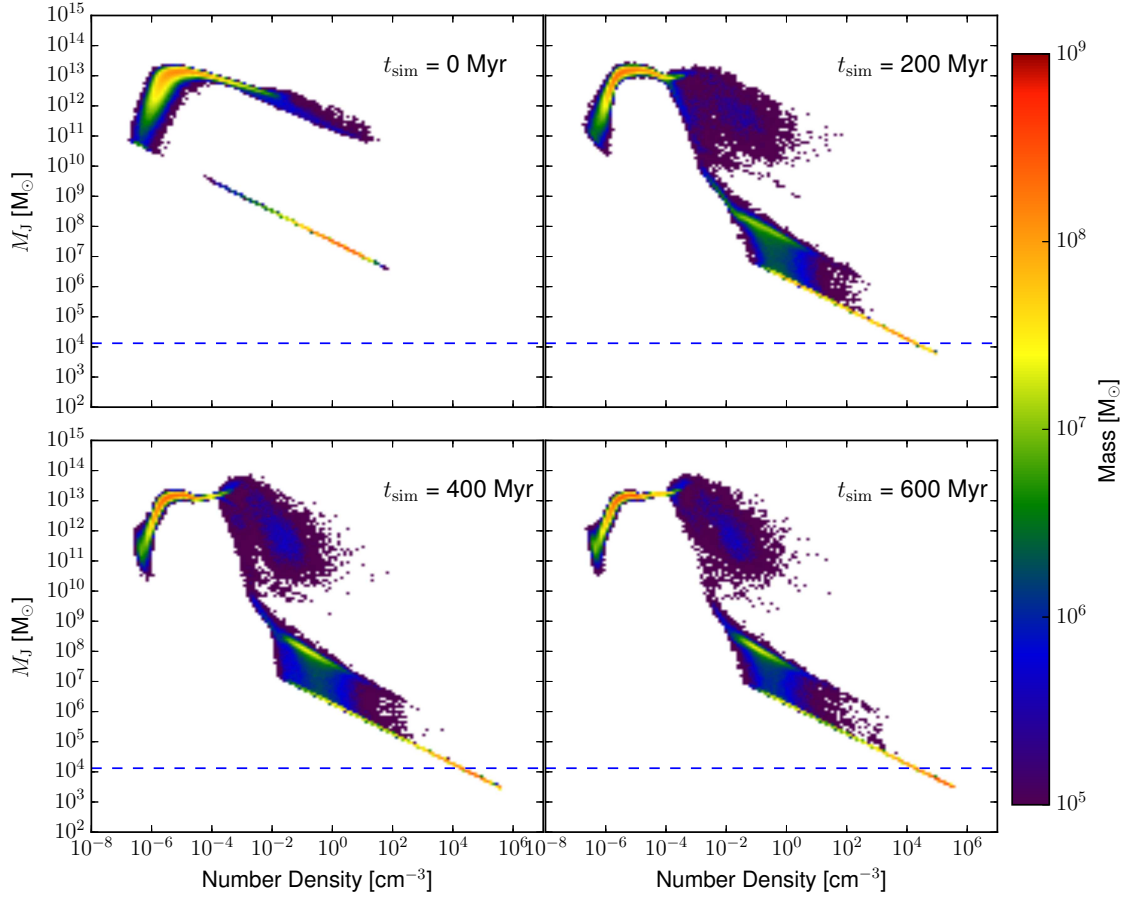


Figure 3.10: The relation between the theoretical Jeans mass (M_J) and the particle density at four timesteps during the evolution of *Giz-B*. The blue dashed line represents the line in which any gas particle that is below will in fact be capable of forming stars. It is the minimum M_J in which if the Jeans mass is below the particle mass, then the gas particle becomes star forming. Gas cells with a Jeans mass below that limit are considered to be star forming. The mass of the particles is given by the colour of the point, as indicated on the colour bar.

CHAPTER 3

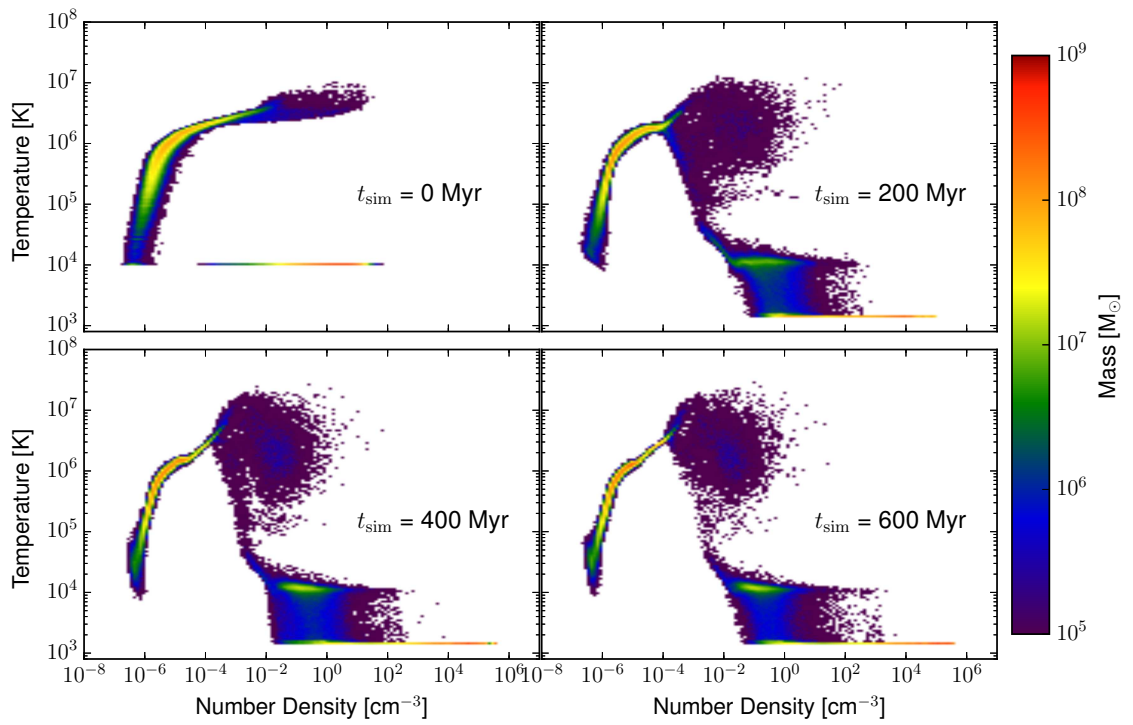


Figure 3.11: The relation between the gas temperature and particle density at four timesteps during the evolution of *Giz-B*. The mass of the particles is given by the colour of the point, as indicated on the colour bar.

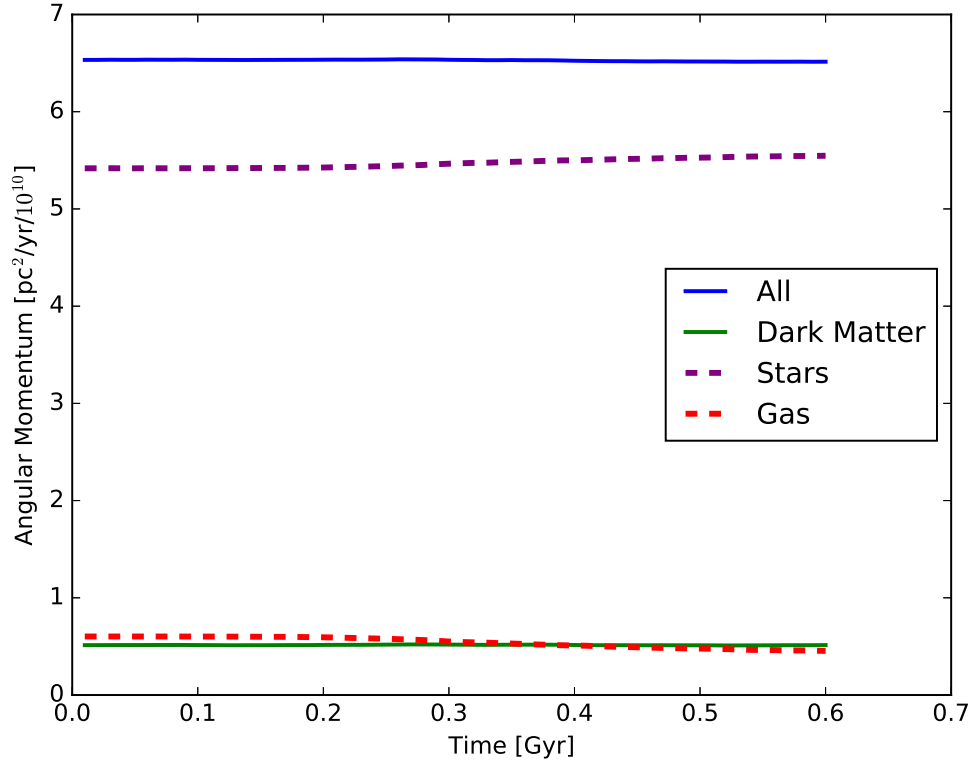


Figure 3.12: The evolution of the magnitude of the angular momentum for the gas, dark matter and stellar components of *Giz-B*. Angular momentum is transferred from the gas to the stars overall with time. The dark matter angular momentum remains unchanged.

conditions and then cools to the temperature floor of 1500 K (or 1000 K in the *Giz-A* run). The properties of these two gas population particles intermix relatively early on as the cooling flow begins. Figure 3.11 shows the relation between the gas temperature and particle density.

Figure 3.12 shows the angular momentum as a function of time. The most important aspect is that the overall angular momentum of our model remains conserved. Additionally, angular momentum is transferred from the gas population to the stellar population as star particles are scattered by the dense molecular clouds.

CHAPTER 3

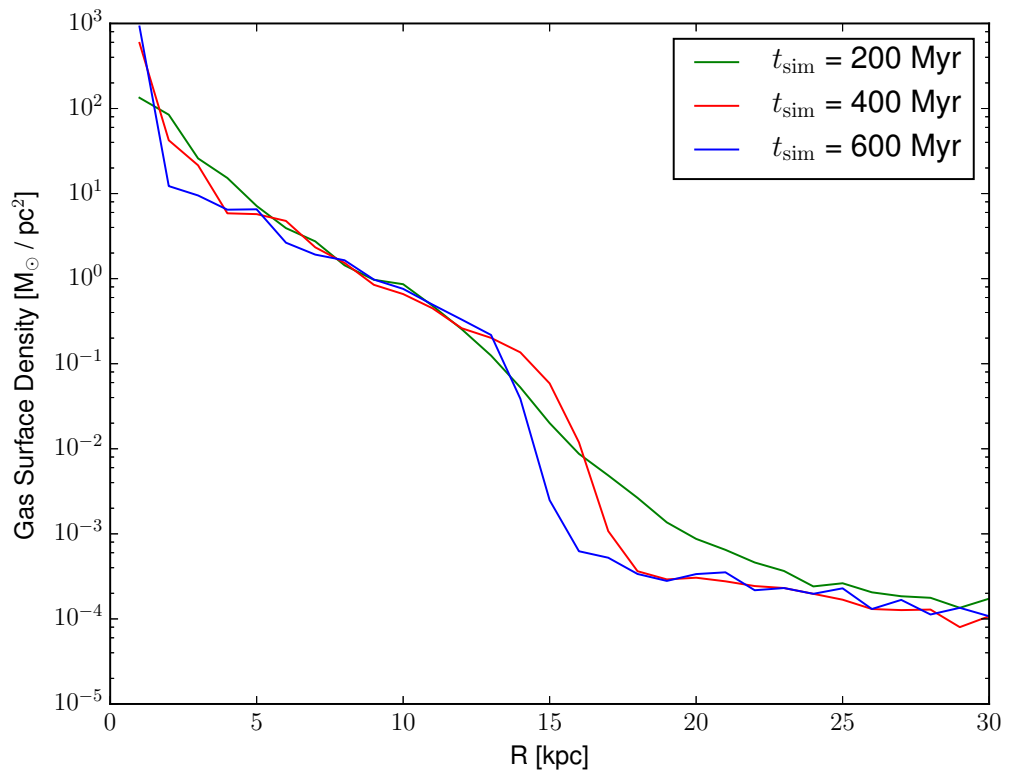


Figure 3.13: The gas surface density as a function of radius for *Giz-B*. As time evolves, the central region of the galaxy becomes denser, and the density of the material decreases in radius.

CHAPTER 3

Figure 3.13 shows the gas disc surface density Σ_g as a function of radius. We visualise the surface density of the disc within a height of 1 kpc. The surface density of the gas disc is visualised in Figure 3.6 of which confirms the hypothesis of a gas disc that gets smaller in radius and denser. Note this plot includes the intermixing of both halo originating and disc originating gas particles at $t = 0$ Myr.

Figure 3.14 shows the evolution of the tangential (dashed) and circular (solid) velocity profiles of the gas disc as a function of time. The circular velocity profile, which is largely dominated by dark matter at the outer radii, remains relatively unchanged which implies the overall distribution of matter remains unchanged. The rotational velocity is a good tracer for the radius of the galactic disc, and this supports the notion that the gas disc is collapsing in radius.

The morphological properties of *Giz-A* are very similar to our galaxy of choice *Giz-B*. As such we do not show the morphological evolution properties of *Giz-A*. The differences become more apparent when studying the outflow properties of the galaxy.

3.5.3 Giant Molecular Cloud Formation

We investigate the formation of giant molecular clouds as a consistency test of this model relative to other galactic evolution simulations. Figure 3.15 shows the evolution of GMCs with time in both *Giz-A* and *Giz-B*. Unsurprisingly, the choice of a lower temperature floor in *Giz-A* leads to the formation of a larger amount of GMCs due to the lower pressure support. These clouds are formed from the rapid collapse of the internal structures of the gas disc. As in Williamson & Thacker (2012) we show that the increase in cloud abundances correlates with the decrease in temperature floor, and again in (Williamson & Thacker 2012) the change in temperature floor does not change the location of the peak of formation of clouds. The peak of GMC formation occurs at 0.13 Gyr in both simulations. Due to time

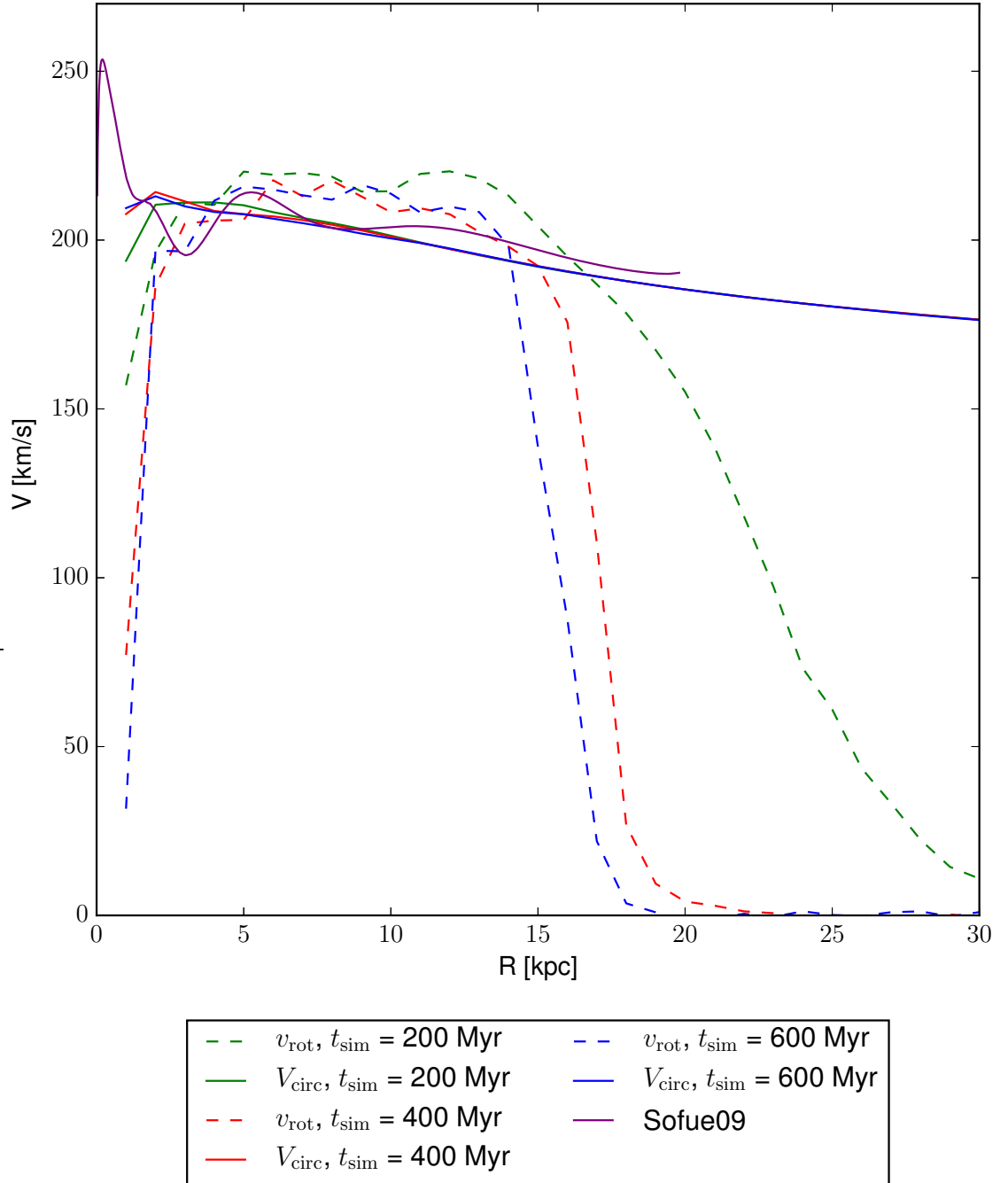


Figure 3.14: The tangential (dashed) and circular (solid) velocity profiles as a function of radius for *Giz-B*. The colours green, red and blue represent 200, 400 and 600 Myr respectively. The tangential velocity decreases as a function of time as the non-rotating gas halo encroaches. We also include the work of Sofue et al. (2009) for comparison from observations of the Milky Way.

CHAPTER 3

constraints, we did not vary the smoothing length. Softening (increasing the size) of the smoothing length would shift the location of the cloud formation peak, as well as limit the formation of clouds. Our distribution of clouds is best compared in literature to the models *LowResMW* and *LowVisc* as shown in Williamson & Thacker (2012) Figure 2. We have a similar softening length to both of these models of 50 pc whereas those models are 60 pc for the gas. Although their galaxy disc is more extended and their dark matter halo is slightly more massive. If we were to increase the softening length, gravity would be smoothed out over larger distances, this will reduce the particle number density over smaller regions of space and as shown in Williamson & Thacker (2012) will reduce the abundance of clouds. Even though Williamson & Thacker (2012) included the Robertson-Kravstov dynamic temperature floor we get similar results here. This means that we have not had to compromise other physical factors.

Figure 3.16 shows the evolution of GMC mass function with time. The most massive clouds exist half way through the evolution of the galaxy at $t = 300$ Myr with the abundances of low mass clouds towards the beginning and end of the simulation. This shows that the self gravitating disc is dissolving which causes clouds to fragment with time. We do not form clouds as massive as in Williamson & Thacker (2012) but this could be due to our disc being smaller in mass and radius. Therefore less material is available to form more massive GMCs in the first place. We do not show the *Giz-A* cloud mass function since in its normalised form is indistinguishable from *Giz-B*. The mass function at the more massive end oscillates, thus is a result of the resulting formation of new GMCs and the evaporation of others.

Figure 3.17 shows the velocity dispersion of the disc originating gas particles and the giant molecular clouds that they form. The velocity dispersion of the clouds is smaller in magnitude in comparison to the disc gas. Since these clouds are more

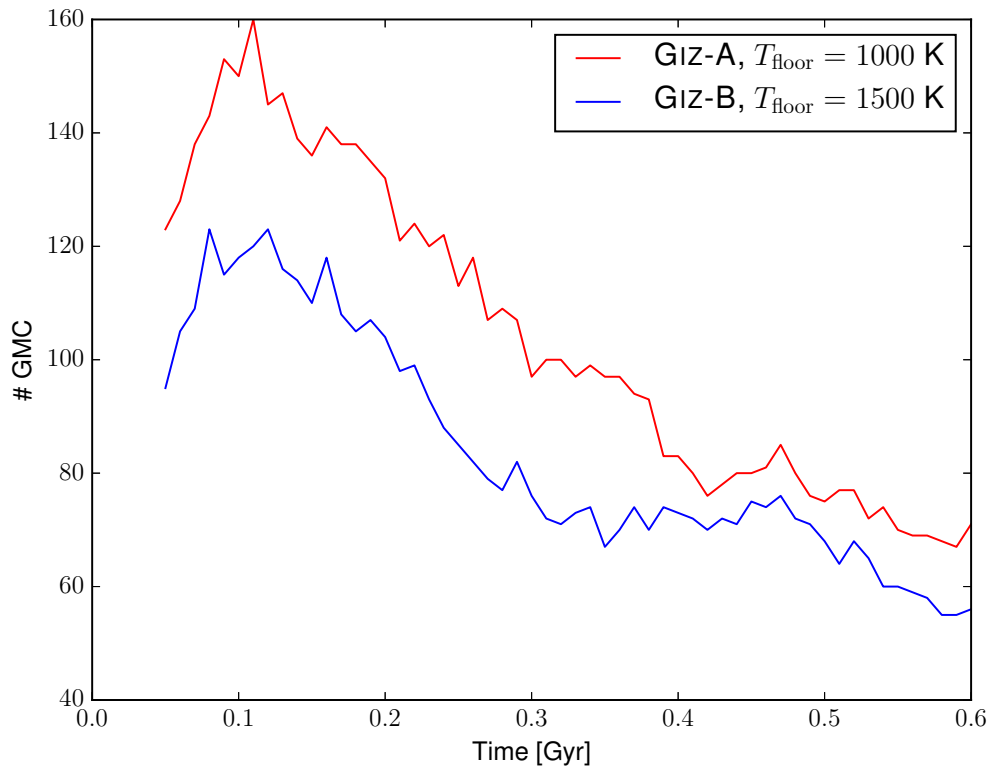


Figure 3.15: The evolution of the GMC number function for *Giz-A* and *Giz-B*. Both functions peak at 130 Myr and then the number of clouds decreases. *Giz-A* has a lower temperature floor, and thus more structure is able to collapse to form GMCs. This figure is consistent with results found in shown in Williamson & Thacker (2012), such that a lower temperature floor corresponds to an increase in cloud abundance.

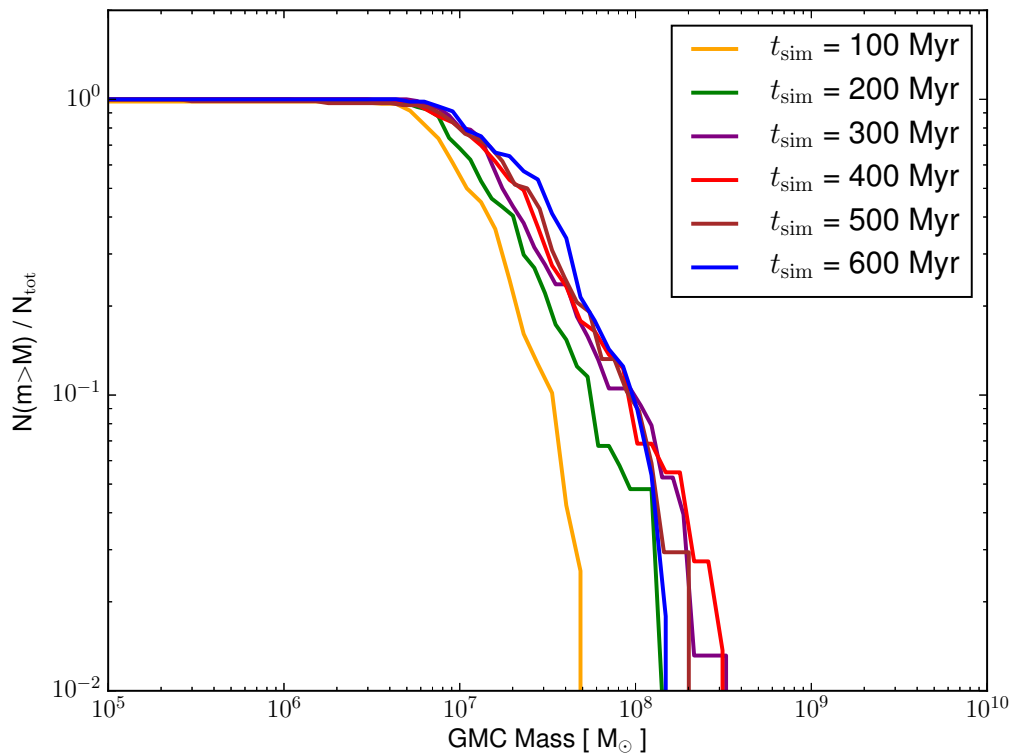


Figure 3.16: The time evolution of the GMC normalised mass function for *Giz-B* (1500 K). The most massive clouds exist at 300400 Myr, and an abundance of low-mass clouds is seen at early times (100 Myr).

CHAPTER 3

massive, they thus drive turbulence and outflow of gas material. We show the difference between the two temperature floors here since at later times there is variation between the two runs as a result of varying the temperature floor. What is interesting is that the velocity dispersion of the clouds in *Giz-A* is greater than *Giz-B* towards later times.

3.5.4 Outflow Physics

Next we discuss the gas outflow rates on the surface of the gas disc of our galaxy. Unless otherwise stated, the discussion here focused on the galaxy *Giz-B* which has a temperature floor of 1500K and we again mainly compare with the work in Sur et al. (2016), although extending to lower surface densities and outflow rates.

Two factors contribute to putting a lower limit on the derived outflow rates. Firstly, by allowing the dense material to go slightly below its Jeans Mass we have created a population of GMCs that are significantly more dense than physically possible. Given their artificially small cross-section, and their comparatively low number this will produce a lower outflows as in effect less of the volume of the galaxy is being stirred. This causes artificial fragmentation within the cores of the GMCs. The physical implications of artificial fragmentation in the most dense regions are not tested overall, but these gas particles belong to structures we cannot fully resolve within this model. Overall artificial fragmentation is not likely to be an issue within our study of gas outflows since we aren't hugely interested in the small scale dynamics of these collapsing objects, rather it is the larger scale collisions the impact the kinetic structure of the outflows. Additionally, we have included an accreting hot gas halo which provides a mass flux on to the disc that would be expected to further suppress disc outflows. Even so, and despite our notably lower resolution, the galaxy outflow rates are broadly similar to the lower surface density galaxies as shown in Sur et al. (2016).

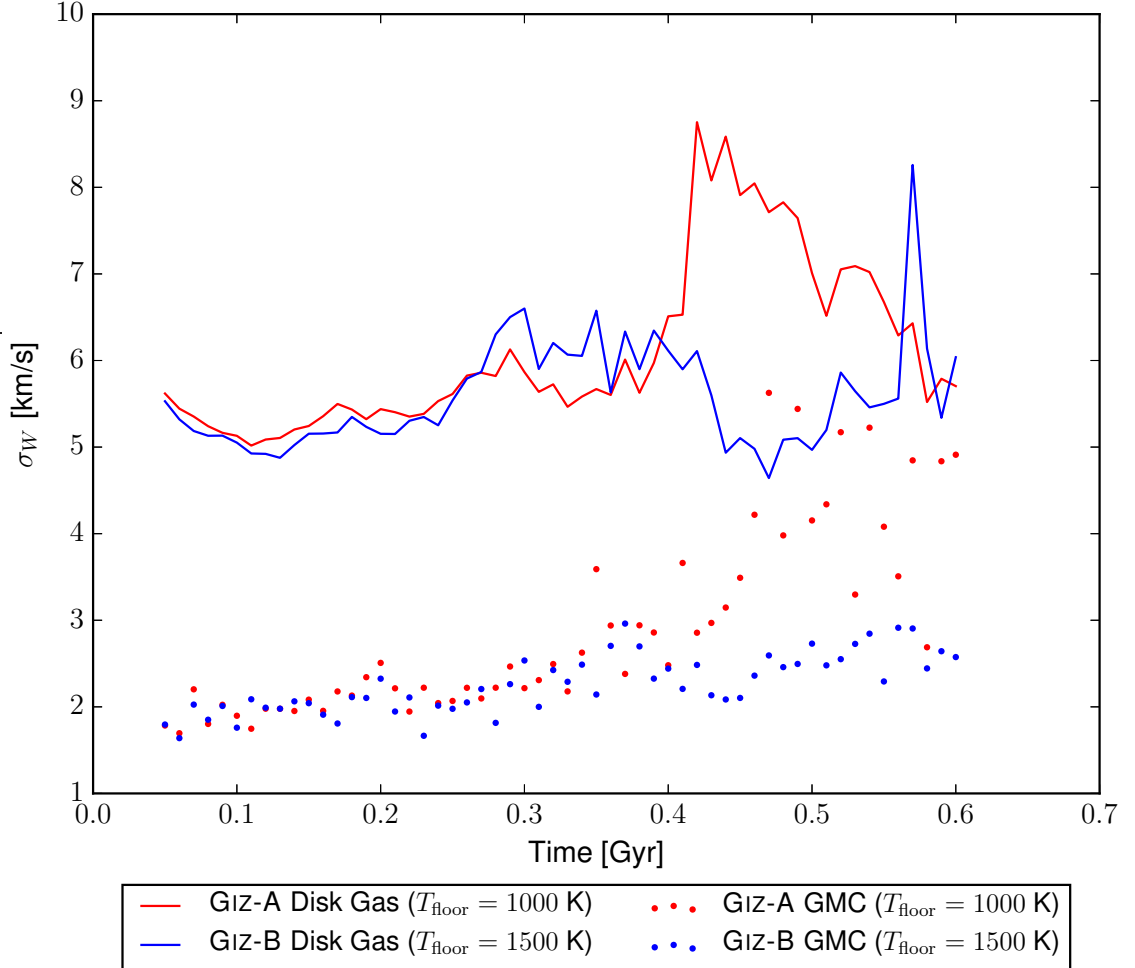


Figure 3.17: The evolution of the velocity dispersion in the z direction for GMCs and disc originating gas for *Giz-A* and *Giz-B*. The gas velocity dispersion is proportional to that of the GMCs that they form. The covariance between σ_z of the gas and the GMCs for *Giz-A* is 0.657 while for *Giz-B* the covariance is 0.077. The positive covariances indicate that the two datasets are directly related, though less related in *Giz-B* than in *Giz-A*. The clouds' velocity dispersion is smaller than the gas particles due to there being a relatively small number of GMCs and are massive structures, and are thus gravitationally bound to the disc.

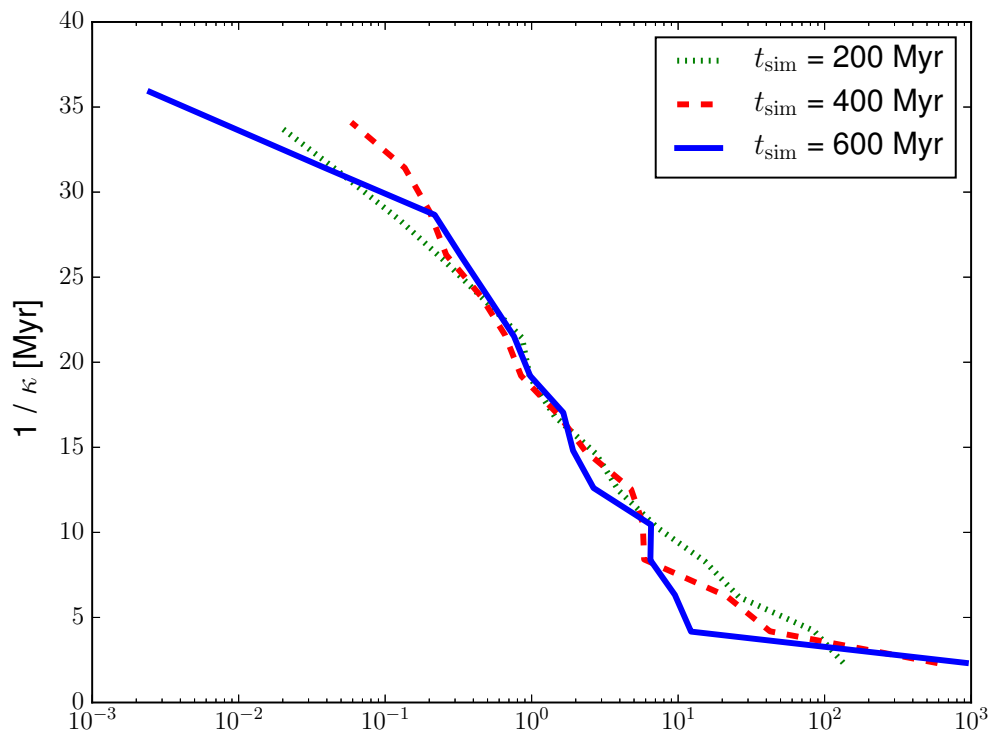


Figure 3.18: Epicycle frequency κ vs. gas surface density Σ_g for *Giz-B*. Regions of lower density have longer epicycle frequencies.

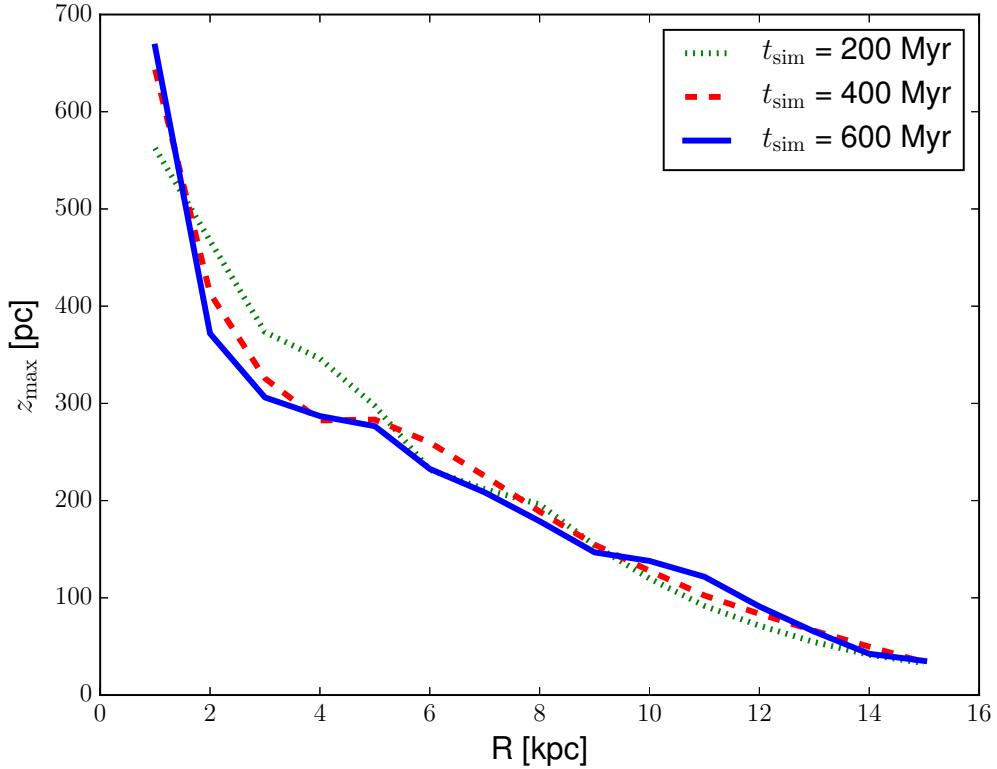


Figure 3.19: The scale height z_{\max} as a function of radius for *Giz-B*. Any disc originating gas material with a position $|z|$ that lies above z_{\max} is considered to be outflowing gas material.

Figure 3.18 shows the relation between the epicycle frequency κ and the gas surface density Σ_g for *Giz-B*. Since κ is related to Σ_g , regions of lower density have longer epicycle frequencies, but these are regions of larger galactic radii.

We show in Figure 3.19 the result of z_{\max} as computed in Equation 3.33. z_{\max} defines a scale height in which any disc originating gas material that lies above this height is considered to be outflowing gas material. Likewise any halo originating gas particle that ends up below this function is considered to be inflowing material. Unlike Sur et al. (2016), who consider boxes parametrized by the local surface density, we need to vary this quantity as a function of radius to reflect the lower surface

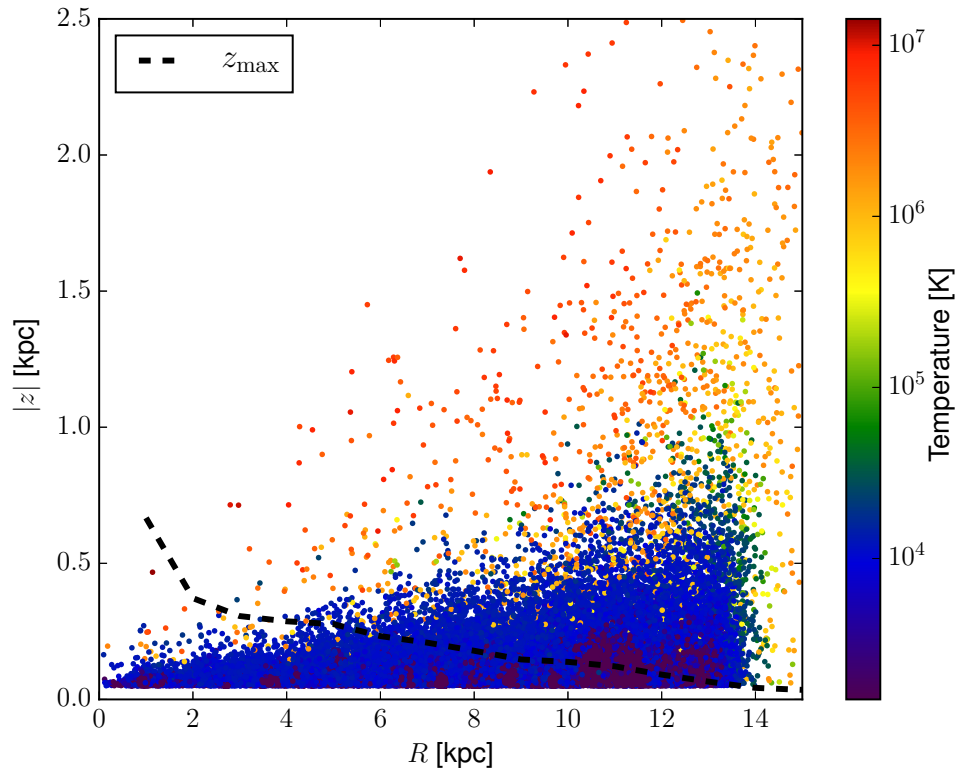


Figure 3.20: A plot of the position of disc originating gas particles at height Z above (or below) the disc at radius R with temperature T for *Giz-B*. This distribution of particles is taken at $t = 600$ Myr. The black dashed line represents z_{\max} at this time which effectively acts as the height of the gas disc. Any gas particle above this is considered to be outflowing. This figure shows that gas particles are pushed more than 1.5 kpc above the gas disc, confirming that turbulence alone can cause outflows.

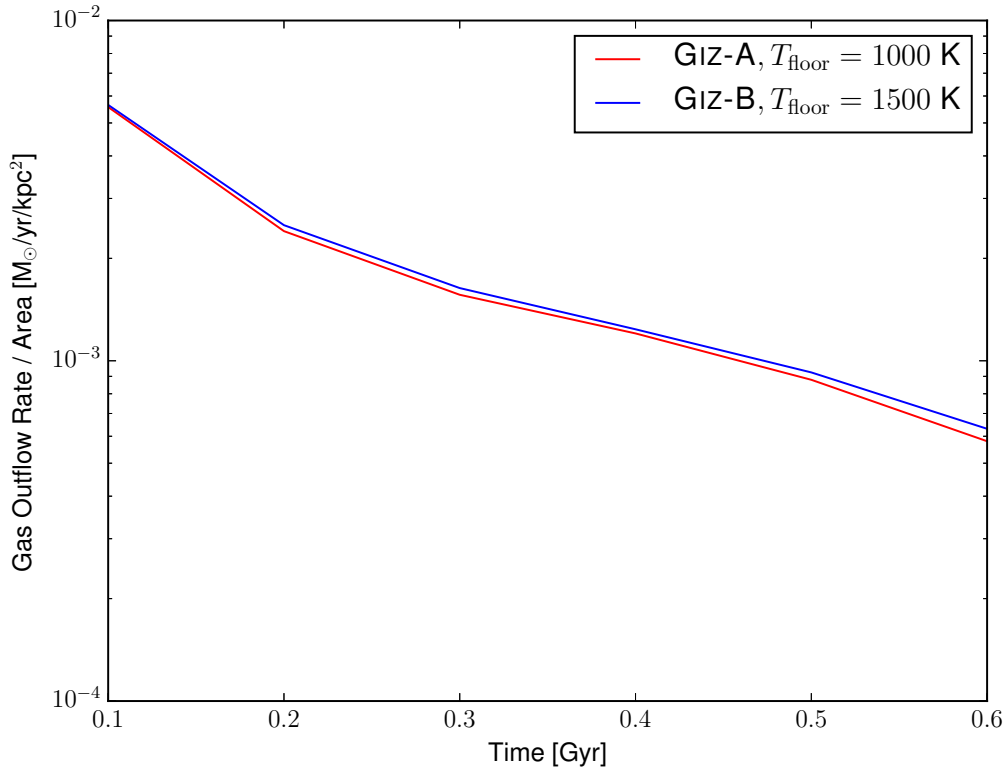


Figure 3.21: Outflow of material per surface area originating from the cold gas disc as a function of time for *Giz-A* and *Giz-B*. As confirmed in Sur et al. (2016), the temperature floor plays little role in the amount of outflowing material.

densities in the outer parts of the galaxy.

In Figure 3.20 we describe the distribution of disc gas originating particles at $t = 600 \text{ Myr}$. This illustrates the distribution of the particles which have been ejected from the disc. Some of these particles reach more than 1.5 kpc above the disc.

Figure 3.21 shows the outflow rate of gas as a function of time for *Giz-A* (1000K) and *Giz-B* (1500K). This elaborates our point that a lower temperature floor (a smaller and denser abundance of clouds) corresponds with a lower outflow rate per unit time. The key point here is that there appears to be very little variation in

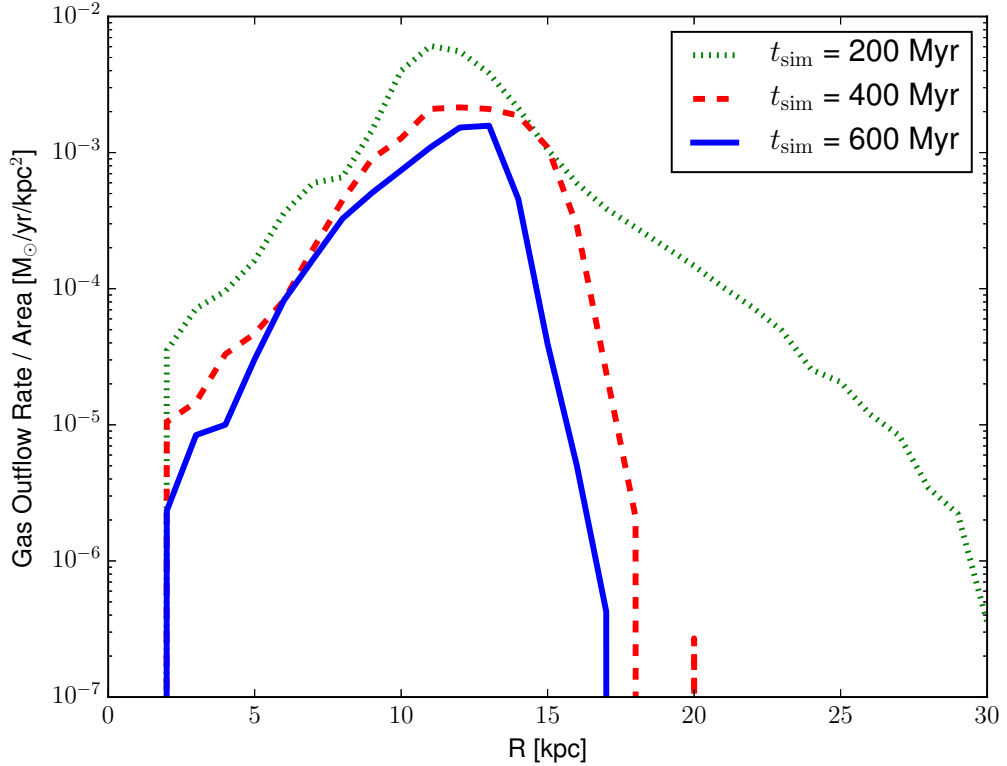


Figure 3.22: Outflow rate of material per surface area originating from the cold gas disc as a function of radius for *Giz-B*. The peak position of the outflowing material is constant over time, though the magnitude of the peak decreases.

outflow upon varying the temperature floor as concluded in Sur et al. (2016). Due to time constraints, we do not have enough time to sample any different temperature floors to further confirm this.

Figure 3.22 shows the outflow rate per surface area as a function of radius. The radius at which peak outflows occur remains consistent with time, but the peak itself decreases with time. This could be due to the transfer of angular momentum from the gas to the stars, which causes the gas disc to collapse and get denser.

Figure 3.23 shows the relation of outflows to the surface surface density. There is a linear relation between the outflow rate per surface area and the surface density on

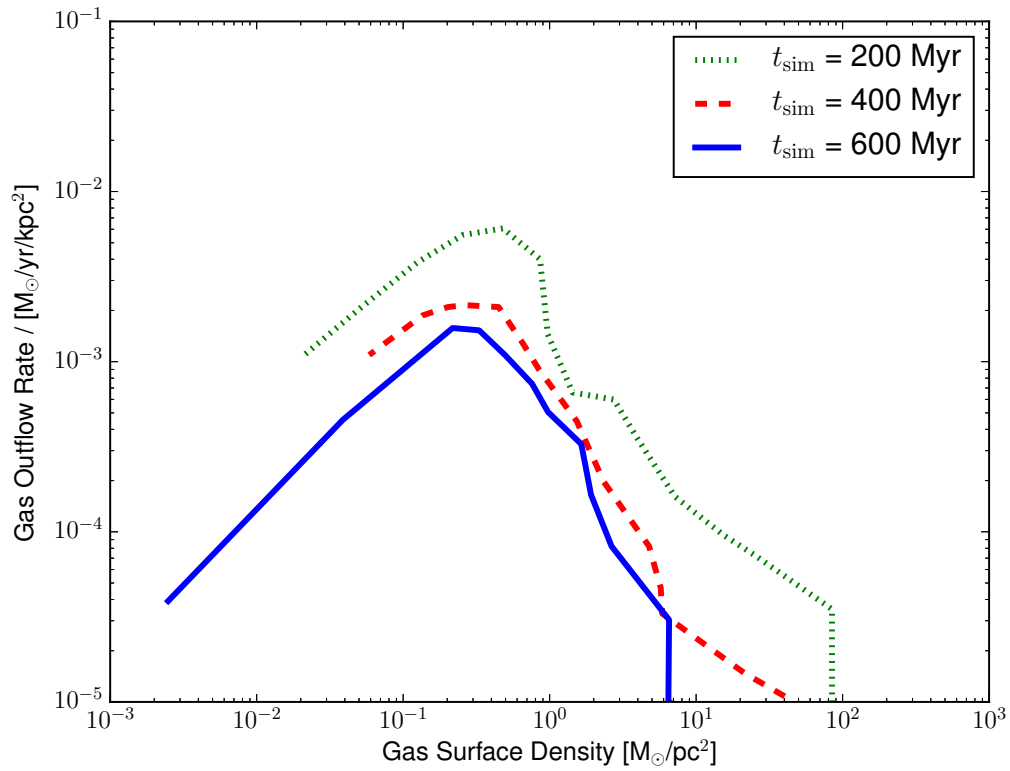


Figure 3.23: Outflow rate of material per surface area as a function of surface density for *Giz-B*. Below $\Sigma_g = 10^0 M_\odot \text{pc}^{-2}$, the data agrees with the logarithmic relationship seen in Sur et al. (2016). However above $\Sigma_g = 10^0 M_\odot \text{pc}^{-2}$ the relationship breaks.

CHAPTER 3

the log scale. This relation remains consistent below $\Sigma_g = 100 M_\odot \text{ pc}^{-2}$. However this relation seems to not exist in denser regions of the galaxy. A galaxy with a larger and more extended radius of material with a dense bulge will have less outflows in the central region. As the galaxy collapses and the surface density additionally smooths out (see Figure 3.13), the linear relation between outflow and surface density appears. This contradicts the discussion in Sur et al. (2016), but their work does not include other physics that our model has. Most notably, we include the inflow of hot gas as shown in Figure 3.24. The inflow rate of hot halo gas is larger at radii closer to the galaxy centre. However due to time constraints, we cannot confirm whether this is the cause of quenching of the outflow rate at larger densities. It could either heat up the outflowing material as it cools, causing more material to outflow, or the pressure of the inflow pushes against any potential outflowing material, causing it to become bound to the disc. Figure 3.25 compares the inflow and outflow rates as a function of time. Whilst the inflow rate is relatively consistent, the outflow rate decreases as a function of time. Additionally, Figure 3.26 shows the velocity dispersion of the gas as a function of surface density. Here we hypothesise that inflows could be driving the velocity dispersion at higher densities (closer to the centre) and disc turbulence at less dense regions.

3.6 Conclusions

In this study, we explored accretion and outflows in a Milky Way-like galaxy solely from the hydrodynamic perspective, i.e. in the absence of stellar feedback. We ran the model for 600 Myr to investigate the impact of turbulence-driven galactic outflows with a focus on quantifying the *lower limits* on the outflow rate produced via this mechanism. We used the GIZMO MFM method due to its accuracy in handling instabilities and turbulence. With the inclusion of an accreting halo and giant molecular clouds with a mass beyond the Jeans limit, thereby reducing their

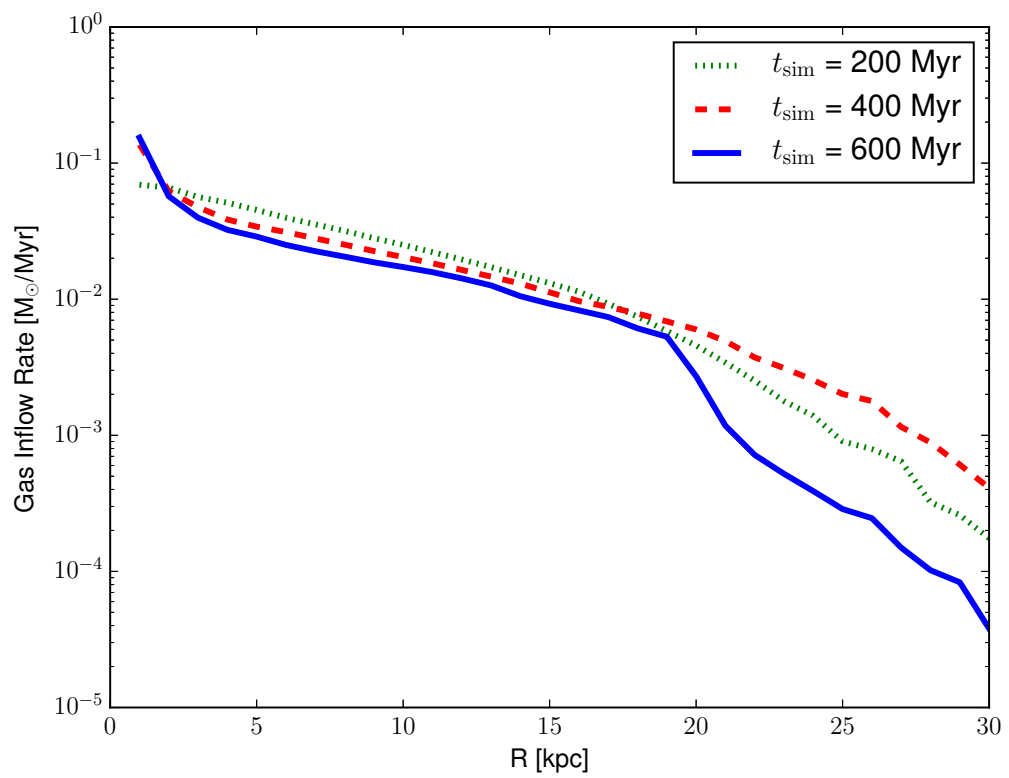


Figure 3.24: Inflow rate of hot halo gas material per surface area as a function of surface density for *Giz-B*.

CHAPTER 3

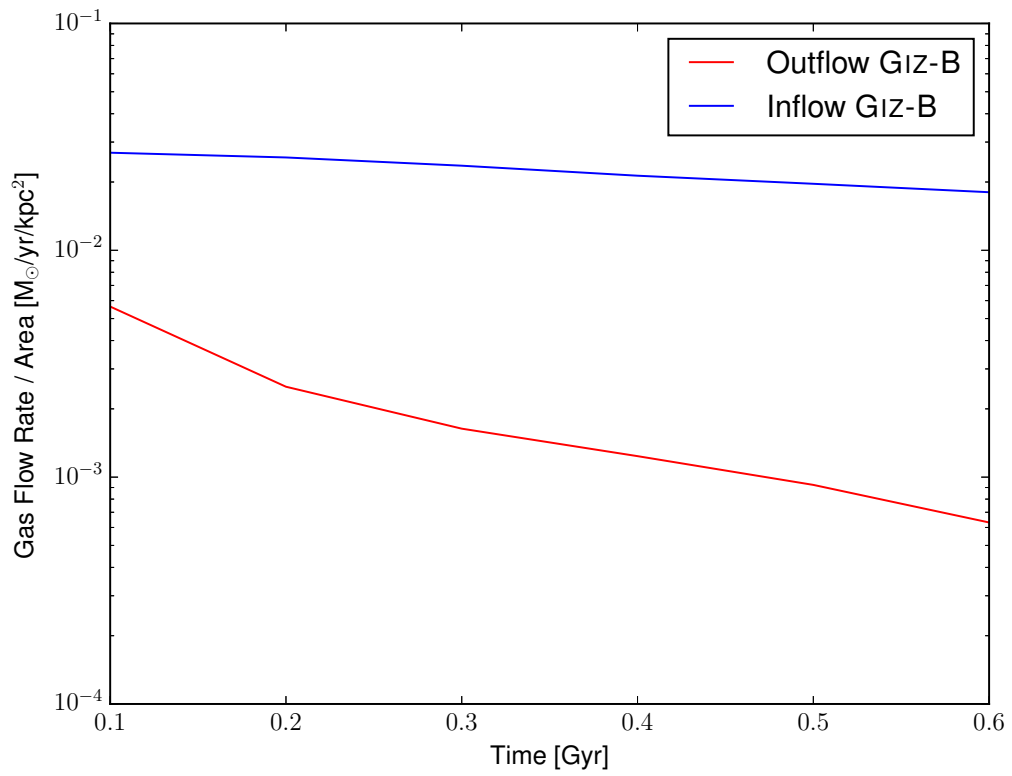


Figure 3.25: Flow of gas as a function of time for *Giz-B*. The inflow is fairly constant over time, while the amount of outflowing material decreases as the models evolve with time.

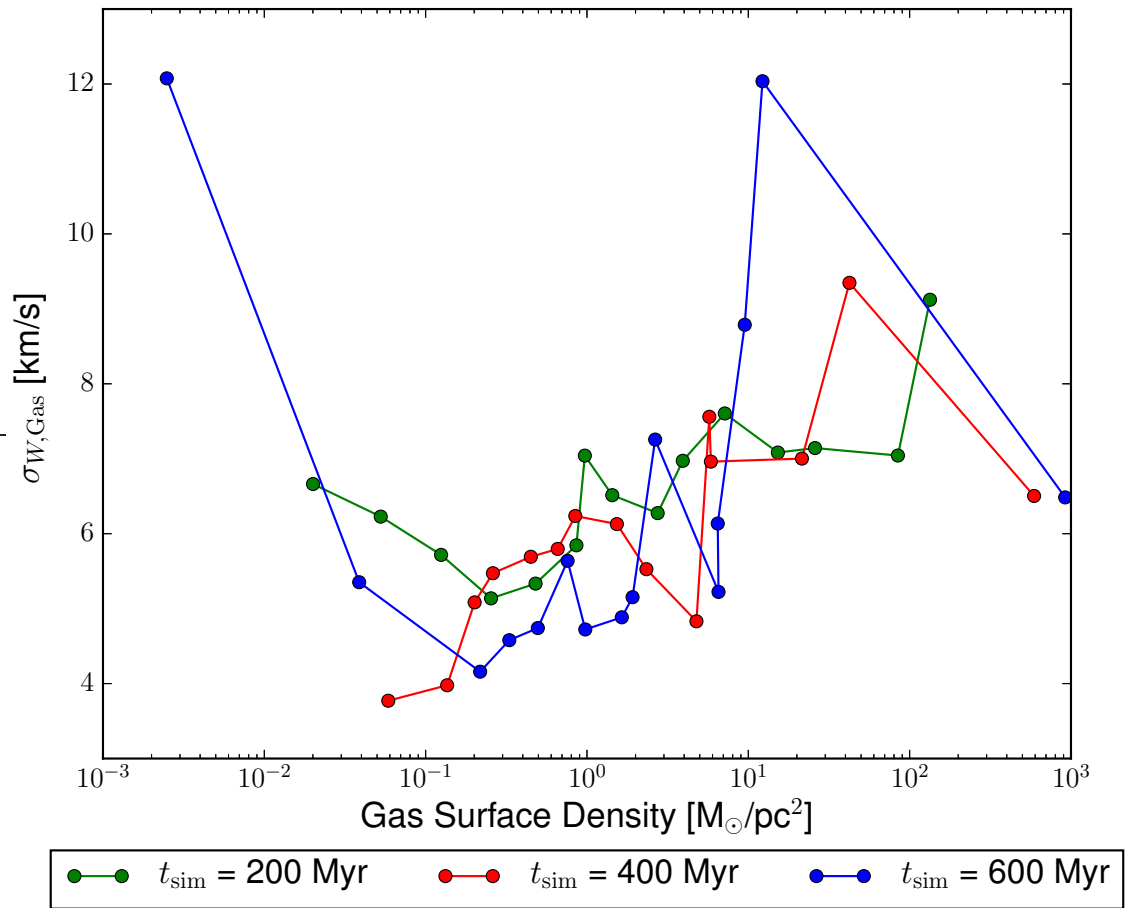


Figure 3.26: The velocity dispersion of the disc z axis σ_z as a function of surface density for *Giz-B*.

CHAPTER 3

cross-section for interaction, we have been probed the lower estimates for outflow rates as a function of surface density. Over the entire period of the simulation the net outflow above the disc (not out of the halo) is $2.67 \times 10^8 M_{\odot}$, whereas we have an inflow of $7.64 \times 10^9 M_{\odot}$.

With respect to the two separate simulations with different temperature floors, we find very little difference between the observed outflows. This confirms reaffirms the conclusion in (Sur et al. 2016) applies within a galaxy simulation in addition to their idealised situation. The temperature floor however does have an impact on the formation of giant molecular clouds, of which are turbulent driving regions of the gas disc (Agertz et al. 2009a). Nonetheless, despite population counts that can differ by 30%, as noted the net outflows remain broadly similar.

The scaling of outflows versus surface density we derive are different to those presented in Sur et al. (2016), but reflect the nature of the problem we are studying rather than actual parameter dependencies. In the disc environment, which includes higher local self-gravity at higher surface densities, the logarithmic relationship for surface densities higher than $\Sigma_g = 100 M_{\odot} \text{ pc}^{-2}$ breaks. Although not fully investigated, this is also likely related to the inflow of hot halo gas. We are, however, reasonably consistent with the outflow abundances as a function of surface density as shown in the top panel of Figure 2. in Sur et al. (2016) for surface densities below $\Sigma_g = 100 M_{\odot} \text{ pc}^{-2}$. We note that the outflow rate of cold disc gas decreases with time whereas the inflow rate is approximately consistent. This is consistent with a reducing population of turbulent drivers, namely the molecular clouds.

Despite different physics models in other simulations, we derive broadly similar velocity dispersion for the gas in the vertical direction. Other work has found values around 5.7 km s^{-1} (e.g. Shetty & Ostriker 2008; Kim et al. 2013) and over the lifetime of the simulation we find values in the range $5\text{--}6 \text{ km s}^{-1}$ with a small number of short-lived peaks. The similarity of these values with other work that includes

CHAPTER 3

feedback is broadly suggestive of a natural scaling that arises out of distinctly different local physics mechanisms. It also highlights the characteristic anisotropy in the velocity dispersion in galaxies.

Overall our results reaffirm that turbulence can lead to outflows, albeit weak ones in evolved low surface-density disc. In terms of unbinding material from the halo, feedback remains the primary candidate. However, in terms of mixing in the circumgalactic environment, turbulence driven outflows could play a significant role. For high redshift galaxies, which both have higher surface densities and significantly more local velocity dispersion the effect will be even more pronounced. Future simulations examining these effects will be of significant relevance in the James Web Space Telescope (JWST) era.

Chapter 4

Conclusions and Future Work

In this thesis, we discussed two physical aspects of galaxy formation models. We focused our attention on the formation of Late-type galaxies with properties similar to that of the Milky Way. Specifically in Chapter 2, we explored chemical evolution of a simulated Milky Way-like galaxy and studied an analogous solar neighbourhood region inhabiting it. We use different analytical techniques to compare the Solar neighbourhood region with the Gaia-ESO and RAVE surveys. In Chapter 3, we discussed the physics of gas outflows on the surface of the gas disc component of the galaxy. In this chapter, we shall re-iterate the conclusions of this work and discuss avenues for possible future work.

4.1 Matching Chemo-Dynamical Simulations to Observations of the Milky Way

We investigated different methodology for comparing a chemodynamical simulated Milky Way-like galaxy. We use the RAMSES-CH code (Few et al. 2012a, 2014), a patch to RAMSES (Teyssier 2002) to chemodynamically simulate *Selene-CH* which is based off the initial conditions for *Selene* presented in Few et al. (2012b). We

CHAPTER 4

compare the chemical properties of *Selene-CH* in an analogous solar neighbourhood with results from the Gaia-ESO (Gilmore et al. 2012; Randich et al. 2013) and RAVE surveys (Steinmetz et al. 2006; Kunder et al. 2016), specifically their fourth internal data release and fifth data release respectively (GES-iDR4 and RAVE-DR5). These methods of study were:

- Take a **spatial cut** and compare the simulated star particles. These particles can be thought of as stellar population particles which present the mean properties of a stellar cluster who share similar ages and metallicities.
- As well as the spatial cut, we also apply **stochastic scattering** to the age and metal abundance properties of these stellar population particles. This is done to mimic the errors of measurements of ages and metal abundances in observational surveys.
- In addition to the stochastic scattering, we apply the *SynCMD* toolkit (Pasetto et al. 2012; Miranda et al. 2014) to match stellar population particle with a suitable stellar evolution isochrones. This allows us to generate synthetic stellar particles from these stellar population particles. We place a simulated observer in the galaxy in an equivalent solar neighbourhood region and apply the **observational selection functions** of RAVE and Gaia-ESO to select synthetic stars with observational properties, such as magnitude and surface gravity and compare with the respected observational data.

Each stage above is designed to further mimic the effects of observational surveys in each additional step. The stochastic scattering is aimed to mimic errors of observational surveys and the application of SYNCMD is designed to include photometric effects and selection functions. The focus of the study was to demonstrate the effects of different observational motivated analysis techniques. From doing this, our findings are:

CHAPTER 4

- We find a reasonable degree of agreement overall between the chemodynamical model employed within *RAMSES-CH* to generate chemical properties of a solar neighbourhood.
- Successive application of the post-processing techniques discussed above produce increasingly better distributions of ages and metal abundances that appear increasingly similar to observational surveys.
- The chemical evolution model employed in *RAMSES-CH* produces a simulated $[\text{Fe}/\text{H}]$ distribution that is narrow in comparison to observational surveys sampling a smaller region such as the Gaia-ESO survey. The application of scattering and SYNCMD broadens the $[\text{Fe}/\text{H}]$ abundances sufficiently to match the Gaia-ESO survey better.
- For larger volumes and with an abundance of giants such as RAVE, *RAMSES-CH* produces a more comparable $[\text{Fe}/\text{H}]$ abundance. However we underestimate the abundance of metal rich stars.
- However in both survey comparisons, *RAMSES-CH* generates a $[\text{Mg}/\text{Fe}]$ distribution that is too narrow.
- Scattering improves the fit with the age- $[\text{Fe}/\text{H}]$ and age- $[\text{Mg}/\text{Fe}]$ relations. The application of SYNCMD does little to improve upon the scattering other than truncate younger distribution of stars.
- The significance of SYNCMD does to light when comparing with different stellar populations abundances and properties. We successfully matched $[\text{Mg}/\text{Fe}]$ abundances for giant populations and are able to closely mimic the $[\text{Fe}/\text{H}]$ for giants. More work is needed to better fit different stellar populations, such as main sequence stars.

We conclude that it is overall important to reduce uncertainty in observed datasets to produce better comparable models of Galaxy formation. The impact of survey selection functions may have a sizeable effect on the results, but in the Gaia-ESO survey this has a relatively small effect. The inclusion of a survey selection function in a simulation is however good for comparing with stars on the giant branch, but more work is required to fit with other stellar populations.

4.2 Investigation of Halo Inflow and Disc Outflow via Disc-Driven Turbulence

We studied the evolution of a Milky Way-like galaxy in an isolated context using GIZMO. This was done with the absence of feedback models to study turbulent driven gas outflows. Primarily we studied the relation between the surface density of the gas disc and its relation to the gas outflow rate and the velocity dispersion of the gas disc. Our model additionally includes a cooling flow of hot gas halo particles which deposits gas into the central regions of the galaxy too.

Our methodology for this study involves the following:

- We generated a galaxy model in GalactICS based on observable parameters of the Milky Way.
- We used GIZMO to run this model for 600 Myr. We ran two simulations of the same model galaxy with two different temperature floors of 1000 K and 1500 K.
- We investigate morphological and evolution properties of the galaxy and its outflow rates.

We found:

CHAPTER 4

- In the absence of feedback, self-gravity is capable of driving outflows from the cold gas disc.
- Varying the temperature floor has a negligible impact on the outflow of the cold gas. Although this has an impact on the abundance of clouds, the variation in disc outflow is not affected at all.
- The relation of gas outflows versus surface density varies on the gas density environment. However the cooling flow of the hot gas halo appears to dampen the outflow rates in the denser regions.
- The physics of gas outflows in galaxy models differs from ideal models (e.g. Sur et al. 2016). But this is more of a consequence of the inclusion of more galactic components, rather than it being a failure in the model.
- We derive broadly similar vertical velocity dispersions for the gas to other work (e.g. Shetty & Ostriker 2008; Kim et al. 2013).

Our study reaffirms that the turbulence of the gas disc can lead to outflows. Although these outflows are very weak in evolved low surface-density discs.

4.3 Future Work

The field of galaxy formation is a broad and evolving topic. Although this thesis provides discussion of chemical evolution and gas outflows, our understanding of those topics, and indeed galaxy formation itself is by far from complete. From the work described in this thesis and as my time as a postgraduate student, we have identified potential subsequent topics of discussion that can be followed up from the work presented here.

From the study of our chemodynamical evolved galaxy and comparisons with observational surveys. We list topics for future study:

CHAPTER 4

- In §2.3.4 we briefly describe a parameter study varying physical feedback properties in RAMSES-CH. Due to time constraints, we were only able to focus on variations of the polytropic temperature $T_{\text{poly,th}}$ and the star formation threshold density $n_{\text{poly,th}}$ in sufficient detail. In reality, one can vary physical effects such as the spatial resolution, the star formation efficiency in addition to varying different modes of either kinetic, thermal or delayed cooling feedback. An extensive parameter study would require a large amount of high performance computing time and analytical time, which we're unable to do in this thesis. One could study the impact of the choice of physical and chemical evolution models on various galactic physical properties, kinematics and chemistry properties of the galaxy. Indeed a study on the impact of the choice of initial mass function and type Ia supernova properties is presented in Few et al. (2014). In the context of the work here, there may indeed be a better set of parameters that we have yet to discover that could best fit chemical properties from observational surveys.
- The current implementation of SYNCMD does not take into account of any sources of extinction such as dust. As observables of colour and magnitude are dependant on the level of extinction including extinction profiles for stellar population particles is important. Implementation wise, extinction is implemented in simulations through proxy of the hydrogen column density. For example the relation between the hydrogen number density and extinction A_V in the V band is $N_{\text{H}} \approx 1.8 \times 10^{21} \text{ cm}^{-2} \times A_V$ (Sparke & Gallagher 2007). Indeed implementations of computing the line of sight hydrogen column density has already been included in simulations (Price & Federrath 2010) and one could modify the inputs of SYNCMD to include the hydrogen density in the surrounding medium. The young stars are more dust reddened by the local environment and therefore in the Gaia-ESO survey are removed in that way.

CHAPTER 4

The young stars are preferentially in the disc and thus susceptible to removal from the observations through reddening. Both of these are dusty environments and therefore could be a contributing factor to the reduction of young stars too.

- Weak outflows are still driven with some disc material rising more than 1.5 kpc above the disc plane, although none of this material reaches the halo escape velocity.
- Further work could use SYNCMD as a means to test different initial mass functions and compare these with observational surveys. Additionally, rather than 100,000 stars in the IMF, the input composite mass should have some dependency on the IMF. More massive stellar population particles should in theory generate a larger abundance of synthetic stars upon applying SYNCMD. We do not take into account of the variation of stellar population particle birth mass in this work and assume this is the same. This is not an issue in this work since the majority of star particles have the same initial mass, and thus can all be weighted by the same number of synthetic stars.
- The application of stochastic scattering to the metal, age and other physical properties to the result of applying SYNCMD to *Selene-CH-G*. I.e. apply the scattering post-application of SYNCMD rather than before has not been explored. In theory this should yield similar results, but this has not been tested.
- The impact of the choice of stellar isochrones has not been explored. An example of another isochrone is found in Salasnich et al. (2000) and extended in Fu et al. (2015) or Marigo et al. (2017). These isochrones are actively being studied and with each iteration comes updates to stellar atmospheric modelling.

CHAPTER 4

- The impact of the choice of IMF shape has not been explored here either. Although it would not be unusual to think that the impact would be similar as previously studied in chemical evolution models such as Few et al. (2014).
- SYNCMD is capable of studying other observational surveys since the selection function is a set of input parameters. For instance, one could study the APOGEE survey (Eisenstein et al. 2011).

From the study of gas outflows, the topics for future study include:

- Due to time constraints, we did not have the chance to vary both the temperature floor and the softening length. Variations of these are thought to alter the abundance and properties of GMC's. Lower temperatures would increase GMC abundances and shorter softening length and since GMC's are turbulent drivers, this should increase turbulence. The investigation of higher temperature floors and softening lengths would be of interest too.
- These simulations are capable of quantifying outflow and velocity dispersion properties of galaxies. With future telescopes such as the JWST. One can model the properties of high redshift galaxies to understand what the JWST observes.
- The relation of outflows may not simply be directly related to the surface density. Our work here suggests that there may be more to it than just the surface density alone. Namely star formation rates, halo gas inflows and other feedback sources will have some impact on the outflow properties, as well as the evolution of metals and metal-based cooling. Investigating the physics of each of these one by one will allow us to probe their impact on the outflow rates of gas.
- Disc material, of which the majority of it resides in both the centre of the galaxy and giant molecular clouds were simulated to collapse beyond its Jeans

CHAPTER 4

limit. This was done as a means to provide a lower estimate for outflow rates since this will reduce interactions. Future simulations should look into modelling the GMC to be constrained to, or reside well above its Jeans limit. Varying this criteria will allow one to sample the range of outflows per surface density of the galaxy. This is essentially a mechanism that increases the cross sectional area of the GMC and the larger the cross sectional area the more interactions there will be.

Bibliography

- Abadi, M. G., Navarro, J. F., Steinmetz, M., & Eke, V. R. 2003, *Astrophys. J.*, 597, 21
- Abel, T. 2011, *Mon. Not. Roy. Astron. Soc.*, 413, 271
- Adelberger, K. L., Shapley, A. E., Steidel, C. C., et al. 2005, *Astrophys. J.*, 629, 636
- Adelberger, K. L., Steidel, C. C., Kollmeier, J. A., & Reddy, N. A. 2006, *Astrophys. J.*, 637, 74
- Agertz, O. & Kravtsov, A. V. 2015, *Astrophys. J.*, 804, 18
- Agertz, O., Kravtsov, A. V., Leitner, S. N., & Gnedin, N. Y. 2013, *Astrophys. J.*, 770, 25
- Agertz, O., Lake, G., Teyssier, R., et al. 2009a, *Mon. Not. Roy. Astron. Soc.*, 392, 294
- Agertz, O., Moore, B., Stadel, J., et al. 2007, *Mon. Not. Roy. Astron. Soc.*, 380, 963
- Agertz, O., Romeo, A. B., & Grisdale, K. 2015, *Mon. Not. Roy. Astron. Soc.*, 449, 2156

- Agertz, O., Teyssier, R., & Moore, B. 2009b, *Mon. Not. Roy. Astron. Soc.*, 397, L64
- Allende Prieto, C., Barklem, P. S., Lambert, D. L., & Cunha, K. 2004, *Astron. Astrophys.*, 420, 183
- Anathpindika, S. 2009, *Astron. Astrophys.*, 504, 451
- Anderson, L., Aubourg, É., Bailey, S., et al. 2014, *Mon. Not. Roy. Astron. Soc.*, 441, 24
- Andrews, B. H. & Martini, P. 2013, *Astrophys. J.*, 765, 140
- Andrews, B. H., Weinberg, D. H., Schönrich, R., & Johnson, J. A. 2016, ArXiv e-prints
- Anguiano, B., De Silva, G. M., Freeman, K., et al. 2016, *Mon. Not. Roy. Astron. Soc.*, 457, 2078
- Anguiano, B., Zucker, D. B., Scholz, R.-D., et al. 2015, *Mon. Not. Roy. Astron. Soc.*, 451, 1229
- Aristotle. 800 BC, *Meteorologica*
- Arnett, W. D. 1978, *Astrophys. J.*, 219, 1008
- Asplund, M., Grevesse, N., Sauval, A. J., & Scott, P. 2009, *Ann. Rev. Astron. Astrophys.*, 47, 481
- Aubert, D., Pichon, C., & Colombi, S. 2004, *Mon. Not. Roy. Astron. Soc.*, 352, 376
- Aumer, M., White, S. D. M., Naab, T., & Scannapieco, C. 2013, *Mon. Not. Roy. Astron. Soc.*, 434, 3142
- Baade, W. 1944, *Astrophys. J.*, 100, 137

- Bahl, H. & Baumgardt, H. 2014, *Mon. Not. Roy. Astron. Soc.*, 438, 2916
- Barnes, J. E. 1988, *Astrophys. J.*, 331, 699
- Barnes, J. E. 1992, *Astrophys. J.*, 393, 484
- Barnes, J. E. & Hernquist, L. 1992, *Ann. Rev. Astron, Astrophys.*, 30, 705
- Barnes, J. E. & Hernquist, L. E. 1991, *Astrophys. J. Letters*, 370, L65
- Barth, T., J. D. 1989, 366
- Battaglia, G., Helmi, A., Morrison, H., et al. 2005, *Mon. Not. Roy. Astron. Soc.*, 364, 433
- Bauermeister, A., Blitz, L., & Ma, C.-P. 2010, *Astrophys. J.*, 717, 323
- Baugh, C. M., Cole, S., & Frenk, C. S. 1996, *Mon. Not. Roy. Astron. Soc.*, 283, 1361
- Baugh, C. M., Lacey, C. G., Frenk, C. S., et al. 2005, *Mon. Not. Roy. Astron. Soc.*, 356, 1191
- Bazan, G. & Mathews, G. J. 1990, *Astrophys. J.*, 354, 644
- Bensby, T. & Feltzing, S. 2006, *Mon. Not. Roy. Astron. Soc.*, 367, 1181
- Benson, A. J., Baugh, C. M., Cole, S., Frenk, C. S., & Lacey, C. G. 2000, *Mon. Not. Roy. Astron. Soc.*, 316, 107
- Benson, A. J., Bower, R. G., Frenk, C. S., et al. 2003, *Astrophys. J.*, 599, 38
- Bergemann, M., Collet, R., Schoenrich, R., et al. 2016, ArXiv e-prints
- Bergemann, M., Kudritzki, R.-P., Gazak, Z., Davies, B., & Plez, B. 2015, *Astrophys. J.*, 804, 113

- Bergemann, M., Ruchti, G. R., Serenelli, A., et al. 2014, *Astron. Astrophys.*, 565, A89
- Berger, M. J. & Olinger, J. 1984, *Journal of Computational Physics*, 53, 484
- Bertelli, G., Girardi, L., Marigo, P., & Nasi, E. 2008, *Astron. Astrophys.*, 484, 815
- Bertelli, G., Nasi, E., Girardi, L., et al. 2003, *Astron. J.*, 125, 770
- Bertelli, G., Nasi, E., Girardi, L., & Marigo, P. 2009, *Astron. Astrophys.*, 508, 355
- Bertschinger, E. 1998, *Ann. Rev. Astron, Astrophys.*, 36, 599
- Bessell, M. S. 1990, *Pub. Astron. Soc. Pac.*, 102, 1181
- Bienaymé, O., Famaey, B., Siebert, A., et al. 2014, *Astron. Astrophys.*, 571, A92
- Bigiel, F., Leroy, A., Walter, F., et al. 2008, *Astron. J.*, 136, 2846
- Bijaoui, A., Recio-Blanco, A., De Laverny, P., & Ordenovic, C. 2012, *Statistical Methodology*, 9, 55
- Binney, J., Burnett, B., Kordopatis, G., et al. 2014, *Mon. Not. Roy. Astron. Soc.*, 437, 351
- Binney, J. & Tremaine, S. 1987, *Galactic dynamics*
- Bird, S., Vogelsberger, M., Haehnelt, M., et al. 2014, *Mon. Not. Roy. Astron. Soc.*, 445, 2313
- Blanchard, A., Valls-Gabaud, D., & Mamon, G. A. 1992, *Astron. Astrophys.*, 264, 365
- Blanton, M., Cen, R., Ostriker, J. P., Strauss, M. A., & Tegmark, M. 2000, *Astrophys. J.*, 531, 1

- Blumenthal, G. R., Faber, S. M., Primack, J. R., & Rees, M. J. 1984, *Nature*, 311, 517
- Blumenthal, G. R., Pagels, H., & Primack, J. R. 1982, *Nature*, 299, 37
- Boeche, C., Siebert, A., Williams, M., et al. 2011, *Astron. J.*, 142, 193
- Bolatto, A. D., Warren, S. R., Leroy, A. K., et al. 2013, *Nature*, 499, 450
- Bomans, D. J., Chu, Y.-H., & Hopp, U. 1997, *Astron. J.*, 113, 1678
- Bond, J. R., Efstathiou, G., & Silk, J. 1980, *Physical Review Letters*, 45, 1980
- Bond, J. R., Kofman, L., & Pogosyan, D. 1996, *Nature*, 380, 603
- Booth, C. M., Agertz, O., Kravtsov, A. V., & Gnedin, N. Y. 2013, *Astrophys. J. Letters*, 777, L16
- Bordoloi, R., Lilly, S. J., Hardmeier, E., et al. 2014, *Astrophys. J.*, 794, 130
- Bovy, J., Rix, H.-W., & Hogg, D. W. 2012, *Astrophys. J.*, 751, 131
- Bower, R. G., Benson, A. J., Malbon, R., et al. 2006, *Mon. Not. Roy. Astron. Soc.*, 370, 645
- Boylan-Kolchin, M., Bullock, J. S., & Kaplinghat, M. 2011, *Mon. Not. Roy. Astron. Soc.*, 415, L40
- Bresolin, F., Kudritzki, R.-P., Urbaneja, M. A., et al. 2016, *Astrophys. J.*, 830, 64
- Brook, C. B., Stinson, G., Gibson, B. K., Wadsley, J., & Quinn, T. 2012a, *Mon. Not. Roy. Astron. Soc.*, 424, 1275
- Brook, C. B., Stinson, G. S., Gibson, B. K., et al. 2012b, *Mon. Not. Roy. Astron. Soc.*, 426, 690

- Brooks, A. M., Kuhlen, M., Zolotov, A., & Hooper, D. 2013, *Astrophys. J.*, 765, 22
- Brooks, A. M., Solomon, A. R., Governato, F., et al. 2011, *Astrophys. J.*, 728, 51
- Bryan, G. L., Norman, M. L., O'Shea, B. W., et al. 2014, *Astrophys. J. Supple.*, 211, 19
- Burkert, A. 2006, *Comptes Rendus Physique*, 7, 433
- Burkert, A. & Bodenheimer, P. 1996, *Mon. Not. Roy. Astron. Soc.*, 280, 1190
- Calura, F., Gibson, B. K., Michel-Dansac, L., et al. 2012, *Mon. Not. Roy. Astron. Soc.*, 427, 1401
- Calura, F. & Menci, N. 2009, *Mon. Not. Roy. Astron. Soc.*, 400, 1347
- Carbon, D. F., Barbuy, B., Kraft, R. P., Friel, E. D., & Suntzeff, N. B. 1987, *Pub. Astron. Soc. Pac.*, 99, 335
- Carigi, L. 1994, *Astrophys. J.*, 424, 181
- Casagrande, L., Ramírez, I., Meléndez, J., Bessell, M., & Asplund, M. 2010, *Astron. Astrophys.*, 512, A54
- Casagrande, L., Schönrich, R., Asplund, M., et al. 2011, *Astron. Astrophys.*, 530, A138
- Castelli, F. & Kurucz, R. L. 2003, in IAU Symposium, Vol. 210, Modelling of Stellar Atmospheres, ed. N. Piskunov, W. W. Weiss, & D. F. Gray, A20
- Cattaneo, A., Blaizot, J., Devriendt, J., & Guiderdoni, B. 2005, *Mon. Not. Roy. Astron. Soc.*, 364, 407
- Cautun, M., Wang, W., Frenk, C. S., & Sawala, T. 2015, *Mon. Not. Roy. Astron. Soc.*, 449, 2576

- Cavaliere, A. & Fusco-Femiano, R. 1976, *Astron. Astrophys.*, 49, 137
- Cen, R. 1992, *Astrophys. J. Supple.*, 78, 341
- Ceverino, D., Dekel, A., & Bournaud, F. 2010, *Mon. Not. Roy. Astron. Soc.*, 404, 2151
- Chabrier, G. 2003, *Astrophys. J. Letters*, 586, L133
- Chamandy, L., Shukurov, A., Subramanian, K., & Stoker, K. 2014, *Mon. Not. Roy. Astron. Soc.*, 443, 1867
- Chandrasekhar, S. 1943, *Astrophys. J.*, 97, 255
- Chen, H.-W., Helsby, J. E., Gauthier, J.-R., et al. 2010, *Astrophys. J.*, 714, 1521
- Chevalier, R. A. & Clegg, A. W. 1985, *Nature*, 317, 44
- Chiappini, C., Matteucci, F., & Gratton, R. 1997, *Astrophys. J.*, 477, 765
- Chiappini, C., Matteucci, F., & Romano, D. 2001, *Astrophys. J.*, 554, 1044
- Chieffi, A. & Limongi, M. 2004, *Astrophys. J.*, 608, 405
- Chiosi, C. & Caimmi, R. 1979, *Astron. Astrophys.*, 80, 234
- Chisholm, J., Tremonti, C. A., Leitherer, C., et al. 2015, *The Astrophysical Journal*, 811, 149
- Clarke, C. J. 1989, *Mon. Not. Roy. Astron. Soc.*, 238, 283
- Clowe, D., Gonzalez, A., & Markevitch, M. 2004, *Astrophys. J.*, 604, 596
- Codis, S., Gavazzi, R., Dubois, Y., et al. 2015, *Mon. Not. Roy. Astron. Soc.*, 448, 3391
- Cole, S. 1991, *Astrophys. J.*, 367, 45

- Cole, S., Aragon-Salamanca, A., Frenk, C. S., Navarro, J. F., & Zepf, S. E. 1994, *Mon. Not. Roy. Astron. Soc.*, 271, 781
- Cole, S., Lacey, C. G., Baugh, C. M., & Frenk, C. S. 2000, *Mon. Not. Roy. Astron. Soc.*, 319, 168
- Colella, P. 1990, *Journal of Computational Physics*, 87, 171
- Colombi, S. 2013, AdaptaHOP: Subclump finder, Astrophysics Source Code Library
- Cooper, J. L., Bicknell, G. V., Sutherland, R. S., & Bland-Hawthorn, J. 2009, *Astrophys. J.*, 703, 330
- Côté, B., O’Shea, B. W., Ritter, C., Herwig, F., & Venn, K. A. 2017, *Astrophys. J.*, 835, 128
- Courant, R., Friedrichs, K., & Lewy, H. 1967, *IBM Journal of Research and Development*, 11, 215
- Cox, D. P. 1972, *Astrophys. J.*, 178, 159
- Crain, R. A., Schaye, J., Bower, R. G., et al. 2015, *Mon. Not. Roy. Astron. Soc.*, 450, 1937
- Crosby, B. D., O’Shea, B. W., Smith, B. D., Turk, M. J., & Hahn, O. 2013, *Astrophys. J.*, 773, 108
- Croton, D. J., Springel, V., White, S. D. M., et al. 2006, *Mon. Not. Roy. Astron. Soc.*, 365, 11
- Curtis, H. D. 1988, *Pub. Astron. Soc. Pac.*, 100, 6
- Czekaj, M. A., Robin, A. C., Figueras, F., Luri, X., & Haywood, M. 2014, *Astron. Astrophys.*, 564, A102

- Dalla Vecchia, C. & Schaye, J. 2008, *Mon. Not. Roy. Astron. Soc.*, 387, 1431
- Das, U. & Mukhopadhyay, B. 2013, *Physical Review Letters*, 110, 071102
- Davé, R., Oppenheimer, B. D., & Finlator, K. 2011, *Mon. Not. Roy. Astron. Soc.*, 415, 11
- Davé, R., Thompson, R. J., & Hopkins, P. F. 2016, ArXiv e-prints
- Davies, B., Kudritzki, R.-P., Bergemann, M., et al. 2015, *The Messenger*, 161, 32
- Davis, M., Efstathiou, G., Frenk, C. S., & White, S. D. M. 1985, *Astrophys. J.*, 292, 371
- Davis, M., Huchra, J., Latham, D. W., & Tonry, J. 1982, *Astrophys. J.*, 253, 423
- de Aveliz, M. A. & Breitschwerdt, D., eds. 2004a, *From Observations to Self-Consistent Modelling of the ISM in Galaxies*
- de Aveliz, M. A. & Breitschwerdt, D. 2004b, *Astron. Astrophys.*, 425, 899
- de Bernardis, P., Ade, P. A. R., Bock, J. J., et al. 2000, *Nature*, 404, 955
- de Blok, W. J. G. 2010, *Advances in Astronomy*, 2010, 789293
- de Jong, R. S. & Lacey, C. 2000, *Astrophys. J.*, 545, 781
- De Lucia, G., Kauffmann, G., & White, S. D. M. 2004, *Mon. Not. Roy. Astron. Soc.*, 349, 1101
- De Silva, G. M., Freeman, K. C., Bland-Hawthorn, J., et al. 2015, *Mon. Not. Roy. Astron. Soc.*, 449, 2604
- Dehnen, W. & Read, J. I. 2011, *European Physical Journal Plus*, 126, 55
- Dekel, A. & Silk, J. 1986, *Astrophys. J.*, 303, 39

- Dekker, H., D'Odorico, S., Kaufer, A., Delabre, B., & Kotzlowski, H. 2000, in , Vol. 4008, Optical and IR Telescope Instrumentation and Detectors, ed. M. Iye & A. F. Moorwood, 534–545
- Devriendt, J. E. G. & Guiderdoni, B. 2000, *Astron. Astrophys.*, 363, 851
- Di Cintio, A., Brook, C. B., Macciò, A. V., et al. 2014, *Mon. Not. Roy. Astron. Soc.*, 437, 415
- Di Matteo, T., Springel, V., & Hernquist, L. 2005, *Nature*, 433, 604
- Dib, S., Bell, E., & Burkert, A. 2006, *Astrophys. J.*, 638, 797
- Dickey, J. M., Hanson, M. M., & Helou, G. 1990, *Astrophys. J.*, 352, 522
- Dilts, G. A. 1999, *International Journal for Numerical Methods in Engineering*, 44, 1115
- Doherty, C. L., Siess, L., Lattanzio, J. C., & Gil-Pons, P. 2010, *Mon. Not. Roy. Astron. Soc.*, 401, 1453
- Dubinski, J., Gauthier, J.-R., Widrow, L., & Nickerson, S. 2008, in *Astronomical Society of the Pacific Conference Series*, Vol. 396, Formation and Evolution of Galaxy Disks, ed. J. G. Funes & E. M. Corsini, 321
- Dubois, Y. & Teyssier, R. 2008, *Astron. Astrophys.*, 477, 79
- Duffell, P. C. & MacFadyen, A. I. 2012, *Astrophys. J.*, 755, 7
- Edvardsson, B., Andersen, J., Gustafsson, B., et al. 1993a, *Astron. Astrophys.*, 275, 101
- Edvardsson, B., Andersen, J., Gustafsson, B., et al. 1993b, *Astron. Astrophys. Suppl.*, 102, 603

- Efstathiou, G. 2000, *Mon. Not. Roy. Astron. Soc.*, 317, 697
- Efstathiou, G., Sutherland, W. J., & Maddox, S. J. 1990, *Nature*, 348, 705
- Eggen, O. J., Lynden-Bell, D., & Sandage, A. R. 1962, *Astrophys. J.*, 136, 748
- Einasto, J., Saar, E., Kaasik, A., & Chernin, A. D. 1974, *Nature*, 252, 111
- Einstein, A. & de Sitter, W. 1932, Proceedings of the National Academy of Science, 18, 213
- Eisenstein, D. J., Weinberg, D. H., Agol, E., et al. 2011, *Astron. J.*, 142, 72
- Ellis, J., Hagelin, J. S., Nanopoulos, D. V., Olive, K., & Srednicki, M. 1984, Nuclear Physics B, 238, 453
- Elmegreen, B. G. & Scalo, J. 2004, *Ann. Rev. Astron. Astrophys.*, 42, 211
- Engel, H., Davies, R. I., Genzel, R., et al. 2010, *Astron. Astrophys.*, 524, A56
- Erb, D. K. 2008, *Astrophys. J.*, 674, 151
- Erb, D. K., Shapley, A. E., Pettini, M., et al. 2006, *Astrophys. J.*, 644, 813
- Ester, M., Kriegel, H. P., Jorg, S., , & Xu, X. 1996, PAAAI Press, 226
- Evrard, A. E. 1988, *Mon. Not. Roy. Astron. Soc.*, 235, 911
- Evrard, A. E., Summers, F. J., & Davis, M. 1994, *Astrophys. J.*, 422, 11
- Fall, S. M. & Efstathiou, G. 1980, *Mon. Not. Roy. Astron. Soc.*, 193, 189
- Faucher-Giguere, C.-A. 2016, ArXiv e-prints
- Faucher-Giguère, C.-A., Hopkins, P. F., Kereš, D., et al. 2015, *Mon. Not. Roy. Astron. Soc.*, 449, 987
- Feltzing, S. & Chiba, M. 2013, , 57, 80

- Ferland, G. J., Korista, K. T., Verner, D. A., et al. 1998, *Pub. Astron. Soc. Pac.*, 110, 761
- Ferrara, A., Scannapieco, E., & Bergeron, J. 2005, *Astrophys. J. Letters*, 634, L37
- Few, C. G. 2012, PhD thesis, University of Central Lancashire (United Kingdom)
- Few, C. G., Courty, S., Gibson, B. K., et al. 2012a, *Mon. Not. Roy. Astron. Soc.*, 424, L11
- Few, C. G., Courty, S., Gibson, B. K., Michel-Dansac, L., & Calura, F. 2014, *Mon. Not. Roy. Astron. Soc.*, 444, 3845
- Few, C. G., Dobbs, C., Pettitt, A., & Konstandin, L. 2016, *Mon. Not. Roy. Astron. Soc.*, 460, 4382
- Few, C. G., Gibson, B. K., Courty, S., et al. 2012b, *Astron. Astrophys.*, 547, A63
- Finlator, K. & Davé, R. 2008, *Mon. Not. Roy. Astron. Soc.*, 385, 2181
- Fleck, Jr., R. C. 1981, *Astrophys. J. Letters*, 246, L151
- Flores, R. A. & Primack, J. R. 1994, *Astrophys. J. Letters*, 427, L1
- Fragile, P. C., Anninos, P., Gustafson, K., & Murray, S. D. 2005, *Astrophys. J.*, 619, 327
- François, P., Matteucci, F., Cayrel, R., et al. 2004, *Astron. Astrophys.*, 421, 613
- Franx, M., Illingworth, G. D., Kelson, D. D., van Dokkum, P. G., & Tran, K.-V. 1997, *Astrophys. J. Letters*, 486, L75
- Freeman, K. & Bland-Hawthorn, J. 2002, *Ann. Rev. Astron. Astrophys.*, 40, 487
- Frenk, C. S., Evrard, A. E., White, S. D. M., & Summers, F. J. 1996, *Astrophys. J.*, 472, 460

- Frenk, C. S., White, S. D. M., Bode, P., et al. 1999, *Astrophys. J.*, 525, 554
- Frenk, C. S., White, S. D. M., Davis, M., & Efstathiou, G. 1988, *Astrophys. J.*, 327, 507
- Frenk, C. S., White, S. D. M., Efstathiou, G., & Davis, M. 1985, *Nature*, 317, 595
- Frenk, C. S., White, S. D. M., Efstathiou, G., & Davis, M. 1990, *Astrophys. J.*, 351, 10
- Frye, B., Broadhurst, T., & Benítez, N. 2002, *Astrophys. J.*, 568, 558
- Fu, X., Bressan, A., Marigo, P., Girardi, L., & Lanza, A. 2015, IAU General Assembly, 22, 2254821
- Fujita, A., Mac Low, M.-M., Ferrara, A., & Meiksin, A. 2004, *Astrophys. J.*, 613, 159
- Fukunaga, M. & Tosa, M. 1989, *Pub. Astron. Soc. Japan*, 41, 241
- Gaburov, E. & Nitadori, K. 2011, *Mon. Not. Roy. Astron. Soc.*, 414, 129
- Galilei, G. 1610, Sidereus nuncius magna, longeque admirabilia spectacula pandens lunae facie, fixis innumeris, lacteo circulo, stellis nebulosis, ... Galileo Galileo : nuper a se reperti beneficio sunt observata in apprime vero in quatuor planetis circa Iovis stellam disparibus intervallis, atque periodis, celeritate mirabili circumvolutis ... atque Medicea sidera nuncupandos decrevit
- Galilei, G. 1989, Sidereus nuncius, or, The Sidereal messenger
- Gammie, C. F. 2001, *Astrophys. J.*, 553, 174
- Gammie, C. F., Ostriker, J. P., & Jog, C. J. 1991, *Astrophys. J.*, 378, 565
- Gatto, A., Walch, S., Low, M.-M. M., et al. 2015, *Mon. Not. Roy. Astron. Soc.*, 449, 1057

- Genel, S., Dekel, A., & Cacciato, M. 2012a, *Mon. Not. Roy. Astron. Soc.*, 425, 788
- Genel, S., Naab, T., Genzel, R., et al. 2012b, *Astrophys. J.*, 745, 11
- Genzel, R., Newman, S., Jones, T., et al. 2011, *Astrophys. J.*, 733, 101
- Gerritsen, J. P. E. & Icke, V. 1997, *Astron. Astrophys.*, 325, 972
- Gibson, B. K., Pilkington, K., Brook, C. B., Stinson, G. S., & Bailin, J. 2013, *Astron. Astrophys.*, 554, A47
- Gill, S. P. D., Knebe, A., & Gibson, B. K. 2004, *Mon. Not. Roy. Astron. Soc.*, 351, 399
- Gilmore, G., Randich, S., Asplund, M., et al. 2012, *The Messenger*, 147, 25
- Gilmore, G. & Reid, N. 1983, *Mon. Not. Roy. Astron. Soc.*, 202, 1025
- Gilmore, G., Wyse, R. F. G., & Kuijken, K. 1989, *Ann. Rev. Astron. Astrophys.*, 27, 555
- Gingold, R. A. & Monaghan, J. J. 1977, *Mon. Not. Roy. Astron. Soc.*, 181, 375
- Giovagnoli, A. & Tosi, M. 1995, *Mon. Not. Roy. Astron. Soc.*, 273, 499
- Girardi, L., Bertelli, G., Bressan, A., et al. 2002, *Astron. Astrophys.*, 391, 195
- Girichidis, P., Walch, S., Naab, T., et al. 2016, *Mon. Not. Roy. Astron. Soc.*, 456, 3432
- Gittins, D. M., Clarke, C. J., & Bate, M. R. 2003, *Mon. Not. Roy. Astron. Soc.*, 340, 841
- Gnedin, N. Y., Tassis, K., & Kravtsov, A. V. 2009, *Astrophys. J.*, 697, 55
- Godunov, S. K. 1959, *Math. Sbornik*, 47, 271

- Gonzalez, A. H., Zaritsky, D., & Zabludoff, A. I. 2007, *The Astrophysical Journal*, 666, 147
- Governato, F., Brook, C., Mayer, L., et al. 2010, *Nature*, 463, 203
- Governato, F., Mayer, L., Wadsley, J., et al. 2004, *Astrophys. J.*, 607, 688
- Governato, F., Willman, B., Mayer, L., et al. 2007, *Mon. Not. Roy. Astron. Soc.*, 374, 1479
- Governato, F., Zolotov, A., Pontzen, A., et al. 2012, *Mon. Not. Roy. Astron. Soc.*, 422, 1231
- Granato, G. L., De Zotti, G., Silva, L., Bressan, A., & Danese, L. 2004, *Astrophys. J.*, 600, 580
- Gregori, G., Miniati, F., Ryu, D., & Jones, T. W. 1999, *Astrophys. J. Letters*, 527, L113
- Gregori, G., Miniati, F., Ryu, D., & Jones, T. W. 2000, *Astrophys. J.*, 543, 775
- Gresho, P. M. & Chan, S. T. 1990, *International Journal for Numerical Methods in Fluids*, 11, 621
- Grevesse, N. & Sauval, A. J. 1998, *Space Sci. Rev.*, 85, 161
- Grimes, J. P., Heckman, T., Strickland, D., & Ptak, A. 2005, *Astrophys. J.*, 628, 187
- Guedes, J., Callegari, S., Madau, P., & Mayer, L. 2011, *Astrophys. J.*, 742, 76
- Guo, Q., White, S., Li, C., & Boylan-Kolchin, M. 2010, *Mon. Not. Roy. Astron. Soc.*, 404, 1111
- Gustafsson, B., Edvardsson, B., Eriksson, K., et al. 2008, *Astron. Astrophys.*, 486, 951

- Guth, A. H. & Pi, S.-Y. 1982, *Physical Review Letters*, 49, 1110
- Haardt, F. & Madau, P. 1996, *Astrophys. J.*, 461, 20
- Hachisu, I., Kato, M., & Nomoto, K. 1999, *Astrophys. J.*, 522, 487
- Hanany, S., Ade, P., Balbi, A., et al. 2000, *Astrophys. J. Letters*, 545, L5
- Hanasz, M., Lesch, H., Naab, T., et al. 2013, *Astrophys. J. Letters*, 777, L38
- Harikane, Y., Ouchi, M., Yuma, S., et al. 2014, *Astrophys. J.*, 794, 129
- Harris, J. & Zaritsky, D. 2001, *Astrophys. J. Supple.*, 136, 25
- Hatton, S., Devriendt, J. E. G., Ninin, S., et al. 2003, *Mon. Not. Roy. Astron. Soc.*, 343, 75
- Hawking, S. W. 1982, *Physics Letters B*, 115, 295
- Hawkins, K., Kordopatis, G., Gilmore, G., et al. 2015, *Mon. Not. Roy. Astron. Soc.*, 447, 2046
- Heckman, T. M. 2003, in *Revista Mexicana de Astronomia y Astrofisica Conference Series*, Vol. 17, *Revista Mexicana de Astronomia y Astrofisica Conference Series*, ed. V. Avila-Reese, C. Firmani, C. S. Frenk, & C. Allen, 47–55
- Heckman, T. M., Armus, L., & Miley, G. K. 1990, *Astrophys. J. Supple.*, 74, 833
- Heckman, T. M. e. 2014
- Heiter, U., Jofré, P., Gustafsson, B., et al. 2015, *Astron. Astrophys.*, 582, A49
- Heiter, U., Soubiran, C., Netopil, M., & Paunzen, E. 2014, *Astron. Astrophys.*, 561, A93
- Henley, D. B. & Shelton, R. L. 2012, *Astrophys. J. Supple.*, 202, 14

- Hennebelle, P. & Iffrig, O. 2014, *Astron. Astrophys.*, 570, A81
- Henry, R. B. C., Kwitter, K. B., Jaskot, A. E., et al. 2010, *Astrophys. J.*, 724, 748
- Hernquist, L. 1993, *Astrophys. J. Supple.*, 86, 389
- Hernquist, L. & Katz, N. 1989, *Astrophys. J. Supple.*, 70, 419
- Hernquist, L. & Quinn, P. J. 1988, *Astrophys. J.*, 331, 682
- Herschel, W. 1785, Philosophical Transactions of the Royal Society of London Series I, 75, 213
- Hill, A. S., Joung, M. R., Mac Low, M.-M., et al. 2012, *Astrophys. J.*, 750, 104
- Hinshaw, G., Larson, D., Komatsu, E., et al. 2013, *Astrophys. J. Supple.*, 208, 19
- Hockney, R. W. & Eastwood, J. W. 1981, Computer Simulation Using Particles
- Hoffmann, V. & Romeo, A. B. 2012, *Mon. Not. Roy. Astron. Soc.*, 425, 1511
- Holmberg, J., Nordström, B., & Andersen, J. 2007, *Astron. Astrophys.*, 475, 519
- Holmberg, J., Nordström, B., & Andersen, J. 2009, *Astron. Astrophys.*, 501, 941
- Hopkins, P. F. 2013, *Mon. Not. Roy. Astron. Soc.*, 428, 2840
- Hopkins, P. F. 2015, *Mon. Not. Roy. Astron. Soc.*, 450, 53
- Hopkins, P. F., Kereš, D., Oñorbe, J., et al. 2014, *Mon. Not. Roy. Astron. Soc.*, 445, 581
- Hopkins, P. F., Quataert, E., & Murray, N. 2011, *Mon. Not. Roy. Astron. Soc.*, 417, 950
- Hopkins, P. F., Quataert, E., & Murray, N. 2012a, *Mon. Not. Roy. Astron. Soc.*, 421, 3522

- Hopkins, P. F., Quataert, E., & Murray, N. 2012b, *Mon. Not. Roy. Astron. Soc.*, 421, 3488
- Hoskin, M. 2002, *Journal for the History of Astronomy*, 33, 57
- Hubble, E. 1926a, *Contributions from the Mount Wilson Observatory / Carnegie Institution of Washington*, 324, 1
- Hubble, E. P. 1926b, *Astrophys. J.*, 64
- Hubble, E. P. 1927, *The Observatory*, 50, 276
- Hubble, E. P. 1929, *Astrophys. J.*, 69
- Hubble, E. P. 1936, *Realm of the Nebulae*
- Huchra, J. & Brodie, J. 1987, *Astron. J.*, 93, 779
- Huchra, J. P., Macri, L. M., Masters, K. L., et al. 2012, *Astrophys. J. Supple.*, 199, 26
- Hunt, J. A. S., Kawata, D., Grand, R. J. J., et al. 2015, *Mon. Not. Roy. Astron. Soc.*, 450, 2132
- Iben, Jr., I. & Truran, J. W. 1978, *Astrophys. J.*, 220, 980
- Iben, Jr., I. & Tutukov, A. V. 1984, *Astrophys. J. Supple.*, 54, 335
- Imaeda, Y. & Inutsuka, S.-i. 2002, *Astrophys. J.*, 569, 501
- Immeli, A., Samland, M., Gerhard, O., & Westera, P. 2004, *Astron. Astrophys.*, 413, 547
- Ivanova, N., Justham, S., Chen, X., et al. 2013, *Astron. Astrophys. Rev.*, 21, 59
- Iwamoto, K., Brachwitz, F., Nomoto, K., et al. 1999, *Astrophys. J. Supple.*, 125, 439

- Izzard, R. G., Tout, C. A., Karakas, A. I., & Pols, O. R. 2004, *Mon. Not. Roy. Astron. Soc.*, 350, 407
- Jeans, J. H. 1902, Philosophical Transactions of the Royal Society of London Series A, 199, 1
- Jeans, J. H. 1928, Astronomy and cosmogony
- Jenkins, A., Frenk, C. S., Pearce, F. R., et al. 1998, *Astrophys. J.*, 499, 20
- Jessop, C., Duncan, M., & Chau, W. Y. 1994, Journal of Computational Physics, 115, 339
- Jofré, P., Heiter, U., Soubiran, C., et al. 2015, *Astron. Astrophys.*, 582, A81
- Jofré, P., Heiter, U., Soubiran, C., et al. 2014, *Astron. Astrophys.*, 564, A133
- Joung, M. K. R. & Mac Low, M.-M. 2006, *Astrophys. J.*, 653, 1266
- Kant, I. 1755, Allgemeine Naturgeschichte und Theorie des Himmels
- Karakas, A. & Lattanzio, J. C. 2007, *Pub. Astron. Soc. Australia*, 24, 103
- Karakas, A. I. 2010, *Mon. Not. Roy. Astron. Soc.*, 403, 1413
- Katz, N. 1992, *Astrophys. J.*, 391, 502
- Katz, N., Hernquist, L., & Weinberg, D. H. 1992, *Astrophys. J. Letters*, 399, L109
- Katz, N., Weinberg, D. H., & Hernquist, L. 1996, *Astrophys. J. Supple.*, 105, 19
- Kauffmann, G., Colberg, J. M., Diaferio, A., & White, S. D. M. 1999, *Mon. Not. Roy. Astron. Soc.*, 303, 188
- Kauffmann, G., White, S. D. M., & Guiderdoni, B. 1993, *Mon. Not. Roy. Astron. Soc.*, 264, 201

- Kaufmann, T., Mayer, L., Wadsley, J., Stadel, J., & Moore, B. 2007, *Mon. Not. Roy. Astron. Soc.*, 375, 53
- Kawata, D. & Gibson, B. K. 2003, *Mon. Not. Roy. Astron. Soc.*, 340, 908
- Kay, S. T., Pearce, F. R., Frenk, C. S., & Jenkins, A. 2002, *Mon. Not. Roy. Astron. Soc.*, 330, 113
- Kennicutt, Jr., R. C. 1998a, *Ann. Rev. Astron. Astrophys.*, 36, 189
- Kennicutt, Jr., R. C. 1998b, *Astrophys. J.*, 498, 541
- Kereš, D., Katz, N., Davé, R., Fardal, M., & Weinberg, D. H. 2009, *Mon. Not. Roy. Astron. Soc.*, 396, 2332
- Kessel-Deynet, O. & Burkert, A. 2003, *Mon. Not. Roy. Astron. Soc.*, 338, 545
- Khokhlov, A. 1998, *Journal of Computational Physics*, 143, 519
- Kim, C.-G., Kim, W.-T., & Ostriker, E. C. 2011, *Astrophys. J.*, 743, 25
- Kim, C.-G. & Ostriker, E. C. 2015, *Astrophys. J.*, 802, 99
- Kim, C.-G., Ostriker, E. C., & Kim, W.-T. 2013, *Astrophys. J.*, 776, 1
- Kim, J.-h., Abel, T., Agertz, O., et al. 2014, *Astrophys. J. Supple.*, 210, 14
- Kim, J.-h., Agertz, O., Teyssier, R., et al. 2016, ArXiv e-prints
- Kim, W.-T. & Ostriker, E. C. 2001, *Astrophys. J.*, 559, 70
- Kim, W.-T. & Ostriker, E. C. 2007, *Astrophys. J.*, 660, 1232
- Kim, W.-T., Ostriker, E. C., & Stone, J. M. 2002, *Astrophys. J.*, 581, 1080
- Kitsionas, S. & Whitworth, A. P. 2007, *Mon. Not. Roy. Astron. Soc.*, 378, 507
- Klein, R. I., McKee, C. F., & Colella, P. 1994, *Astrophys. J.*, 420, 213

- Klypin, A., Kravtsov, A. V., Valenzuela, O., & Prada, F. 1999, *Astrophys. J.*, 522, 82
- Knollmann, S. R. & Knebe, A. 2009, *Astrophys. J. Supple.*, 182, 608
- Kobayashi, C. 2004, *Mon. Not. Roy. Astron. Soc.*, 347, 740
- Kobayashi, C. & Nakasato, N. 2011, *Astrophys. J.*, 729, 16
- Kobayashi, C., Tsujimoto, T., & Nomoto, K. 2000, *Astrophys. J.*, 539, 26
- Kobayashi, C., Umeda, H., Nomoto, K., Tominaga, N., & Ohkubo, T. 2006, *Astrophys. J.*, 653, 1145
- Kodama, T. 1997, PhD thesis, PhD thesis, Institute of Astronomy, Univ. Tokyo , (1997)
- Kodama, T. & Arimoto, N. 1997, *Astron. Astrophys.*, 320, 41
- Kordopatis, G. 2014, in SF2A-2014: Proceedings of the Annual meeting of the French Society of Astronomy and Astrophysics, ed. J. Ballet, F. Martins, F. Bournaud, R. Monier, & C. Reyl e, 431–435
- Kordopatis, G., Binney, J., Gilmore, G., et al. 2015, *Mon. Not. Roy. Astron. Soc.*, 447, 3526
- Kordopatis, G., Gilmore, G., Steinmetz, M., et al. 2013a, *Astron. J.*, 146, 134
- Kordopatis, G., Gilmore, G., Wyse, R. F. G., et al. 2013b, *Mon. Not. Roy. Astron. Soc.*, 436, 3231
- Kordopatis, G., Recio-Blanco, A., de Laverny, P., et al. 2011, *Astron. Astrophys.*, 535, A106
- Kormendy, J. & Bender, R. 1996, *Astrophys. J. Letters*, 464, L119

- Kormendy, J. & Djorgovski, S. 1989, *Ann. Rev. Astron. Astrophys.*, 27, 235
- Kormendy, J., Fisher, D. B., Cornell, M. E., & Bender, R. 2009, *Astrophys. J. Supple.*, 182, 216
- Kos, J., Zwitter, T., Wyse, R., et al. 2014, *Science*, 345, 791
- Kravtsov, A. V. & Klypin, A. A. 1999, *Astrophys. J.*, 520, 437
- Kravtsov, A. V., Klypin, A. A., & Khokhlov, A. M. 1997, *Astrophys. J. Supple.*, 111, 73
- Kroupa, P. 2001, *Mon. Not. Roy. Astron. Soc.*, 322, 231
- Kroupa, P., Theis, C., & Boily, C. M. 2005, *Astron. Astrophys.*, 431, 517
- Kroupa, P., Tout, C. A., & Gilmore, G. 1993, *Mon. Not. Roy. Astron. Soc.*, 262, 545
- Kuhnert, J. 2003, *Lecture Notes in Computational Science and Engineering*, Vol. 26, *Meshfree Methods for Partial Differential Equations*, ed. M. Griebel M. Schweitzer, 239–249
- Kuijken, K. & Dubinski, J. 1995, *Mon. Not. Roy. Astron. Soc.*, 277, 1341
- Kunder, A., Bono, G., Piffl, T., et al. 2014, *Astron. Astrophys.*, 572, A30
- Kunder, A., Kordopatis, G., Steinmetz, M., et al. 2016, ArXiv e-prints
- Kwak, K., Henley, D. B., & Shelton, R. L. 2011, *Astrophys. J.*, 739, 30
- Lacey, C. & Silk, J. 1991, *Astrophys. J.*, 381, 14
- Lacey, C. G. & Fall, S. M. 1983, *Mon. Not. Roy. Astron. Soc.*, 204, 791
- Lanson, N. & Vila, J. P. 2008a, *SIAM J. Numer. Anal.*, 46, 1912

- Lanson, N. & Vila, J. P. 2008b, *SIAM J. Numer. Anal.*, 46, 1935
- Lara-López, M. A., Hopkins, A. M., López-Sánchez, A. R., et al. 2013, *Mon. Not. Roy. Astron. Soc.*, 433, L35
- Larson, D., Dunkley, J., Hinshaw, G., et al. 2011, *Astrophys. J. Supple.*, 192, 16
- Larson, R. B. 1972, *Nature*, 236, 21
- Larson, R. B. 1974, *Mon. Not. Roy. Astron. Soc.*, 169, 229
- Larson, R. B. 1981, *Mon. Not. Roy. Astron. Soc.*, 194, 809
- Larson, R. B. 1998, *Mon. Not. Roy. Astron. Soc.*, 301, 569
- Leroy, A. K., Walter, F., Brinks, E., et al. 2008, *Astron. J.*, 136, 2782
- Lia, C., Portinari, L., & Carraro, G. 2002, *Mon. Not. Roy. Astron. Soc.*, 330, 821
- Libeskind, N. I., Frenk, C. S., Cole, S., et al. 2005, *Mon. Not. Roy. Astron. Soc.*, 363, 146
- Libeskind, N. I., Frenk, C. S., Cole, S., Jenkins, A., & Helly, J. C. 2009, *Mon. Not. Roy. Astron. Soc.*, 399, 550
- Libeskind, N. I., Hoffman, Y., Tully, R. B., et al. 2015, *Mon. Not. Roy. Astron. Soc.*, 452, 1052
- Libeskind, N. I., Knebe, A., Hoffman, Y., & Gottlöber, S. 2014, *Mon. Not. Roy. Astron. Soc.*, 443, 1274
- Libeskind, N. I., Knebe, A., Hoffman, Y., et al. 2011, *Mon. Not. Roy. Astron. Soc.*, 411, 1525
- Limongi, M. & Chieffi, A. 2003, *Astrophys. J.*, 592, 404

- Lin, D. N. C. & Pringle, J. E. 1987, *Astrophys. J. Letters*, 320, L87
- Linde, A. D. 1982a, *Physics Letters B*, 108, 389
- Linde, A. D. 1982b, *Physics Letters B*, 116, 335
- Lovell, M. R., Eke, V., Frenk, C. S., et al. 2012, *Mon. Not. Roy. Astron. Soc.*, 420, 2318
- Lovell, M. R., Eke, V. R., Frenk, C. S., & Jenkins, A. 2011, *Mon. Not. Roy. Astron. Soc.*, 413, 3013
- Lovell, M. R., Frenk, C. S., Eke, V. R., et al. 2014, *Mon. Not. Roy. Astron. Soc.*, 439, 300
- Lucy, L. B. 1977, *Astron. J.*, 82, 1013
- Luo, H., Baum, J. D., & Löhner, R. 2008, *Journal of Computational Physics*, 227, 8875
- Lupi, A., Haardt, F., Dotti, M., et al. 2016, *Mon. Not. Roy. Astron. Soc.*, 456, 2993
- Mac Low, M.-M. & Ferrara, A. 1999, *Astrophys. J.*, 513, 142
- Mac Low, M.-M. & Klessen, R. S. 2004, *Reviews of Modern Physics*, 76, 125
- Mac Low, M.-M., McCray, R., & Norman, M. L. 1989, *Astrophys. J.*, 337, 141
- Mac Low, M.-M. & Zahnle, K. 1994, *Astrophys. J. Letters*, 434, L33
- Macciò, A. V. & Fontanot, F. 2010, *Mon. Not. Roy. Astron. Soc.*, 404, L16
- Macciò, A. V., Paduroiu, S., Anderhalden, D., Schneider, A., & Moore, B. 2012a, *Mon. Not. Roy. Astron. Soc.*, 424, 1105
- Macciò, A. V., Stinson, G., Brook, C. B., et al. 2012b, *Astrophys. J. Letters*, 744, L9

- Maddison, S. T., Murray, J. R., & Monaghan, J. J. 1996, *Pub. Astron. Soc. Australia*, 13, 66
- Maeder, A. 1992, *Astron. Astrophys.*, 264, 105
- Maeder, A. & Meynet, G. 1989, *Astron. Astrophys.*, 210, 155
- Maller, A. H. & Dekel, A. 2002, *Mon. Not. Roy. Astron. Soc.*, 335, 487
- Mannucci, F., Cresci, G., Maiolino, R., Marconi, A., & Gnerucci, A. 2010, *Mon. Not. Roy. Astron. Soc.*, 408, 2115
- Mannucci, F., Della Valle, M., & Panagia, N. 2006, *Mon. Not. Roy. Astron. Soc.*, 370, 773
- Maoz, D., Mannucci, F., & Nelemans, G. 2014, *Ann. Rev. Astron. Astrophys.*, 52, 107
- Marcolini, A., Strickland, D. K., D'Ercole, A., Heckman, T. M., & Hoopes, C. G. 2005, *Mon. Not. Roy. Astron. Soc.*, 362, 626
- Marigo, P. 2001, *Astron. Astrophys.*, 370, 194
- Marigo, P. & Girardi, L. 2007, *Astron. Astrophys.*, 469, 239
- Marigo, P., Girardi, L., Bressan, A., et al. 2017, ArXiv e-prints
- Marinacci, F., Binney, J., Fraternali, F., et al. 2010, *Mon. Not. Roy. Astron. Soc.*, 404, 1464
- Marinacci, F., Fraternali, F., Nipoti, C., et al. 2011, *Mon. Not. Roy. Astron. Soc.*, 415, 1534
- Maron, J. L. & Howes, G. G. 2003, *Astrophys. J.*, 595, 564

- Maron, J. L., McNally, C. P., & Mac Low, M.-M. 2012, *Astrophys. J. Supple.*, 200, 6
- Martin, C. L. 1999, *Astrophys. J.*, 513, 156
- Martin, C. L. 2005, *Astrophys. J.*, 621, 227
- Martin, C. L., Scannapieco, E., Ellison, S. L., et al. 2010, *Astrophys. J.*, 721, 174
- Martin, C. L., Shapley, A. E., Coil, A. L., et al. 2012, *Astrophys. J.*, 760, 127
- Martin, C. L., Shapley, A. E., Coil, A. L., et al. 2013, *Astrophys. J.*, 770, 41
- Martínez-Serrano, F. J., Serna, A., Domínguez-Tenreiro, R., & Mollá, M. 2008, *Mon. Not. Roy. Astron. Soc.*, 388, 39
- Martizzi, D., Faucher-Giguère, C.-A., & Quataert, E. 2015, *Mon. Not. Roy. Astron. Soc.*, 450, 504
- Mastropietro, C., Moore, B., Mayer, L., Wadsley, J., & Stadel, J. 2005, *Mon. Not. Roy. Astron. Soc.*, 363, 509
- Mathews, W. G. 1978, *Astrophys. J.*, 219, 413
- Mathews, W. G. & Baker, J. C. 1971, *Astrophys. J.*, 170, 241
- Matijević, G., Zwitter, T., Bienaymé, O., et al. 2012, *Astrophys. J. Supple.*, 200, 14
- Matteucci, F. & Francois, P. 1989, *Mon. Not. Roy. Astron. Soc.*, 239, 885
- Matzner, C. D. 2002, *Astrophys. J.*, 566, 302
- McKee, C. F. & Ostriker, J. P. 1977, *Astrophys. J.*, 218, 148
- McMillan, P. J. 2011, *Mon. Not. Roy. Astron. Soc.*, 414, 2446
- McNally, C. P., Lyra, W., & Passy, J.-C. 2012, *Astrophys. J. Supple.*, 201, 18

- Melioli, C., de Gouveia dal Pino, E. M., & Raga, A. 2005, *Astron. Astrophys.*, 443, 495
- Mellema, G., Kurk, J. D., & Röttgering, H. J. A. 2002, *Astron. Astrophys.*, 395, L13
- Merle, T., Thévenin, F., Pichon, B., & Bigot, L. 2011, *Mon. Not. Roy. Astron. Soc.*, 418, 863
- Messier, C. 1781, Catalogue des Nébuleuses & des amas d'Étoiles (Catalog of Nebulae and Star Clusters), Tech. rep.
- Metz, M., Kroupa, P., & Jerjen, H. 2009, *Mon. Not. Roy. Astron. Soc.*, 394, 2223
- Metz, M., Kroupa, P., & Libeskind, N. I. 2008, *Astrophys. J.*, 680, 287
- Metzler, C. A. & Evrard, A. E. 1994, *Astrophys. J.*, 437, 564
- Meusinger, H., Stecklum, B., & Reimann, H.-G. 1991, *Astron. Astrophys.*, 245, 57
- Michael, D. G., Adamson, P., Alexopoulos, T., et al. 2006, *Physical Review Letters*, 97, 191801
- Mihos, J. C. & Hernquist, L. 1994a, *Astrophys. J.*, 437, 611
- Mihos, J. C. & Hernquist, L. 1994b, *Astrophys. J. Letters*, 425, L13
- Mihos, J. C. & Hernquist, L. 1996, *Astrophys. J.*, 464, 641
- Minchev, I., Chiappini, C., Martig, M., et al. 2014, *Astrophys. J. Letters*, 781, L20
- Miranda, M. S., Macfarlane, B. A., & Gibson, B. K. 2014, in *Proceedings of XIII Nuclei in the Cosmos (NIC XIII)*, 149
- Miranda, M. S., Pilkington, K., Gibson, B. K., et al. 2016, *Astron. Astrophys.*, 587, A10

- Miyoshi, T. & Kusano, K. 2005, *Journal of Computational Physics*, 208, 315
- Mo, H., van den Bosch, F. C., & White, S. 2010, *Galaxy Formation and Evolution*
- Mocz, P., Vogelsberger, M., Sijacki, D., Pakmor, R., & Hernquist, L. 2014, *Mon. Not. Roy. Astron. Soc.*, 437, 397
- Mollá, M., Cavichia, O., Gavilán, M., & Gibson, B. K. 2015, *Mon. Not. Roy. Astron. Soc.*, 451, 3693
- Monaco, P. 2004, *Mon. Not. Roy. Astron. Soc.*, 352, 181
- Monaco, P. & Fontanot, F. 2005, *Mon. Not. Roy. Astron. Soc.*, 359, 283
- Monaghan, J. J. 1992, *Ann. Rev. Astron. Astrophys.*, 30, 543
- Moore, B., Ghigna, S., Governato, F., et al. 1999, *Astrophys. J. Letters*, 524, L19
- Mori, M., Yoshii, Y., Tsujimoto, T., & Nomoto, K. 1997, *Astrophys. J. Letters*, 478, L21
- Mosconi, M. B., Tissera, P. B., Lambas, D. G., & Cora, S. A. 2001, *Mon. Not. Roy. Astron. Soc.*, 325, 34
- Moster, B. P., Macciò, A. V., Somerville, R. S., Naab, T., & Cox, T. J. 2011, *Mon. Not. Roy. Astron. Soc.*, 415, 3750
- Moster, B. P., Naab, T., & White, S. D. M. 2013, *Mon. Not. Roy. Astron. Soc.*, 428, 3121
- Moster, B. P., Somerville, R. S., Maulbetsch, C., et al. 2010, *Astrophys. J.*, 710, 903
- Mulchaey, J. S. & Stocke, J. T., eds. 2002, *Astronomical Society of the Pacific Conference Series*, Vol. 254, *Extragalactic gas at low redshift : proceedings of a*

- workshop : held at Carnegie Observatories, Pasadena, California, USA, 4-6 April 2001, ed. J. S. Mulchaey & J. T. Stocke
- Muldrew, S. I., Croton, D. J., Skibba, R. A., et al. 2012, *Mon. Not. Roy. Astron. Soc.*, 419, 2670
- Munari, U., Henden, A., Frigo, A., et al. 2014, *Astron. J.*, 148, 81
- Murray, N. 2011, *Astrophys. J.*, 729, 133
- Murray, N., Ménard, B., & Thompson, T. A. 2011, *Astrophys. J.*, 735, 66
- Murray, N., Quataert, E., & Thompson, T. A. 2010, *Astrophys. J.*, 709, 191
- Navarro, J. F. & Benz, W. 1991, *Astrophys. J.*, 380, 320
- Navarro, J. F., Frenk, C. S., & White, S. D. M. 1995, *Mon. Not. Roy. Astron. Soc.*, 275, 56
- Navarro, J. F. & Steinmetz, M. 1997, *Astrophys. J.*, 478, 13
- Navarro, J. F. & Steinmetz, M. 2000, *Astrophys. J.*, 538, 477
- Navarro, J. F. & White, S. D. M. 1993, *Mon. Not. Roy. Astron. Soc.*, 265, 271
- Nelson, D., Genel, S., Vogelsberger, M., et al. 2015, *Mon. Not. Roy. Astron. Soc.*, 448, 59
- Nittmann, J., Falle, S. A. E. G., & Gaskell, P. H. 1982, *Mon. Not. Roy. Astron. Soc.*, 201, 833
- Noh, W. F. 1987, *Journal of Computational Physics*, 72, 78
- Nomoto, K., Thielemann, F.-K., & Wheeler, J. C. 1984, *Astrophys. J. Letters*, 279, L23

- Norberg, P., Baugh, C. M., Hawkins, E., et al. 2002, *Mon. Not. Roy. Astron. Soc.*, 332, 827
- Nordström, B., Mayor, M., Andersen, J., et al. 2004, *Astron. Astrophys.*, 418, 989
- Okamoto, T., Eke, V. R., Frenk, C. S., & Jenkins, A. 2005, *Mon. Not. Roy. Astron. Soc.*, 363, 1299
- Okamoto, T., Jenkins, A., Eke, V. R., Quilis, V., & Frenk, C. S. 2003, *Mon. Not. Roy. Astron. Soc.*, 345, 429
- Oliver, S. J., Bock, J., Altieri, B., et al. 2012, *Mon. Not. Roy. Astron. Soc.*, 424, 1614
- Oppenheimer, B. D. & Davé, R. 2008, *Mon. Not. Roy. Astron. Soc.*, 387, 577
- Orlando, S., Bocchino, F., Peres, G., et al. 2006, *Astron. Astrophys.*, 457, 545
- Orlando, S., Bocchino, F., Reale, F., Peres, G., & Pagano, P. 2008, *Astrophys. J.*, 678, 274
- Orlando, S., Peres, G., Reale, F., et al. 2005, *Astron. Astrophys.*, 444, 505
- O'Shea, B. W., Nagamine, K., Springel, V., Hernquist, L., & Norman, M. L. 2005, *Astrophys. J. Supple.*, 160, 1
- Ostriker, J. P. & Peebles, P. J. E. 1973, *Astrophys. J.*, 186, 467
- Ostriker, J. P., Peebles, P. J. E., & Yahil, A. 1974, *Astrophys. J. Letters*, 193, L1
- Padovani, P. & Matteucci, F. 1993, *Astrophys. J.*, 416, 26
- Pagel, B. E. J. 1997, *Nucleosynthesis and Chemical Evolution of Galaxies*, 392
- Pagel, B. E. J. & Patchett, B. E. 1975, *Mon. Not. Roy. Astron. Soc.*, 172, 13

- Pagel, B. E. J. & Tautvaisiene, G. 1995, *Mon. Not. Roy. Astron. Soc.*, 276, 505
- Pakmor, R. & Springel, V. 2013, *Mon. Not. Roy. Astron. Soc.*, 432, 176
- Panter, B., Jimenez, R., Heavens, A. F., & Charlot, S. 2007, *Mon. Not. Roy. Astron. Soc.*, 378, 1550
- Papastergis, E., Giovanelli, R., Haynes, M. P., & Shankar, F. 2015, *Astron. Astrophys.*, 574, A113
- Pasetto, S., Chiosi, C., & Kawata, D. 2012, *Astron. Astrophys.*, 545, A14
- Patrick, L. R., Evans, C. J., Davies, B., et al. 2017, ArXiv e-prints
- Pawlowski, M. S. & McGaugh, S. S. 2014, *Astrophys. J. Letters*, 789, L24
- Pawlowski, M. S., Pflamm-Altenburg, J., & Kroupa, P. 2012, *Mon. Not. Roy. Astron. Soc.*, 423, 1109
- Pearce, F. R., Jenkins, A., Frenk, C. S., et al. 1999, *Astrophys. J. Letters*, 521, L99
- Pecaut, M. J. & Mamajek, E. E. 2013, *Astrophys. J. Supple.*, 208, 9
- Peebles, P. J. E. 1969, *Astrophys. J.*, 155, 393
- Peebles, P. J. E. 1980, The large-scale structure of the universe
- Perez, J., Michel-Dansac, L., & Tissera, P. B. 2011, *Mon. Not. Roy. Astron. Soc.*, 417, 580
- Perlmutter, S., Aldering, G., Goldhaber, G., et al. 1999, *Astrophys. J.*, 517, 565
- Petric, A. O. & Rupen, M. P. 2007, *Astron. J.*, 134, 1952
- Pettini, M., Shapley, A. E., Steidel, C. C., et al. 2001, *Astrophys. J.*, 554, 981
- Pichon, C., Scannapieco, E., Aracil, B., et al. 2003, *Astrophys. J. Letters*, 597, L97

- Piffel, T., Binney, J., McMillan, P. J., et al. 2014a, *Mon. Not. Roy. Astron. Soc.*, 445, 3133
- Piffel, T., Scannapieco, C., Binney, J., et al. 2014b, *Astron. Astrophys.*, 562, A91
- Pilkington, K., Few, C. G., Gibson, B. K., et al. 2012a, *Astron. Astrophys.*, 540, A56
- Pilkington, K., Gibson, B. K., Brook, C. B., et al. 2012b, *Mon. Not. Roy. Astron. Soc.*, 425, 969
- Piontek, F. & Steinmetz, M. 2011, *Mon. Not. Roy. Astron. Soc.*, 410, 2625
- Pipino, A., Devriendt, J. E. G., Thomas, D., Silk, J., & Kaviraj, S. 2009, *Astron. Astrophys.*, 505, 1075
- Planck Collaboration, Ade, P. A. R., Aghanim, N., et al. 2014a, *Astron. Astrophys.*, 571, A15
- Planck Collaboration, Ade, P. A. R., Aghanim, N., et al. 2014b, *Astron. Astrophys.*, 571, A16
- Prantzos, N. & Aubert, O. 1995, *Astron. Astrophys.*, 302, 69
- Preskill, J., Wise, M. B., & Wilczek, F. 1983, *Physics Letters B*, 120, 127
- Press, W. H. & Schechter, P. 1974, *Astrophys. J.*, 187, 425
- Price, D. J. & Federrath, C. 2010, *Mon. Not. Roy. Astron. Soc.*, 406, 1659
- Price, D. J. & Monaghan, J. J. 2007, *Mon. Not. Roy. Astron. Soc.*, 374, 1347
- Prochaska, J. X. & Wolfe, A. M. 2009, *Astrophys. J.*, 696, 1543
- Prugniel, P. & Simien, F. 1997, *Astron. Astrophys.*, 321, 111

- Querejeta, M., Eliche-Moral, M. C., Tapia, T., et al. 2015, *Astron. Astrophys.*, 573, A78
- Quinn, P. J., Hernquist, L., & Fullagar, D. P. 1993, *Astrophys. J.*, 403, 74
- Rafikov, R. R. 2009, *Astrophys. J.*, 704, 281
- Rahimi, A., Kawata, D., Brook, C. B., & Gibson, B. K. 2010, *Mon. Not. Roy. Astron. Soc.*, 401, 1826
- Ramírez, I., Allende Prieto, C., & Lambert, D. L. 2007, *Astron. Astrophys.*, 465, 271
- Randich, S., Gilmore, G., & Gaia-ESO Consortium. 2013, *The Messenger*, 154, 47
- Rasmussen, J., Sommer-Larsen, J., Pedersen, K., et al. 2009, *Astrophys. J.*, 697, 79
- Rauch, M., Haehnelt, M. G., & Steinmetz, M. 1997, *Astrophys. J.*, 481, 601
- Read, J. I., Agertz, O., & Collins, M. L. M. 2016, *Mon. Not. Roy. Astron. Soc.*, 459, 2573
- Read, J. I., Lake, G., Agertz, O., & Debattista, V. P. 2008, *Mon. Not. Roy. Astron. Soc.*, 389, 1041
- Recchi, S. & Hensler, G. 2007, *Astron. Astrophys.*, 476, 841
- Recio-Blanco, A., Bijaoui, A., & de Laverny, P. 2006, *Mon. Not. Roy. Astron. Soc.*, 370, 141
- Reddy, B. E., Lambert, D. L., & Allende Prieto, C. 2006, *Mon. Not. Roy. Astron. Soc.*, 367, 1329
- Rees, M. J. & Ostriker, J. P. 1977, *Mon. Not. Roy. Astron. Soc.*, 179, 541

- Renda, A., Fenner, Y., Gibson, B. K., et al. 2004, *Mon. Not. Roy. Astron. Soc.*, 354, 575
- Revaz, Y., Arnaudon, A., Nichols, M., Bonvin, V., & Jablonka, P. 2016, *Astron. Astrophys.*, 588, A21
- Ricciardelli, E., Quilis, V., & Planelles, S. 2013, *Mon. Not. Roy. Astron. Soc.*, 434, 1192
- Riess, A. G., Filippenko, A. V., Challis, P., et al. 1998, *Astron. J.*, 116, 1009
- Robertson, B., Yoshida, N., Springel, V., & Hernquist, L. 2004, *Astrophys. J.*, 606, 32
- Robertson, B. E. & Kravtsov, A. V. 2008, *Astrophys. J.*, 680, 1083
- Roe, P. L. 1981, *Journal of Computational Physics*, 43, 357
- Romaniello, M., Primas, F., Mottini, M., et al. 2008, *Astron. Astrophys.*, 488, 731
- Romano, D., Chiappini, C., Matteucci, F., & Tosi, M. 2005, *Astron. Astrophys.*, 430, 491
- Romeo, A. B. 1992, *Mon. Not. Roy. Astron. Soc.*, 256, 307
- Romeo, A. B., Burkert, A., & Agertz, O. 2010, *Mon. Not. Roy. Astron. Soc.*, 407, 1223
- Romeo, A. B. & Falstad, N. 2013, *Mon. Not. Roy. Astron. Soc.*, 433, 1389
- Romeo, A. D., Portinari, L., & Sommer-Larsen, J. 2005, *Mon. Not. Roy. Astron. Soc.*, 361, 983
- Rosen, A. & Bregman, J. N. 1995, *Astrophys. J.*, 440, 634

- Roškar, R., Debattista, V. P., Quinn, T. R., Stinson, G. S., & Wadsley, J. 2008, *Astrophys. J. Letters*, 684, L79
- Rubin, V. C. & Ford, Jr., W. K. 1970, *Astrophys. J.*, 159, 379
- Ruiz-Lara, T., Few, C. G., Gibson, B. K., et al. 2016, *Astron. Astrophys.*, 586, A112
- Rupke, D. S., Veilleux, S., & Sanders, D. B. 2005, *Astrophys. J. Supple.*, 160, 115
- Sahijpal, S. 2013, *Journal of Astrophysics and Astronomy*, 34, 297
- Saito, M. 1979, *Pub. Astron. Soc. Japan*, 31, 193
- Saitoh, T. R. & Makino, J. 2009, *Astrophys. J. Letters*, 697, L99
- Saitoh, T. R. & Makino, J. 2013, *Astrophys. J.*, 768, 44
- Salasnich, B., Girardi, L., Weiss, A., & Chiosi, C. 2000, *Astron. Astrophys.*, 361, 1023
- Salem, M. & Bryan, G. L. 2014, *Mon. Not. Roy. Astron. Soc.*, 437, 3312
- Salpeter, E. E. 1955, *Astrophys. J.*, 121, 161
- Saltzman, J. 1994, *Journal of Computational Physics*, 115, 153
- Samui, S., Subramanian, K., & Srianand, R. 2010, *Mon. Not. Roy. Astron. Soc.*, 402, 2778
- Sánchez-Blázquez, P., Courty, S., Gibson, B. K., & Brook, C. B. 2009, *Mon. Not. Roy. Astron. Soc.*, 398, 591
- Sawala, T., Frenk, C. S., Fattahi, A., et al. 2014, ArXiv e-prints
- Sawala, T., Frenk, C. S., Fattahi, A., et al. 2015, *Mon. Not. Roy. Astron. Soc.*, 448, 2941

- Scalo, J. 1998, in Astronomical Society of the Pacific Conference Series, Vol. 142, The Stellar Initial Mass Function (38th Herstmonceux Conference), ed. G. Gilmore & D. Howell, 201
- Scalo, J. M. 1986, *Fundamentals of Cosmic Physic*, 11, 1
- Scannapieco, C., Tissera, P. B., White, S. D. M., & Springel, V. 2005, *Mon. Not. Roy. Astron. Soc.*, 364, 552
- Scannapieco, C., White, S. D. M., Springel, V., & Tissera, P. B. 2009, *Mon. Not. Roy. Astron. Soc.*, 396, 696
- Scannapieco, E. 2013, *Astrophys. J. Letters*, 763, L31
- Scannapieco, E. & Brüggen, M. 2010, *Mon. Not. Roy. Astron. Soc.*, 405, 1634
- Scannapieco, E. & Brüggen, M. 2015, *Astrophys. J.*, 805, 158
- Scannapieco, E., Ferrara, A., & Madau, P. 2002, *Astrophys. J.*, 574, 590
- Scannapieco, E., Gray, W. J., & Pan, L. 2012, *Astrophys. J.*, 746, 57
- Scannapieco, E., Pichon, C., Aracil, B., et al. 2006a, *Mon. Not. Roy. Astron. Soc.*, 366, 1118
- Scannapieco, E., Pichon, C., Aracil, B., et al. 2006b, *Mon. Not. Roy. Astron. Soc.*, 365, 615
- Scannapieco, E., Thacker, R. J., & Davis, M. 2001, *Astrophys. J.*, 557, 605
- Schaye, J., Aguirre, A., Kim, T.-S., et al. 2003, *Astrophys. J.*, 596, 768
- Schaye, J., Crain, R. A., Bower, R. G., et al. 2015, *Mon. Not. Roy. Astron. Soc.*, 446, 521

- Schmidt, M. 1956, Bulletin of the Astronomical Institutes of the Netherlands., 13, 15
- Schmidt, M. 1959, *Astrophys. J.*, 129, 243
- Schmidt, M. 1963, *Astrophys. J.*, 137, 758
- Schneider, A., Anderhalden, D., Macciò, A. V., & Diemand, J. 2014, *Mon. Not. Roy. Astron. Soc.*, 441, L6
- Schönrich, R. & McMillan, P. J. 2017, *Mon. Not. Roy. Astron. Soc.*
- Schuster, K. F., Kramer, C., Hitschfeld, M., Garcia-Burillo, S., & Mookerjea, B. 2007, *Astron. Astrophys.*, 461, 143
- Searle, L. & Zinn, R. 1978, *Astrophys. J.*, 225, 357
- Sedov, L. I. 1959, Similarity and Dimensional Methods in Mechanics
- Sellwood, J. A. & Merritt, D. 1994, *Astrophys. J.*, 425, 530
- Serenelli, A. M., Bergemann, M., Ruchti, G., & Casagrande, L. 2013, *Mon. Not. Roy. Astron. Soc.*, 429, 3645
- Shapley, H. 1918, *Pub. Astron. Soc. Pac.*, 30, 42
- Shapley, H. & Curtis, H. D. 1921, Bulletin of the National Research Council, Vol. 2, Part 3, No. 11, p. 171-217, 2, 171
- Shaposhnikov, M. 2008, Journal of Physics Conference Series, 136, 022045
- Shen, S., Madau, P., Aguirre, A., et al. 2012, *Astrophys. J.*, 760, 50
- Shen, S., Wadsley, J., & Stinson, G. 2010, *Mon. Not. Roy. Astron. Soc.*, 407, 1581
- Shetty, R. & Ostriker, E. C. 2008, *Astrophys. J.*, 684, 978

- Shetty, R. & Ostriker, E. C. 2012, *Astrophys. J.*, 754, 2
- Shin, M.-S., Stone, J. M., & Snyder, G. F. 2008, *Astrophys. J.*, 680, 336
- Shukurov, A., Sokoloff, D., Subramanian, K., & Brandenburg, A. 2006, *Astron. Astrophys.*, 448, L33
- Siebert, A., Williams, M. E. K., Siviero, A., et al. 2011, *Astron. J.*, 141, 187
- Sijacki, D. & Springel, V. 2006, *Mon. Not. Roy. Astron. Soc.*, 371, 1025
- Silk, J. 1977, *Astrophys. J.*, 211, 638
- Simcoe, R. A., Sargent, W. L. W., & Rauch, M. 2002, *Astrophys. J.*, 578, 737
- Simon, J. D. & Geha, M. 2007, *Astrophys. J.*, 670, 313
- Skibba, R. A., Sheth, R. K., Croton, D. J., et al. 2013, *Mon. Not. Roy. Astron. Soc.*, 429, 458
- Skibba, R. A., Smith, M. S. M., Coil, A. L., et al. 2014, *Astrophys. J.*, 784, 128
- Skillman, S. W., Warren, M. S., Turk, M. J., et al. 2014, ArXiv e-prints
- Skrutskie, M. F., Cutri, R. M., Stiening, R., et al. 2006, *Astron. J.*, 131, 1163
- Smiljanic, R., Korn, A. J., Bergemann, M., et al. 2014, *Astron. Astrophys.*, 570, A122
- Smith, B. D. 2007, PhD thesis, The Pennsylvania State University
- Smith, R., Duc, P. A., Bournaud, F., & Yi, S. K. 2016, *Astrophys. J.*, 818, 11
- Smith, R. J., Glover, S. C. O., Clark, P. C., Klessen, R. S., & Springel, V. 2014, *Mon. Not. Roy. Astron. Soc.*, 441, 1628
- Snaith, O., Haywood, M., Di Matteo, P., et al. 2015, *Astron. Astrophys.*, 578, A87

- Snaith, O. N., Bailin, J., Gibson, B. K., et al. 2016, *Mon. Not. Roy. Astron. Soc.*, 456, 3119
- Socrates, A., Davis, S. W., & Ramirez-Ruiz, E. 2008, *Astrophys. J.*, 687, 202
- Sofue, Y., Honma, M., & Omodaka, T. 2009, *Pub. Astron. Soc. Japan*, 61, 227
- Sokolowski, J. A. 2010, Monte Carlo Simulation, in *Modeling and Simulation Fundamentals: Theoretical Underpinnings and Practical Domain*
- Somerville, R. S. & Kolatt, T. S. 1999, *Mon. Not. Roy. Astron. Soc.*, 305, 1
- Somerville, R. S. & Primack, J. R. 1999, *Mon. Not. Roy. Astron. Soc.*, 310, 1087
- Somerville, R. S., Primack, J. R., & Faber, S. M. 2001, *Mon. Not. Roy. Astron. Soc.*, 320, 504
- Sommer-Larsen, J. & Fynbo, J. P. U. 2008, *Mon. Not. Roy. Astron. Soc.*, 385, 3
- Songaila, A. & Cowie, L. L. 1996, *Astron. J.*, 112, 335
- Soto, K. T., Martin, C. L., Prescott, M. K. M., & Armus, L. 2012, *Astrophys. J.*, 757, 86
- Sparke, L. S. & Gallagher, III, J. S. 2007, *Galaxies in the Universe: An Introduction* (Cambridge University Press)
- Springel, V. 2005, *Mon. Not. Roy. Astron. Soc.*, 364, 1105
- Springel, V. 2010a, *Mon. Not. Roy. Astron. Soc.*, 401, 791
- Springel, V. 2010b, *Ann. Rev. Astron. Astrophys.*, 48, 391
- Springel, V. & Hernquist, L. 2002, *Mon. Not. Roy. Astron. Soc.*, 333, 649
- Springel, V. & Hernquist, L. 2003, *Mon. Not. Roy. Astron. Soc.*, 339, 312

- Springel, V., White, S. D. M., Jenkins, A., et al. 2005, *Nature*, 435, 629
- Stark, A. A. & Brand, J. 1989, *Astrophys. J.*, 339, 763
- Starobinsky, A. A. 1982, *Physics Letters B*, 117, 175
- Steidel, C. C., Erb, D. K., Shapley, A. E., et al. 2010, *Astrophys. J.*, 717, 289
- Steinmetz, M. & Mueller, E. 1993, ArXiv Astrophysics e-prints
- Steinmetz, M. & Muller, E. 1995, *Mon. Not. Roy. Astron. Soc.*, 276, 549
- Steinmetz, M., Zwitter, T., Siebert, A., et al. 2006, *Astron. J.*, 132, 1645
- Stinson, G., Seth, A., Katz, N., et al. 2006, *Mon. Not. Roy. Astron. Soc.*, 373, 1074
- Stinson, G. S., Bailin, J., Couchman, H., et al. 2010, *Mon. Not. Roy. Astron. Soc.*, 408, 812
- Stinson, G. S., Brook, C., Macciò, A. V., et al. 2013, *Mon. Not. Roy. Astron. Soc.*, 428, 129
- Stinson, G. S., Brook, C., Prochaska, J. X., et al. 2012, *Mon. Not. Roy. Astron. Soc.*, 425, 1270
- Stone, J. M., Gardiner, T. A., Teuben, P., Hawley, J. F., & Simon, J. B. 2008, *Astrophys. J. Supple.*, 178, 137
- Stonkutè, E., Kaposov, S. E., Howes, L. M., et al. 2016, *Mon. Not. Roy. Astron. Soc.*, 460, 1131
- Strickland, D. K. & Heckman, T. M. 2007, *Astrophys. J.*, 658, 258
- Strickland, D. K. & Heckman, T. M. 2009, *Astrophys. J.*, 697, 2030
- Strickland, D. K. & Stevens, I. R. 2000, *Mon. Not. Roy. Astron. Soc.*, 314, 511

- Sturm, E., González-Alfonso, E., Veilleux, S., et al. 2011, *Astrophys. J. Letters*, 733, L16
- Suchkov, A. A., Balsara, D. S., Heckman, T. M., & Leitherer, C. 1994, *Astrophys. J.*, 430, 511
- Sur, S., Scannapieco, E., & Ostriker, E. C. 2016, *Astrophys. J.*, 818, 28
- Sur, S., Shukurov, A., & Subramanian, K. 2007, *Mon. Not. Roy. Astron. Soc.*, 377, 874
- Swinbank, A. M., Papadopoulos, P. P., Cox, P., et al. 2011, *Astrophys. J.*, 742, 11
- Tacconi, L. J., Neri, R., Chapman, S. C., et al. 2006, *Astrophys. J.*, 640, 228
- Talbot, Jr., R. J. & Arnett, W. D. 1971, *Astrophys. J.*, 170, 409
- Tantalo, R., Chinellato, S., Merlin, E., Piovan, L., & Chiosi, C. 2010, *Astron. Astrophys.*, 518, A43
- Tasker, E. J., Brunino, R., Mitchell, N. L., et al. 2008, *Mon. Not. Roy. Astron. Soc.*, 390, 1267
- Tasker, E. J. & Tan, J. C. 2009, *Astrophys. J.*, 700, 358
- Taylor, G. 1950, Proceedings of the Royal Society of London Series A, 201, 159
- Tegmark, M. 1996, The Astrophysical Journal Letters, 464, L35
- Tegmark, M. & Zaldarriaga, M. 2002, *Phys. Rev. D*, 66, 103508
- Tenorio-Tagle, G. & Muñoz-Tuñón, C. 1998, *Mon. Not. Roy. Astron. Soc.*, 293, 299
- Terzić, B. & Graham, A. W. 2005, *Mon. Not. Roy. Astron. Soc.*, 362, 197
- Teyssier, R. 2002, *Astron. Astrophys.*, 385, 337

- Teyssier, R., Chièze, J.-P., & Alimi, J.-M. 1998, *Astrophys. J.*, 509, 62
- Teyssier, R., Moore, B., Martizzi, D., Dubois, Y., & Mayer, L. 2011, *Mon. Not. Roy. Astron. Soc.*, 414, 195
- Teyssier, R., Pontzen, A., Dubois, Y., & Read, J. I. 2013, *Mon. Not. Roy. Astron. Soc.*, 429, 3068
- Thacker, R. J. & Couchman, H. M. P. 2000, *Astrophys. J.*, 545, 728
- Thacker, R. J., Tittley, E. R., Pearce, F. R., Couchman, H. M. P., & Thomas, P. A. 2000, *Mon. Not. Roy. Astron. Soc.*, 319, 619
- Thomas, D., Maraston, C., Bender, R., & Mendes de Oliveira, C. 2005, *Astrophys. J.*, 621, 673
- Thompson, R. 2014, pyGadgetReader: GADGET snapshot reader for python, Astrophysics Source Code Library
- Thompson, T. A., Quataert, E., & Murray, N. 2005, *Astrophys. J.*, 630, 167
- Timmes, F. X., Woosley, S. E., & Weaver, T. A. 1995, *Astrophys. J. Supple.*, 98, 617
- Tinsley, B. M. 1980, *Fundamentals of Cosmic Physics*, 5, 287
- Tissera, P. B., Machado, R. E. G., Sanchez-Blazquez, P., et al. 2016, *Astron. Astrophys.*, 592, A93
- Tissera, P. B., White, S. D. M., & Scannapieco, C. 2012, *Mon. Not. Roy. Astron. Soc.*, 420, 255
- Tolstoy, E., Hill, V., & Tosi, M. 2009, *Ann. Rev. Astron. Astrophys.*, 47, 371
- Tomkin, J., Lambert, D. L., & Balachandran, S. 1985, *Astrophys. J.*, 290, 289

- Tonry, J. & Davis, M. 1979, *Astron. J.*, 84, 1511
- Toomre, A. 1964, *Astrophys. J.*, 139, 1217
- Toomre, A. & Toomre, J. 1972, *Astrophys. J.*, 178, 623
- Tornatore, L., Borgani, S., Matteucci, F., Recchi, S., & Tozzi, P. 2004, *Mon. Not. Roy. Astron. Soc.*, 349, L19
- Toro, E. 1997, Chemical enrichment in cosmological, smoothed particle hydrodynamics simulations
- Toro, E. 1999, Chemical enrichment in cosmological, smoothed particle hydrodynamics simulations, 2nd ed.
- Tosi, M. 1982, *Astrophys. J.*, 254, 699
- Tremonti, C. A., Heckman, T. M., Kauffmann, G., et al. 2004, *Astrophys. J.*, 613, 898
- Trenti, M. & Hut, P. 2008, ArXiv e-prints
- Truelove, J. K., Klein, R. I., McKee, C. F., et al. 1997, *Astrophys. J. Letters*, 489, L179
- Turk, M. J., Smith, B. D., Oishi, J. S., et al. 2011, *Astrophys. J. Supple.*, 192, 9
- Tyson, J. A., Valdes, F., & Wenk, R. A. 1990, *Astrophys. J. Letters*, 349, L1
- Tytler, D., Fan, X.-M., Burles, S., et al. 1995, in QSO Absorption Lines, ed. G. Meylan, 289
- Uhlig, M., Pfrommer, C., Sharma, M., et al. 2012, *Mon. Not. Roy. Astron. Soc.*, 423, 2374
- Valdarnini, R. 2003, *Mon. Not. Roy. Astron. Soc.*, 339, 1117

- Valentini, M., Chiappini, C., Davies, G. R., et al. 2016, ArXiv e-prints
- van de Voort, F., Quataert, E., Hopkins, P. F., Kereš, D., & Faucher-Giguère, C.-A. 2015, *Mon. Not. Roy. Astron. Soc.*, 447, 140
- van de Voort, F., Schaye, J., Booth, C. M., Haas, M. R., & Dalla Vecchia, C. 2011, *Mon. Not. Roy. Astron. Soc.*, 414, 2458
- van den Bergh, S. 1962, *Astron. J.*, 67, 486
- van den Hoek, L. B. & Groenewegen, M. A. T. 1997, *Astron. Astrophys. Suppl.*, 123
- van Leer, B. 1984, *SIAM Journal on Scientific and Statistical Computing*, 5
- Veilleux, S., Cecil, G., & Bland-Hawthorn, J. 2005, *Ann. Rev. Astron, Astrophys.*, 43, 769
- Vilchez, J. M. & Esteban, C. 1996, *Mon. Not. Roy. Astron. Soc.*, 280, 720
- Vogelsberger, M., Genel, S., Springel, V., et al. 2014, *Nature*, 509, 177
- Vogelsberger, M., Sijacki, D., Kereš, D., Springel, V., & Hernquist, L. 2012, *Mon. Not. Roy. Astron. Soc.*, 425, 3024
- Vollmer, B. & Beckert, T. 2002, *Astron. Astrophys.*, 382, 872
- Vollmer, B. & Beckert, T. 2003, *Astron. Astrophys.*, 404, 21
- Wada, K., Meurer, G., & Norman, C. A. 2002, *Astrophys. J.*, 577, 197
- Wada, K. & Norman, C. A. 2007, *Astrophys. J.*, 660, 276
- Wadsley, J. W., Stadel, J., & Quinn, T. 2004, *New Astron.*, 9, 137
- Walch, S., Girichidis, P., Naab, T., et al. 2015, *Mon. Not. Roy. Astron. Soc.*, 454, 238

- Walker, I. R., Mihos, J. C., & Hernquist, L. 1996, *Astrophys. J.*, 460, 121
- Wallerstein, G. 1962, *Astrophys. J. Supple.*, 6, 407
- Walter, F., Weiss, A., & Scoville, N. 2002, *Astrophys. J. Letters*, 580, L21
- Wang, J., Kauffmann, G., Overzier, R., et al. 2011, *Mon. Not. Roy. Astron. Soc.*, 412, 1081
- Wang, J., Nardini, E., Fabbiano, G., et al. 2014, *Astrophys. J.*, 781, 55
- Webbink, R. F. 1984, *Astrophys. J.*, 277, 355
- Weiner, B. J., Coil, A. L., Prochaska, J. X., et al. 2009, *Astrophys. J.*, 692, 187
- Weiss, A. & Schlattl, H. 2008, *Astrophys. Space Sci.*, 316, 99
- Westmoquette, M. S., Smith, L. J., Gallagher, J. S., & Exter, K. M. 2009a, *Astrophys. Space Sci.*, 324, 187
- Westmoquette, M. S., Smith, L. J., Gallagher, III, J. S., et al. 2009b, *Astrophys. J.*, 696, 192
- Whelan, J. & Iben, Jr., I. 1973, *Astrophys. J.*, 186, 1007
- White, S. D. M., Davis, M., Efstathiou, G., & Frenk, C. S. 1987a, *Nature*, 330, 451
- White, S. D. M. & Frenk, C. S. 1991, *Astrophys. J.*, 379, 52
- White, S. D. M., Frenk, C. S., & Davis, M. 1983, *Astrophys. J. Letters*, 274, L1
- White, S. D. M., Frenk, C. S., Davis, M., & Efstathiou, G. 1987b, *Astrophys. J.*, 313, 505
- White, S. D. M., Navarro, J. F., Evrard, A. E., & Frenk, C. S. 1993, *Nature*, 366, 429

- White, S. D. M. & Rees, M. J. 1978, *Mon. Not. Roy. Astron. Soc.*, 183, 341
- Whitehurst, R. 1995, *Mon. Not. Roy. Astron. Soc.*, 277, 655
- Widrow, L. M. 2008, *Astrophys. J.*, 679, 1232
- Widrow, L. M. & Dubinski, J. 2005, *Astrophys. J.*, 631, 838
- Widrow, L. M., Pym, B., & Dubinski, J. 2008, *Astrophys. J.*, 679, 1239
- Wiersma, R. P. C., Schaye, J., & Theuns, T. 2011, *Mon. Not. Roy. Astron. Soc.*, 415, 353
- Wiersma, R. P. C., Schaye, J., Theuns, T., Dalla Vecchia, C., & Tornatore, L. 2009, *Mon. Not. Roy. Astron. Soc.*, 399, 574
- Wijesinghe, D. B., Hopkins, A. M., Brough, S., et al. 2012, *Mon. Not. Roy. Astron. Soc.*, 423, 3679
- Williams, J. P., Blitz, L., & McKee, C. F. 2000, *Protostars and Planets IV*, 97
- Williams, M. E. K., Steinmetz, M., Binney, J., et al. 2013, *Mon. Not. Roy. Astron. Soc.*, 436, 101
- Williamson, D. J. & Thacker, R. J. 2012, *Mon. Not. Roy. Astron. Soc.*, 421, 2170
- Williamson, D. J., Thacker, R. J., Scannapieco, E., & Brüggen, M. 2014, *Mon. Not. Roy. Astron. Soc.*, 441, 389
- Wojno, J., Kordopatis, G., Piffl, T., et al. 2017, *Mon. Not. Roy. Astron. Soc.*, 468, 3368
- Wojno, J., Kordopatis, G., Steinmetz, M., et al. 2016, *Mon. Not. Roy. Astron. Soc.*, 461, 4246

- Woods, R. M., Wadsley, J., Couchman, H. M. P., Stinson, G., & Shen, S. 2014, *Mon. Not. Roy. Astron. Soc.*, 442, 732
- Woodward, P. & Colella, P. 1984, *Journal of Computational Physics*, 54, 115
- Woodward, P. R. 1976, *Astrophys. J.*, 207, 484
- Woolley, S. E. & Weaver, T. A. 1995, *Astrophys. J. Supple.*, 101, 181
- Wright, T. 1750, *An original theory or new hypothesis of the universe : founded upon general phaenomena of the visible creation; and particularly the Via the laws of nature, and solving by mathematical principles : the Lactea ...compris'd in nine familiar letters from the author to his friendand : illustrated with upward of thirty graven and mezzotinto plates ...*
- Wurster, J. & Thacker, R. J. 2013, *Mon. Not. Roy. Astron. Soc.*, 431, 2513
- Wyse, R. F. G. & Gilmore, G. 1995, *Astron. J.*, 110, 2771
- Yahagi, H. & Yoshii, Y. 2001, *Astrophys. J.*, 558, 463
- Yanny, B., Rockosi, C., Newberg, H. J., et al. 2009, *Astron. J.*, 137, 4377
- Yates, R. M., Henriques, B., Thomas, P. A., et al. 2013, *Mon. Not. Roy. Astron. Soc.*, 435, 3500
- York, D. G., Adelman, J., Anderson, Jr., J. E., et al. 2000, *Astron. J.*, 120, 1579
- Zel'dovich, Y. B. 1970, *Astron. Astrophys.*, 5, 84
- Zhang, W. & MacFadyen, A. I. 2006, *Astrophys. J. Supple.*, 164, 255
- Zhao, G., Zhao, Y.-H., Chu, Y.-Q., Jing, Y.-P., & Deng, L.-C. 2012, *Research in Astronomy and Astrophysics*, 12, 723
- Zwicky, F. 1933, *Helvetica Physica Acta*, 6, 110

Zwitter, T., Siebert, A., Munari, U., et al. 2008, *Astron. J.*, 136, 421